DIAMOND RESORPTION MORPHOLOGY AS A FLUID PROXY IN DIAMOND-BEARING ENVIRONMENTS: CONSTRAINTS FROM EMPIRICAL AND EXPERIMENTAL STUDIES

by

Zhihai Zhang

Submitted in partial fulfilment of the requirements
for the degree of Doctor of Philosophy

at

Dalhousie University
Halifax, Nova Scotia
March 2016

TABLE OF CONTENTS

LIST OF TABLES

LIST OF FIGURES

ABSTRACT

Volatiles play significant roles in modifying the composition of sub-continental lithospheric mantle, in the formation, ascent and emplacement of kimberlites, and in diamond preservation. Despite of numerous studies the compositions of C-O-H fluids in the mantle and kimberlites remain uncertain due to limitations of conventional methods (e.g. fluid inclusions). Previous experimental studies have suggested that diamond resorption morphology has a great potential for constraining the composition of diamond etching C-O-H fluids.

My study investigates the internal and external factors on diamond resorption. I examined the morphologies of 733 diamonds from five Ekati kimberlite pipes (Canada), and internal properties (N contents and aggregation states, C isotopic composition, internal structures) of 82 diamonds. The lack of correlation between the internal properties in diamond outer rims and resorption morphologies suggests little effect of internal factors on resorption morphologies. Diamond dissolution experiments were conducted at 1-3 GPa and 1150 – 1400 ºC in C-O-H fluids with X_{CO2} =0 -1, monitored in-situ by synthetic fluid inclusions. Etch pits on {111} faces were measured with an atomic force microscope. The experimental results show that 1) a miscibility gap exists in the CO_2-H_2O-dominated system at 1250 ºC under 1 and 3 GPa, 2) circular pits form on tetrahexahedral faces in pure H_2O at 1 GPa buffered by MgO-forsterite, and 3) the bulk composition of C-O-H fluids controls the pressure effects on diamond rounding rates and resorption morphologies, including etch pits on {111} faces.

The combined empirical and experimental studies permit a new classification of diamonds based on resorption morphologies, suggest etch pits forming under a defect-initiated and condition-controlled kink mechanism, and demonstrate the condition-dependent resorption morphology as a robust semi-quantitative proxy of fluid composition in diamond-bearing environments. Application to the Ekati diamonds suggests that either pure CO_2 or carbonate melts acted as the metasomatic medium in the lithospheric mantle beneath the central Slave craton, and that the reconstructed pre-eruption column of the Ekati kimberlites show a “sandwich” structure beginning with a CO_2–rich fluid zone, followed by a H_2O-rich fluid zone and a magma zone at tail.

LIST OF ABBREVIATIONS AND SYMBOLS USED

General Abbreviations	
Abbreviation	Description
SCLM	Subcontinental Lithospheric Mantle
RVK	Resedimented Volcaniclastic Kimberlite
MVK	Massive Volcaniclastic Kimberlite
CK	Coherent Kimberlite
Ol	Olivine
Qtz	Quartz
Prv	Perovskite
P	Pressure in GPa
T	Temperature in Celsius
f_{O2}	Oxygen Fugacity
NNO	Nickle-Nickle Oxide Assemblage
FMQ	Fayalite-Magnetite-Quartz Assemblage
X	Fluid composition
CS	Calcite + SiO_2
CMS	Calcite +MgO+ SiO_2
MSCH-1	$MgO+SiO_2+H_2C_2O_4$
MSCH-2	$MgO+SiO_2+H_2C_2O_4 \cdot 2H_2O$
P_{vol}	Proportion of the Vapour to Inclusions Volume
T_m^{ice}	Ice Melting Temperature
L_{carb}	Carbonic Liquid
L_{aq}	Aqueous Liquid
V_{carb}	Carbonic Vapor
FI	Fluid Inclusions
VPDB	Vienna Pee Dee Belemnite Standard
AFM	Atomic Force Microscopy
CL	Cathodoluminescence
FTIR	Fourier Transform Infrared Spectroscopy
SIMS	Secondary Ion Mass Spectrometry
SEM-EDS	Scanning Electron Microscope with X-ray Microanalysis
emf	Electromotive Force

Diamond-related Symbols	
Symbols	Description
TTH	Tetrahexahedron
OCT	Octahedron
CM	Complex Mantle-derived Resorption Morphology
SM	Step-faced Mantle-derived Resorption Morphology
KIM	Kimberlite-induced Resorption
p/b	Point-bottomed
f/b	Flat-bottomed
N	Nitrogen
C	Carbon
K	Diamond Dissolution Rate
$K_{\{111\}}$	Rounding Rates in Pure H_2O
$K_{\{111\}}^{CO2}$	Rounding Rates in Carbonic Fluids
a100	$L_{100}/(L_{100}+L_{111})$, where L_{100} and L_{111} are the Length of {100} Wall and {111} Wall of Etch Pits Respectively
$a_{\{111\}}$	Wall Angle of W_{111} relative to {111} faces
$a_{\{100\}}$	Wall Angle of W_{1oo} relative to {111} faces
$\alpha_{\{111\}}$	Pit Wall Angle
V_p	Enlargement Rate of W_{111} Parallel to {111}
V_p'	Enlargement Rate of W_{100} Parallel to {111}
Vd	Vertical Dissolution Rate at Defects Normal to {111}
ΔC	Diamond-fluid/melt Fractionation Factor of Carbon
K_N	Diamond-fluid/melt Partitioning Coefficient of Nitrogen
X_{CO2}	$X_{CO2}= CO_2/ (CO_2+H_2O)$, Mole Fraction
$\delta^{13}C$	Carbon Isotope Composition of Diamonds

CL Patterns Symbols	
in Chapter 2	
Symbols	Description
P1	Homogenous Irregular Zone
P2a	Homogenous and Rectilinear Zone
P2b	Layer-by-layer Rectilinear Zone
P3a	Homogenous Zone with a Stepped Rectilinear Outline
P3b	Layer-by-layered and Stepped Rectilinear Zone
P4	Agate Texture
P5	Multi-core Zone
P7	Blurry Rectilinear Zone
P8	Octagonal Zone
P9	Four-sided Star Zone
P10	Plaid Zone
P11	Black Rim
in Chapter 3	
P1	Homogeneous Zone
P2	Rectilinear Zone
P3	Stepped Rectilinear Zone
P4	Agate Texture
P5	Multi-core Pattern
P6	Sector Zone
P7	Dendritic Zone
P8	Octagonal Zone
P9	Four-sided Star Zone
P10	Plaid Structure
P11	Black Rim
P12	Shattered Pattern

ACKNOWLEDGEMENTS

I would like to express special thanks to my supervisor, Yana Fedortchouk, for introducing me into this brilliant project, guiding me with enthusiasm and knowledge, and encouraging me to attend variable conferences. Yana has always been available for help and discussion whenever requested. Most importantly, Yana has taught me how to stick to the primary goal when wandering in the world of ideas.

I am deeply thankful to my awesome thesis committee crew: Yana Fedortchouk, Jacob Hanley, and Rebecca Jamieson, who have provided precious contributions to this work. I have learned a lot from each of them during the thesis design, committee meetings, and thesis writing. Their extensive knowledge and great patience have created a very inspiring and motivating atmosphere for me to develop scientific reasoning and writing skills.

I would like to direct my gratitude to all the people who helped me during this study: Aleisha Crowell (UofA), Mitch Kerr (SMU), Alla Logvinova (Sobolev Institute of Geology and Mineralogy), Craig Manning (UCAL), Sergei Matveev (UofA), Kate Nicolas (UofA), Pat Patterson (Dal), Mati Raudsepp (UBC), Cliff Shaw (UNB), Evan Smith (UBC), Thomas Stachel (UofA), Richard Stern (UofA), Bruce Watson (Rensselaer Polytechnic Institute). Particularly, I'd like to thank Bruce Watson for spiritually supporting my experimental work with priceless suggestions for solving endless problems related with the piston cylinder apparatus, Craig Manning for providing the invaluable suggestion for preservation of olivine at high temperature and pressure, Cliff Shaw for providing the Pakistan olivine crystals, and Alla Logvinova for providing experimental diamonds.

I have spent a wonderful and memorable time in Halifax with the excellent company of

graduate students in Dalhousie University and precious friends. Mostly, I thank Luke Hilchie for sharing his expertise in experimental work and discussing things from science to religion to politics, Ryan Kressall for accompanying me to swim across the Chocolate Lake, and Holly Steenkamp for teaching me how to be a professional driver, and Hao Wang, Connie Jess, and Sam Jess for introducing me into the God's world.

The *China Scholarship Council (CSC)*, *SEG Canada Foundation, Shell research grant,* and the *Natural Sciences and Engineering Research Council of Canada* are thanked for the support of this research.

Finally, I would like to dedicate my thesis to my family for their patience and unconditional support during my study. I want to express my sincere appreciation to my wife, Zhenhua Han, for encouraging me to study oversea, and doing her best in taking care of Adeline and Caroline, and to my two daughters, Adeline and Caroline, for the happiness they bring to my life.

.

CHAPTER 1. INTRODUCTION

Diamonds undergo dissolution during residence in the mantle and during the ascent in kimberlite magmas (Robinson, 1979; Hall and Smith, 1984; Gurney et al., 2004; Fedortchouk et al., 2005; Fedortchouk et al., 2007; Fedortchouk et al., 2010). Their resorption morphologies have been recently used to constrain speciation and contents of fluids during diamond dissolution (Fedortchouk et al., 2005; Fedortchouk et al., 2010; Khokhryakov and Pal'yanov, 2010; Logvinova et al., 2015). In this PhD thesis, the empirical study of natural diamonds and diamond dissolution experiments are used to investigate the roles of internal properties of diamonds, pressure, and fluid compositions on diamond dissolution in order to address the fundamental question: how to quantify fluid composition in the mantle and kimberlites robustly using diamond resorption morphology? This chapter reviews diamond resorption morphology, followed by summaries of the Ekati kimberlites (Canada) and the lithospheric mantle beneath the central Slave craton (Canada).

1.1. DIAMOND RESORPTION MORPHOLOGY

1.1.1. Classification of Diamonds

Diamond morphology, including crystal forms and surface features, results directly from growth and/or dissolution. It records the conditions, mechanisms, and history of growth

and dissolution that the diamond experienced (Sunagawa, 1984). The existing morphological classifications of diamonds are based on the crystal forms related to diamond growth conditions (Orlov, 1977; Sunagawa, 1984), although morphological changes due to dissolution are noted (Robinson, 1979; Sunagawa, 1984; McCallum et al., 1994; Gurney et al., 2004; Fedortchouk et al., 2010). For example, primary (e.g. cubic, octahedral), resorbed primary (resorbed diamonds with recognizable growth faces), and secondary (e.g. tetrahexahedral) forms are used to characterize diamonds with growth and resorption morphologies (Gurney et al., 2004).

Natural diamonds from primary deposits and mantle xenoliths display variable and complex surface features, such as hillocks and etch pits (Figure 1.1). The current classifications based on growth forms are insufficient to decipher dissolution history of diamonds. For example, diamonds in the single crystalline diamond group (Sunagawa, 1984) can have pointed or rounded corners and smooth or pitted surfaces. A novel classification based on diamond resorption morphology is required for understanding diamond dissolution history. Recent experimental results of diamond dissolution show that the resultant morphologies are comparable to those observed on natural diamonds (Kozai and Arima, 2005; Sonin et al., 2006; Fedortchouk et al., 2007; Khokhryakov and Pal'yanov, 2007; Arima and Kozai, 2008; Khokhryakov and Pal'yanov, 2010; Logvinova et al., 2015). The morphological similarities between experimental and natural diamonds

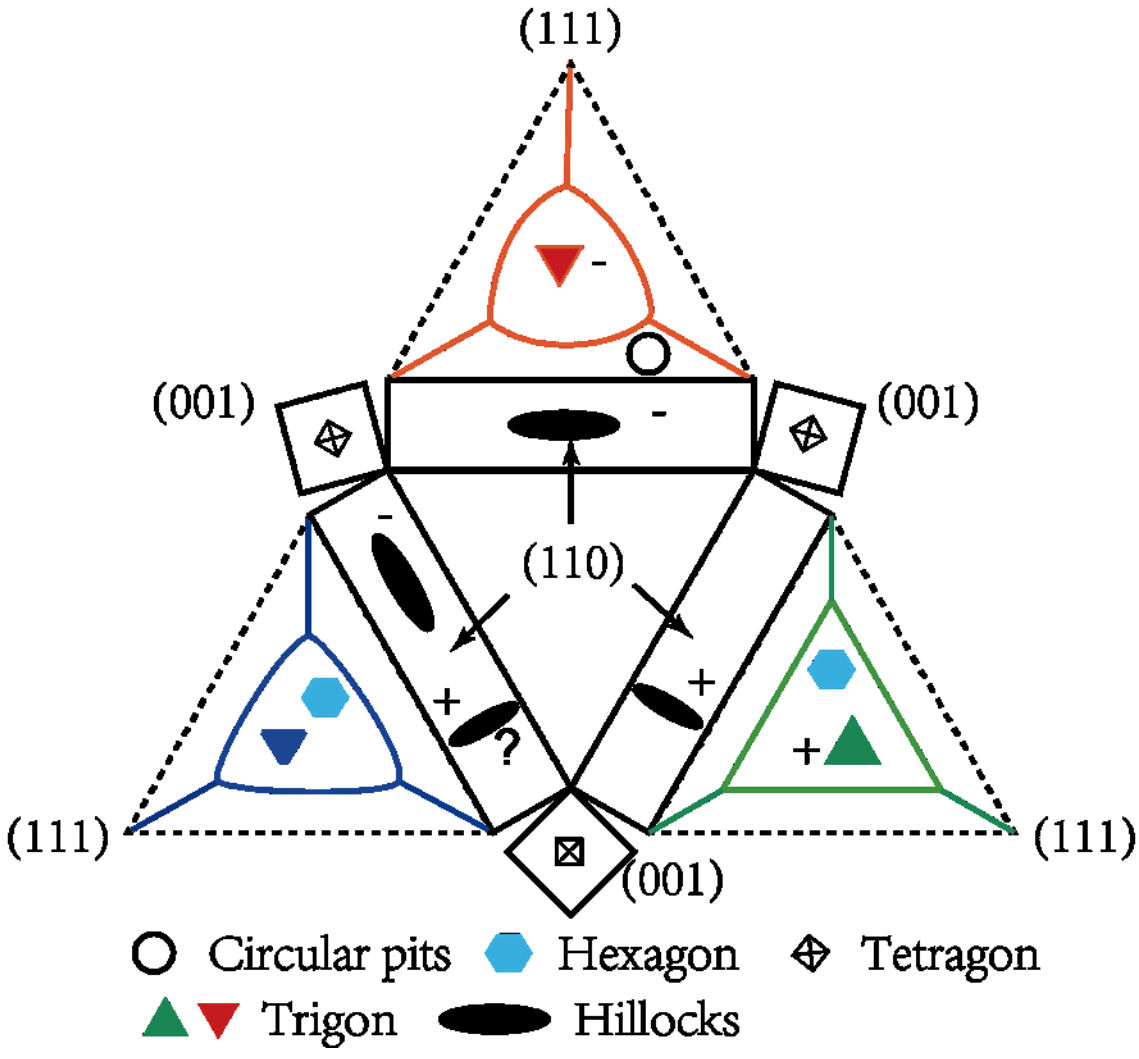

Figure 1.1 Sketch of morphological features observed on natural diamond faces (after Williams 1932). The morphological data were collected from diamonds from kimberlites located in the Kaapvaal craton in southern Africa (Robinson, 1979; Viljoen et al., 2004), the Slave craton, Canada (Gurney et al., 2004; Creighton et al., 2008; Aulbach et al., 2009; De Stefano et al., 2009; Fedortchouk et al., 2010), and the Siberia Craton, Russia (Sobolev et al., 1994; Spetsius, 1995; Anand et al., 2004; Logvinova et al., 2015). The dashed lines represent the theoretical <110> edges, which now are replaced by curved (red solid line), slightly curved (blue solid line), or rigid edges (green solid line). '+' and '-' represent the positive and negative orientations of surface features following Robinson (1979).

permit a classification based on resorption morphology.

1.1.2. Diamond Resorption Morphology

Most diamonds show resorption morphologies. Diamonds have face-centered cubic crystal structure and should form primary cubic, cubo-octahedral, and octahedral growth forms with sharp corners and straight edges, as observed in synthetic diamonds (Sunagawa, 1984; Arima et al., 1993; Sokol et al., 2001; Gurney et al., 2004; Palyanov and Sokol, 2009; Fagan and Luth, 2011; Palyanov et al., 2015). In contrast, most natural octahedral diamonds show rounded corners and edges and curved faces, and many display tetra-hexahedral (THH) forms. Although the curvature of diamond faces was proposed to result from growth (Tolansky and Wilcock, 1947), a dissolution origin of the morphologies on most diamonds is substantially supported in empirical and experimental studies by form transformation from octahedron to rounded octahedron to tetrahexahedron and resorption surface features. The dissolution origin of diamond forms with rounded corners and edges is evident from the discontinuous growth zones revealed by cathodoluminescence (Bulanova, 1995; Harte et al., 1999) and controlled etching (Seal, 1965), pseudohemimorphic diamonds with partially intact and partially resorbed octahedral forms resulting from being partially protected by xenoliths from kimberlites (Robinson, 1979; Stepanov et al., 2007; Creighton et al., 2008), and evolutionary paths of crystal forms from octahedron to rounded octahedron to tetrahexahedron observed in diamond dissolution

experiments (Kozai and Arima, 2005; Fedortchouk et al., 2007; Khokhryakov and Pal'yanov, 2007; Arima and Kozai, 2008; Khokhryakov and Pal'yanov, 2010).

The most common features on octahedral faces are trigonal etch pits (Figure 1.1), referred to as "trigons" (Frank et al., 1958; Evans and Sauter, 1961; Robinson, 1979). The orientation of trigons is often opposite to the octahedral faces (-, Figure 1.1), named negative trigons (Robinson, 1979; Gurney et al., 2004), and is rarely parallel to the direction of the octahedral faces, called positive trigons (+, Figure 1.1, Robinson, 1979). The origin of negative trigons has been debated for a long period. The growth origin suggests that trigons are bound by growth layers and form as a growth failure at defects (Williams, 1932; Tolansky and Wilcock, 1947; Omar and Kenawi, 1957; Varma, 1967). This model heavily relies on only positive trigons created after diamond dissolution in exotic etchants, such as fused potassium chlorate, or at temperature < 1000 ºC (Omar and Kenawi, 1957; Patel and Ramanathan, 1962; Patel and Patel, 1973; de Theije et al., 2001), which is lower than the temperature estimates of 1,030–1,170◦C from geothermometry studies (1030-1170 ºC, Fedortchouk et al., 2004) and the model temperature >1000 ºC of shallow kimberlite magams with less than 10 wt% H_2O (Kavanagh and Sparks, 2009).

Alternatively, the dissolution origin was theoretically proposed to be in the defect-controlled kink mechanism, where etch pits nucleate at defects and then are enlarged in width through removal of atomic carbon steps by propagation of kinks (atomic pits formed

by random removal of three-bonded carbon atoms) to the ends of steps (Figure 1.2) (Frank and Puttick, 1958; Frank et al., 1958). The proposed dissolution origin of trigons is immediately and substantially supported by trigon formation in diamond dissolution experiments under conditions similar to those of natural diamond-bearing environments. The resulting surface features of diamonds, including negative trigons, hillocks, sheaf striations, and crystal forms with different resorption degree, are similar to those observed on natural diamonds (Frank and Puttick, 1958; Kanda et al., 1977; Yamaoka et al., 1980; Kozai and Arima, 2005; Fedortchouk et al., 2007; Khokhryakov and Pal'yanov, 2007). In addition, circular pits on THH faces (Robinson, 1979; Tappert and Tappert, 2011), hexagonal pits on octahedral faces, and tetragons on cubic faces are suggested to result from diamond dissolution, confirmed by the experimental studies of diamond dissolution (Yamaoka et al., 1980; Kozai and Arima, 2005; Fedortchouk et al., 2007; Khokhryakov and Pal'yanov, 2010).

In conclusion, most diamond morphologies evidently result from dissolution in kimberlites or in their mantle reservoirs. However, the controlling factors of diamond resorption morphologies and details of formation mechanism of etch pits are not well known, as reviewed in the following section.

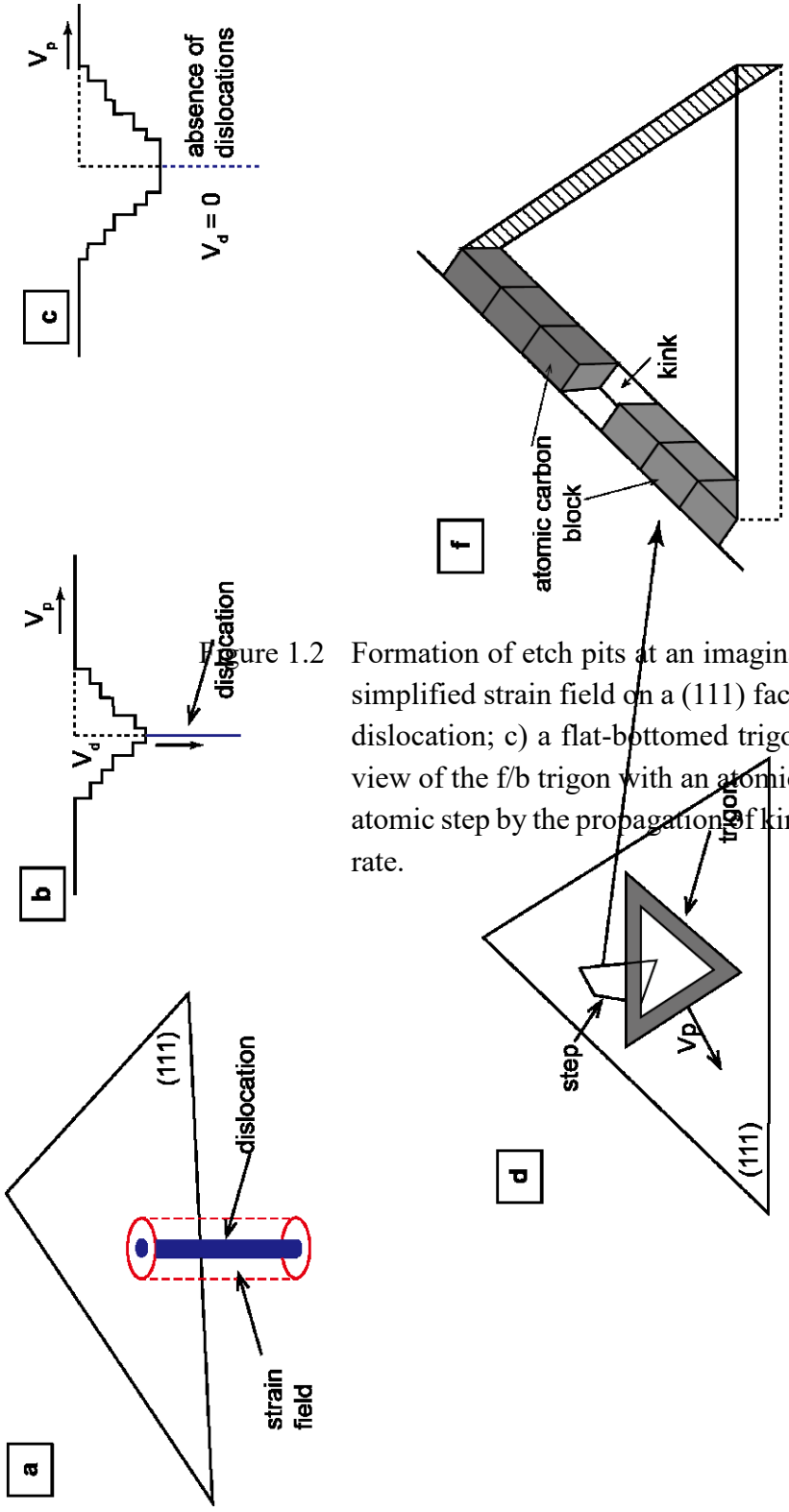

Figure 1.2 Formation of etch pits at an imaginary dislocation in the kink mechanism. a) simplified strain field on a (111) face (Hull and Bacon, 2011); b) a point-bott dislocation; c) a flat-bottomed trigon starts to replace the p/b trigon when th view of the f/b trigon with an atomic step; f): enlargement of the f/b trigon in atomic step by the propagation of kinks. Vp = Horizontal enlargement rate of e rate.

1.1.3. Diamond Dissolution

Our knowledge of factors affecting diamond resorption has been progressively advancing due to experimental and theoretical studies since 1892. Since the first diamond-etching experiment in fused kimberlites at atmospheric pressure (100 kPa) (Luzi, 1892), diamond dissolution experiments have not only reproduced many resorption morphologies, but have also revealed initiating conditions of diamond dissolution, demonstrated effects of oxygen fugacity (f_{O2})–temperature (T)–etchants on dissolution rates and resorption morphologies, and examined dissolution mechanisms. The minimum T required for initiating dissolution at 100 kPa is ≥ 600 ºC in oxygen (Evans and Phaal, 1962) and > 950 ºC in H_2O and CO_2 (Sauter, 1961). Although iron content in the kimberlites is suggested to affect diamond dissolution (Harris and Vance, 1974), experimental studies demonstrate that T, f_{O2}, and the compositions of the etchants (CO_2 vs. H_2O vs. melts) are the most important factors affecting diamond dissolution. Dissolution rates of diamonds increase with T (Cull and Meyer, 1986; Kozai and Arima, 2005; Fedortchouk et al., 2007; Arima and Kozai, 2008; Zhang et al., 2015) and f_{O2} (Cull and Meyer, 1986; Kozai and Arima, 2005), and are independent on the H_2O:CO_2 ratio of the reacting fluids (Fedortchouk et al., 2007).

Diamond resorption morphologies also depend on T, f_{O2}, and the compositions and nature of etching agents. At similar dissolution conditions, diamonds with different internal properties show similar resorption morphologies (Yamaoka et al., 1980; Kozai and Arima,

2005; Fedortchouk et al., 2007; Khokhryakov and Pal'yanov, 2007; Arima and Kozai, 2008; Fedortchouk and Canil, 2009; Khokhryakov and Pal'yanov, 2010; Zhang et al., 2015). T and f_{O2} show the opposite influence on the orientation of trigons (Yamaoka et al., 1980). As T increases from 800 to 1000 ^{o}C, the orientation of trigons switches from the positive to the negative direction (Evans and Sauter, 1961), while, as f_{O2} increases, the orientation of trigons changes from the negative to the positive direction (Yamaoka et al., 1980; Kozai and Arima, 2005). T and f_{O2} have little effect on diamond resorption forms at P>1 GPa and T> 1100 ^{o}C at f_{O2} maintained above the carbon-oxygen and below the hematite-magnetite (HM) buffers (Kanda et al., 1977; Kozai and Arima, 2005; Fedortchouk et al., 2007; Khokhryakov and Pal'yanov, 2010; Zhang et al., 2015). T and f_{O2} effects on resorption forms and the orientation of trigons was proposed to be due to the changes in dissolution rates in <111> and <110> direction (Yamaoka et al., 1980; Kozai and Arima, 2005).

The active etchants of diamond by oxidation at 1 GPa are argued to be C-O-H fluids rather than silicate or carbonate melts (Fedortchouk et al., 2007), while, at 5-7 GPa, silicate or carbonate melts can also oxidize diamonds (Khokhryakov and Pal'yanov, 2007, 2010). Etchants influence both resorption forms and orientation of trigons and hillocks. Three evolution trends of diamond dissolution forms are addressed: octahedron to octahedron with tetra-hexahedral faces to tetra-hexahedron in H_2O-rich environments (Fedortchouk et

al., 2007; Khokhryakov and Pal'yanov, 2010), octahedron to octahedron with tri-octahedral faces to TTH in pure CO_2 (Fedortchouk et al., 2007; Arima and Kozai, 2008), and octahedron to octahedron with tri-octahedral faces to tri-octahedron in CO_2-rich or fluid-free carbonate melts (Khokhryakov and Pal'yanov, 2010). Accompanying the form transformation, only negative trigons occur on {111} faces in H_2O-rich systems, both hexagons and negative trigons coexist in the pure CO_2 system, and positive trigons form in CO_2-rich or CO_2-free carbonate melts (Khokhryakov and Pal'yanov, 2007, 2010). Although resorption features on most natural diamonds are reproduced in experiments, there are still many types of resorption morphologies formed at unknown conditions. One possible factor is pressure (P) (Arima and Kozai, 2008; Khokhryakov and Pal'yanov, 2010), which evidently affects diamond dissolution in carbonate melts but has not been systematically studied yet. For example, diamonds oxidized in carbonate melts at 1 GPa show graphitization but at 5.7-7.5 GPa dissolution features (Fedortchouk et al., 2007; Khokhryakov and Pal'yanov, 2010).

At the atomic level, octahedral diamonds are dissolved through removal of two-bonded and triple-bonded carbon atoms on {110} and {111} faces, respectively, and one- or two-bonded carbon atoms at defects on {111} faces (Angus and Dyble, 1975; Rudenko et al., 1979). Based on the difference of activation energies between one, two, and three C-C bonds, the most energetically favorable chemical dissolution mechanism of diamonds

involves breaking of one carbon bond (347 kJ/mol) (Rudenko et al., 1979). In this process, volatile molecules (H_2O, CO_2) attach to the dangling carbon bonds on the diamond surfaces, and the remaining C-C bonds break one by one to create new molecular clusters, C-O-H-OH or C-O-C-O, whose formation energy is higher than the energy required to break a single C-C bond (Rudenko et al., 1979). These various compounds then break down into CO and CO_2 as the final products of diamond oxidation. The predicted activation energy to break one C-C bond in this process agrees with the measured activation energy (~ 342 kJ/mol) for diamond oxidation (Fedortchouk et al., 2007; Arima and Kozai, 2008).

Removal of carbon atoms around defects via the kink mechanism creates trigons (Figure 1.2) and hexagons on octahedral faces (Frank et al., 1958; Ponton et al., 1974; Angus and Dyble, 1975). In this mechanism, competition of removal rates between two- and three-bonded carbons controls the orientation of trigons; removal rates of carbon atoms in <111> and <110> direction decide the geometry (depth, diameter, and wall angles) of trigons. For negative trigons, removal of two-bonded carbons is faster, while for positive trigons, removal of three-bonded carbons is faster. When the two rates are equal, hexagons form (Angus and Dyble, 1975; Ponton et al., 1974). This mechanism is supported by the correlation between trigons and dislocations on natural diamonds (Lang, 1964) and development of trigons at defects in diamond dissolution experiments (Khokhryakov and

Palyanov, 2006, 2007). However, this mechanism is not tested due to lack of quantitative geometrical data of trigons developed under known oxidation conditions similar as the natural systems.

One important feature of this model is the formation of hexagons under restricted conditions where neither negative or positive trigons should occur. However, empirical and experimental studies of diamond resorption morphologies do not support this formation process of hexagons. These inconsistencies make the formation mechanism of trigons still elusive. On natural diamonds hexagons commonly coexist with negative trigons (Robinson, 1979; Hall and Smith, 1984; Fedortchouk et al., 2005; Zhang and Fedortchouk, 2012) and rarely with positive trigons (only on one sample to my knowledge) (Robinson, 1979). In diamond dissolution experiments under the conditions where hexagons should occur, etch pits on {111} faces are not hexagonal but circular (Evans and Sauter, 1961) or both negative and positive trigons (Yamaoka et al., 1980). In contrast, hexagons created in experiments commonly coexist with negative trigons (Fedortchouk et al., 2007; Arima and Kozai, 2008). In addition, diamonds oxidized in synthetic CO_2-bearing kimberlite melts show both hexagons and negative trigons in the shorter run, and positive trigons in the longer runs (Arima and Kozai, 2008), indicating a possible evolutionary path of etch pits from negative trigons to hexagons to positive trigons.

In addition to the tetragons and trigons on cubic and octahedral faces respectively, circular pits occur on THH, cubic and broken faces (Robinson, 1979; Tappert and Tappert, 2011). Although etch pits on cubic and octahedral faces are suggested to form by the defect-oriented kink mechanism, formation of circular pits on THH faces is an exception. They are proposed to form after the formation of main resorption morphology (e.g. trigons) by attachment of CO_2 bubbles to THH faces (Robinson, 1979; Tappert and Tappert, 2011). However, the origin and formation mechanism of circular pits are still unknown.

1.1.4. Diamond Resorption Morphology as a Potential Fluid Proxy

The high minimum T (>650 ºC, Evans and Phaal, 1962) to initiate diamond dissoluiton indicates that diamond resorption features in most cases form prior to the kimberlite eruption. Since continuous resorption would eliminate early resorption features, diamond resorption morphology must record information about the latest resorption process. For example, diamonds in kimberlite matrix preserve kimberlite-induced morphologies rather than mantle-derived resorption morphologies, as illustrated by pseudohemimorphic diamonds in xenoliths (Robinson, 1979; Hall and Smith, 1984; Aulbach et al., 2011).

Sensitivity of diamond resorption features to the composition of the etchants under the conditions similar to most diamond-bearing environments suggests diamond resorption morphology as a potential proxy of the composition of etchants. Diamonds resorbed in the

pure H_2O and CO_2 at 1 GPa and 1150-1350 ^oC show distinct H_2O (ditrigonal {111} faces, negative trigons, and smooth surface) and CO_2 (trigonal {111} faces, hexagons, rough surface) resorption morphologies (Fedortchouk et al., 2007). Diamonds oxidized in carbonate and kimberlite melts at 5.7- 7.5 GPa and 1400-1750 ^oC display a typical H_2O resorption morphology in H_2O-rich carbonate and kimberlite melts and the carbonate resorption features (trigonal {111} faces, positive trigons, positive hillocks) in volatile-free and CO_2-rich carbonate melts. The compositional boundary between two types of resorption morphology is X_{CO2} = 0.65-0.7 in carbonate melts (Khokhryakov and Pal'yanov, 2007, 2010).

The pioneering application of diamond resorption morphologies to diamonds from kimberlites suggests that kimberlites are H_2O-rich magmas at great depth (Khokhryakov and Pal'yanov, 2010) and have free H_2O-rich fluids at shallow depth (Fedortchouk et al., 2010). One important criterion is the absence of hexagons on {111} faces of natural diamonds. The application of diamond resorption morphologies is based on three assumptions: 1) hexagons on {111} faces form under restricted conditions; 2) P does not affect resorption morphology; 3) diamonds oxidized within C-O-H fluids with variable molar ratios of CO_2:H_2O (X_{CO2}= CO_2/ (CO_2+H_2O)) only develop resorption features same as those in pure H_2O or pure CO_2. However, all three assumptions are questionable. The first assumption is problematic because the predicted etch pits in the model contradict the

etch pits observed on natural and post-experimental diamonds (§ 1.1.3). The lack of P effects is challenged by diamond graphitization at 1 GPa but resorption at 5.7- 7 GPa in carbonate melts (Kozai and Arima, 2005; Fedortchouk et al., 2007; Khokhryakov and Pal'yanov, 2010). Therefore, using the results of diamond resorption experiments at high pressure on natural diamonds to constrain fluid composition in kimberlites at depth (Khokhryakov and Pal'yanov, 2010) is debatable. The third assumption is not experimentally constrained due to the limited results of diamond resorption in etchants with variable composition. Diamond resorption experiments in melts with bulk X_{CO2} =0.24 - 0.77 were conducted at 1 GPa and 1420 ºC under the iron-wüstite buffer, but the effects of etchant composition on resorption morphology were not reported (Kozai and Arima, 2005). In addition, the composition of diamond-etching fluids at the run conditions is unknown. The boundary (X_{CO2} = 0.65-0.7) between typical H_2O and carbonate resorption features is constrained by diamond resorption experiments in volatile-containing carbonate and kimberlite melts at 5.7- 7.5 GPa and 1400-1750 ºC (Khokhryakov and Pal'yanov, 2010). There are no experimental data of diamond resorption in carbonate melts with X_{CO2} = 0.65-0.7, where hexagons are assumed to form (Khokhryakov and Pal'yanov, 2010). The experimental conditions are also far beyond the P-T conditions of carbonate melts in the mantle (Kavanagh and Sparks, 2009).

In summary, given some of unknown effects of other factors (e.g. P, X_{CO2},) involved in diamond resorption, diamond resorption morphologies can provide the most unambiguous record of conditions in diamond bearing environments (mantle reservoirs and kimberlite magmas).

1.2. DIAMONDIFEROUS KIMBERLITES IN THE EKATI MINE

1.2.1. Geology of the Ekati Kimberlites

Kimberlites as the most important primary source of gem-quality diamonds are deep-seated magmas and are different from other common magmas (e.g., basalts) by showing no evidence of long-lived magma chambers or their surface features, such as calderas or ring faulting (Mitchell, 1986; Field and Scott Smith, 1999). Kimberlites in the Ekati mine area (Northwest Territories, Canada), were well characterized in a 10-year exploration (1991–2001) and provide a great opportunity to understand kimberlite volcanism (Field and Scott Smith, 1999; Creaser et al., 2004; Fedortchouk and Canil, 2004; Nowicki et al., 2004; Canil and Bellis, 2007; Porritt et al., 2008; Scott Smith, 2008; Kamenetsky et al., 2013). The Ekati kimberlites occur over a region of ~1800 km^2, and are located in the central Slave craton. 150 kimberlite pipes occupy a significant proportion of the Lac de Gras kimberlite field (Figure 1.3) (Nowicki et al., 2004). All kimberlites form single small (surface diameter mostly < 200 m but up to 450 m) pipes, except for the Misery pipe with

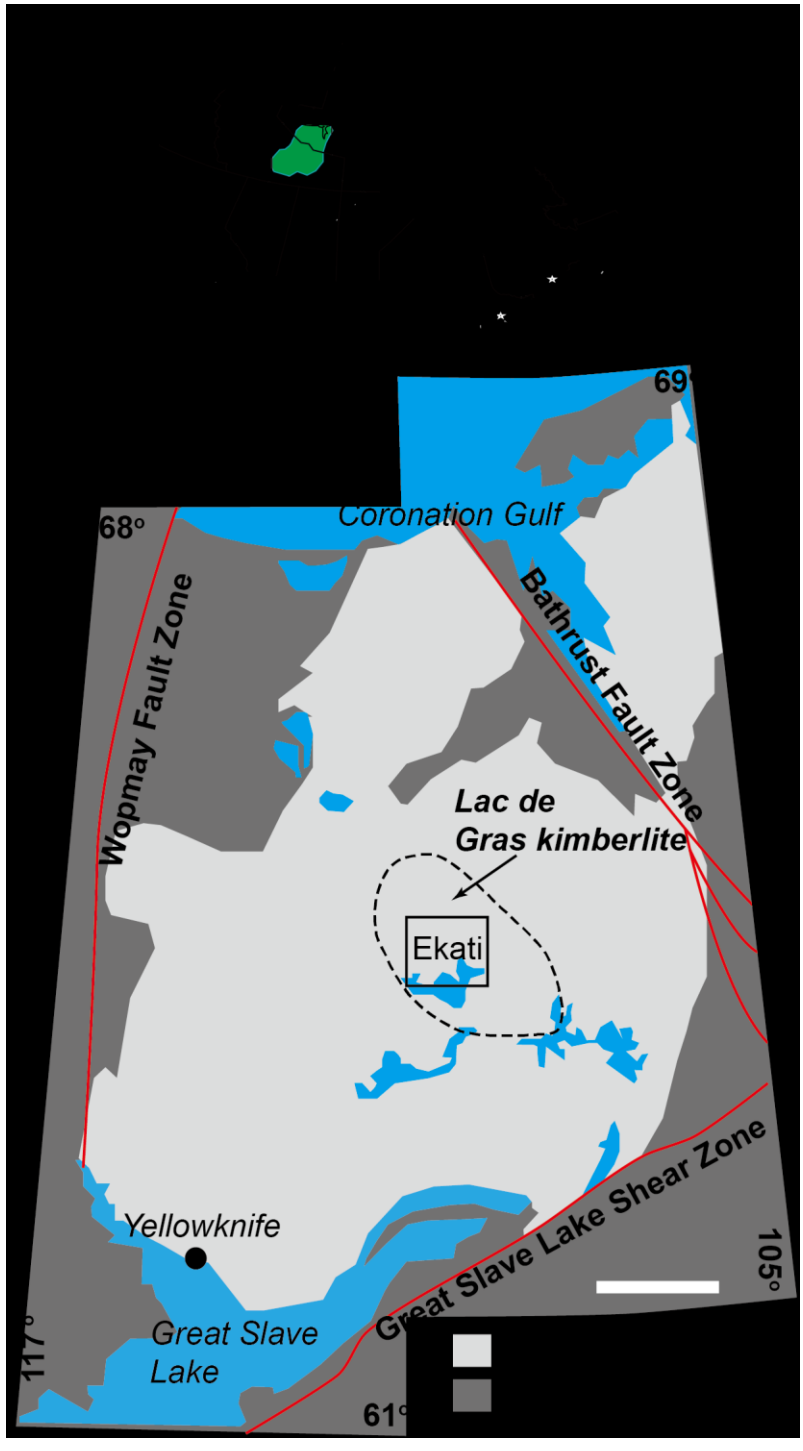

Figure 1.3 Locality map showing the position of the Ekati mine in relation to the Slave craton and the Lac de Gras kimberlite field. This map is modified after Donnelly et al. (2007).

nine small bodies (Nowicki et al., 2004).

Five kimberlite pipes, Fox, Misery, Koala, Leslie and Grizzly, were selected for my study because they represent three types of kimberlites found in the Lac de Gras kimberlite field and the diamond grade in the five pipes is variable (Table 1.1). All five pipes were emplaced into 2.66–2.58 Ga granitoids at 50-70 Ma (Creaser et al., 2004; Sarkar et al., 2015) and are exposed at same erosion levels (Nowicki et al., 2004). The kimberlite T ranges from the modeled source T 1350-1450 ^{o}C (Kavanagh and Sparks, 2009) to the crystallization T 1030-1170 ^{o}C estimated by the olivine-spinel geothermometry (Fedortchouk and Canil, 2004). The f_{O2} estimated by olivine-spinel oxygen barometry at a silica activity limited by the presence of monticellite (Fedortchouk and Canil, 2004) is ~3 log units bellow the Ni-NiO buffer (NNO - 3), which is in a range from NNO - 2.3 to NNO + 5 estimated using the Fe content of groundmass perovskite (Table 1.1) (Canil and Bellis, 2007). Because perovskite generally crystallizes after chromite, olivine and spinel (Mitchell, 1986), kimberlite magmas in the Misery and Grizzly pipes are suggested to have experienced oxidation during differentiation and emplacement (Canil and Bellis, 2007).

The internal geology of kimberlites in the Ekati mine is well characterized through detailed mineralogical and petrological studies (Nowicki et al., 2004; Nowicki et al., 2008; Porritt et al., 2008; Carlson et al., 2015). The following description follows the new nomenclature

Table 1.1 Geology and diamond grades for the Fox, Misery, Koala, Leslie, and Grizzly kimberlite pipes.

Kimberlite	Fox	Misery	Koala	Leslie	Grizzly
Grade (ct/t) [a]	0.3	4.5	0.8	0.3	0.5
Age (Ma)	56.2±3.2 [b]	68.9±5.4 [b]	53.3±0.9 [c]	53.1±0.7 [c]	50.9±7.3 [c]
T (^oC)[d]		1053-1138		1031-1102	1015-1115
ΔNNO (Ol-Sp)[e]		-2.9		-2.8	-2.8
ΔNNO (Prv)[f]		5.7			0
Petrology[g]	Single pipe, RVK at upper layer; MVK at lower layer	Cluster of nine pipes, predominantly RVK, some PK, minor CK	Single layered pipe, predominantly RVK, and PK, minor CK at the base	Single pipe filled with CK and trace MVK	Single piep filled with CK
Class[h]	1	3a	3a	3b	3b

a: Diamond grades (Carlson et al., 2015);

b: U-Pb age of pervoskite (Sarkar et al., 2015);

c: Rb–Sr age of phlogopite (Creaser et al., 2004);

d: Crystallization T of kimberlites (Fedortchouk et al, 2004; Fedortchou et al., 2005);

e: f_{O2} estimated by olivine (Ol)-spinel (Sp) oxygen barometry at 1 Gpa (Fedortchouk et al., 2005). ΔNNO= $\log f_{O2}$ sample -log f_{O2} NNO buffer at P and T.

f: $\log f_{O2}$ by Fe contents in pervoskite (Prv) (Canil and Bellis, 2007);

g: Petrology of kimberlites (Nowiki et al., 2004). PK: pyroclastic kimbelrite; RVK: resedimented volcaniclastic kimberlite; CK: coherent kimberlite;

h: Kimberlite classificaiton following Skinner and Marsh (2004);

of kimberlites (Figure 1.4 a), which describes internal geology in a non-genetic sense (Sparks et al., 2006; Cas et al., 2008; Nowicki et al., 2008). There are three main rock types in the five Lac de Gras kimberlite pipes: resedimented volcaniclastic kimberlite (RVK), massive volcaniclastic kimberlite (MVK), and coherent kimberlite (CK) (Table 1.1). The RVK is composed of angular olivine fragments in a predominated very fine-grained mud matrix. To date, MVK found only in the diatreme zone of the Fox pipe is highly fragmented and comprises consistently high (40% to 50%) proportions of country rock material and moderate abundances (15 to 30%) of medium-grained (up to 5 mm) olivine in a matrix of pure serpentine with abundant microlites. Coherent kimberlite (CK) is a massive and porphyritic kimberlite (Nowicki et al., 2004; Scott Smith, 2008).

Kimberlites are grouped into Class 1 (southern African kimberlites), Class 2 (Canadian Prairies kimberlites), and Class 3 (Lac de Gras kimberlites) based on their internal geology and pipe morphologies (Figure 1.4) (Field and Scott Smith, 1999; Nowicki et al., 2004; Skinner and Marsh, 2004; Scott Smith, 2008). The five selected kimberlites belong to Class 1(Fox, Figure 1.4 a) and 3 (Figure 1.4 c) (Field and Scott Smith, 1999; Nowicki et al., 2004; Skinner and Marsh, 2004; Scott Smith, 2008). Variation of internal geology in Class 3 allows subdivisions into Class 3a (Misery and Koala) and 3b (Grizzly and Leslie) (Table 1.1, Figure 1.4 c). The reasons for variable pipe morphologies and internal geology among Ekati kimberlites are still unknown and the mechanisms for kimberlite

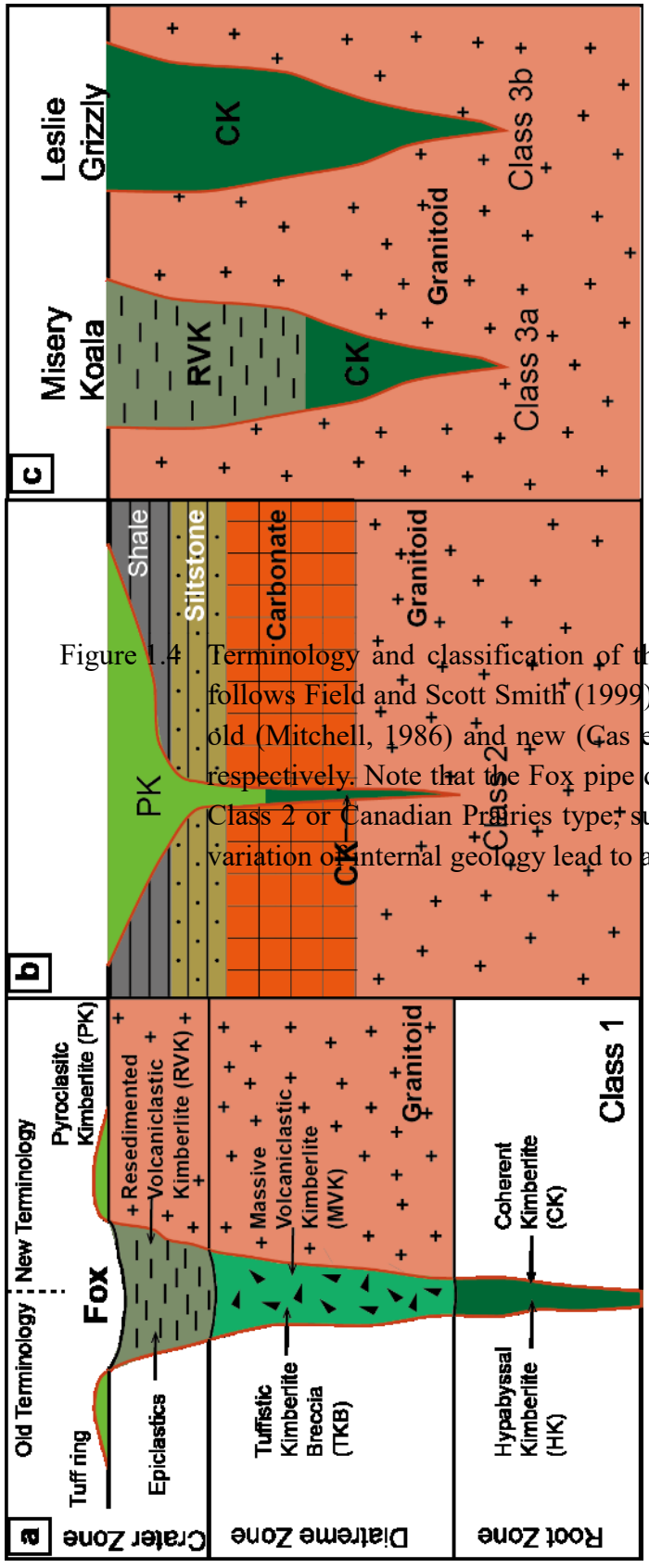

Figure 1.4 Terminology and classification of the Fox, Misery, Koala, Leslie and Grizzly kim follows Field and Scott Smith (1999) and Skinner and Marsh (2004). a) Class 1 or cl old (Mitchell, 1986) and new (Gas et al., 2008) terminology of kimberlites are illus respectively. Note that the Fox pipe does not show signs of a root zone (Nowicki et Class 2 or Canadian Prairies type, such as the Fort à la Corne kimberlite field; c) C variation of internal geology lead to a subdivision: 3a filled with predominant RVK ar

emplacement in Lac de Gras are still in debate (Field and Scott Smith, 1999; Nowicki et al., 2004; Skinner and Marsh, 2004; Cas et al., 2008) due to lack of common volcanic features, such as magma chambers, ring faulting (Field and Scott Smith, 1999), and poorly constrained primary composition of kimberlites, especially volatile compositions.

1.2.2. Volatiles in Kimberlites

Kimberlites have high volatile contents, indicated by primary carbonate and phlogopite found in kimberlites (Mitchell, 1986) and ascent at high speed from the mantle source to the Earth's surface (Canil and Fedortchouk, 1999; Sparks et al., 2006; Russell et al., 2012; Brett et al., 2015). The bulk chemical analysis of kimberlites leads to two contradicting models: CO_2- vs. H_2O-rich kimberlites. Kimberlites are traditionally believed to be CO_2-rich, supported by the bulk composition of aphanitic kimberlites (Price et al., 2000; Kopylova et al., 2007). The H_2O-rich kimberlites are recently suggested by the volatile composition of worldwide hypabyssal kimberlites (Kjarsgaard et al., 2009) and morphology and geology of southern African kimberlites (Skinner and Marsh, 2004), and are supported by diamond resorption morphology and distinct infrared spectra of olivine (Fedortchouk et al., 2010). Modeling of volatile properties during kimberlite ascent suggests the presence of free fluids evolving in composition from CO_2-rich at depth to H_2O-rich (Russell et al., 2008). However, there is still no unambiguous method to quantify volatile composition in kimberlites before eruption.

1.2.3. Kimberlite Emplacement Models

Understanding kimberlite emplacement will significantly advance diamond exploration and mining by assisting in interpreting geophysical data, our understanding of deep-seated volcanism, and material exchange between the mantle and the crust. However, the mechanisms of kimberlite emplacement are still under debate because of elusive primary compositions, significant post-eruption alteration, and lack of typical volcanic features, such as magma chambers, volcanic cones, or maars (Mitchell, 1986; Field and Scott Smith, 1999; Kopylova et al., 2007; Kjarsgaard et al., 2009).

Two contrasting emplacement models in terms of the driving force are proposed to explain geologies and morphologies of kimberlites: phreatomagmatic and magmatic mechanism. The phreatomagmatic process was originally proposed to explain the spatial relationship between maar-type volcanos and river valleys, and then was suggested to be applicable to kimberlites (Lorenz, 1973; Lorenz, 1975; Lorenz and Kurszlaukis, 2007). In this process, magmas and external water bodies are the keys for explosive eruption and the roles of volatiles exsolved from magmas are negligible. Rising hot magmas contact with external water bodies, such as a river or a shallow sea, causing thermohydraulic explosions, initiating kimberlite craters (Zimanowski, 1998; Lorenz, 2003; Lorenz and Kurszlaukis, 2007). For Class 1 kimberlites, sufficiently large water bodies and continuously rising magmas result in downward sequential explosions, which widen and deepen the craters

with time, creating the diatreme and root zones of kimberlites (Figure 1.3 a). Absence of water bodies leads to a flared and shallow crater similar to that of Class 2 kimberlites (Figure 1.3 b) (Zimanowski, 1998; Lorenz, 2003; Lorenz and Kurszlaukis, 2007). Post-explosion intrusion of kimberlitic magmas into craters forms scoria or lava lakes at surface levels (Lorenz, 2003). Volcanoes with maar–diatremes can form under the phreatomagmatic process either in water-saturated soft sediment or hard-rock environments with aquifers in joints and faults (Lorenz, 2003).

Alternatively, a magmatic process is suggested for the southern African kimberlites (Mitchell, 1986 and references therein), and was adopted for most kimberlites until the discovery of Class 2 and 3 kimberlites in Canada (Field and Scott Smith, 1999). In this model, the pre-eruption kimberlite column is stratified with a top CO_2-dominated fluid phase and a magmatic phase at the bottom (Mitchell, 1986; Field and Scott Smith, 1999; Skinner and Marsh, 2004; Sparks et al., 2006; Wilson and Head, 2007; Cas et al., 2008; Russell et al., 2012; Brett et al., 2015). A crater is initiated by an explosion resulting from over-pressurization of the fluid phase relative to the atmosphere either through connecting with a present fracture system (Sparks et al., 2006; Cas et al., 2008) or creating new hydraulic fractures by the top CO_2-dominated gas to the surface (Field and Scott Smith, 1999; Skinner and Marsh, 2004). The enlargement of the crater can result from either upwards (Field and Scott Smith, 1999) or downwards explosion of kimberlitic magmas

(Sparks et al., 2006; Cas et al., 2008). The MVK in the diatreme zone forms directly from pyroclastic kimberlites (Cas et al., 2008) or from pyroclastic kimberlites undergoing fluidization because of degassing of below magma (Skinner and Marsh, 2004; Sparks et al., 2006). Coherent kimberlites in the root zone form by either welding of hot pyroclastic kimberlites (Sparks et al., 2006; Cas et al., 2008) or intrusion of kimberlite magmas (Skinner and Marsh, 2004).

Pursuing a universal model for kimberlite emplacement becomes unrealistic after discovery of three classes of kimberlites (Field and Scott Smith, 1999), although both models are modified to incorporate features from each other (Sparks et al., 2006; Kjarsgaard, 2007). The two models are adapted to interpret geology and morphologies of kimberlites worldwide (Field and Scott Smith, 1999; Sparks et al., 2006; Kjarsgaard, 2007; Cas et al., 2008). The factors controlling the emplacement models are suggested to be country rocks (Field and Scott Smith, 1999) and CO_2/H_2O ratios of the fluid in kimberlites (Skinner and Marsh, 2004). Availability of aquifers in unconsolidated rocks permits a phreatomagmatic process (e.g., Class 2 kimberlites), while consolidated rocks act as barriers where juvenile gases exsolved from kimberlites accumulate and exploded finally to create kimberlite pipes, such as the southern African kimberlites (Field and Scott Smith, 1999). Alternatively, the CO_2/H_2O ratio of the fluid phase controlling the kimberlite solidus determines the crystallization depth of kimberlites (Skinner and Marsh, 2004). The

crystallization depth not only controls the potential for contact between magmas and surface aquifers, but also governs whether the thermohydraulic explosion, having a depth limit (< 300 m, Lorenz and Kurszlaukis, 2007), can happen.

The emplacement mechanism in the Lac de Gras kimberlites is still in debate, although it is believed to be similar to Class 1 kimberlites (Field and Scott Smith, 1999; Skinner and Marsh, 2004). Because of the identical geological setting (Figure 1.3), lack of aquifers across the Ekati mine area (Field and Scott Smith, 1999), and insufficient groundwater supply for phreatomagmatic emplacement of kimberlites in crystalline basement rocks (Sparks et al., 2006), the only factor contributing to variable geology among the Lac de Gras kimberlites is variable H_2O/CO_2 ratios of fluid phases in kimberlites. However, Fedortchouk et al., (2010) proposed that fluid exsolution depth and degree of fluid retention during kimberlite ascent control geology in the Ekati kimberlite pipes based on similar resorption features on diamonds from six Ekati pipes and variation of FTIR spectra of olivine. In order to test if a variable H_2O/CO_2 ratio of kimberlitic fluid could play a role in the kimberlite emplacement and resulting kimberlite geology, we need a quantitative and robust method to constrain volatile composition of kimberlites, and diamond resorption moprhology provides such an opportunity.

1.3. LITHOSPHERIC MANTLE BENEATH THE CENTRAL SLAVE CRATON

1.3.1. General Structure of Lithospheric Mantle

The Slave craton is surrounded on three sides by the Proterozoic mobile belts (Figure 1.3) (Davis and Bleeker, 1999). Although the subcontinental lithospheric mantle (SCLM) reconstructed with mantle samples from different parts of the craton is spatially different, the lithospheric mantle beneath the central Slave craton shows a two-layered structure (Figure 1.5 a) (Kopylova et al., 1998; Griffin et al., 1999a; Griffin et al., 2004; Menzies et al., 2004; Creighton et al., 2008; Creighton et al., 2010). The stratified lithospheric mantle is supported by 3-D conductivity models reconstructed from magnetotelluric data (Snyder et al., 2014). The upper layer comprises a high proportion of depleted harzburgite and scattered eclogite (<~140 km), and the lower diamond-bearing layer is less depleted but more oxidized lherzolite and scattered eclogite (>~140 km) (Griffin et al., 1999a; Jacob et al., 2003; Griffin et al., 2004; Menzies et al., 2004; Creighton et al., 2008; Creighton et al., 2010). The geothermal gradient in the Lac de Gras area estimated from peridotite is comparable to the conduction model with a surface heat flow of 35 to 40 mW/m^2 (Figure 1.5 b) (Menzies et al., 2004). The age of the lower layer lies on a 3.2-3.5 Ga Re–Os isochron constrained by sulfide inclusions in olivine and diamonds (Aulbach et al., 2004; Westerlund et al., 2006). The f_{O2} recorded by peridotites under the Slave Craton ranges from NNO-6 to NNO+1 (Creighton et al., 2010; Stachel and Luth, 2015).

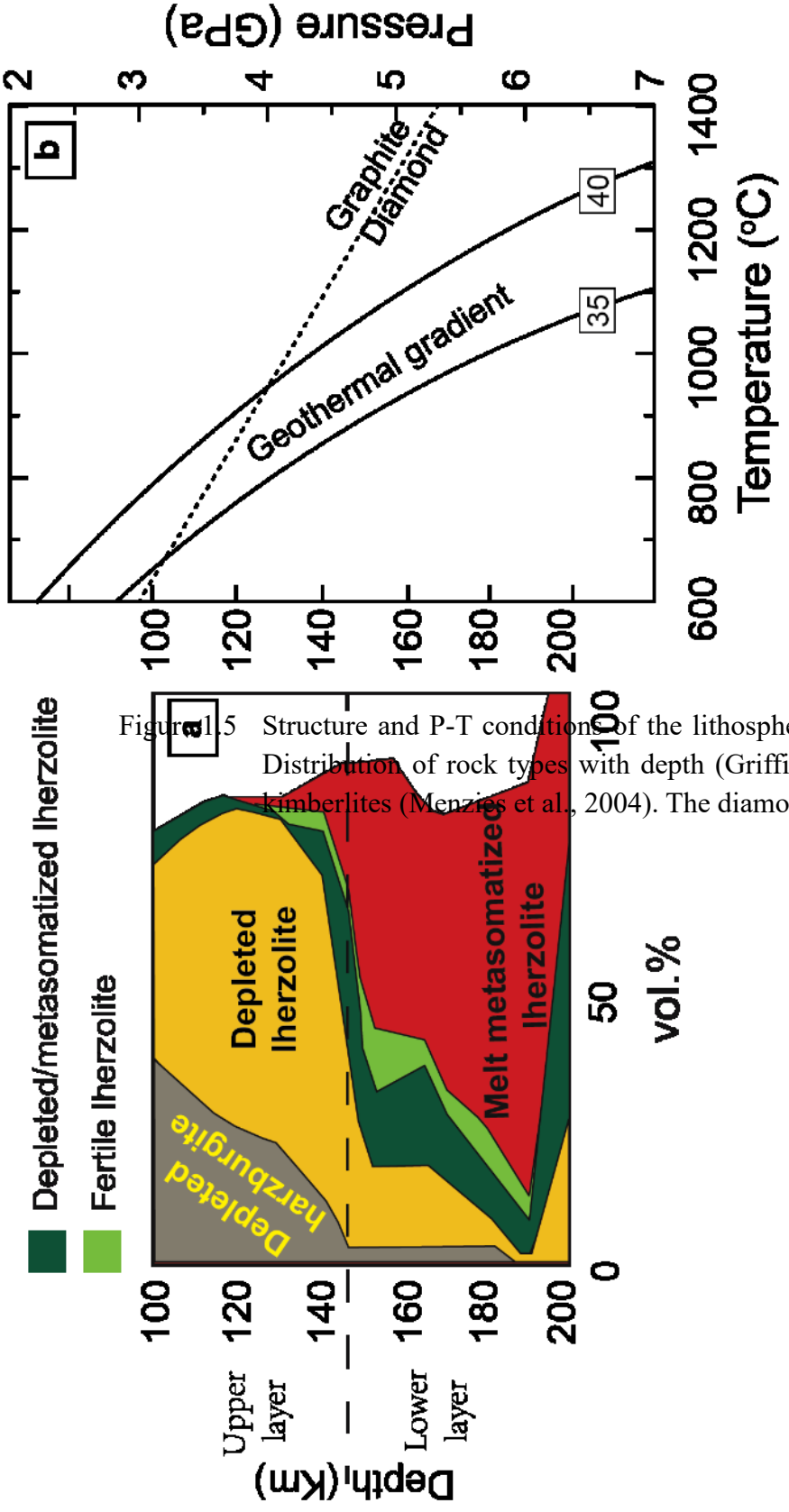

Figure 1.5 Structure and P-T conditions of the lithospheric mantle beneath the central Slav
Distribution of rock types with depth (Griffin et al., 2004); (b) Geothermal gra
kimberlites (Menzies et al., 2004). The diamond-graphite boundary is from Day (

The origin of the stratified structures of SCLM beneath the central Slave craton is still in debate. The plume model is supported by lower mantle inclusions in diamonds and olivine-hosted sulfides with lower mantle geochemical signatures, such as Ni-Co rich sulfides (Davies et al., 1999; Griffin et al., 1999a; Aulbach et al., 2004; Davies et al., 2004; Griffin et al., 2004; Aulbach et al., 2007). Alternatively, the stacking of oceanic lithosphere model is suggested by high Cr/Al ratios in diamond-hosted garnet requiring melting in the spinel stability field (Stachel et al., 2003; Creighton et al., 2008; Creighton et al., 2010). Geochemical features of eclogite scattered in both layers suggest its origin from both subducted oceanic crust and mantle magmas (Aulbach et al., 2004; Westerlund et al., 2006). Regardless of the origin of the lithospheric mantle, many lines of evidence indicate secondary enrichment events, as summarized below.

1.3.2. Volatiles in Mantle Metasomatism

Metasomatic enrichment of sub-continental lithospheric mantle beneath the central Slave craton has contributed to enrichment of trace elements (e.g., Y) and major elements (e.g., Ca) in mantle minerals (Griffin et al., 1999a; Griffin et al., 2004; Stachel et al., 2004; Aulbach et al., 2007; Creighton et al., 2010; Aulbach et al., 2013) and diamond formation and destruction (Klein-BenDavid et al., 2004; Stachel et al., 2004; Klein-BenDavid et al., 2007a; Klein-BenDavid et al., 2007b; Creighton et al., 2010). To date, four types of metasomatic media have been proposed: carbonatite melts, C-O-H fluids, silicate melts,

and brine (Griffin et al., 1999a; Griffin et al., 2004; Stachel et al., 2004; Aulbach et al., 2007; Creighton et al., 2010; Aulbach et al., 2013), simulation of melts in equilibrium with garnet (Aulbach et al., 2013), and fluid inclusions in diamonds (Klein-BenDavid et al., 2004; Klein-BenDavid et al., 2007a). However, the composition of the metasomatic media is still not well constrained due to limitations of conventional methods. Enrichment in Y, Zr and other incompatible elements and complex sinusoidal patterns of rare earth elements (REE) in garnet are interpreted to reflect a reaction with oxidizing silicate melts (Griffin et al., 1999b; Stachel and Harris, 2009; Bataleva et al., 2012) and carbonate-bearing C-O-H fluids (Creighton et al., 2010; Aulbach et al., 2013), respectively. However, this method is only descriptive instead of quantitative, and is also ambiguous because signatures of trace elements could result from two or more metasomatic events or from reactions of garnet with evolving media in a single metasomatic event, such as from initial silicate melts to C-O-H fluids (Griffin et al., 1999a; Griffin et al., 2004; Stachel et al., 2004; Creighton et al., 2010; Aulbach et al., 2013). Because diamonds are generally thought to result from C-bearing metasomatism in peridotite and eclogite (Anand et al., 2004; Taylor and Anand, 2004; Stachel and Harris, 2008; Stachel and Luth, 2015), diamond-forming metasomatic media recorded by micro-fluid inclusions in diamonds range from silicate or carbonate melts to hydrous C-O-H or brine fluids (Schrauder and Navon, 1993; Klein-BenDavid et al., 2004; Klein-BenDavid et al., 2007a). However, new estimates of the

oxidation states of the mantle f_{O2} support aqueous fluids or carbonate-poor silicate melts as the diamond-precipitating agent (Stagno et al., 2013). Therefore, constraining the mantle metasomatic media requires an independent, quantitative, and unambiguous method.

1.4. OBJECTIVES AND THESIS STRUCTURE

Despite considerable progress in constraining volatile composition associated with kimberlites and mantle metasomatism, quantitative and unambiguous constraints on volatile composition are still elusive owing to limitations of conventional methods. The sensitivity of diamond resorption features to the composition of C-O-H fluids permits its use as a potential and robust proxy of fluid composition in the latest diamond-destroying event in most diamond-bearing environments. To successfully applying diamond resorption morphology to natural diamonds, the following research objectives are required:

1. To establish a classification of diamonds in terms of resorption morphologies;
2. To examine the effects of internal properties of diamonds on resorption morphologies;
3. To investigate the effects of P-T-fluid composition on diamond resorption;

4. To analyze the formation mechanisms of etch pits.

The present work develops a new method for semi-quantitative assessment of composition of C-O-H fluids from diamond resorption morphology, and applies it to constrain the composition of fluids in diamond-bearing environments. The contributions of co-authors are listed in Appendix A. The thesis includes two parts. The first part (Chapters 2 and 3) classified diamond resorption features into kimberlite-induced and mantle-derived resorption morphologies, and then examines the effects of internal properties (N contents and aggregation states, zonings) on diamond resorption morphology.

In Chapter 2, I establish the novel diamond classification based on diamond resorption morphologies through introducing new nomenclature, examining the relationships between resorption morphologies and diamond growth zones and the estimate T of diamond storage in the mantle. The novel diamond classification characterizes kimberlite-induced and mantle-derived resorption morphologies. Diamond resorption morphologies show no relationships with diamond internal zones or N contents and aggregation states, indicating minor effects of internal properties on diamond resorption morphology. Comparison N content and aggregation states of diamonds to those of diamonds from xenoliths worldwide lead me to propose that most diamonds with the hexagon-bearing mantle-derived morphology may be from peridotite. Comparison to published experimental results allows me to hypothesize that the kimberlite-induced resorption

morphologies result from resorption in H_2O-rich fluid exsolved from kimberlites and the hexagon-bearing resorption features resulting from resorption in CO_2 fluid or carbonate melt under the mantle conditions.

Chapter 3 presents a more detailed study of diamond internal zones using high-resolution cathodoluminescence (CL) on diamonds studied in Chapter 2, focusing on the relationships between the mantle-derived diamond resorption morphologies and in-situ N and C isotope contents of diamonds obtained on diamond outer rims using the secondary ion probe (SIMS). New data continue supporting negligible effects of growth forms and N contents on diamond resorption morphologies (Chapter 2). The rim-ward increase and decrease trends of carbon isotopes in diamonds suggest the presence of oxidizing (CO_2 and carbonate melts) and reducing (CH_4) growth media respectively.

The second part (Chapters 4 and 5) presents results of diamond resorption experiments using a piston cylinder apparatus, addresses the P-T-X effects on diamond resorption, and shows the application results of diamond resorption morphologies to the Ekati diamonds. This experimental part is distinguished from previous experimental work in the following aspects: 1) for the first time a systematic investigation of P effect on diamond resorption has been made; 2) the composition of diamond-etching C-O-H fluids using in-situ entrapment of fluid inclusions at run conditions has been monitored; 3) the presence of miscibility gap in the CO_2-H_2O-dominated system at 1-3 GPa and the effects of bulk fluid

composition on diamond resorption have been documented; 4) atomic force microscopy (AFM) has been employed to observe evolution of etch pits on diamonds during resorption.

Chapter 4 addresses the P-T effects on diamond resorption in a pure H_2O system at 1-3 GPa and 1150-1400 ^oC. The experimental results demonstrate that increasing P suppresses diamond resorption rate, accelerates diamond rounding rate, and has little effect on resorption morphologies, except for the formation of circular pits. Circular pits on the THH faces always accompany main resorption features at 1 GPa under the MgO-forsterite silica buffer, leading me to propose that circular pits form in a defect- and condition-controlled kink mechanism. The evolutionary path of trigons from trumpet-shaped point-bottomed trigons to trumpet-shaped flat-bottomed trigons to trapezoid-shaped flat-bottomed trigons measured using AFM suggests a modified defect-oriented and condition-controlled kink mechanism. Application of experimental results of diamond resorption to Ekati diamonds confirms the presence of H_2O-rich fluids in kimberlites, suggests the presence of a predominantly H_2O zone in the kimberlites before eruption, and imply that preservation of diamond estimated by the octahedral:THH ratio (Oct/THH) of diamond forms may not be an indicator of weight loss but the depth where free aqueous fluids exist. My experimental results approve the formation hypothesis of kimberlite-induced resorption morphologies in a H_2O-rich fluid system (Chapter 2).

Chapter 5 addresses the P-X effects on diamond resorption in fluids with X_{CO2} ranging from 0 to 1 at 1-3 GPa and 1150 -1350 ºC. The immiscible binary system CO_2-H_2O at the run conditions contradicts the traditional view of a single CO_2-H_2O fluid at high P and T. The miscibility gap decreases as P increases from 1 to 3 GPa at 1250 ºC. Absence of circular pits at 1 GPa in the immiscible CO_2-H_2O system does not agree with the proposed formation of circular pits by attachment of CO_2 bubbles (Robinson, 1979), but indicates a condition-controlled forming mechanism (Chapter 4). In CO_2-dominated fluids, increasing P suppresses diamond rounding rates and resorption rates, but does not affect resorption morphology. Evolution of etch pits from trigons to hexagons suggests a defect- and condition-controlled kink mechanism in three stages: a defect-controlled stage where initial etch pits nucleate at defects, condition-controlled stage in strain-free areas, and the competition stage between defect- and condition-controlled resorption in strain fields around defects. My experimental results confirm the formation conditions of hexagons (Chapter 2) and demonstrate diamond resorption morphology as a robust and semi-quantitative proxy of the fluid composition in the latest diamond resorption event. In combination with previous results of diamond resorption experiments, I identify four types of diamond resorption morphology in terms of bulk fluid composition: pure H_2O, aqueous, carbonic, and CO_2/carbonate melts. Application to the Ekati diamonds suggests that the pre-eruption kimberlite column is stratified with a top CO_2–rich fluid cap, a H_2O-rich fluid

layer at the middle, and an aqueous fluid-bearing kimberlite magma at the bottom, and the presence of CO_2 or carbonate melts in the lithospheric mantle beneath the central Slave craton.

Chapter 6 reviews factoring affecting diamond resorption, presents a preliminary model of diamond morphologies according to the evolving fluid phases in kimberlites, comments on the general application of resorption morphologies to natural diamonds, provides suggestions for future studies, and concludes with a list of the main scientific outcomes of the thesis.

CHAPTER 2. MANTLE-DERIVED MORPHOLOGY OF DIAMOND: RECORDS OF DIAMOND-DESTROYING MANTLE METASOMATISM IN THE SLAVE CRATON

2.1. PREFACE

This chapter is based on the article '*Records of mantle metasomatism in the morphology of diamonds from the Slave craton.*' by Z. Zhang and Y. Fedortchouk, published in the European Journal of Mineralogy (Zhang and Fedortchouk, 2012). The copyright agreement forms for this and subsequent chapters derived from published manuscripts are present in Appendix G.

2.2. ABSTRACT

Every population of kimberlitic diamonds contains crystals with remnants of mantle-derived resorption features that carry the information about diamond-destroying mantle metasomatic events. We investigated 109 octahedral and tetrahedral diamonds (with {111} faces) representing unresorbed, kimberlite-induced (KIM), and mantle-derived (MR) resorption morphologies selected from 630 crystals from Grizzly, Misery, Leslie, and Koala kimberlites (Ekati mine, Northwest Territories, Canada). The MR category is further

subdivided into morphologies with complex features (CM-1/2/3) and with resorption-born step-faces (SM-1/2/3a, b/4) and the classification criteria are proposed. In order to test if the different morphological styles have a common residence history in the mantle we obtained cathodoluminescence (CL) images on polished surfaces of each diamond and measured content and aggregation state of nitrogen defects using Fourier transform infrared (FTIR) spectroscopy. Zoning patterns on CL images also helped to distinguish between growth and resorption step-faced morphologies. Nitrogen data of diamond rims form two clusters: I) total nitrogen above ~ 400 ppm and low state of aggregation (< 30% of B centers); II) total nitrogen < 1000 ppm (mostly < 400 ppm) and high state of aggregation (~ 20 to 98% of B centers, mostly above 30%). The study shows a clear correlation between the mantle resorption styles and the internal properties - nitrogen data and zoning patterns on CL images. Comparison of our results to the existing experimental data on diamond dissolution at high pressure and to the published datasets of diamonds recovered from eclogitic and peridotitic xenoliths shows that, in the Slave craton, metasomatism in peridotite develops complex resorption features (CM-1) most likely in the presence of CO_2-rich fluid and step-faced (SM-2) diamonds in the presence of H_2O fluid, whereas metasomatic fluid in eclogite is probably H_2O-rich.

2.3. INTRODUCTION

The prolonged mantle residence back to the Archaean (Richardson et al., 1984) allows diamonds to bear the records of different events of diamond-destroying metasomatism, which are documented by truncated growth zoning of inner parts of diamond crystals (Bulanova, 1995) and by resorption features on the surface of xenolith-hosted diamonds (Robinson, 1979; Viljoen et al., 2004). Composition of micro-cavities in fibrous and cloudy diamonds from kimberlites indicates the existence of oxidizing H_2O-rich metasomatic fluid/melts in the mantle during diamond resorption events (Klein-BenDavid et al., 2007b). Our knowledge of diamond-destroying mantle metasomatism is still very limited and diamond resorption features could provide new constrains on the compositions and conditions of the metasomatic media.

Large diversity of diamond resorption morphologies indicates variable composition of the oxidizing media. Since the first diamond-etching experiments under ambient pressure in 1892 (Luzi, 1892), our knowledge of diamond resorption features has been progressively increasing. Not only did the experiments reproduce many of the diamond surface features (Fedortchouk et al., 2007; Khokhryakov and Pal'yanov, 2007; Arima and Kozai, 2008), but they also revealed that: 1) temperature and oxygen fugacity (fO_2) mainly control diamond dissolution rate, and 2) the composition of volatiles determines the styles of the

resorption. These characteristics allow to use the morphology of natural kimberlite-hosted diamond for constraining presence and composition of the reacting fluid(s) in kimberlite magma (Fedortchouk et al., 2010) and in the mantle (Fedortchouk and Zhang, 2011).

Diamond morphology captures the very last evolutionary stage of crystal growth or resorption. Internal structures of diamond revealed by cathodoluminescence (CL) images document the oscillating growth, cessation of growth and resorption, re-growth, and deformation (e.g. Bulanova, 1995; Harte et al., 1999). Growth conditions affect the concentration of defects in diamond lattice including the most common, nitrogen (Boyd et al., 1994; Cartigny et al., 2001). When diamond crystals with similar style of mantle-derived resorption also share similar growth patterns on CL images and the range of nitrogen content and aggregation state, this could indicate their residence (and perhaps origin) in the same mantle reservoir. Styles of diamond resorption would then characterize metasomatic conditions in the particular mantle lithology.

Our previous study (Fedortchouk and Zhang, 2011) comparing the morphology of natural diamonds with the experimental products of diamond dissolution under kimberlitic conditions established the criteria for distinction between kimberlite-induced and mantle-derived resorption features. The relationship between diamond resorption morphologies and the nitrogen defects have been noticed (Fedortchouk and Zhang, 2011). One of the

limitations in the previous study is the ambiguous origin of the step-faced crystals that could be results of growth (Sunagawa, 1984) or resorption (Viljoen et al., 1992).

Here we perform a systematic and comprehensive study of morphology, internal textures (using CL images), and nitrogen defects of diamond populations from four Ekati Mine kimberlites in the central Slave craton in order to investigate the relationship between the growth, resorption, and deformation history of diamond crystals with similar mantle-derived resorption features. We also examine the origin of step-faced crystals through examining zoning patterns on CL images and further develop the resorption-based classification. Finally, we compare our results with the diamonds recovered from kimberlite-hosted xenoliths and with the products of diamond dissolution experiments to learn more about the resorption conditions and metasomatic processes in the different mantle reservoirs.

2.4. SAMPLES AND ANALYTICAL METHODS

The study uses micro-diamond parcels (< 1 mm crystals) from Grizzly, Misery, Koala, and Leslie kimberlites and some macro-diamonds (> 1 mm) from the Grizzly pipe (total 630 stones). Details on kimberlites and the diamond parcels are given elsewhere (Fedortchouk et al., 2010, and references therein). All diamonds are non-fibrous and most show resorption features, suggesting diamond resorption before or after the formation of fibrous

diamonds. All diamonds were examined under an optical microscope to select non-fragmental and non-fibrous octahedral and tetrahedral crystals with {111} faces and to break them further into: 1) unresorbed octahedral crystals; 2) octahedrons and tetrahedrons with kimberlite-induced resorption features; 3) crystals with variable resorption features that, we believe, are products of resorption events prior to the entrainment in kimberlite magma. The criteria for distinction between kimberlite-induced and mantle-derived resorption are described elsewhere (Fedortchouk and Zhang, 2011). The representative examples of each morphological category from the four parcels (total 109 crystals) were selected for further studies. One corner of these crystals was polished parallel or sub-parallel to {100} using a conventional, cast iron scaife with electro-coated diamond dusts at the University of British Columbia (UBC) and the internal textures were observed on these polished surfaces using CL. CL images were collected using a Philips XL-30 scanning electron microscope (SEM) with attached CL consisting of a Hamamatsu R376 photomultiplier tube at UBC. The accelerating voltage was 15 - 20 kV at 70 - 100 uA and no coating was applied to the diamonds. The working spectra of the system ranged from 360 to 1000 nm. Nitrogen concentration and aggregation state of all the cut diamonds were determined by Fourier transform infrared (FTIR) spectroscopy using a liquid nitrogen cooled Thermo Nicolet Nexus 470 FTIR spectrometer linked to an IR microscope at the Department of Earth and Atmospheric Sciences, University of Alberta. All diamond

crystals were mounted on the edge of a glass slide with the polished surface facing the IR light. CL images provided a map of the growth zoning for picking the spots for FTIR analyses. Absorption spectra were measured in the transmission mode in the range of 4000 - 650 cm-1 with a resolution of 8 cm-1, and were collected for 200 s through a 100 × 100 um spot. A Type II diamond of a known thickness was used as a standard for the background correction for our diamonds with variable thickness. For data processing see Stachel et al. (2006). The detection limits depending on the diamond quality are generally in the 10 - 20 ppm range, and the relative errors for the concentration and aggregation state calculation are 10 and 20%, respectively.

2.5. RESULTS

The summary of morphology, color, sequences of growth zoning revealed on CL images, and the range of nitrogen defects of the studied diamond crystals from the four Ekati kimberlites is presented in Table B.1.

2.5.1. Morphological Grouping

Following the resorption-based classification of Fedortchouk & Zhang (2011), we divided each parcel into four morphological categories (Figure 2.1): no apparent resorption features (UnR), kimberlite-induced resorption (KIM) (KIM-1/2/3 styles on Figure 2.2),

Figure 2.1 Classification tree for the recognition of different resorption styles in studied diam
mantle-derived resorption; KIM: kimberlite-induced resorption; UnR: unresorbed

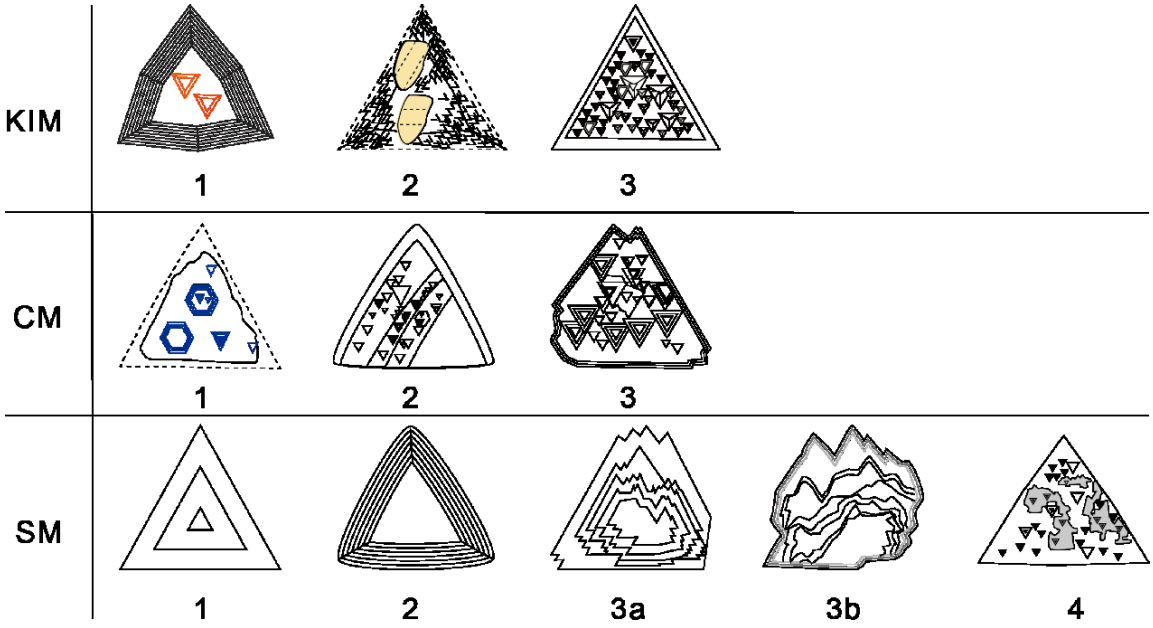

Figure 2.2 Sketches of morphological styles of studied diamonds. Sketches are after (Fedortchouk and Zhang, 2011). KIM- ditrigonal outlines of {111} faces: 1) with few individual trigonal etch-pits with flat and point bottoms, leaf striations on {110} faces, and smooth surface of {111} faces; 2) with frosted islands, and multi-sharp corners; 3) with numerous point-bottomed trigons and rough surfaces. CM - trigonal outline of {111} faces: 1) with deep and step-walled hexagonal pits; 2) with very deep but small trigonal pits; 3) with highly dense and trigonal pits. SM - trigonal outline of {111} 1) with only a few well-formed triangular widely step-faces; 2) with numerous triangular step-faces and bevelled edges; 3) a. with thin and irregular layers bearing straight edges and sharp multi-corners; b. with thin and irregular layers bearing curved edges and rounded multi-corners; 4) with irregular and trigon-bearing layers at different height.

mantle-derived resorption (MR) (CM-1/2/3 and SM-1/2/3/4 styles on Figure 2.2), and undefined features (UnD) that we could not assigned to any present category. Although diamond populations in the four kimberlites have profound morphological differences (Gurney et al., 2004) the majority of each diamond population carries KIM-resorption features in similar proportions (Grizzly - 61%, Misery - 70%, Koala - 79%, and Leslie - 58%) (Figure 2.3a). Diamond crystals from Misery and Koala commonly have few large individual trigonal etch pits, sheaf-striation on (110) edges, which characterize H_2O-rich kimberlite resorption (Figure 2.2 KIM-1). The resorbed edges and corners of KIM-style diamonds from Grizzly and some from Leslie develop protrusions pointing in [100] direction and “frosting islands” (Figure 2.2 KIM-2) ("shallow depressions" according to Robinson (1979, Figure 40b) that have been interpreted as an indication of resorption in H_2O-poor/lost kimberlites (Fedortchouk et al., 2010).

The proportions of MR-bearing diamonds are similar in Grizzly (18%), Misery (15%) and Leslie (17%) parcel, and is slightly lower in the Koala parcel (9%) (Figure 2.3a). In MR category, we distinguish: 1) CM - diamonds with intensive etching of trigonal {111} face producing deep trigonal and often hexagonal pits; and 2) SM - various types of step-faced resorption that develops triangular or irregular layers on trigonal {111} face (Figure 2.1 and 2.2). We further discern three styles of morphologies with complex features (CM-1/2/3) and five styles of step-faced diamonds (SM-1/2/3a, b/4) (Figure 2.1 and 2.2).

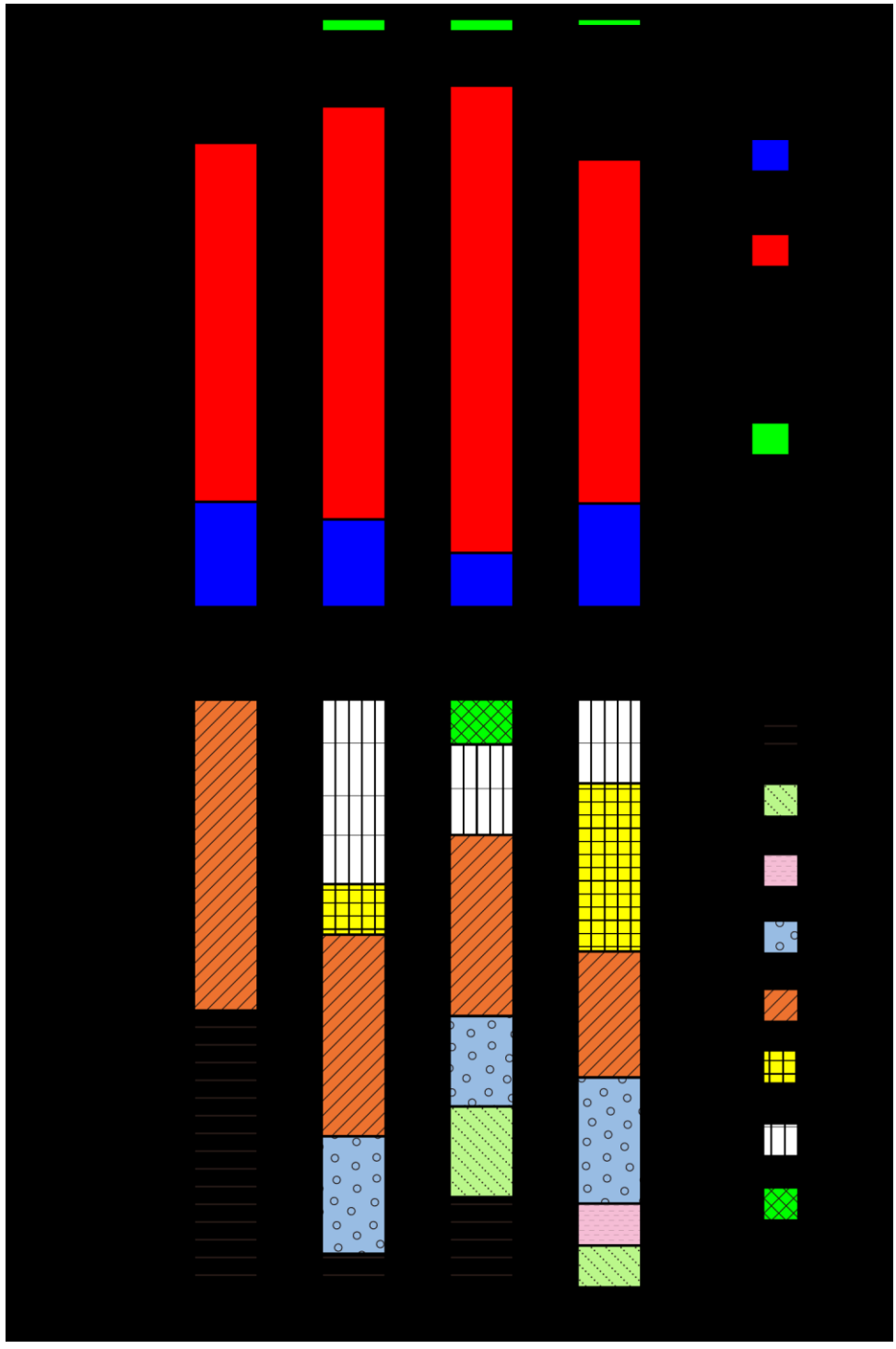

Figure 2.3 Morphological proportions of studied diamonds in the Grizzly, Misery, Koala, and Leslie parcels. a). Proportion of unresorbed, KIM, MR, and undefined diamonds; b). The style proportion of diamond in MR category. The abbreviations are the same as those in Figure 2.1.

The criteria for the distinction between the styles are given on Figure 2.2. The same MR resorption styles are present in all four kimberlites regardless of the styles of the KIM-resorption. For example, CM-1 style is common in three parcels except the Leslie parcel and SM-2 is widespread in all four pipes (Table B.1, Figure 2.3b). The color of the studied diamonds varies from colorless to brown of different intensities (Fedortchouk et al., 2010), and no correlation between the color and the morphology was found. Worthy of notice, brown stones make ~ 90% of Grizzly parcel.

2.5.2. Internal Texture

We collected CL images for all the polished surfaces of 109 diamonds, and based on the characters of luminescence, we recognized eleven zoning patterns for the studied diamond populations (Figure 2.4). In addition, one crystal (L97-A2-8, Table B.1) shows a deformation pattern crossing all the growth zones. We use truncated zoning of diamond rims on CL images to identify which surface features are the results of resorption vs. growth (Table B.1). All unresorbed stones have non-stepped rectilinear oscillating growth pattern (pattern 2b on Fig. 4, Seal, 1965), and their rims are continuous.

Most stones with KIM-resorption (total 14 stones) selected for this study have rims with non-stepped or stepped rectilinear oscillating growth zoning (pattern 2b and 3b on Figure 2.4), except for the homogeneous rims of diamond L97-5-4 and K95-5-4 (pattern 1 on

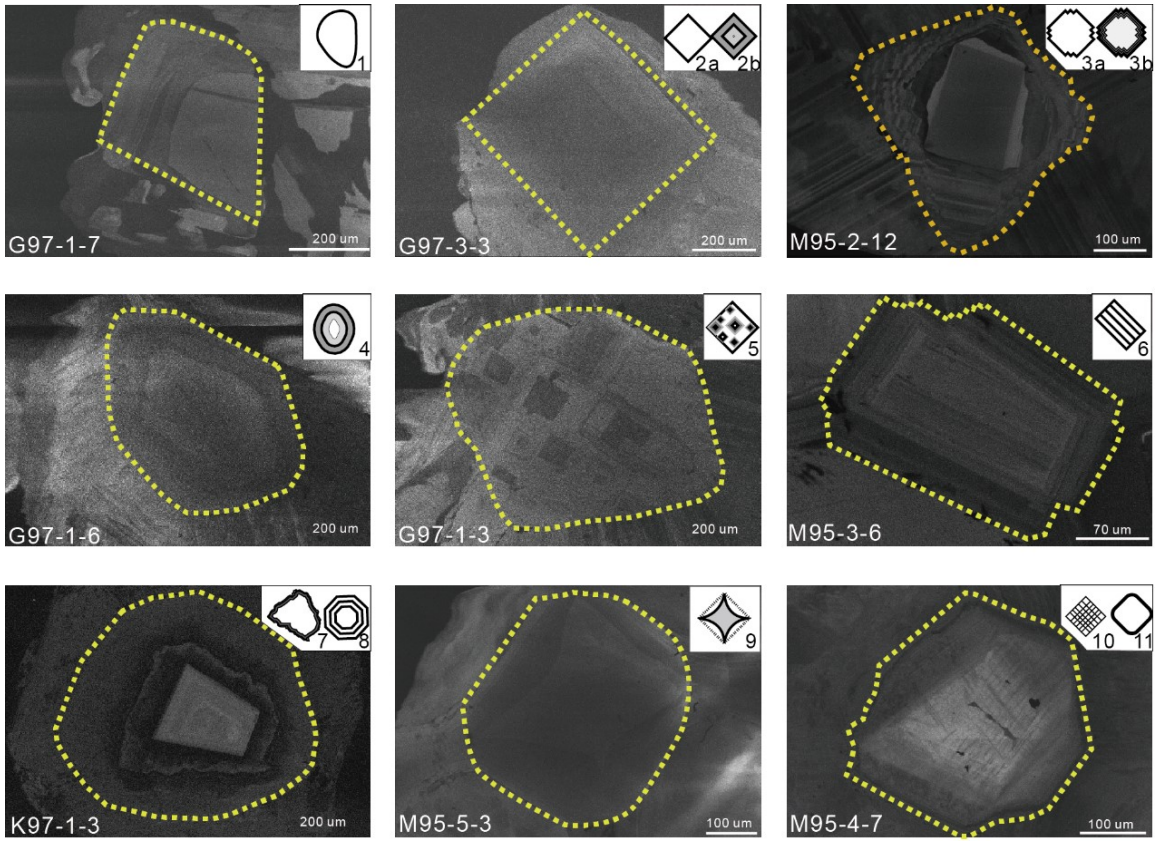

Figure 2.4 Zoning patterns on CL images of analyzed diamond stones from the four kimberlites. 1). Homogenous irregular zoning (Seal, 1965); 2) a. homogenous and rectilinear zoning; b. layer-by-layer rectilinear growth zone; 3) a. homogenous zoning with a stepped rectilinear outline; b. layer-by-layered and stepped rectilinear growth zoning; 4) oval zoning or agate texture; 5) multi-core zoning with two or more seeds; 6) banding sector; 7) blurry rectilinear growth zoning; 8) thin layer-by-layered octagonal growth zoning; 9) four-sided star zone; 10) 'plaid' structure; 11) black rim with weak to no CL, termed as dead zones (Harte et al., 1999).

Figure 2.4), and regardless of the rim patterns the final growth layers are always truncated. In MR-morphological category, rims of complex- and step-faced diamonds show different CL patterns. Stones with CM-1 features show no preferred patterns of rims. All four stones in CM-2 styles have the irregular and homogeneous rims, and the three CM-3 diamonds show truncated rims. All step-faced stones clearly prefer pattern 2 and 3 as the rims.

We use continuing or truncated zoning pattern on CL images to distinguish diamonds with step-faced morphology caused by resorption from those with growth step-faces. Even though the formation mechanism of steps on some crystals with weak luminescent rims is uncertain, we still generally distinguished resorption from growth steps (Table B.1). It is commonly believed that diamonds develop step faces during growth (Sunagawa, 1984). CL images of the SM diamonds from our study show that 67% have truncated resorption zoning patterns. Only one SM-1 stone has unambiguously continuous rim, and the other ~ 30% of the SM diamonds have blurry rims with ambiguous origin of the step faces (Table B.1).

Variation in the growth and resorption history of the studied diamonds is expressed by growth sequences (Table B.1). The internal textures are divided into five modes: 1) 2b or 3b patterns forming cores and rims (e.g. M95-2-3); 2) multi-seed pattern in the core (e.g. M95-3-2); 3) core with pattern 9 surrounded by rims with pattern 2 or 1 (e.g. sK95-3-3); 4) core with pattern 4 surrounded by rims with pattern 2 or 3 (e.g. K95-1-1); and 5) other

combinations of patterns (e.g. M95-4-7). In the studied population the two unresorbed diamonds and the SM-1 diamond with growth step-faces belong to mode 1. Diamonds with KIM-resorption show various internal textures. Although CL patterns in CM-1 diamonds generally vary, two crystals from Grizzly show very similar patterns (G97-1-3 and G97-1-4) and one with agate texture (pattern 4, G97-1-6) is very different from the rest of the style. All four stones with CM-2 style have blurry zoning (pattern 7) and weakly luminescent rims (pattern 11). Step-faced stones are various and have all 5 CL modes.

2.5.3. Nitrogen Content and Aggregation State

We made an attempt to analyze nitrogen data from the cores and rims of individual crystals using CL images as a map. However, in the transmitted mode the rim analyses would have some signal from the underlying core zones; some crystals only have high quality data from the core or from the rim. The total nitrogen content in the studied diamonds ranges from 20 to 1697 ppm. The diamonds are IaA–IaB type with 0 to 98% of the Type IaB defects (Table B.1). Within analytical uncertainties of FTIR, the cores of diamond normally show higher or similar nitrogen aggregation relative to that of the rims. One exception is diamond M95-1-4 where aggregation state of the core is lower than that of the rim.

In this study we focused only on the nitrogen data from diamond rims as the indicator of

the latest diamond growth event in the most recent mantle reservoir assuming that diamond surface features represent resorption conditions in this reservoir. Nitrogen data from the rims define two distinct clusters. Diamonds in cluster I bear high nitrogen contents (above ~ 400 ppm) but low states of aggregation (mainly below 30% of B centers); diamonds in cluster II show nitrogen concentration below 1000 ppm (mostly below 400 ppm) but with high states of aggregation (~ 20 to 98% of B centers, mostly above 30%) (Figure 2.5 and Table B.1). Diamonds from the Misery, Koala and Leslie pipes plot into both clusters (Figure 2.5 b, c, and d), while most of the Grizzly diamonds plot into the cluster II, except G97-3-3 in the cluster I (Figure 2.5a). The isotherms calculated using the equation from Taylor et al. (Taylor et al., 1996) and the diamond age from the neighboring Panda kimberlite (Westerlund et al., 2006) gave a range 1020 - 1070 ºC for cluster I and 1120 - 1170 ºC for cluster II (Figure 2.5).

Correlation between the nitrogen defects and diamond morphology noticed in our earlier study (Fedortchouk and Zhang, 2011) is further supported by the new data combined with the internal growth patterns on CL images (Figure 2.6). Six unresorbed diamonds plot in the cluster I with very similar values, and two polished diamonds show nearly identical continuous growth rims on CL images (Figure 2.6a). KIM diamonds with various CL patterns prefer cluster I (eight stones), but the three stones (G97-5-3, M95-5-4 and L97-5-4) fall into cluster II (Figure 2.6a). However, the M95-5-4 diamond preserves pre-existing

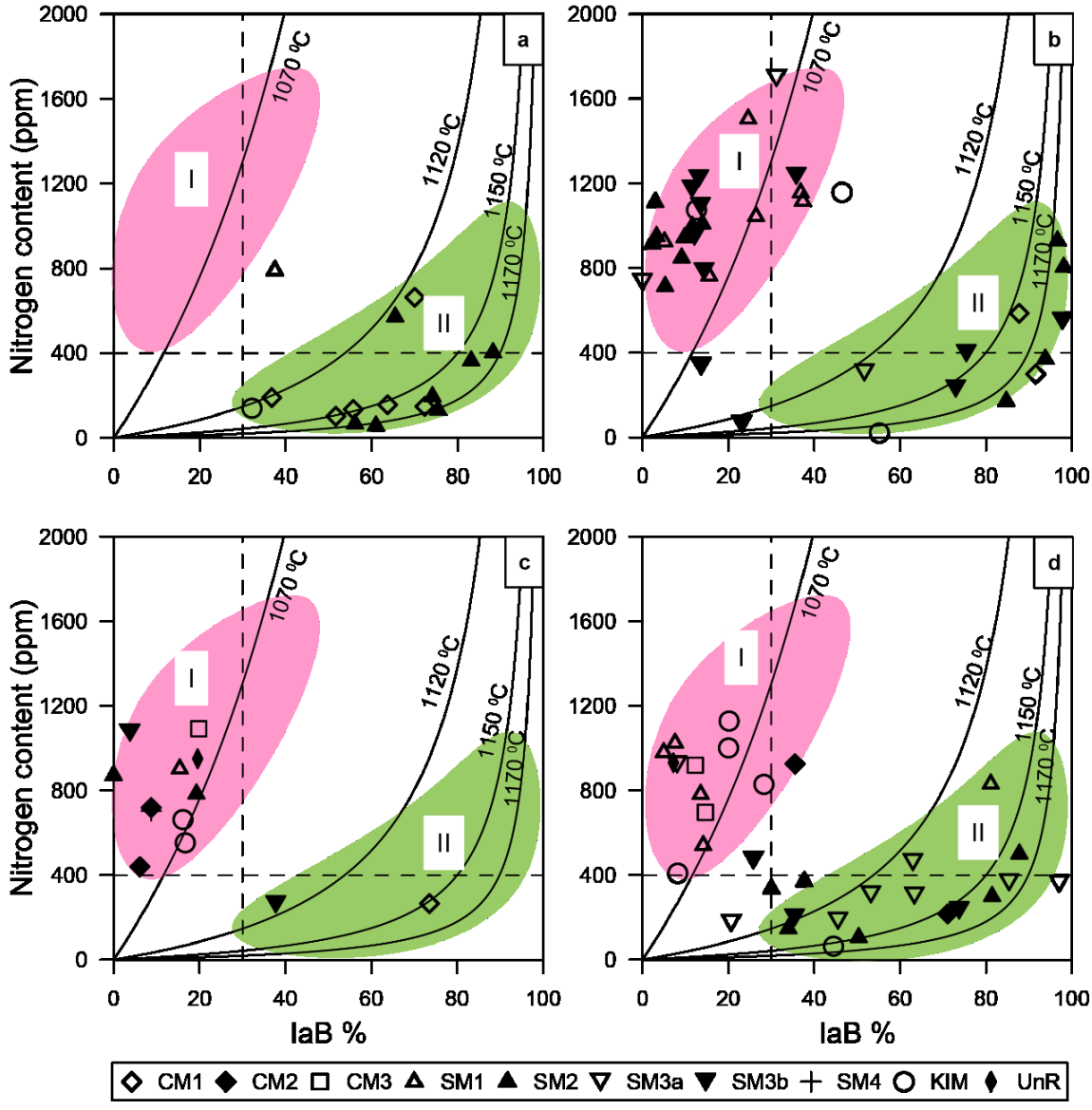

Figure 2.5 Total nitrogen contents vs. degree of aggregation of the studied diamonds from the Ekati mine. Only FTIR data through the rim are plotted. a. diamond stones from Grizzly kimberlite; b. stones from Misery kimberlite; c. crystals from Leslie kimberlite; d. crystals from Koala kimberlite. The isotherms were calculated using the equation from Taylor et al. (1996) at a given 3.5 Ga mantle residence time (Westerlund et al., 2006).

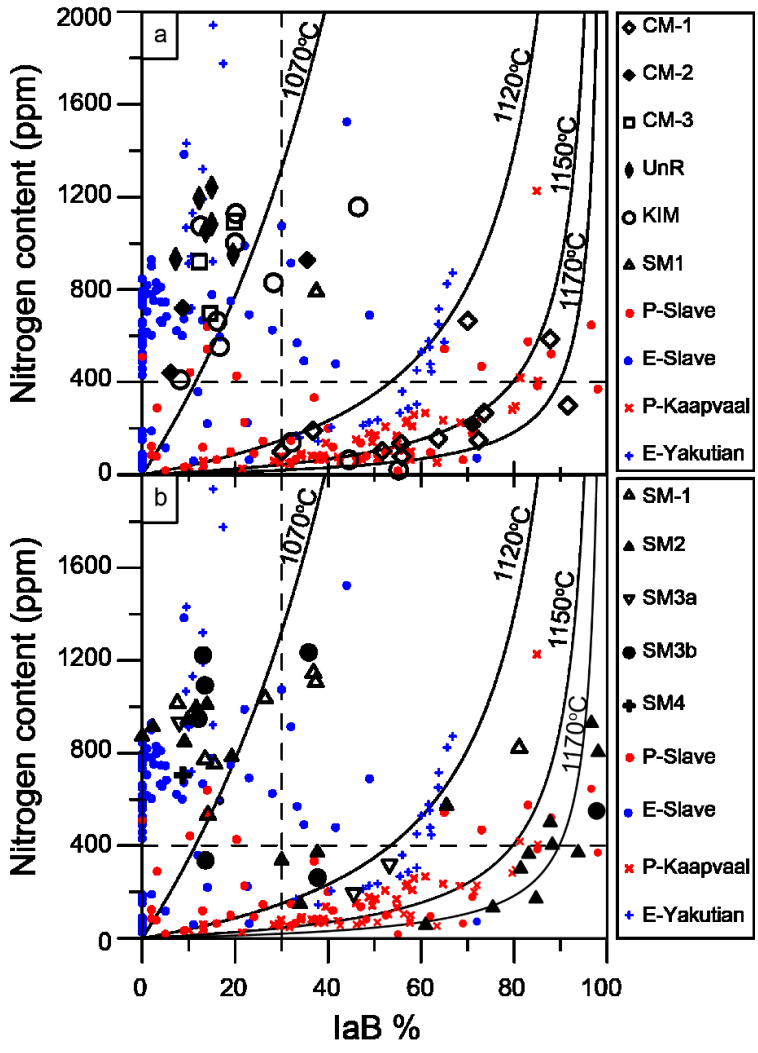

Figure 2.6 Total nitrogen contents vs. degree of aggregation of the analyzed diamonds with morphological styles. Only FTIR data through the rims of diamond are plotted. a. diamonds with complex features (CM), growth features (UnR and one SM-1), and kimberlite-induced features (KIM); b. step-faced diamonds (SM). The open circles and filled circles represent diamonds from peridotitic and eclogitic xenoliths in the Slave craton (Aulbach et al., 2011), respectively. The small crosses are the nitrogen data of diamond from an eclogitic xenolith in the Yakutian craton (Stepanov et al., 2007), and inclined crosses are nitrogen data of peridotitic diamonds from Lherzlite from the Kaapvaal Craton (Viljoen et al., 2004). The isotherms are the same as those in Figure 2.4.

SM morphology that probably pre-dated the KIM-resorption. All CM-1crystals plot in cluster I (Figure 2.6a). Interestingly, the two stones with similar internal patterns (G97-1-3 and G97-1-4) also have very similar nitrogen values, whereas the G97-1-6 diamond with notably different CL pattern has nitrogen content much higher (663 ppm) than the rest of the style. Four CM-2 diamond crystals scatter between the two clusters: three colorless stones are in cluster I and one brown (L97-1-3) in cluster II.

SM diamond crystals with stepped faces of growth, resorption, and uncertain origin based on the CL images plot into both clusters (Figure 2.6). Only diamond G97-3-3 with unambiguous growth steps has similar nitrogen content to the unresorbed crystals and plot into cluster I (Figure 2.6a). Seven out of eight SM-1 stones plot into cluster I and the only diamond in cluster II is LS97-A2-8 showing deformation pattern. SM-2 diamonds break into two distinct groups based on the nitrogen defects: one group in cluster I have total nitrogen content in 800 - 1000 ppm range and nitrogen aggregation < 30% and the other group is following the 1120 and 1170 ^{0}C isotherm in cluster II (Figure 2.6b). In cluster II). Crystals with SM-3a and -3b styles plot into both clusters and the only diamond with SM-4 features is in cluster I (Figure 2.6b). It is worth notice that two SM-3a stones (L97-4-8 and L97-4-5) that have nearly identical nitrogen data also show the very similar rim pattern.

2.6. DISCUSSION

2.6.1. Relationship between Diamond Morphology and Internal Properties

The main goal of this study was to test if the diamond stones with different types of mantle-derived resorption (Fedortchouk and Zhang, 2011) also share similar mantle residence conditions. Diamonds brought to the surface by kimberlite magmas suffer resorption in the mantle further modified by the resorption in kimberlite unless protected by the xenoliths (Gurney et al., 2004; Fedortchouk and Zhang, 2011). The existence of pseudohemimorphic diamonds is the evidence for such a shielding effect of xenoliths (e.g., Robinson, 1979). We earlier proposed that this 'shielding effect' preserves different types of mantle-derived morphologies (Fedortchouk and Zhang, 2011). Comparison of the morphological and internal characteristics of diamonds and including two more diamond populations in this study allow us to refine the relationship between the resorption morphology and the mantle history of the Ekati diamonds.

Nitrogen data from this study shows that diamonds with the same morphological styles have very similar nitrogen content or follow the same isotherm indicating similar residence conditions (Figure 2.6). For example, two unresorbed and one SM-1 diamond stones with nearly identical internal textures have similar nitrogen content within cluster I (~ 930 ppm and 791 ppm, respectively) (Figure 2.6a). All crystals in SM-1 style plot within cluster I,

except the one showing evidence of deformation (L97-A2-8) that could enhance the migration of nitrogen (Evans, 1992). This suggests that SM-1 crystals have younger rims or lower temperature of mantle storage prior to the last resorption event. All CM-1 crystals plot in cluster II (Figure 2.6a). Although eight out of eleven CM-1 diamonds in our study are from Grizzly population, which almost entirely fall in cluster II, CM-1 stones from the other three kimberlites also plot very close as one group. Furthermore, the only CM-1 stone (G97-1-6) with distinct agate growth zoning is an outlier on the nitrogen diagram, whereas the three CM-1 stones with very similar internal textures (pattern 5) plot tightly indicating their similar growth and resorption history under the same mantle conditions. SM-2 diamond crystals common in all four pipes fall into both clusters (Figure 2.6b). This clearly indicates two populations formed in different diamond growth events that experienced last resorption at similar conditions. Interpretation of KIM diamonds is complicated due to the assumption that the simple {111} faces with only few shallow trigons indicates the absence of any resorption prior to the entrainment into kimberlite magma. This agrees well with the preferential plotting of these crystals into cluster I together with the other unresorbed stones. However, some of the KIM diamonds started perhaps as a SM morphology that was completely overwritten during resorption in kimberlite. Some of the KIM diamonds that plot in cluster II show remnants of step faces supporting this suggestion.

Examining the relationship between the surface morphology of diamonds and their internal properties such as nitrogen data and zoning pattern revealed in CL images has shown that some of the diamond stones with similar type of mantle-derived resorption share exceptionally similar internal characteristics. This confirms similar mantle history of these diamond morphological styles and indicates their derivation from the same mantle "block" (Gurney et al., 2004). Thus, the resorption morphology of different MR diamond styles from Ekati kimberlites becomes an important record of past resorption events affecting the diamondiferous lithospheric mantle beneath the central Slave craton and could be used to constrain the fluid history during diamond-destructive metasomatism in the different mantle "blocks".

2.6.2. Resorption-based Classification

The existing morphological classifications of diamond are based on the general crystal morphology related to the growth conditions of diamond (Orlov, 1977). We earlier proposed to base morphological classification on the resorption features in order to constrain fluid history of diamondiferous mantle and of diamond-bearing magmas (Fedortchouk and Zhang, 2011). Detailed examination of nitrogen data and zoning patterns on CL images of diamond with different mantle-derived resorption styles allowed us to refine the proposed classification. We further subdivided the CM diamond crystals into three styles CM-1, -2, and -3 (Figure 2.1). This morphological subdivision is supported by

variation in the nitrogen data and internal textures. We also identified more groups of stepped-faced diamonds (SM-1, 2, 3a and 3b, 4 on Figure 2.1 and 2.2), whose ambiguous origin can be a result of growth (Sunagawa, 1984) or resorption (Viljoen et al., 1992). Analysis of CL images in our study demonstrated that about 65% of the stepped faced morphologies are caused by resorption because of the truncation of the zoning patterns on the CL images. The other 35% of the stepped faced diamonds are most likely the product of growth because of the continuous zoning revealed in their CL images. However, more detailed study of the rims is necessary to confirm the growth origin of step-faced diamonds. It is worth notice that even though the simple SM-1 style is more often showing a growth-related development of stepped-faces than the other SM diamond stones, it still has many stones where step-faces are most likely a result of resorption.

2.6.3. Diamondiferous Sectors and Their Resorption Morphology

In this study we propose three mantle-derived morphologies. Unresorbed step-faced diamonds (with possibly growth zoning on CL images) have similarly high total nitrogen, low aggregation state, and plot within cluster I with unresorbed flat-faced diamonds. Among the diamonds with complex dissolution features (CM-1/2/3) the CM-1 style is better represented in the four studied kimberlites. CM-1 stones have similarly low total nitrogen and high aggregation state (plotting within cluster II on Figure 2.6a). Finally, step-

faced diamonds (SM-1 to -4) fall into both clusters of high and low nitrogen aggregation (Figure 2.6b).

Reported morphologies in the literature of diamond crystals extracted from eclogitic and peridotitic xenoliths include unresorbed octahedral, cube, dodecahedral, and step-faced crystals (Robinson, 1979; Shee et al., 1982; Spetsius, 1995; Viljoen et al., 2004; Stepanov et al., 2007; Aulbach et al., 2011). The well-documented morphologies of octahedral and cubo-octahedral diamond crystals from an eclogitic xenolith from Udachnaya kimberlite (Stepanov et al., 2007) correspond to our SM-1 and SM-2 resorption styles. The origin of diamonds with complex features (CM) is less clear. Complex features with hexagonal pits somewhere similar to our CM-1 style are reported from eclogitic xenoliths from the Kaapvaal craton (Robinson, 1979). However, the quality of the images precludes the direct comparison of these morphologies with the CM-1 resorption style in this study. Diamond crystals from peridotitic xenolith recovered from the Argyle lamproite pipe, Western Australia, show irregular and shallow hexagonal pits (Hall and Smith, 1984), which yet are very different from the CM-1 resorption style. More morphological studies on xenolith-host diamonds are necessary to confirm the association of CM resorption types with certain mantle lithology. The unresorbed and step-faced diamonds similar to our SM styles are commonly found in both peridotitic and eclogitic mantle xenoliths brought by kimberlites.

Experimental data on diamond dissolution are abundant for kimberlite emplacement conditions (P < 1 GPa) and are very scarce for higher pressure corresponding to the mantle conditions. Experimental data at 1 GPa (Fedortchouk et al., 2007; Arima and Kozai, 2008) helped to establish morphological criteria of KIM resorption in fluid-rich and fluid-poor kimberlite magmas. Ditrigonal shape of {111} face is one of the characteristic features of resorption at low pressure of kimberlite emplacement (Fedortchouk et al., 2010; Fedortchouk et al., 2011) and is common for 1 GPa experimental runs (Fedortchouk et al., 2007; Arima and Kozai, 2008). It is therefore an important observation that diamond dissolution in dry and fluid-bearing carbonate melts at 5 - 7 GPa reported only trigonal shape of {111} (Khokhryakov and Pal'yanov, 2010). Diamond dissolution at 5 - 7 GPa in carbonate melts in volatile-free and CO_2-bearing conditions, produced positively oriented trigons and hillocks on diamond surface that differ from any mantle-derived resorption types from the present study. Only dissolution in carbonate melt with aqueous fluid developed shallow negatively-oriented flat-bottomed trigons and negative hillocks on step-faced octahedra with trigonal {111} face (Khokhryakov and Pal'yanov, 2010) of similar morphology to the step-faced SM–2 resorption type from the present study (Figure 2.2). Crystal forms similar to our CM-1 morphology were not reported in diamond-dissolution experiments. However, some products of diamond dissolution at 2.5 GPa in CO_2-rich synthetic kimberlite (Arima and Kozai, 2008) produced deep hexagonal pits on

the {111} face. Dissolution at 1 GPa in CO_2-rich fluid also reported complex but shallow hexagonal pits (Fedortchouk et al., 2007), which overall morphology still differs from the CM-1 resorption style. Although it is possible that CM-1 morphology is indicative of elevated CO_2 content in the oxidizing fluid, more experimental data at high pressure are needed to confirm the origin of CM-1 resorption style. Indeed, hexagonal pits are believed to be a combination between negative and positive trigons (Evans and Sauter, 1961) and experiments by Khokhryakov & Pal'yanov (2010) suggest that the appearance of hexagonal pits requires certain CO_2:H_2O ratio of etchants.

The two main types of diamondiferous xenoliths from kimberlites are peridotitic (65%, P-type diamonds) and eclogitic (33%, E-type diamonds) (Stachel et al., 2009). Both types are reported from the Slave craton (Tappert et al., 2005; Creighton et al., 2008; Aulbach et al., 2011). Nitrogen content of diamond reflects diamond growth environment – availability of nitrogen, growth rates, and growth conditions that could have affected the partitioning of nitrogen into diamond lattice (Stachel et al., 2009). These parameters might be variable for different diamondiferous reservoirs in the mantle. The residence time and thermal regime are reflected in the nitrogen aggregation state. We compare nitrogen data of diamonds with mantle resorption features from this study to the nitrogen data reported in the literature for the diamonds recovered from xenoliths of eclogites or peridotites (Viljoen et al., 2004; Stepanov et al., 2007; Creighton et al., 2008; De Stefano et al., 2009;

Aulbach et al., 2011). We do not use the data when determination of the host mantle lithology is based on mineral inclusions since the focus of our study is metasomatism during the latest diamond residence in the mantle. Diamond crystals from diamondiferous peridotite xenoliths mainly plot into cluster II (low nitrogen content and high aggregation), and the majority of eclogitic diamonds plot into cluster I (high total nitrogen and low aggregation) (Figure 2.6). Diamonds from an eclogite xenolith from Udachnaya kimberlite in Siberia also plot into cluster I but the cores of some zoned stones follow an isotherm with much higher nitrogen aggregation due to an earlier episode of diamond growth (Stepanov et al., 2007) (Figure 2.6). Based on the comparison of nitrogen data for mantle-derived resorption styles from this study and the diamonds derived from xenoliths hosted in other Ekati kimberlites (Aulbach et al., 2011) we propose that CM-1 resorption style is characteristic of peridotitic source while unresorbed and SM-1 resorption represent in eclogitic source. The SM-2 resorption occurs in both mantle lithologies (Figure 2.6).

The zoning patterns revealed by CL images also show some correlation with nitrogen data (Figure 2.7). Most of the crystals with multiple growth centres have low nitrogen and high aggregation (mode 2 on Figure 2.7). Such internal structure may indicate higher rate of nucleation over crystal growth and agrees with the low nitrogen content. Indeed, slow growth would eliminate defects of the crystal structure limiting the amount of nitrogen. The high nitrogen and low aggregated cluster is dominated by the crystals with simple

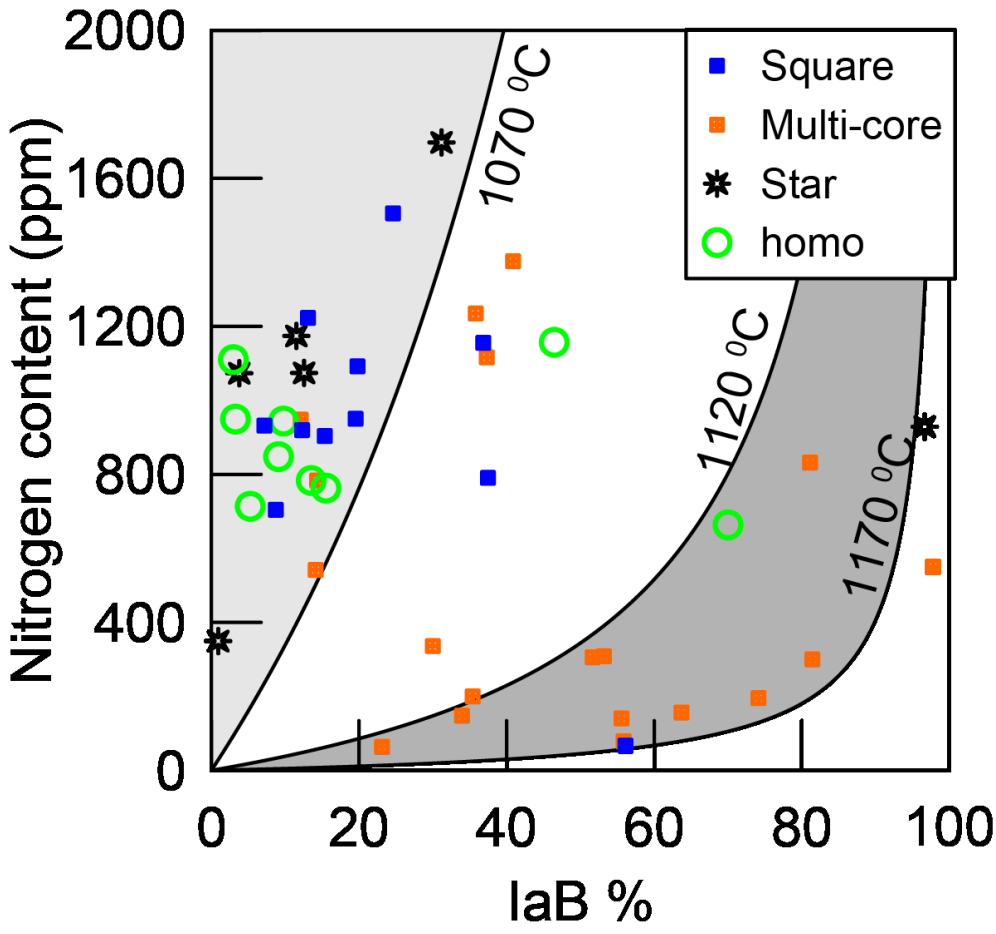

Figure 2.7 Total nitrogen contents vs. degree of aggregation of the analyzed diamonds with different CL modes. Blue solid square: one with pattern 2b or 3b forming cores and rims; orange solid square one with multi-seed pattern in the core; black star: core with pattern 9 surrounded by rims with pattern 2 or 1; and green circle: core with pattern 4 surrounded by rims with pattern 2 or 3.

zoning and cores of irregular shape (mode 3 and 4 on Figure 2.7). This indicates faster crystallization rate and therefore incorporation of more nitrogen defects in diamond crystal lattice (Boyd et al., 1994; Cartigny et al., 2001).

2.6.4. Diamond-destroying Metasomatism in the Slave Craton

Our data clearly shows that diamond population sampled by the Ekati kimberlites from the sub-continental mantle of the Slave craton records not only few diamond growth events in peridotitic and eclogitic diamond sources but also different episodes of diamond-destroying metasomatism. Variable mantle-derived resorption styles indicate that H_2O:CO_2 ratios of the media were very different during these diamond-destructive events. We propose that diamond crystals with deep hexagonal pits with step-walls on trigonal {111} face (CM-1) are a product of resorption in peridotite. The existing experimental data indicate that the media (fluid) had perhaps elevated CO_2 content during development of CM-1 resorption. However, presences of SM-2 style in peridotite xenoliths and among the diamonds with high nitrogen aggregation suggest that aqueous metasomatism was also common in this environment. Residence temperature of these presumably peridotitic diamonds is ~100 ^{0}C higher than for eclogitic diamonds. Even if eclogitic diamonds under the Slave craton are much younger (~ 1.9 Ga, Aulbach et al., 2011) than peridotitic stones (Westerlund et al., 2006), the temperature difference between the two clusters is still about 100 ^{0}C. Resorption conditions in eclogite favour the development of simple step-faced

morphologies (SM-1 and a group of SM-2 on Figure 2.6). We propose that composition of media during diamond-destructive metasomatism in the eclogitic mantle is H_2O-rich. In addition, all unresorbed flat-faced and step-faced micro-diamonds from this study also plot in the cluster of eclogitic diamonds suggesting a relatively recent diamond crystallization event, which was not followed by any resorption.

2.7. CONCLUSIONS

To summarize, our study demonstrated a distinct correlation between the characters of mantle-derived resorption and the internal properties of diamond crystals related to their history in the mantle. Therefore, diamond crystals with different mantle-derived resorption can help to constrain the conditions during the different episodes of diamond-destructive metasomatism in various mantle reservoirs. Comparison of diamond nitrogen data from this study to the published datasets for diamonds from eclogitic and peridotitic xenoliths indicates that metasomatism in peridotite develops complex resorption features (CM-1) most likely in the presence of CO_2-rich fluid and step-faced (SM-2) diamonds in the presence of H_2O fluid, whereas metasomatic fluid in eclogite is probably H_2O-rich. However, further experimental data is needed to better understand the conditions that produce the range of reported here mantle-derived resorption styles.

2.8. ACKNOWLEDGEMENTS

We are grateful to the BHP Billiton Diamonds Inc. for the access to diamond parcels. We thank Maya Kopylova and Evan Smith at UBC for their help with diamond polishing. We also thank Mati Raudsepp and Jenny Lai at UBC for the help with the CL work. Thomas Stachel and Sergei Matveev at UofA are thanked for the help with FTIR analyses. Funding for this research was provided by an NSERC Discovery grants to YF and a doctoral scholarship from the China Scholarship Council (CSC) to ZZ.

CHAPTER 3. DIAMOND RESORPTION IN THE MANTLE: A STUDY OF INTERNAL STRUCTURES, $\Delta^{13}C$ AND N CONTENTS IN DIAMONDS FROM THE EKATI MINE, CANADA

3.1. PREFACE

This chapter explores the relationship between diamond resorption morphologies and internal properties and attempts to constrain lithology of diamond mantle reservoirs. Although the results shown here will form the foundation of a future paper, the conclusions should be considered preliminary.

3.2. INTRODUCTION

Most complex surface features observed on natural diamonds result from dissolution, affecting diamond preservation in mantle reservoirs and diamond grades in kimberlites. The resorption morphologies can be divided into kimberlite-induced and mantle-derived groups (Zhang and Fedortchouk, 2012). Extensive experimental studies of diamond dissolution suggest that kimberlite-induced and the hexagonal-bearing type of the mantle-derived resorption morphologies depend on pressure (P), temperature (T), oxygen fugacity (f_{O2}), and the composition of etchants (X) (Kozai and Arima, 2005; Fedortchouk et al.,

2007; Khokhryakov and Pal'yanov, 2007; Arima and Kozai, 2008; Khokhryakov and Pal'yanov, 2010; Zhang et al., 2015).

Three factors not well explored in diamond dissolution experiments include the crystal growth forms (e.g. cubic, cubo-octahedral), the role of variable defects in diamonds, and the effect of different mantle lithology on the composition of the metasomatic media (e.g. C saturation) (Stagno et al., 2013; Stachel and Luth, 2015; Stagno et al., 2015). All three factors may affect diamond resorption morphology. Diamond primary growth forms can vary due to changes of growth mechanisms under different growth conditions (Sunagawa, 2005), and affect diamond dissolution by exposing different crystallographic faces, which can have different arrangements of carbon atoms and diverse density of defects inherited during growth, to the etchants. Primary forms are eliminated, at least partially, after subsequent dissolution in the mantle and in kimberlite magmas, but can be reconstructed with internal structures revealed by cathodoluminescence (CL) images and etching (Harrison and Tolansky, 1964; Bulanova, 1995).

The effect of diamond defects on resorption morphology is evident from the correlation between the location of trigons and dislocations and planar defects (Lang, 1964; Khokhryakov and Palyanov, 2006, 2007). However, it is not clear whether defects, including nitrogen (N) and dislocations, play a marked role in the formation of resorption features. For example, the effect of the content and aggregation state of the most abundant

lattice-substitutional impurity in diamond, nitrogen (N) (Cartigny, 2005), on resorption morphology is still elusive. N contents and aggregation state were suggested to affect sizes and densities of etch pits in diamond dissolution experiments at low T within exotic etchants, such as KNO_3 (Harrison and Tolansky, 1964; Mendelssohn and Milledge, 1995). In contrast, the dissolution experimental results under conditions similar to those of kimberlites show no effect of N contents and N aggregation states, obtained by infra-red spectroscopy (FTIR), on diamond resorption morphologies (Fedortchouk et al., 2007). Because N contents of diamonds measured by FTIR spectra of whole diamonds are values of mixed zones and N contents can fluctuate significantly at micro-scale in diamonds as documented by secondary ion mass spectrometry (SIMS) (Harte et al., 1999; Smart et al., 2011), it is necessary to examine the relationship between *in-situ* N contents of diamond outer rims and external resorption morphology before applying characterized resorption morphology to define fluid composition in diamond-destroying media.

There are limited data on resorption morphologies of diamonds recovered from eclogitic and peridotitic xenoliths (See references in Appendix C). Lacking of morphological data of most xenolithic diamonds in literature only allows to roughly classify diamonds based on their resorption features (Zhang and Fedortchouk, 2012). >3248 diamonds are extracted from diamondiferous eclogitic xenoliths (total 248, see references in Appendix C.1). Only 327 diamonds morphologically described are divided into five morphological groups: 1)

12 undefined stones; 2) 234 unresorbed octahedral and cubic single and aggregate diamonds with unpitted flat faces or unknown surface features; 3) 50 step-faced diamonds with/without etch pits, similar to mantle-derived step-faced resorption morphologies (Zhang and Fedortchouk, 2012); 4) 28 diamonds displaying ditrigonal {111} faces, negative trigonal etch pits, matching those produced in H_2O-rich systems (Fedorthcouk, et ah, 2007; Kozai and Arima, 2005; Khokhryakov and Pal'yanov, 2007, 2010). Some diamonds on the surface of xenoliths show partial kimberlite-induced morphologies, such as pseudohemimorphic stones; 5) three diamonds from three eclogitic xenoliths in South African kimberlites bearing regular hexagons on trigonal {111} faces (Robinson, 1979), identical to those on run-of-mine diamonds from other diamondiferous pipes (Robinson, 1979; Hall and Smith, 1984; Zhang and Fedortchouk, 2012). Those features resembles diamond resorption morphologies created in pure CO_2 systems (Fedortchouk et al., 2008, Arima and Kozai, 2008) or under extreme oxidizing condition (Kozai and Arima, 2005).

In 80 diamondiferous peridotitic xenoliths (lherzolite and harzburgite, see references in Appendix C.2), only 323 stones out of are grouped in to 3271 reported diamonds were briefly described and are five morphological groups: 1) 5 undefined stones; 2) 43 intact diamonds with sharp corners and straight edges and flat unpitted {111} faces; 3) 140 step-faced diamonds with or without etch pits; 4) 53 diamonds showing ditrigonal {111} faces and negative trigonal etch pits, same as those created in H_2O-dominated systems

(Fedortchouk et al., 2007; Khokhryakov and Pal'yanov, 2007; Zhang et al., 2015); 5) 82 diamonds from two peridotite xenoliths (AK1 in the Argyle lamproite pipe, Australia and No-177 in the Roberts Victor pipe, South Africa) displaying irregular hexagonal pits (cavities?) on rough, frosted, and pitted surfaces, so-called a 'cokey' surfaces (Hall and Smith, 1984). The cokey surfaces is suggested to result from diamond resorption during mantle metasomatism (Hall and Smith, 1984). Run-of-mine diamonds displaying regular hexagons on smooth trigonal {111} faces, which is evidently different from the cokey surface features, are proposed to be mantle-derived surfaces (Hall and Smith, 1984). However, the cockey surfaces do not resemble any resorption feature created on diamonds in dissolution experiments. The presence of different hexagon-bearing features on diamonds from eclogitic and peridotitic xenoliths suggests the effect of lithology of diamond mantle reservoirs on resorption morphologies, probably by influencing the nature of metasomatic media (e.g., C saturation, compositions, f_{O2}) (Stachel and Harris, 2009; Stagno et al., 2013; Stachel and Luth, 2015; Stagno et al., 2015).

Some diamonds contain both peridotitic and eclogitic inclusions (Bulanova, 1995) and even inclusions from the lower mantle (Stachel et al., 2005) suggesting diamond mobility within the mantle. P-T conditions of diamond residence in the mantle can be estimated using the N-thermometer (Taylor et al., 1996), local geothermal gradient constrained by P-T data from xenoliths (Stachel and Luth, 2015), and diamond plastic properties

(DeVries, 1975). The f_{O2} in the mantle can be buffered by the host rocks or percolating fluids with the later having much higher capacity as a f_{O2} buffer (Luth and Stachel, 2014). Since carbonated eclogite is stable over a wider P-T range and has lower solidus temperature than carbonated peridotite, infiltration of carbonate melts from peridotite into eclogite is suggested to cause more melting and more extraction of carbon from eclogite (Stagno et al., 2013; Stagno et al., 2015). Because of the well-characterized reaction between CO_2 and olivine under mantle conditions (Newton and Sharp, 1975) and the constrained solidus of peridotite and eclogite (Stachel and Luth, 2015 and references therein), the possible carbon-bearing diamond-growing media are suggested to be CH_4 in harzburgite, CH_4 and carbonate melts in lherzolite and CO_2, CH_4 and carbonate melts in eclogite (Stachel and Luth, 2015).

Diamond-hosting mantle lithology is typically constrained from the composition of silicate (Stachel et al., 2009) and sulfide (Bulanova et al., 1996) inclusions in diamonds and C isotopes of inclusion-free diamonds. The N incorporation into diamonds during growth is thought to correlate with growth media (Thomassot et al., 2007; Stachel et al., 2009; Smart et al., 2011), lithologies (Stachel et al., 2009), and growth mechanisms (Cartigny et al., 2001). Its covariations with carbon isotopes in continuous growth bands of individual stones (Smart et al., 2011; Stachel and Luth, 2015) can be used to constrain diamond

growth media, and in turn could constrain diamond growth environments based on the reactions between growth media and lithologies (Stachel and Luth, 2015).

The semi-quantitative correlation between diamond resorption morphologies and compositions of diamond-etching C-O-H fluids documented in diamond dissolution experiments suggests that diamond resorption morphology is an unambiguous fluid proxy in most diamond-bearing environments (Chapter 5). However, the forming conditions of step-faced mantle-derived resorption morphologies proposed to form during mantle metasomatism (Zhang and Fedortchouk, 2012) are still unknown. For example, morphologies of step-faced diamonds do not like any resorption morphologies of flat- and step-faced octahedral stones resorbed in H_2O- or CO_2- dominated systems (Kozai and Arima, 2005; Fedortchouk et al., 2007; Khokhryakov and Pal'yanov, 2007; Arima and Kozai, 2008; Khokhryakov and Pal'yanov, 2010; Zhang et al., 2015).

Variable surface features on natural diamonds with diverse types of defects experiencing dissolution provide a good opportunity to examine the relationship(s) between diamond resorption morphologies, defects, and diamond-hosting mantle lithology constrained by geochemical signatures of diamonds. Here I report diamond growth history constrained from high-resolution CL images and *in-situ* N and C isotope contents using SIMS and examine the relationship between diamond internal properties and resorption morphologies of the Ekati diamonds. My results show that diamond resorption

morphologies do not correlate with growth habit and N contents, supporting diamond resorption morphology as a robust proxy of diamond-destroying fluid composition independent of diamond growth.

3.3. GEOLOGICAL BACKGROUND

The study used micro- (< 1 mm) and macro- (> 1 mm) diamonds from the Grizzly, Misery, Leslie and Koala kimberlite pipes from the Ekati Mine, located ~300 km northeast of Yellowknife (Northwest Territory, Canada) in the central Slave craton. The craton consists of Archean basement complex (Nowicki et al., 2004 and references therein), and all four kimberlite pipes were emplaced into 2.64–2.58 Ga granites (Figure 3.1) (Nowicki et al., 2004) at 50-68 Ma (Creaser et al., 2004; Sarkar et al., 2015).

Geochemical, mineralogical, and petrological studies suggest that the subcontinental lithospheric mantle (SCLM) beneath the central Slave craton consists of an upper depleted harzburgite layer at depth < ~140 km and a lower less depleted diamondiferous lherzolite at depth > ~140 km (Figure 1.5a) (Griffin et al., 1999a; Menzies et al., 2004; Creighton et al., 2010; Aulbach et al., 2013). Eclogite and pyroxenite bodies are present in both layers. The stratified lithospheric mantle is also supported by 3-D conductivity models reconstructed from magnetotelluric data (Snyder et al., 2014). The geothermal gradient in the Lac de Gras area estimated by peridotitic xenoliths at the eruption time of Ekati

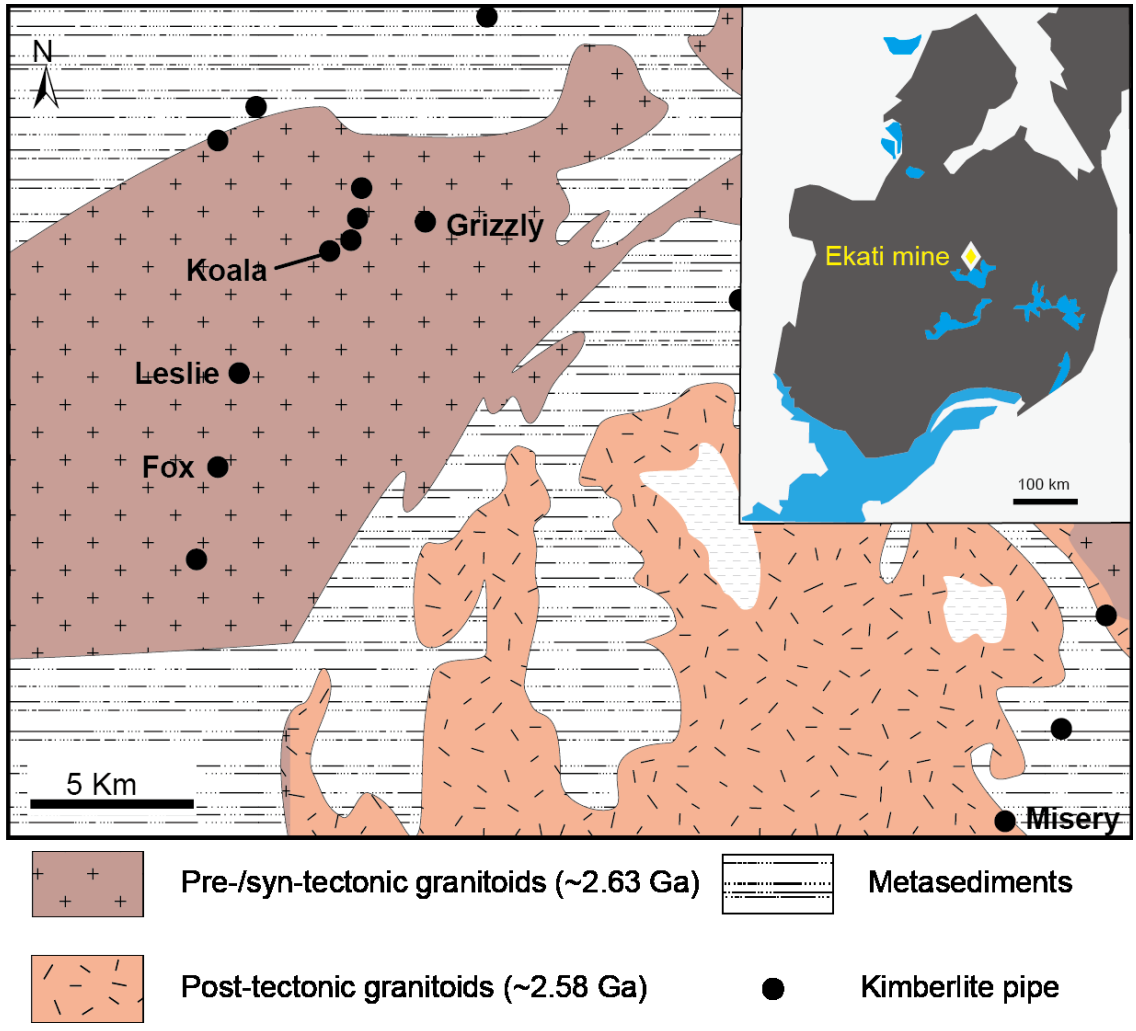

Figure 3.1 Geological map showing the similar country rocks intruded by the Ekati kimberlites in the central Slave craton. This map is modified after Nowicki et al. (2004).

kimberlites is comparable to the conduction model with a surface heat flow at 35 to 40 mW/m^2 (Figure 1.5b) (Menzies et al., 2004). The age of lower peridotite lithospheric mantle is ~ 3.5 Ga Re–Os isochron based on sulfide inclusions in diamonds (Westerlund et al., 2006). The emplacement of eclogitic bodies in the SCLM is at ~2.1 Ga Lu-Hf isochron (Schmidberger et al., 2007).

Studies of inclusions in diamonds, and major, trace-element, and isotopic composition of xenoliths from kimberlites show that the lower lithospheric mantle was complexly metasomatized (Creighton et al., 2010; Aulbach et al., 2013). Chronically, metasomatic events in the lower diamondiferous lithospheric mantle can be divided into four stages: 1) at ~ 3.5 Ga, infiltration of carbonate-bearing C-O-H fluids/brine or melts into harzburgite triggered diamond crystallization (Klein-BenDavid et al., 2004, 2009; Creighton et al., 2008, 2010; Aulbach et al., 2011, 2013); 2). at 3.5 Ga – 350 Ma, the diamond-bearing harzburgite mantle was metasomatized by oxidizing C-O-H fluids and kimberlite-like melts converting harzburgite into lherzolite (Creighton et al., 2008, 2010; Aulbach et al., 2011, 2013); 3) at 2.1- 1.9 Ga, the formation of eclogitic diamonds resulted from metasomatism by reducing C-O-H-N fluids from deserpentinisation of subducted oceanic mantle (Aulbach et al., 2011); 4) at max. 350 Ma to ~ 55Ma (kimberlite eruption age, Sarkar et al., 2015), a part of the diamond-bearing harzburgite mantle was converted into lherzolite by kimberlite-like melts (Creighton et al., 2008, 2010; Aulbach et al., 2011,

2013). Although metasomatic media characterized by trace elements in garnets and estimated f_{O2} in diamondiferous peridotite are suggested to be harmless to diamond preservation, diamonds can undergo dissolution at P-T conditions corresponding to diamond stability when the carbonate activity in melts/fluids increases (McCammon et al., 2001). In addition, diamond stability during metasomatic events in the mantle does not only depend on f_{O2}, but also relies on C saturation in metasomatic media, which is experimentally documented by diamond dissolution in volatile-free/-containing carbonate and silicate melts under the graphite-oxygen buffer (Khokhryakov and Pal'yanov, 2007, 2010) and theoretically predicated when carbonate melts pass from peridotite to eclogite (Stagno et al., 2015).

3.4. ANALYTICAL METHODS

67 examined diamonds are micro-diamonds (<1 mm) from exploration reverse circulation (RC) drilling samples of the Misery, Leslie and Koala kimberlite pipes, and 15 macro-diamonds (>1 mm) from the RC drilling samples of the Grizzly kimberlite pipe. One corner of the studied 82 diamonds was cut by polishing parallel to (100) to approximately ¼ of diamond diameter. The physical characteristics of studied diamonds (resorption features and color), internal structures, and N contents and aggregation states measured by FTIR spectroscopy are reported in Chapter 2 (Table B.1, Zhang and Fedortchouk, 2012).

The selected diamonds are octahedral crystals (seven twined and 75 single stones) of which 60 % are white stones and 40 % brown stones, and represent mantle-derived resorption morphologies (Table D.1). Each diamond was analyzed in the core and the rim of polish plans, and for seven diamonds analyzes were done along the profile from the core to the rim of polish plans. (Table D.1).

The analytical work (internal structures and geochemical compositions of diamonds) was done at the Canadian Centre for Isotopic Microanalysis (CCIM, University of Alberta). All diamonds were mounted in epoxy with the facets exposed at the surface. High-resolution internal structures of gold-coated diamonds were examined and imaged with cathodoluminescence (CL) using a Zeiss EVO 15 scanning electron microscope with both Gatan Chroma and Robinson CL detectors. This was operated at an accelerating voltage of 15-20 kV and a beam current of 3-7 nA to obtain the best quality images.

After CL imaging, each cuboid epoxy mount was pressed into indium next to three reference materials (two from S0233 and one synthetic S0011), and were subsequently coated with 30 nm gold. The carbon isotope composition and nitrogen (N) contents were obtained using a Cameca IMS 1280 multi-collector ion microprobe (SIMS). The analysis points were located in different growth zones on the CL images. The carbon isotope composition (^{12}C and ^{13}C) of diamonds is expressed as $\delta^{13}C$ (measured in ‰) relative to the international Vienna Pee Dee Belemnite (VPDB) standard. All measurements for $\delta^{13}C$

and N contents were referenced to the isotopically homogeneous synthetic diamond standard S0011 (Stern et al., 2014), which was analyzed at regular intervals after every four analyses in the case of $\delta^{13}C$ and ten analyses for N analyses. No biases due to stage position were observed based on analysis on the two S0233 references.

Following pre-analysis sputtering to remove surface contaminants and automated secondary ion tuning, diamond facets parallel to {100} were bombarded using a primary $^{133}Cs^{+}$ ion beam with a 20 keV impact energy, a current of ~3 nA, spot size of ~ 15 um, and sampling depth <5 μm. The secondary negative ions sputtered were extracted to the mass analyzer. C-isotopes and N were analyzed at the same spot with two separate multi-collectors at variable mass resolution (R) to avoid spectral interferences. No sample charge correction is required due to the high conductivity of diamond (Harte et al., 1999). For C-isotopes, the $^{13}C^{-}/^{12}C^{-}$ ratios were obtained with dual Faraday cups at R= 2900 during the 75s collecting time after 30s pre-analysis sputtering. The standard error (2σ) for individual point δ^{13} analyses ranged from 0.17 to 0.20 ‰. N concentration in diamond was calculated using $[^{12}C^{14}N]^{-}$ and $[^{12}C^{12}C]^{-}$ ions simultaneously measured by dual Faraday cups, or an electron multiplier for diamonds with low counting rates ($<1\times10^{5}$ counts/sec) at mass resolution R = 7000. Measurements using the dual Faraday cup pre-sputtered 60s per spot, followed by total 50s collecting time; when using the electron multiplier individual

analyses comprise a 75s counting period after the pre-analysis sputtering (120s). The 2σ error for nitrogen concentration for the unknowns is ±10%.

3.5. RESULTS

3.5.1. Internal Structures and Corresponding Forms

Internal patterns of the studied diamonds were classified into twelve types based on the luminescence characteristics revealed in high-resolution CL images (Table 3.1, Figure 3.2). Internal zones can be recognized by the sharp contrast in brightness or discontinuous growth layers (Figure 3.2). Two patterns of internal zoning in diamonds, plaid and shattered patterns, are named because of the presence of plastic deformation (P10, Figure 3.2a) and fragmentation (Figure 3.2 b, h) respectively. The black lines crossing the whole polished face (Figure 3.2a) are interpreted as lamella parallel to the growth surface (Lang and Meaden, 1991). Some Ekati diamonds show two groups of parallel lamellae, creating the plaid structure (P10) (e.g. L97-2-4, Figure 3.2a). The multiple core pattern (P5) results from either multiple diamond seeds or multiple octahedral apices at the cubic face (Zedgenizov et al., 2006). The latter is experimentally reproduced on {100} faces covered with tetragonal pyramids in the SiO_2-H_2O-C and Mg_2SiO_4–H_2O–C system at 7.5 GPa and 1600 ^oC (Sokol and Pal'yanov, 2008).

The most common internal patterns of Ekati diamonds are homogeneous (P1, 17-42%), stepped rectilinear (P3, 15-30%), rectilinear (P2, 13-32%) and agate (P4, 4-15%), multiple (P5, 2-14%), octagonal (P8, 3-11%), and dark rim without oscillating zoning (P11, 2-6%) (Table 3.1). The remaining five internal patterns (sector, dendritic, four-sided star, plaid; and shattered) are present only in some pipes (Table 3.1). For example, three diamonds from the Koala pipe show shattered patterns and two stones from Leslie pipe bear dendritic and shattered internal patterns.

Table 3.1 Features of twelve growth patterns of the Ekati diamonds.

Symbols	Patterns	Growth habit	Growth layer(s)
P1	Homogenous	Octahedron, irregular	Homogenous
P2	Rectilinear	Octahedron	Homogenous or oscillatory
P3	Stepped Rectilinear	Stepped-octahedron	Oscillatory
P4	Agate	Spherulitic, Octahedron, Stepped-octahedron	Concentric layers
P5	Multi-core	Octahedron	Multiple small octahedral cores
P6	Sector	Octahedron	Planner growth layers
P7	Dendritic	Dendritic form on early cubo-octahedron	Dendritic growth sectors
P8	Octagonal	Cubo-octahedron	Oscillatory
P9	Four-sided Star	Hopper octahedron	Concentric layers
P10	Plaid	Octahedron	Plastic lamellae on growth layers
P11	Black Rim	Octahedron, cubo-octahedron	Concentric layers or homogenous
P12	Shattered	Octahedron, or stepped octahedron, cubo-octahedron	Fragmentation of growth layers

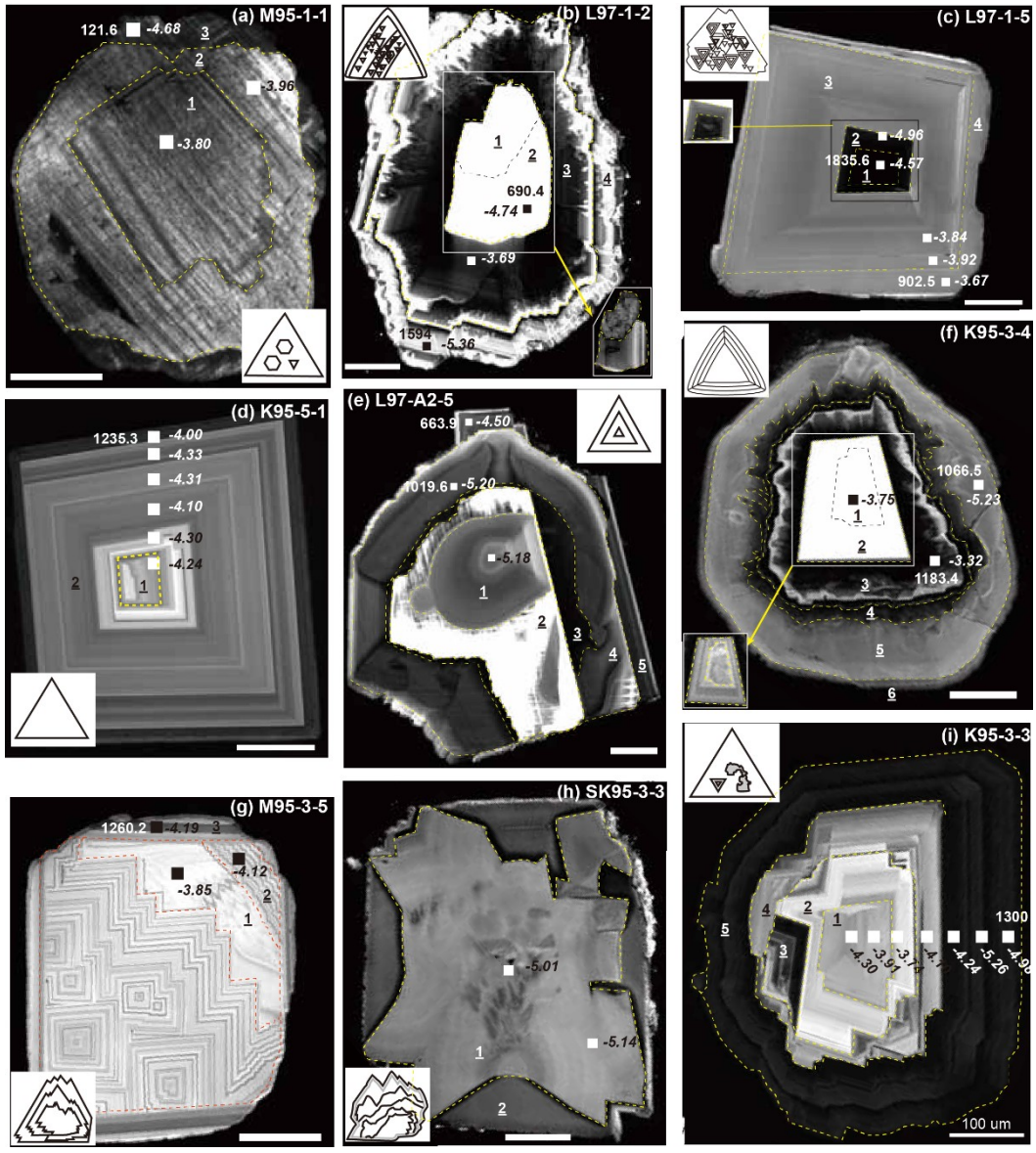

Figure 3.2 CL images of Ekati diamonds with $\delta^{13}C$ (in italic text) and N contents in ppm. The inserted sketches are the resorption morphologies and underlined numbers show diamond growth sequence outlined by the dashed lines. a) plaid zone (P10) in **1** and **2**; b) shattered zone (P12) in **3** and **4**; c) agate texture (P4) in **4**; d) sector zone (P6) in **1** and rectilinear pattern (P2) in **2**; e) agate zone in **1** and octagonal pattern (P8) in **4**; f) homogeneous zone (P1) in **1**, octagonal pattern (P8) in **5**, dendritic structure (P7) in **4** and black rim (P11) in **6**; g) multi-core pattern (P5) and stepped rectilinear zone (P3) in **2**; h) a four-sided star zone (P9) in **1**; note the broken corner; i) protruding domains in **5**.

The internal structures of diamonds revealed by the CL images show complex histories of growth and post-growth physical (fragmentation and plastic deformation) and chemical (dissolution) destruction. However, polishing only to ¼ of diamond diameter allows us to decipher only partial history of diamond growth. Crystal forms corresponding to the growth patterns are octahedron, stepped octahedron, hopper octahedron, cubo-octahedron, and spherulitic form as listed in Table 3.1. Continuous growth sequences without signs of dissolution include are (1) agate to rectilinear zones with or without steps (Figure 3.2h, M95-3-3); (2) agate to four-sided star to rectilinear zone with or without steps (G97-1-3); (3) rectilinear to octagonal pattern (M95-2-8). The observed growth sequences correspond to diamond growth under different mechanisms during one growth period (Figure 3.3 a, Sunagawa, 2005), suggesting changes of growth conditions and mechanisms during diamond growth.

Features resulting from post-growth physical destruction includes plastic deformation and fragmentation (Table 3.2). In all four kimberlite pipes, diamonds with plastic lamella are rare (<5%). The plastic deformation lamella showing as black lines in CL images (Figure 3.2a) can be present on both white and brown diamonds (Table D.1). Broken sectors in diamonds (Figure 3.2 b, h) are very common, comprising up to 31% of diamonds from the Koala pipe. In one case, a broken diamond (Figure 3.2h) shows that one corner after being broken simultaneously reunited with the remaining part during the subsequent growth

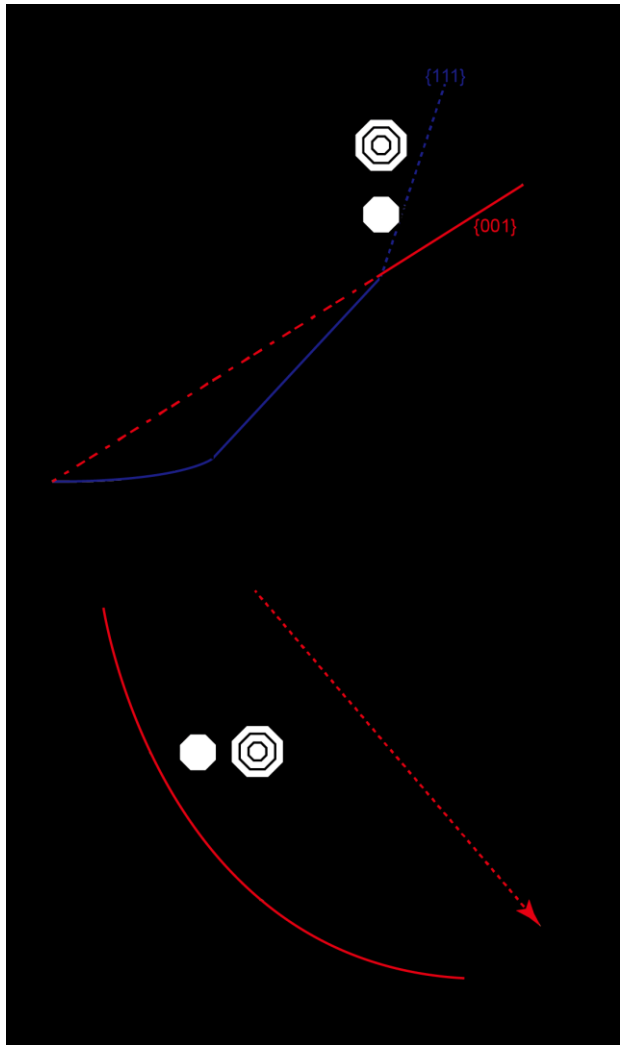

Figure 3.3 Schematic morphology and internal growth pattern changes during growth. a) diamond growth morphologies under different mechanisms. The growth mechanism is a function of the driving force (σ) and growth rates (Sunagawa, 2005). The driving force σ on each crystallographic face ($\sigma^*_{\{111\}}$ vs. $\sigma^*_{\{001\}}$) is different and changes of σ ($\sigma^*_{\{111\}}$ vs. $\sigma^{**}_{\{111\}}$) determines which growth mechanism operates on the face during diamond growth. It is assumed that the values of $\sigma^*_{\{111\}}$ and $\sigma^{**}_{\{111\}}$ of {111} faces are larger than $\sigma^*_{\{001\}}$ and $\sigma^{**}_{\{001\}}$ values of {100} (Sunagawa, 2005). Blue and red lines represent growth rates in <111> and <100> direction respectively; b) evolution of diamond growth morphologies as the C supersaturation level drops with time for one growth period. The solid red line represents growth curves (after Alexandrov and Nizovtseva, 2014). The dashed line shows the correlation between C isotopes, N contents and growth morphologies.

Table 3.2 Proportion of internal structures of diamonds from the Grizzly, Misery, Koala, and Leslie pipes.

CL features	Kimberlite Pipe			
	Grizzly	Misery	Koala	Leslie
Homogeneous zone	42%	24%	17%	35%
Rectilinear zone	15%	15%	32%	13%
Stepped rectilinear zone	17%	30%	15%	24%
Agate texture	5%	15%	4%	6%
Multi-core zone	14%	6%	2%	10%
Black rim	2%	3%	6%	2%
Octagonal zone	3%	4%	11%	4%
Sector	3%	2%	0%	2%
Dendritic	0%	0%	6%	2%
Four-sided star	0%	1%	2%	0%
Shattered	0%	0%	4%	2%
Plastic deformation	5%	1%	2%	2%
Fragment	20%	3%	32%	14%
Dissolution	93%	97%	92%	100%

(Figure 3.2 h, SK95-3-3), and one stone has two combined irregular parts (L97-3-4). The presence of fragmented domains in diamonds suggests that diamond reservoir T was lower than 1000 ºC (DeVries, 1975), in agreement with low N aggregation states in these diamonds (Zhang and Fedortchouk, 2012). Diamond dissolution in the mantle is evident from discontinuous growth zones and rounded internal domains (Figure 3.2 e, i). Analysis of high-resolution CL images shows that some stones record up to three distinct resorption events (e.g. sm95-3-1).

The dominant patterns of diamond rims are rectilinear growth zones (octahedron, 27%), stepped rectilinear (step-faced octahedron, 18%), homogeneous (19%) and black rim

(12%). No correlation between diamond resorption morphologies and rim growth patterns is observed (Figure 3.4), suggesting no effect of growth habit on diamond resorption features. For example, the hexagonal pit-bearing resorption morphology (CM-1) can form on diamonds with all types of growth patterns. Diamonds with sharp-steps (SP1) show rectilinear and stepped rectilinear, black rim and homogeneous zones (Figure 3.4). The shattered pattern of diamonds (P12, Figure 3.2b) seems to correlate with the formation of deep trigon-bearing resorption morphology (CM-2), probably due to faster etching rates at fractures than the surrounding area in the normal direction of {111} faces (P12, Figure 3.2b). The island-bearing resorption feature observed on one diamond is most likely due to the presence of small domains, probably resistant to dissolution (Figure 3.2i). Diamonds with CM-2 and SP-4 morphologies are in a small population in this study, and the correlation may be strongly biased, which thus requires further investigation.

3.5.2. Carbon Isotopic Compositions of Diamonds

The carbon isotopic composition of diamonds determined by SIMS is presented in Table D.1. All studied diamonds have average $\delta^{13}C$ around -5‰ and comprise three groups: − 6 to −4.75‰, −4.75 to −3.75‰, and -3.25 to -2.5 ‰ (Table D.1, Figure 3.5), consistent with the three modes of peridotitic diamonds worldwide (Stachel et al., 2009). Carbon isotopes show no correlation with diamond growth patterns (Table D.1), Figure 3.5).

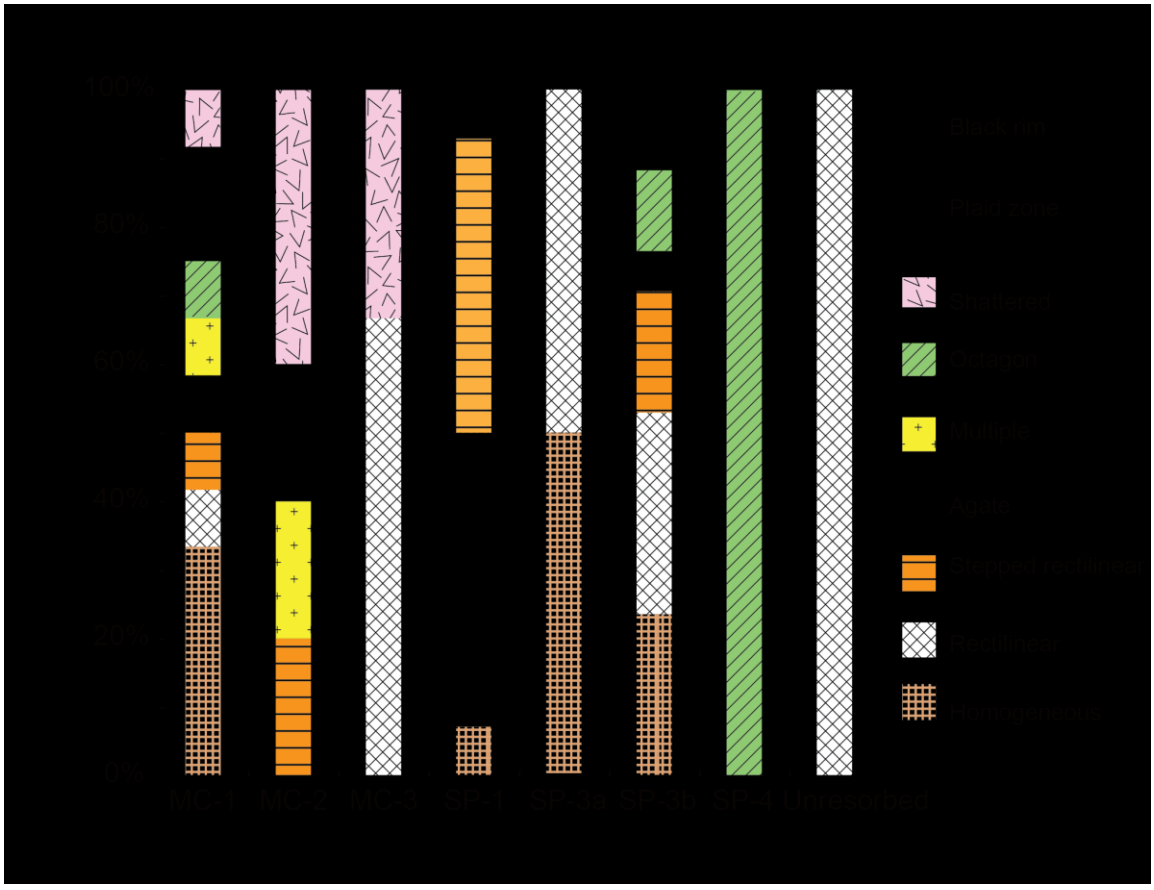

Figure 3.4 Percentage of internal zoning pattern on the diamond rims vs. mantle-derived resorption morphologies on diamonds.

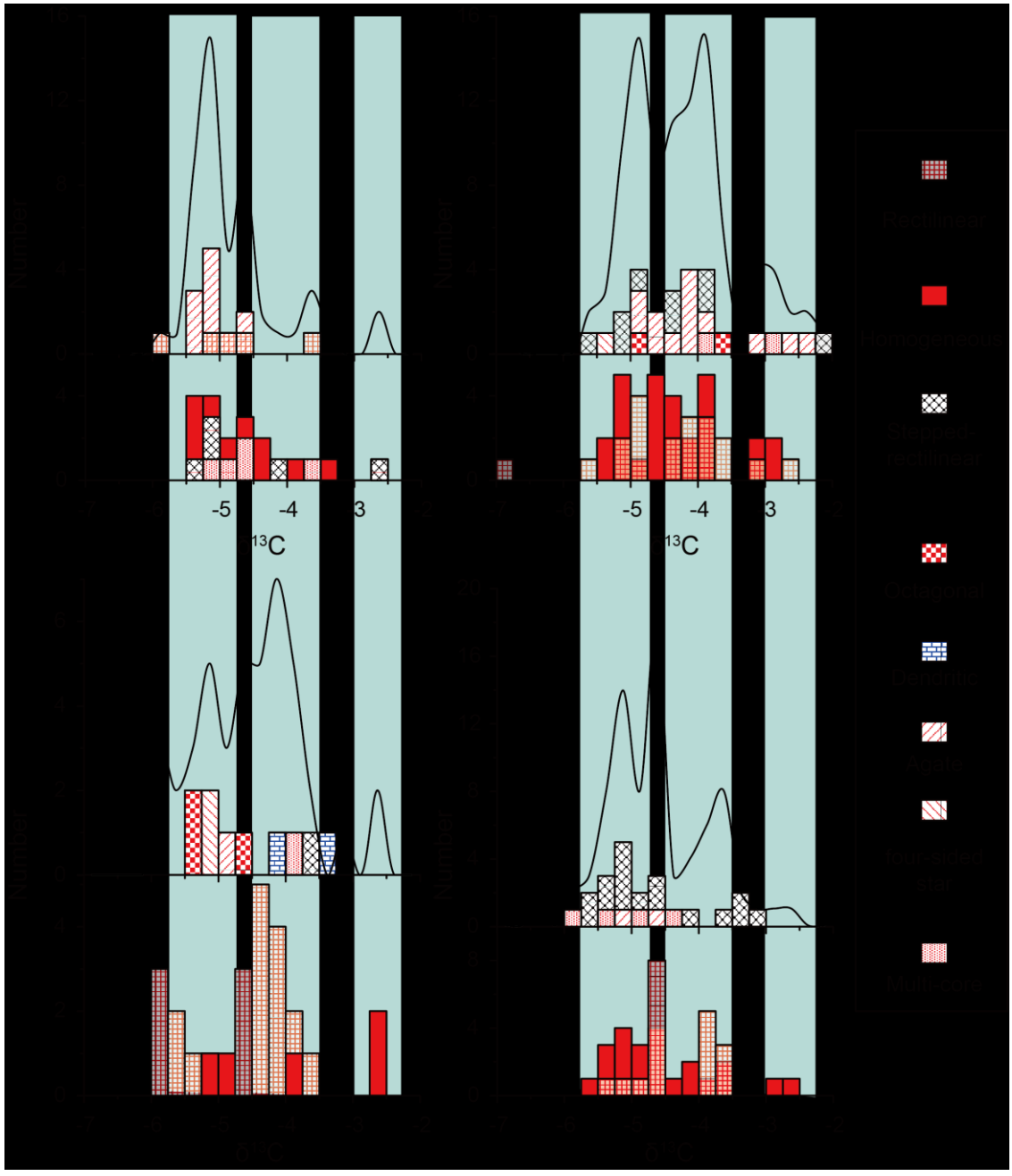

Figure 3.5 Histograms of $\delta^{13}C$ compositions of diamonds (bin size 0.25‰). All diamonds were characterized by a main mode in $\delta^{13}C$ at ~5‰. Black solid lines represent $\delta^{13}C$ variation of all data from one pipe. The shaded bands show the $\delta^{13}C$ frequency distribution of harzburgite and lherzolite diamonds worldwide (Stachel et al., 2009).

For a continuous growth period, fractionation of C isotopes correlates with growth forms. In individual diamonds with continuous growth revealed by CL images, $\delta^{13}C$ increases as the growth forms reconstructed from internal growth patterns change to be more regular with smooth faces, such as from spherulite to octahedron (Figure 3.3 b), in agreement with trends observed in Yakutia diamonds (Zedgenizov et al., 2006). For example, $\delta^{13}C$ increases from -4.5 to -3.7 ‰ when the internal zoning of the diamond G97-1-3 changes from agate (spherulitic form) to rectilinear pattern (octahedral form). The correlation between $\delta^{13}C$ and growth forms during one growth episode suggests the effects of diamond growth kinetics on fractionation of C isotopes or changes in C isotopic composition in growth media.

For any given growth pattern, $\delta^{13}C$ from core to rim are generally indistinguishable within uncertainty (0.12 – 0.16%, e.g. K95-5-1). Exceptions are two stones from the Misery pipe (M95-1-4 and M95-4-2) that show rimwards $\delta^{13}C$ decrease up to 0.81 ‰ (Table D.1), similar as the $\delta^{13}C$ trend of diamonds fractionated from an oxidizing medium (CO_2 or carbonate melts). In contrast, the core of one stone M95-3-3 bears a rimwards $\delta^{13}C$ increase from -5.37 to -4.79 ‰ (Table D.1), indicating a reducing diamond growth medium, probably CH_4 (Deines, 1980; Stachel et al., 2009; Smart et al., 2011; Cartigny et al., 2014).

3.5.3. N Contents in Diamonds

The N contents of diamonds range from 0 to 2128 ppm, with significant variation even in an individual diamond (Table D.1, Figure 3.2). Comparison of N_{SIMS} with N_{FTIR} contents on diamond rims shows that out of 82 diamonds only 17 stones show identical values within the uncertainty (Figure 3.6, Table D.1). Polish phans of diamonds displaying simple CL patterns show different N contents obtained by SIMS and FTIR (Figure 3.6), probably resulting from fluctuating N contents in growth zones unrevealed by polish plans. This marked discrepancy between N_{SIMS} and N_{FTIR} suggests that using N_{FTIR} of whole diamonds obtained in Chapter 2 to constrain the potential diamond host lithology in the mantle is questionable.

N_{SIMS} incorporation into diamonds during growth correlates with growth forms in one growth episode. As with the $\delta^{13}C$ increase, N contents decrease as diamond growth forms change to be more regular (e.g. SL97-A2-5, Figure 3.3 b), in agreement with the N trends observed in Yakutia diamonds (Zedgenizov et al., 2006). The correlation between N_{SIMS} contents and growth forms indicates that the effects of diamond growth kinetics on N partitioning incorporation into diamonds can be either positive or negative, depending on the compatibility into diamonds, given in an open system where P and T are stable and diamonds growth mechanism changes from disequilibrium adhesive to equilibrium dislocation mechanism (Sunagawa, 1995).

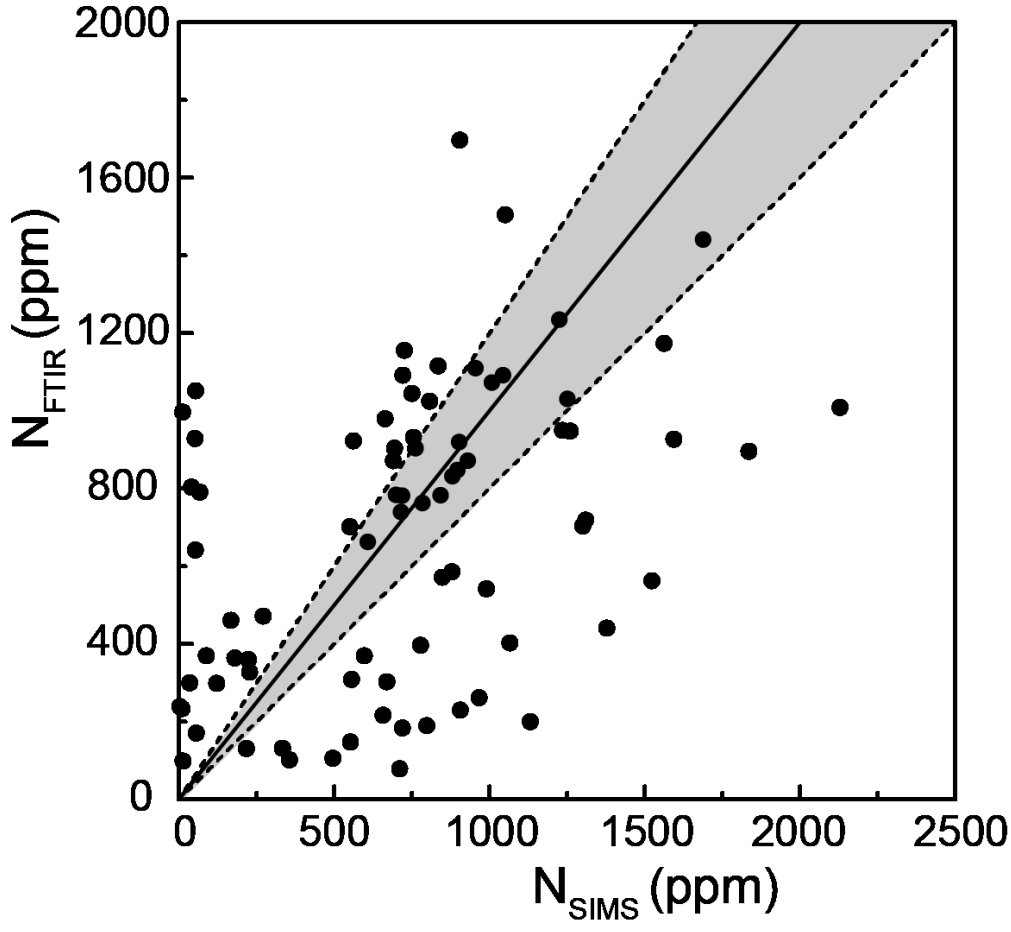

Figure 3.6 Comparison of N contents measured by infrared spectroscopy and SIMS. The grey zone shows the analytical uncertainty. Note the decoupled N_{FTIR} and N_{SIMS} data for most diamonds.

No correlation is observed between CL patterns and N contents in the studied diamonds when all diamonds are considered (Figure 3.7a). Diamonds with the same CL pattern could display variable N_{SIMS} contents (Figure 3.7a, Table D.1). To eliminate the effect of accelerating voltage and currents on the brightness of CL images (Lang et al., 2007), only diamonds with multiple analyses (total 19 stones) were selected for comparison of CL brightness and N_{SIMS} contents. Generally, the brighter zones have more N_{SIMS}, confirming the correlation between CL brightness and N contents (Harte et al., 1999). This correlation results from more optical systems created by higher N contents in diamonds, which increase the intensity of diamond luminescence (Collins, 1992). Five stones show the opposite correlation, which may be correlated with aggregation state of N in diamonds (Harte et al., 1999).

To examine the correlation between N_{SIMS} at outer rims and resorption morphologies, all 82 diamonds from the four pipes are considered (Figure 3.7b). No relationship between morphological types SP-2, SP-3a, and SP-3b and N_{SIMS} contents was observed. Some resorption morphology show correlation with N_{SIMS} content. For example, diamonds with MC-1 show low N_{SIMS} contents (<900 ppm), and diamonds with MC-2, MC-3 and SP-1 morphologies have N_{SIMS} contents in the range of 600-1600 ppm. However, the overlapping range of N_{SIMS} contents of diamonds with MC-2, MC-3 and SP-1 morphologies suggests that the apparent correlation may be due to sampling bias.

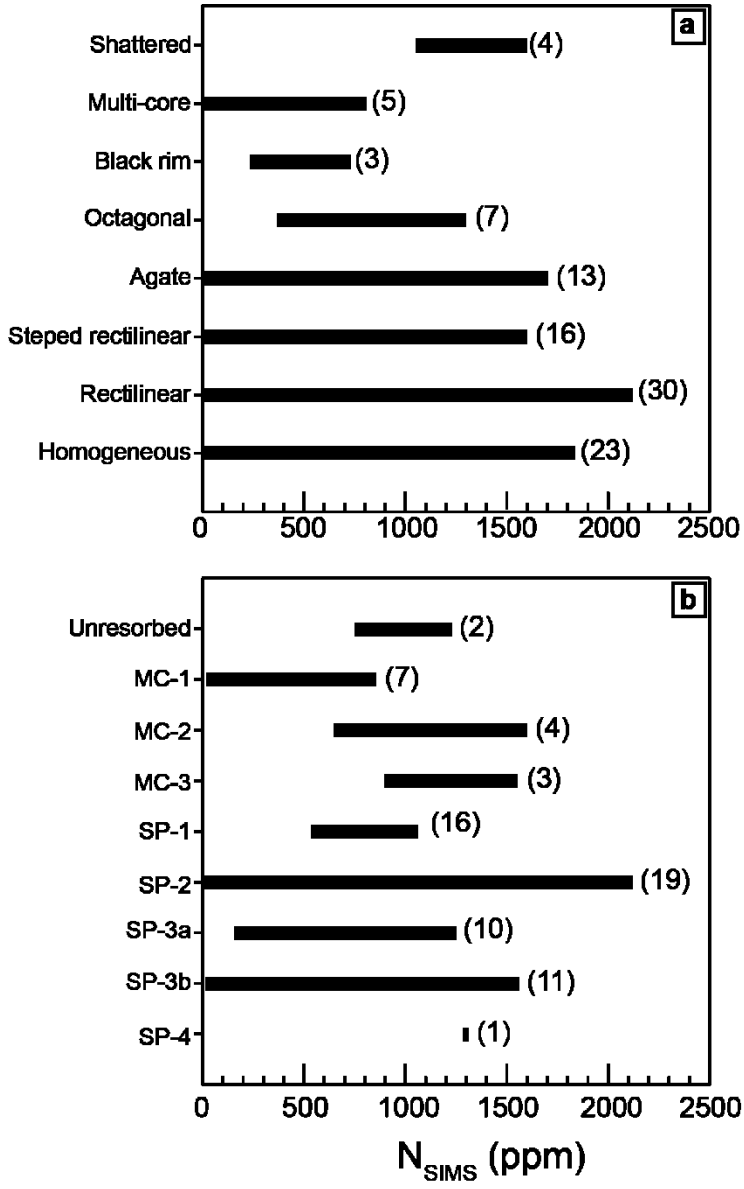

Figure 3.7 Range of N_{SIMS} in rims of diamonds from the Misery, Grizzly, Leslie, and Koala pipes. Total number of examined stones in each group is in bracket. a) N contents in growth patterns of diamonds; b) N_{SIMS} contents vs. mantle-derived diamond resorption morphologies.

3.5.4. Correlation between $\delta^{13}C$ and N Contents of Diamonds

Covariation between $\delta^{13}C$ and N contents allows further investigation of diamond forming-media and N compatibility in diamonds (Smart et al., 2011; Stachel and Luth, 2015). The core of two diamonds, M95-4-2 and M95-1-4 from the Misery pipe, show rimwards N_{SIMS} decrease and $\delta^{13}C$ increase in the agate (P4) and rectilinear (P2) zones respectively (Figure 3.8). The observed covariation is identical to the predicted relationship between $\delta^{13}C$ and N contents of diamonds growing in an oxidizing media (CO_2 and carbonate melts) (Stachel et al., 2009).

The partition coefficient of N into diamonds is estimated in Smart et al. (2011). Nitrogen incorporation are suggested to follow the Henry's Law similar to other trace elements and fractionation of C isotopes into diamonds is controlled Rayleigh equilibrium fractionation, respectively (Smart et al., 2011). The co-variation between $\delta^{13}C$ and N contents is expressed as:

$$\delta^{13}C = a * \ln(N) - a*c + b \quad (3.1)$$

$$a = \Delta_C/(K_N-1) \quad (3.2)$$

$$b = \delta^{13}C_o \quad (3.3)$$

$$c = \ln(N_o) \quad (3.4)$$

where N_o and $\delta^{13}C_o$ are the initial N contents and C isotope compositions of diamond-growth media respectively, K_N is the diamond-fluid/melt partition coefficient of N, Δ_C is

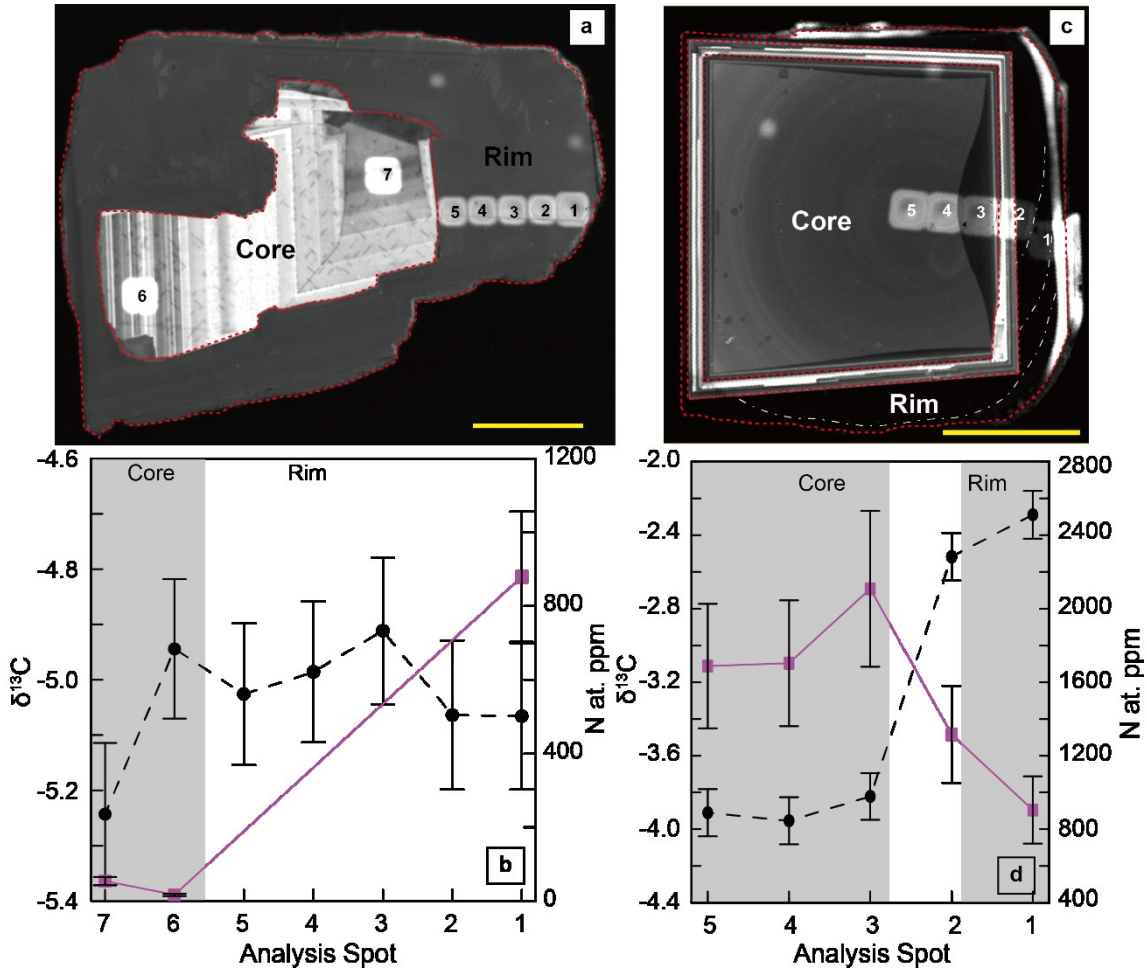

Figure 3.8 $\delta^{13}C$ and N contents profiles of diamond from core to rim. The diamond core and rim are separated by the dash lines, and numbers representing analysis sequence. (a-b) Diamond M95-1-4 with the rimwards trends of $\delta^{13}C$ (circle) and N contents (square). Note that the rectilinear core zone shows rimwards increase in $\delta^{13}C$ and decrease in N content. (c-d) Diamond M95-4-2 with the rimwards trends of δ13C (circle) and N contents (square). The dot-dashed lines show weak growth layers. Note that $\delta^{13}C$ increases as N content increases in the core agate zone (analysis 4 to 3), and the opposite correlation in the rim zone with agate zone (analysis 2 to 1). The scale bar is equal to 100 μm.

the diamond-fluid/melt fractionation factor for C isotopes, and N and $\delta^{13}C$ are N content and the C isotope compositions of diamond, respectively. Using equation (1), the estimated partition coefficient of nitrogen (K_N) is 3.8 (range from -63.1 to 2.3) for the agate structure (M95-4-2) and 7.6 (range from 2.1 to 77.5) for the rectilinear structure (M95-1-4). In the calculation, equilibrium isotopic fractionation between diamond and carbonate melts is -1.7‰ (ΔC) at 1100 ºC (Chacko et al., 1991), which is the average T of diamond reservoirs based on the N -thermometer (Zhang and Fedortchouk, 2012). Although there is a large uncertainty due to the limited data, the empirical K_N estimated is within the range (10 - 1.5) obtained for a homogeneous diamond zone (Smart et al., 2011), indicating N is a compatible element into diamond during growth.

3.6. SUMMARY

1. No correlation was found between growth forms, N contents, and mantle-derived resorption morphologies, suggesting no effect of those factors on resorption morphologies in nature. This supports the hypothesis that diamond resorption morphology is a robust recorder of diamond-etching conditions.

2. The $\delta^{13}C$ in the studied Ekati diamonds is in the mantle range. There is no evidence of involvement of crustal materials during diamond growth in these samples.

3. $\delta^{13}C$ and N contents in diamonds correlate with diamond growth forms revealed by CL images during one growth period, indicating the effects of diamond growth kinetics on fractionation of C isotopes and N partition coefficient.

3. The rimwards trends of decrease and increase of $\delta^{13}C$ in diamonds indicates that the diamond growth media in the mantle can be reduced (CH_4) and oxidizing (CO_2 or carbonate melts) respectively.

4. The co-variation between $\delta^{13}C$ increase and N decrease in the same growth patterns suggests that N is compatible into diamond during diamond growth from oxidizing media.

CHAPTER 4. EVOLUTION OF DIAMOND RESORPTION IN A SILICIC AQUEOUS FLUID AT 1-3 GPA: APPLICATION TO KIMBERLITE EMPLACEMENT AND MANTLE METASOMATISM

4.1. PREFACE

This chapter is based on the article 'Evolution of diamond resorption in a silicic aqueous fluid at 1-3 GPa: application to kimberlite emplacement and mantle metasomatism.' by Z. Zhang, Y. Fedortchouk and J. J. Hanley, published in Lithos (*Zhang et al., 2015*).

4.2. ABSTRACT

Natural diamonds grow and partially dissolve during mantle metasomatism and undergo further resorption during the ascent to the Earth's surface in kimberlite magmas. This study uses atomic force microscopy (AFM) for quantitative characterization of diamond resorption morphology in order to provide robust constraints of the composition of kimberlitic and mantle metasomatic fluids. We performed experiments in a piston-cylinder apparatus at pressures (P) of 1 - 3 GPa and temperatures (T) of 1150 – 1400 ^{o}C to examine the impact of P, T, and silica content of an aqueous fluid on diamond dissolution. Petrographic observation and microthermometery of synthetic fluid inclusions trapped in

olivine at the run conditions provide constraints on the composition and density of the fluid reacting with the diamond. Our results confirm an inverse relationship between P and T on diamond dissolution kinetics. A P increase of 1 GPa suppresses diamond oxidation rates by the same value as a T decrease by ~ 50 ^{o}C, while the transformation rate of diamond crystal morphology from octahedron to tetrahexahedron increases with both P and T. All dissolved diamonds develop glossy surfaces, ditrigonal {111} faces, sheaf striations, and negative trigons, while circular pits only occur in aqueous fluids with low silica content (≤ 4.2 mole/kg) at 1 GPa. We identify five distinct morphological groups of trigons: two types of point-bottomed (p/b) (trumpet- and V-shaped) and three types of flat-bottomed (f/b) (trumpet-shaped, trapezoid-shaped and rounded). AFM measurements of trigons from two successive runs showed three stages of their evolution. Etch pits nucleate at defects as trumpet p/b trigons with the vertical dissolution rate (V_d) faster than the dissolution rates at the surface free of defects; they further develop by growth of the bottoms in (111) plane to create trumpet-shaped f/b trigons accompanied by decrease in V_d; and finally form trapezoid-shaped f/b trigon with constant wall angles. The diameter of f/b trigons developed in the aqueous fluids depends on the diamond weight loss and dissolution kinetics, and does not correlate with their depth. Integration of our AFM data with the theoretical model for trigon formation suggests that the change from point- to flat-bottomed trigons depends on the defect sizes and dissolution conditions. Application of

our results to the diamonds from Ekati diamond Mine, Canada, suggests that variations in diamond rounding in different pipes implies variable depth of fluid exsolution; presence of circular pits on diamonds indicates predominantly aqueous fluid during the latest stages of kimberlite emplacement; and comparison to the mantle-derived morphologies on Ekati diamonds implies the importance of CO_2-rich fluids and / or carbonate melts during mantle metasomatism. The constrained effect of P on diamond dissolution kinetics indicates that appreciable diamond weight loss can only happen at P < 1GPa and therefore the conditions at the latest stages of kimberlite emplacement are very important for assessments of diamond preservation in a kimberlite pipe.

4.3. INTRODUCTION

Natural diamonds grow in the mantle from fluids or melts (e.g. Stachel and Harris, 2009; Smit et al., 2014), and undergo destruction due to partial dissolution by mantle metasomatism (Gurney et al., 2004), thermal abnormalities caused by tectonic processes (Smit et al., 2014), and oxidation in host magmas (e.g. kimberlites) during the ascent to the Earth's surface (e.g. Gurney et al., 2004). Surface features on diamond crystals fingerprint the conditions during growth (Sunagawa, 1990) and destruction both in host magmas and in the mantle, and can indirectly constrain fluid composition during these

processes (Khokhryakov and Pal'yanov, 2010; Fedortchouk and Zhang, 2011; Zhang and Fedortchouk, 2012).

Many lines of evidence indicate metasomatic enrichment of sub-continental lithospheric mantle contributing to diamond growth and triggering kimberlite magmatism (e.g.Klein-BenDavid et al., 2007a; Stachel and Harris, 2009; Aulbach et al., 2011). However, the conditions and composition of the metasomatic agents are still not well constrained due to the complexity of mantle assemblages. Garnet from mantle xenoliths and diamond inclusions shows rims enriched in Y, Zr and other incompatible elements implying a reaction with an oxidizing silicate metasomatic agent (Griffin et al., 1999b; Stachel and Harris, 2009; Bataleva et al., 2012). Variable enrichment in light and heavy rare earth elements (REE) recorded by complex sinusoidal REE patterns of harzburgitic and lherzolitic garnet inclusions in diamond suggest two or more overlapping metasomatic events caused by COH fluids and silicate melts (Griffin et al., 1999b; Stachel and Harris, 2009). Some diamonds show significant co-variations in carbon isotopes and nitrogen content indicating diamond precipitation controlled by a Rayleigh fractionation from CO_2-/carbonate media or from methane fluids (Stachel and Harris, 2009). However, this model is not yet confirmed due to the lack of experimental data on partitioning and isotopic fractionation of carbon and nitrogen during diamond precipitation. Additionally, fibrous diamonds contain numerous fluid micro-inclusions with composition ranging from silicate

or carbonate melt to hydrous CHO or brine fluids (e.g. Klein-BenDavid et al., 2007a) suggesting a continuous spectrum of diamond-precipitating silicate, aqueous, and carbonatitic fluids and melts (Dasgupta and Hirschmann, 2010). The new estimates of the mantle oxygen fugacity (f_{O2}) support aqueous fluid or silicate melt poor in carbonate as the diamond-precipitating agent (Stagno et al., 2013). The formation of fibrous diamonds is either before or after diamond resorption.

Diamonds have been a subject of investigation of controlling factors of dissolution and related mechanisms. Experimental studies examining the mechanism and kinetics of diamond dissolution (e.g. Frank et al., 1958; Kozai and Arima, 2005; Fedortchouk and Canil, 2009) demonstrated diamond dissolution as an oxidation process involving breakage of C-C bonds in diamond lattice to form CO or CO_2. The process depends on the content of elements with variable valence state (e.g. Fe) (Harris and Vance, 1974) and on the solvent types (fluids or melts) (Kozai and Arima, 2005; Fedortchouk et al., 2007; Khokhryakov and Pal'yanov, 2010). However, most of the previous experimental work primarily focused on the kinetics of diamond oxidation and its dependence on T and f_{O2} (Kozai and Arima, 2005; Fedortchouk et al., 2007; Arima and Kozai, 2008; Fedortchouk and Canil, 2009). The effect of P (Arima and Kozai, 2008; Khokhryakov and Pal'yanov, 2010) is not systematically studied, which impedes our understanding of diamond dissolution.

Presence and types of the etch features created in experiments were often reported and described (Frank et al., 1958; Kanda et al., 1977; Khokhryakov and Palyanov, 2006), but only recently their morphology and relationship with fluid/melt characteristics in the mantle and kimberlites became a focus of experimental studies (Fedortchouk et al., 2007; Arima and Kozai, 2008; Khokhryakov and Pal'yanov, 2010). Diamond dissolution in the presence of H_2O- and CO_2-fluids produces remarkably different dissolution morphology and configuration of etch pits on {111} faces (Fedortchouk et al., 2007; Khokhryakov and Pal'yanov, 2010; Bataleva et al., 2012). T and f_{O2} affect the orientation of trigonal and square etch pits (Kozai and Arima, 2005; Fedortchouk and Canil, 2009; Khokhryakov and Pal'yanov, 2010), and CO_2 -dominated media produces hexagonal pits (Fedortchouk et al., 2007; Arima and Kozai, 2008; Khokhryakov and Pal'yanov, 2010). Comparison of experimental data to the morphologies of natural diamonds from Ekati Diamond Mine led Fedortchouk et al. (2010) to proposing predominantly aqueous magmatic fluids in kimberlites and developing criteria for distinction kimberlite-induced from mantle-derived diamond resorption morphologies (Fedortchouk and Zhang, 2011; Zhang and Fedortchouk, 2012). However, characterizing fluids in kimberlites and diamond-destructive mantle metasomatic media requires understanding of P effect on diamond dissolution morphology and the formation mechanism of etch pits.

Formation of trigonal pits depends on diamond defects. Mendelssohn and Milledge (1995) linked nitrogen defects with diamond dissolution. Diamond dissolution experiments showed a relationship between the geometry of trigonal pits and the types of the outcropping defects revealed by X-ray topography (Khokhryakov and Palyanov, 2006). The abundance, geometry, and dimensions of trigonal pits depend on oxidation conditions (Fedortchouk et al., 2007). The fundamental theoretical attempt was made to describe the mechanism of etch pits development and to interpret their geometry (Angus and Dyble, 1975). However, testing this model requires high-precision quantitative data of geometry of trigonal pits developed under known oxidation conditions. The employment of atomic force microscopy (AFM) makes it possible (e.g. Gainutdinov et al., 2013).

Here we oxidized diamond crystals in aqueous fluids to investigate the effects of P, T and silica content on diamond dissolution. AFM measurements of trigonal pits allow analyzing the theoretical model by Angus and Dyble (1975) and shed light on diamond dissolution mechanism. Our data applied to natural diamonds constrain fluid composition in diamond-bearing environments and evaluate diamond preservation in diamond mantle reservoirs and kimberlites during ascent.

4.4. EXPERIMENTAL AND ANALYTICAL METHODS

Flat-faced, inclusion-free natural octahedral diamond crystals (< 1 mm) from Yakutian kimberlites were used. Before and after runs, the cleaned crystals were weighed on a microbalance (± 0.01 mg; Denver Instruments) to calculate weight loss, and all crystal faces were photographed in reflected light using an optical microscope for morphological comparison. The surface areas of crystal faces were measured using ImageJ (NIH USA) software. We trapped fluid inclusions in annealed olivine or quartz at most run conditions to monitor the compositions of diamond-etching fluids. We selected inclusion-free crystals of gem-quality olivine from Pakistan and synthetic quartz by optical microscopy and fractured them by heating with a Bunsen burner for 3 seconds followed by quenching in deionized water.

We used simple synthetic systems $H_2O \pm MgO \pm SiO_2$ (Table 4.1 and 4.2). Two starting mixtures, MS20 and MS30, were prepared from reagent grade SiO_2 and $Mg(OH)_2$ (> 99 % purity; Alfa Aesar) in weight ratio 2:8 and 3:7, respectively. Water was introduced as $Mg(OH)_2$ by thermal decomposition $Mg(OH)_2 \rightarrow MgO + H_2O$ (Johnson and Walker, 1993) and/or as deionized water with a micro-syringe. All starting materials were stored at 110 ^oC in an oven. Experiments were performed at 1, 2, and 3 GPa and 1150 – 1400 ^oC for 1 to 72 hours (Table 4.1) using a piston-cylinder apparatus with a 12.7 mm NaCl-Pyrex

Table 4.1 Experimental conditions

Run no.	Diamond	Starting materials	SiO_2 molality (mole/kg) [c]	T (^oC)	fO_2 [d]	Time (min)	Initial diamond weight (mg)
1 GPa							
PC-104[a]	ALZ14	$Mg(OH)_2$		1350	NNO	60	0.59
PC-105[a]	ALZ7	$Mg(OH)_2$		1350	NNO	60	1.49
PC-114[a]	ALZ16	$Mg(OH)_2$		1350		60	1.16
PC-115[a]	ALZSR1	$Mg(OH)_2$		1350		60	1.12
PC-116[c]	ALZSR2	$Mg(OH)_2$		1350		60	0.87
PC-117[a]	ALZSR3	$Mg(OH)_2$		1350		60	0.96
PC-118[a]	ALZSR3	$Mg(OH)_2$		1350		60	0.92
PC-119[a]	AZLSR3	$Mg(OH)_2$		1350		60	0.92
PC-120	AZLSR3	$Mg(OH)_2$+Ol	3.1	1350		60	0.96
P-250[b]	M31	$Mg(OH)_2$		1350		120	1.61
P-292[b]	P2	$Mg(OH)_2$		1250		330	1.88
PC-148	ALZSP25	SiO_2+Qtz+H_2O	61.9	1250		300	0.73
	ALZSP26						1.21
PC-157	ALZ33	MS30+Ol	23.1	1250		300	0.33
	ALZ34						0.60
P-298[b]	M83	$Mg(OH)_2$		1150		2700	1.19
2 GPa							
PC-95[a]	ALZ5	$Mg(OH)_2$		1400		60	0.41
PC-98	ALZ6	$Mg(OH)_2$		1400		60	0.36
PC-90[a]	ALZ1	$Mg(OH)_2$		1350		60	1.15
PC-99[a]	ALZ2	$Mg(OH)_2$+Ol	3.0	1350		60	1.03
PC-100[a]	ALZ3	$Mg(OH)_2$+Ol	4.5	1350	NNO	60	1.08
PC-103[a]	ALZ3	$Mg(OH)_2$		1350	NNO	60	1.06
PC-106	ALH4	$Mg(OH)_2$		1350	NNO	60	1.18
PC-113[a]	ALZ15	$Mg(OH)_2$		1350		60	0.84
PC-121	ALZ13	$Mg(OH)_2$+Ol	4.7	1350		300	1.63
PC-132	ALZ13	MS30+Ol	23.1	1350		300	1.59
PC-122[a]	ALZSP4	$Mg(OH)_2$+Ol	7.0	1350		300	1.13
PC-123[a]	ALZSP4	$Mg(OH)_2$+Ol	6.5	1350		300	1.15
PC-109[a]	ALH3	$Mg(OH)_2$		1250	NNO	600	1.41
PC-111[a]	ALH3	$Mg(OH)_2$		1250	NNO	600	1.39
PC-110[a]	ALZ12	$Mg(OH)_2$		1250	NNO	600	0.90

Continued on next page

Run no.	Diamond	Starting materials	SiO_2 molality (mole/Kg)	T (^oC)	fO_2[b]	Time (min)	Initial diamond weight (mg)
PC-112[a]	ALZ11	$Mg(OH)_2$		1250	NNO	600	1.46
PC-126	ALZSP7	$Mg(OH)_2$+Ol+Qtz	9.2	1250		600.3	1.12
PC-128[a]	ALZSP7	$Mg(OH)_2$+Ol+Qtz		1250		600	1.06
PC-129	ALZSP7	MS30+Ol	23.1	1250		600	1.07
PC-130	AlZSP9	MS20+Ol	18.5	1250		1440	0.91
PC-131	AlZSP10	MS30+Ol	23.1	1250		1200	1.49
PC-127	ALZSP8	$Mg(OH)_2$+Ol+Qtz	8.3	1150		4291	1.04
PC-133	ALZSP11	MS30+Ol	23.1	1150		4320	0.87
3 GPa							
PC-134	ALZSP12	MS30+Ol	23.1	1350		300	0.67
PC-141	ALZSP17	MS30+Ol	23.1	1250		600	0.77
	ALZSP18						0.49

[a] water-lost

[b] runs reported in Fedortchouk et al. (2007);

[c] SiO_2 molality = moles of SiO_2 / mass of H_2O (kg)

[d] NNO Nickel-nickel oxide buffer;
Ol: olivine; Qtz: quartz.

assembly (Figure 4.1) (Experimental Petrology Laboratory, Dalhousie University, Canada).

For each experiment, a third amount of the starting materials were packed inside a 3 mm O.D., 0.127 mm wall thickness, Pt capsule welded using the 'ash-can' design (Sneeringer and Watson, 1985). One or two diamond crystals were loaded, followed by packing the rest materials (without olivine/quartz) or by placing olivine/quartz chips and then packing the remaining material firmly around olivine/quartz (Figure 4.1). The capsules were welded using a Lampert PUK 3 welder in micro mode with output power increasing from

Experimental results on diamond dissolution.

Run no.	T (°C)	Time (min)	Initial weight (mg)	Preserved weight (wt%)	Dissolution rate (mg/mm^2*min^{-1}) $*10^3$	Preserved (111) face (%)	Trigon types [b]					f/b trigon diameter,um (median) [c]
							p/b		f/b			
							1	2	1	2	3	
1 GPa												
PC-120	1350	60	0.96	81%	1.166667	19%	1		12	2		18-122(47)
P-250[a]	1350	120	1.61	93%	0.269743	28%						22-152(77)
P-292[a]	1250	330	1.88	95%	0.072373	56%						24-165(62)
PC-148	1250	300	0.73	97%	0.033239	64%	3		5	5	4	3-28(8)
			1.21	96%	0.059331	68%	2		10	3	4	4-71(11)
PC-157	1250	300	0.33	88%	0.112863	40%	1		4		5	12-97(34)
			0.60	88%	0.132586	50%	6	1	19	2		3-89(37)
P-298[a]	1150	2700	1.19	97%	0.005333	-						12-160(19)
2 GPa												
PC-98	1400	60	0.36	92%	0.399384	2%		1	7	1		17-112(41)
PC-106	1350	60	1.18	86%	1.025648	22%	4	1	11			7-160(41)
PC-121	1350	300	1.63	98%	0.038914	55%	3		12		3	28-135(46)
PC-132	1350	300	1.59	89%	0.138473	10%	2		10	2	1	21-118(52)
PC-126	1250	600.3	1.12	95%	0.037462	57%	9		26	6	3	10-47(16)
PC-129	1250	600	1.07	91%	0.032200	46%	1		11	9		15-73(43)
PC-130	1250	1440	0.91	88%	0.031503	20%	1		7	1		21-53(29)
PC-131	1250	1200	1.49	90%	0.041315	27%	1		6	2	1	17-167(13)
PC-127	1150	4291	1.04	93%	0.006424	31%	1		12	2		7-39(10)
PC-133	1150	4320	0.87	94%	0.005134	13%	1		13	1		10-35(13)
3 GPa												
PC-134	1350	300	0.67	94%	0.070390	25%	1	1	10	1		20-98(16)
PC-141	1250	600	0.77	96%	0.024058	53%	1		19	3	1	5-69(13)
			0.49	94%	0.032518	54%	2		16	5	1	8-53(12)

[a] runs reported in Fedrotchouk et al. (2007);

[b] p/b: point-bottomed, f/b: flat-bottomed;

[c] diameter measured under optical microscopy;

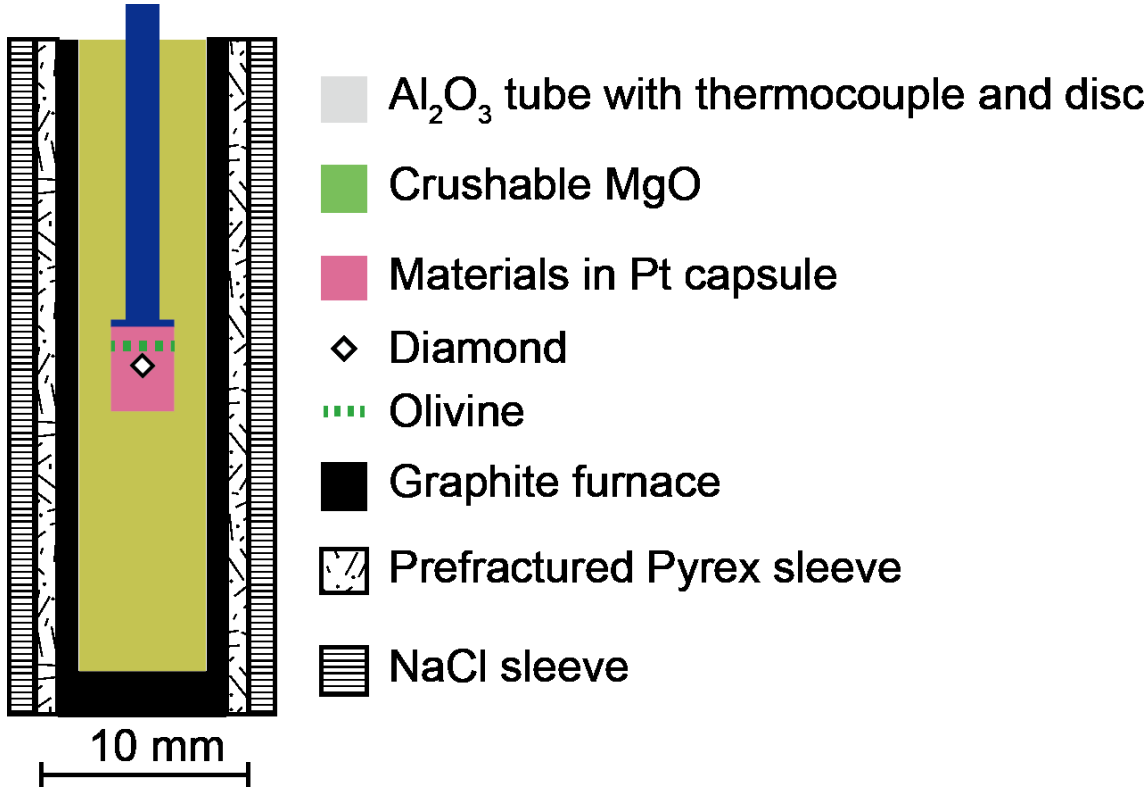

Figure 4.1 Configuration of the 12.7 mm, high-temperature NaCl-Pyrex assembly used for diamond dissolution experiments.

7 to 21 % giving experimental success rate > 80 %. The amount of the H_2O added in each run was sufficient to completely oxidize diamond crystal(s) (0.5–2.0 mg each). The capsules were inserted into pressure assemblies and stored at 110 ºC for > 12 hours in a vacuum oven. The Pyrex sleeves were pre-fractured at 600 ºC. The accuracy of pressure calibrated using diopside melting at 1 GPa and 1530 ºC (Williams and Kennedy, 1969) was better than 5 %, and no pressure correction was applied. The temperatures were monitored with a Eurotherm controller using $W_{95}Re_5$-$W_{74}Re_{26}$ thermocouple without any correction of pressure on *emf*. Thermal gradients within the capsule were ±20 ºC established by the spinel thermometer (Watson et al., 2002). All runs at 1 GPa used N_2 flow to prevent thermocouple oxidation (Walter and Presnall, 1994). Few runs were buffered using the nickel-nickel oxide assemblage (NNO) with double capsule technique (Arima and Kozai, 2008). However, we noticed faster resorption rates in the buffered runs than in the unbuffered ones, and suspected that Ni diffusing through capsule walls could act as a catalyst affecting our results. Therefore, we conducted the rest of our experiments unbuffered but believed f_{O2} of our NaCl-Pyrex assembly close to NNO (Fedortchouk et al., 2007).

For each run, the sample was pressurized to ~ 0.1 GPa, heated to 600 ºC at 60 ºC/min, and then held for 6 min while the pressure increased to the final value. The temperature was then brought to the final value at 100 ºC/min. During the run the pressure was adjusted

when the reading dropped by more than 10 % of the desired pressure. Experiments were quenched by terminating power to the graphite furnace followed by slow depressurization at ~ 0.1 GPa/min preventing decrepitation of inclusions. The recovered capsules were punctured to observe water release to confirm retention of fluids during the runs.

No run products contained any preserved quartz. The recovered olivine chips were mounted and polished for examination. Ratios of vapor bubble to inclusion volume were estimated using ImageJ software on images from optical microscopy (Table 4.3), which is only accurate for isometric inclusions (Roedder, 1984). Microthermometric analysis was done with an FTIR600 heating-freezing stage (Linkam Scientific Instruments) mounted on an Olympus BX51 microscope (Ore Fluids Laboratory, Saint Mary's University, Canada). The stage was calibrated using synthetic fluid inclusion standards containing pure CO_2 (melting at -56.6 ºC) and pure, critical density H_2O (melting at 0 ºC and homogenizing at 374.1 ºC). The absolute uncertainty is better than 3 °C within the measuring range (-190 to 560 °C) and better than 0.2 °C near 0 °C. One olivine grain (PC-157), densely populated with fluid inclusions, and solid phases within several inclusions were imaged and analyzed with a LEO 1450 VP Scanning Electron Microscope with X-ray microanalysis (SEM-EDS) at 5 nA current and 20 keV accelerating voltage (Saint Mary's University, Canada).

ic inclusions trapped in post-experimental olivine chips.

Run no.	P (GPa)	T (^{o}C)	Size (um)	Volatile Phases (20^{o}C)	Vapor (vol.%) (No. of measured inclusions)[a]	T_m^{ice}(^{o}C)[b]	T_h(^{o}C)[c]	No.[d]	SD[e]	Density (g/cm^3) measured	Density (g/cm^3) simulated	Solubility (mol./kg, Qtz_{equiv})
PC-157	1	1250	4-40	$L_{aq} + V_{aq}$	25.2 (14)	-2.0	376.0	9	12	0.574	0.827	4.2
PC-133	2	1150	4-14	$L_{aq} + V_{aq}$	14.8 (5)	-3.3	202.8	3	-	0.905	0.985	1.3
PC-131	2	1250	4-66	$L_{aq} + V_{aq}$	16.3 (13)	-2.5	228.2	2	-	0.865	0.960	1.6
PC-132	2	1350	17-58	$L_{aq} + V_{aq}$	18.7 (30)	-2.0	233.0	16	4	0.825	0.927	1.7
PC-141	3	1250	18-38	$L_{aq} + V_{aq}$	3.0 (2)	-	-	-	-	-	-	-
PC-134	3	1350	10-50	$L_{aq} + V_{aq}$	19.1 (3)	-	-	-	-	-	-	-

[a] Vapor (vol%) - average vapor proportions

[b] T_m^{ice} - ice melting temperatures.

[c] T_h - homogenization temperatures.

[d] N - the number of analyzed inclusions

[e] SD - standard deviation

The diamonds cleaned in a mixture of concentrated nitric and sulfuric acids in a volume ratio 3:5 were imaged by a Veeco MultiMode 8 AFM equipped with a 125 μm × 125 μm × 5 μm (in x, y and z dimension) J scanner under ambient conditions. The accuracy in x, y and z directions was ± 1.4 % calibrated using a VGRP-15M reference. AFM images were collected in tapping mode using Si_3N_4 tips (Bruker, TESP) with resonant frequency of 320 kHz at a scan rate of 0.4 Hz with 512 or 1024 sample lines. The trigon geometry (diameter, depth, wall angles, and profile configuration) were obtained using the section analysis of Nanoscope Software (V 8.10). There are three sources of errors in the measurement of trigon diameter (distance from an apex to the middle of the opposite side) and angle $\alpha_{\{111\}}$ between the trigon walls and (111) plane: 1) the AFM uncertainty (1.4 %); 2) tilting (0 - 2 ^{o}) of {111} face relative to the horizontal plane causing ~ 1 % in angle measurements; 3) random errors (<2%) due to the performance of the measurement. The total uncertainty comprises < 1.5 % for the distance (diameter and depth) and < 6 % for angle measurements. We examined at least ten representative trigons on each diamond crystal.

4.5. RESULTS

4.5.1. Synthetic Fluid Inclusions in Olivine

Only the runs with 30 wt% SiO_2 (MS30) preserved olivine implying stability of forsterite and periclase at run conditions (Wunder, 1998). Olivine size decreased after the runs. At

23 ºC, fluid inclusions show mainly isometric forms, often with negative crystal shapes, or less commonly water-drop or hour-glass shapes indicating necking down processes (Figure 4.2 a-d). The inclusions appear to be distributed within wide, healed fractures. However, X-ray mapping reveals that the inclusion-hosted structures actually contain freshly crystallized (primary) olivine (Ol II) within dissolution-reprecipitation structures in the olivine (Ol I); inclusions are hosted within this new generation of olivine (Figure 4.2 d). The isolated fluid inclusions vary in size from ~4 to 66 um (Table 4.3) and contain abundant solids (graphite, pyroxene and chlorite), a vapor bubble and an aqueous liquid phase (Figure 4.2 e). The proportion of the vapor to inclusion volume is constant and independent of the inclusion size for each experiment (Figure 4.2 a-c, Table 4.3) but changes with fluid density at different run conditions (Roedder, 1984). It increases with T due to the decrease of fluid density, such that at 2 GPa at 1150 ºC and 1350 ºC the volume proportion increased from 14.8 to 18.7 vol. % (Table 4.3), and decreases with P due to fluid density increase (Table 4.3).

Entrapment of homogeneous (single-phase) aqueous fluids was confirmed by microthermometry and petrography. Inclusions show final ice melting temperature (T_m^{ice}) between -3 and 0 ºC (Table 4.3, Figure 4.2 e), consistent with H_2O containing minor dissolved constituents. Since MgO solubility at our run conditions is negligible compared to SiO_2 solubility (Zhang and Frantz, 2000), dissolved SiO_2 is likely responsible for T_m^{ice}

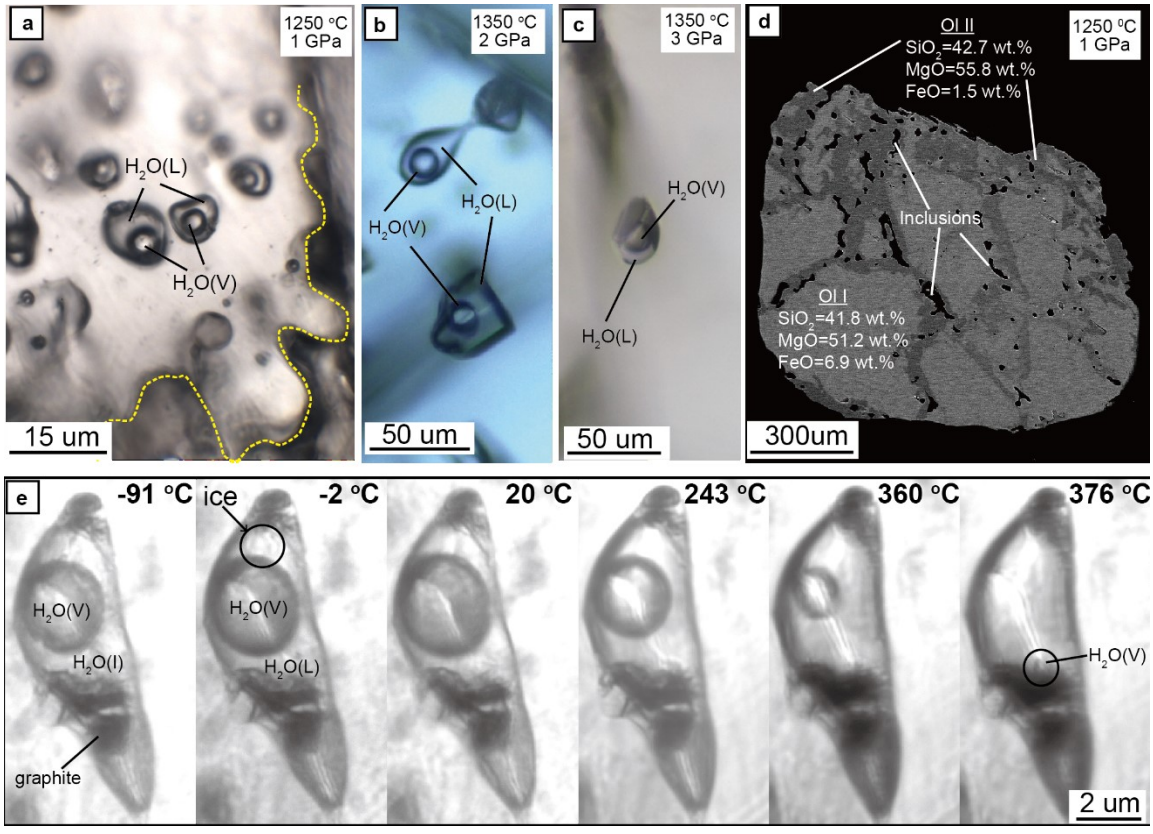

Figure 4.2 Synthetic aqueous fluid inclusions trapped in olivine chips. (a-c) fluid inclusions with a bubble photographed in transmitted plane-polarized light at ~23 °C, showing negative crystal and water-drop shapes; (d) backscattered electron image showing dissolution-reprecipitation channels, where aqueous fluid inclusions were trapped. Fe-rich primary olivine (Ol I, Fo93.0) is bright and newly-crystalized Fe-poor olivine (Ol II, Fo98.5) dark. Major element composition was determined by EDS. (e) behavior of a synthetic aqueous inclusion (~10 µm) in olivine during heating from −91.5 to 376.0 °C. The dotted line shows the embayed outline of the host olivine, and the black solid materials in the inclusion may be a graphite. H_2O(L)=liquid H_2O; H_2O(V)=vapor H_2O; H_2O(I)=ice H_2O.

below 0 ºC. As there is no appropriate equation of state to estimate bulk solute load for a $MgO\text{-}SiO_2\text{-}H_2O$ system as a function of freezing point depression, calculated isochores were estimated for pure water measured homogenization temperature (T_h, L+V→L) for several inclusions from each run product (Table 4.3, Figure 4.2 e). All inclusions trapped at 3 GPa decrepitated at ~ 130 ºC, may due to limited confining strength to accommodate the internal pressure on heating. Extrapolating isochores to the T of our experiments yield trapping P well below experimental conditions (e.g. at 1250 ºC, $P_{trapping}$ = 0.5 GPa vs. 1 GPa expected), consistent with the inclusions containing a much lower solute load at homogenization condition than at run conditions. We simulated isochores intersecting the P-T run conditions and the resulting bulk fluid densities were significantly higher than those obtained from microthermometry (Table 4.3). The density discrepancy requires between 1.3 and 4.2 mol/Kg dissolved SiO_2 in the aqueous fluids, comparable with the reported SiO_2 solubility in equilibrium with forsterite and enstatite (Newton and Manning, 2002).

Known dehydration conditions of brucite and petrographic observations confirm all fluid inclusions were trapped at the run conditions during olivine reprecipitation. Thermal decomposition of brucite releases water at ≥ 900 ºC (Johnson and Walker, 1993) precluding trapping the inclusions during the heating stage. Textural maturation of

individual inclusions to show negative crystal shape is a slow process (Tingle et al., 1992), excluding their formation on quench.

Decreasing olivine size, embayed outlines of inclusions (Figure 4.2a), and the dissolution-reprecipitation channels observed in olivine (Figure 4.2d) suggest a dissolution-reprecipitation mechanism for entrapment of synthetic fluid inclusions in olivine (e.g. Roedder, 1984). Solubility of olivine in aqueous fluid is enhanced by the T (Wykes et al., 2011), defects in natural olivine (Tingle et al., 1992), and faster dissolution rate of silica similar to the forsterite-enstatite-H_2O system (Newton and Manning, 2002). Dissolution of Fe-rich olivine created dissolution channels (Ol I, Figure 4.2d) resulted in enstatite:

$$Mg_2SiO_{4\ solid} + SiO_{2,\ aqueous} \rightarrow Mg_2Si_2O_{6\ aqueous} \quad (4.1)$$

Newly-formed enstatite decomposes into MgO and SiO_2 due to the excess MgO:

$$MgO_{\ solid} + Mg_2Si_2O_{6\ aqueous} \rightarrow 2\ SiO_{2,\ aqueous} + 3\ MgO_{\ aqueous} \quad (4.2)$$

Combining 1 and 2 reactions gives:

$$Mg_2SiO_{4\ solid} \rightarrow SiO_{2,\ aqueous} + 2\ MgO_{\ aqueous} \quad (4.3)$$

When the forsterite-periclase equilibrium is achieved, the silica molality decreases similar as in forsterite-enstatite-H_2O system (Newton and Manning, 2002). CO_2 increase due to diamond oxidation also suppressed silica solubility due to reducing water activity (Newton

and Manning, 2009). Decreasing silica molality triggered re-precipitation of Fe-poor olivine (Ol II, Figure 4.2 d):

$$2\ MgO_{\ aqueous} + SiO_{2\ aqueous} \rightarrow Mg_2SiO_{4\ solid} \quad (4.4)$$

The precipitated Fe-poor olivine sealed up dissolution channels and trapped aqueous fluids in equilibrium with newly-crystallized olivine, explaining the discrepancy between the initial high silica molality (Table 4.1) and the low silica molality in fluid inclusions (Table 4.3).

4.5.2. Pressure Effect on Diamond Oxidation Kinetics

Our experiments confirm that P depresses diamond dissolution rate and this effect is an exponential function of P at a constant T (Figure 4.3). Dissolution rates (K) at each P and T were obtained by fitting a linear regression through the experimental data points and the origin of the coordinates (Figure 4.3 a, b). A P increase by 1 GPa has equivalent effect on diamond dissolution rate as a T increase by ~50 ºC (Figure 4.3 c). The P effect on diamond dissolution rates can be expressed at 1350 ºC as:

$$K = -1.63 \times ln(P) - 7.89 \quad (4.5)$$

where K is in $mg/mm^2 \bullet min^{-1}$ and P in GPa. However, at 1150 ºC the dissolution rate in our study was significantly higher than that in the earlier work (Fedortchouk et al., 2007).

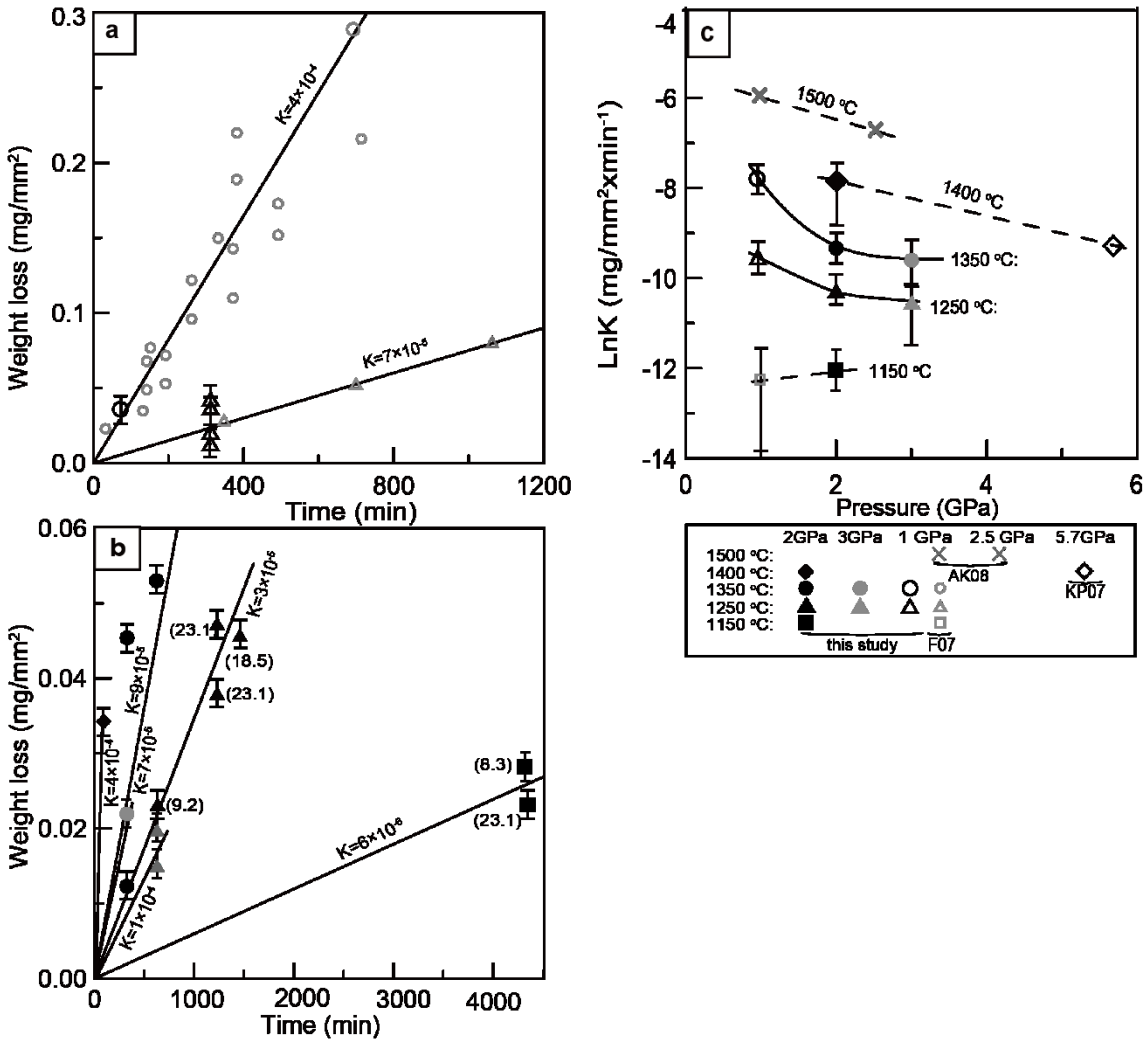

Figure 4.3 Diamond dissolution rate (K) calculated from diamond weight loss as a function of time in our experiments compared to the previous data from the literature: (a) at 1 GPa, (b) at 2, 3 GPa and variable SiO_2 content of the starting mixtures in brackets. (c) the pressure effect on diamond dissolution rate. AK08:(Arima and Kozai, 2008); F07: (Fedortchouk et al., 2007); KP07: (Khokhryakov and Pal'yanov, 2007).

This might be explained by f_{O2} increase during the longer run duration at 2 GPa (72 hours, this study) than at 1 GPa (45 hours, Fedortchouk et al., 2007) due to the limited buffering capability of the assembly (Ferry et al., 2002). We noticed no effect of SiO_2 molality on diamond dissolution kinetics at our run conditions (Table 4.2, Figure 4.3 b).

4.5.3. Diamond resorption morphology

During dissolution diamond crystals evolved from octahedron to tetrahexahedron (THH) morphology and developed various surface etch features (Figure 4.4). We adopt the morphological terminology from Robinson (1979).

4.5.3.1. Crystal Morphological Transformation

The degree of diamond rounding depends not only on the crystal weight loss but also on dissolution conditions. We examined the effect of P and T on diamond morphology transformation to establish the relationship between the dissolution conditions and the resorption morphology (Table 4.2 and Figure 4.5). Our data show that surface graphitization preserves octahedral morphology, while increase in both P and T enhances diamond rounding. To quantify P and T effects we calculated a rounding rate ($K_{\{111\}}$) obtained for each P and T by fitting a linear regression through the experimental data points (Figure 4.5 a, b). The rounding rate compares the percentage of the preserved area of initial {111} faces and the percentage of the preserved diamond weight (Table 4.2). Figure 4.5c

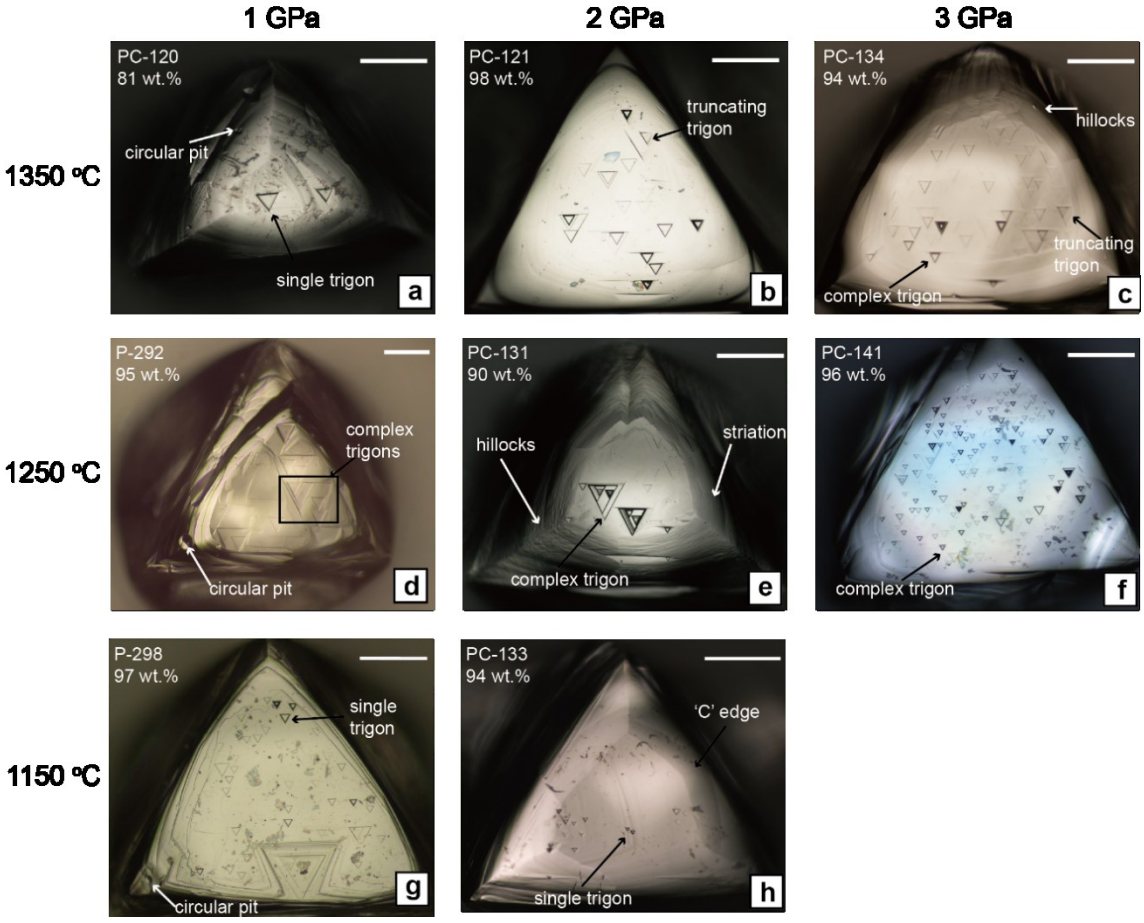

Figure 4.4 Microphotographs of diamond resorption morphology and etch features produced at different P and T. The percentage of the initial weight preservation and most common etch features produced during dissolution are shown on each photograph. Note the presence of circular etch pits only in 1 GPa runs. Scale bar is equal to 200 μm.

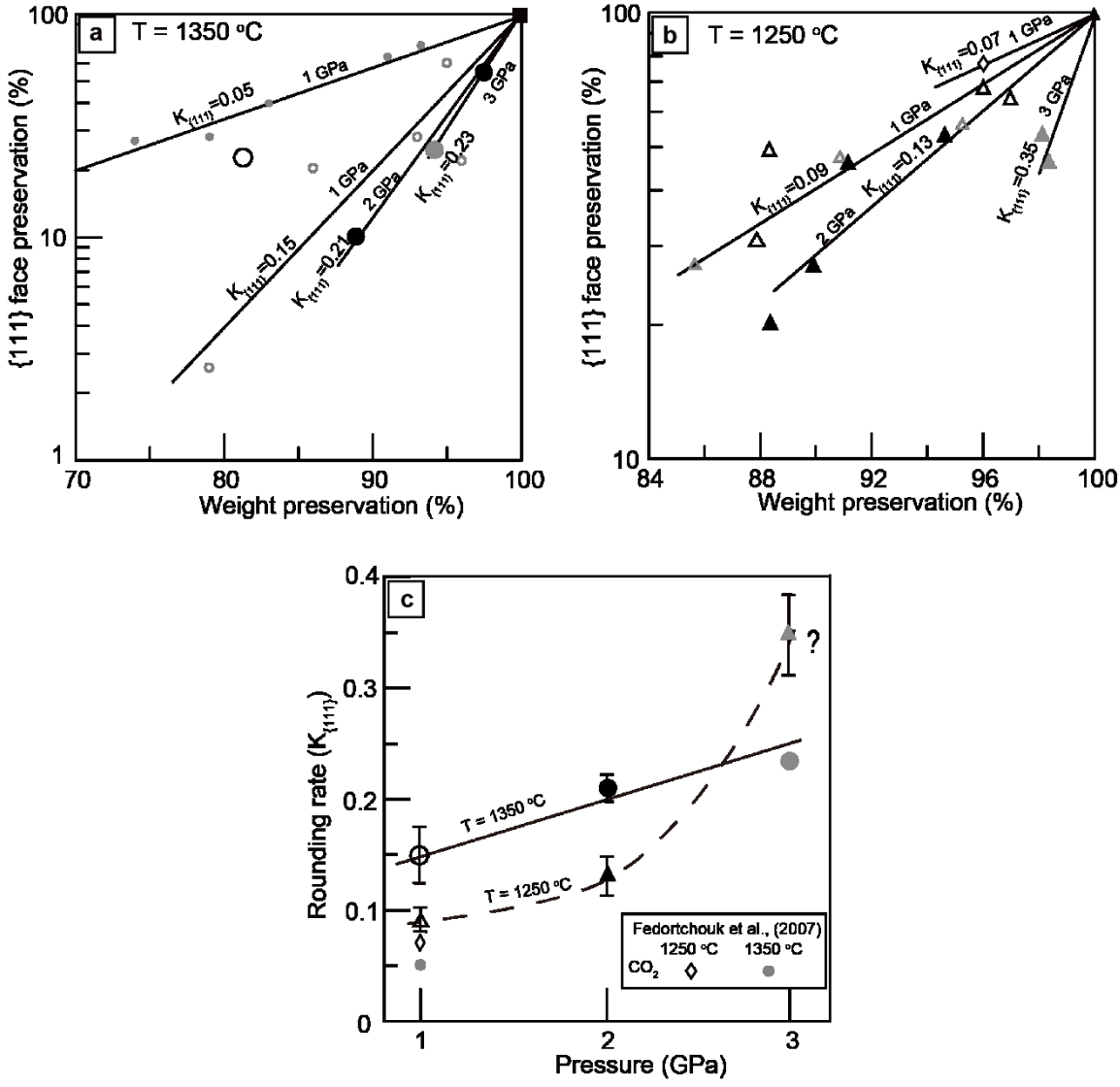

Figure 4.5 The rate of diamond morphological rounding ($K_{\{111\}}$) presented as preservation of {111} face vs. preservation of the initial diamond weight: (a) at 1350 ºC, (b) at 1250 ºC. (c) the pressure effect on rounding rate ($K_{\{111\}}$). Symbols used refer to Fig. 3. Error bars are within the size of the symbols.

shows a notable P effect on morphological transformation, such that at 1250 ^{o}C a P increase from 1 to 3 GPa results in $K_{\{111\}}$ increase from 0.09 to 0.35. The faster rounding rate at 3 GPa in 1250 ^{o}C run than in 1350 ^{o}C run might be due to properties of the particular diamond crystals (Figure 4.5 c).

Capsule piercing after some runs did not release water indicating fluid loss. Diamond crystals from these runs always showed surface graphitization. Removal of graphite in an acetone bath revealed trigonal {111} faces, frosted {110} faces, sharp multi-corners, and irregular negative trigonal and tetragonal etch pits.

4.5.3.2. Surface Features and Geometry of Trigonal Pits

The oxidized diamond crystals develop typical water-resorption features: glossy surface, ditrigonal {111} faces, sheaf striations, and regular negative trigons on {111} faces (Figure 4.4). Negative trigons are the most common features and can be divided into single (Figure 4.4 a, g, h) and complex (or 'nested' single) trigons (Figure 4.4 d, e, f). Both groups of trigons get truncated by the resorbed faces (Figure 4.4 b, c). Trigons are dominantly flat-bottomed (f/b) with the bottom parallel to (111) and seldom point-bottomed (p/b) trigons. The occurrence of p/b and f/b trigons shows no correlation with diamond weight loss or P-T conditions (Table 4.2).

A semi-quantitative analysis under an optical microscope shows that the diameter of f/b trigons depends on the weight loss, P-T conditions, and dissolution kinetics (Table 4.2, Figure 4.6). Diamond crystals from two subsequent runs show an increase in diameter. For example, at 2 GPa and 1350 ^{o}C after weight loss of 2 % diamond ALZ13 had trigons with the median diameter 46 um and after 11 % weight loss – with diameter 52 um. Overall, the correlation of f/b trigon diameter with the weight loss is weak (Figure 4.6 a). The diameter notably increases with T and decreases with P (Figure 4.6 b), which results in a positive correlation between trigon diameter and the dissolution kinetics (Figure 4.6 c).

The quantitative AFM measurements of geometry of individual and complex trigons allow further refining types of single trigons (Figure 4.7, Table 4.2 and D.1) based on their profile configuration. For p/b trigons we distinguished: 1) 'trumpet-shaped' (Figure 4.7 a), with diameter 1 - 18 um, depth 26 nm to 2.1 um, and $\alpha_{\{111\}}$ = 0.5 to 43 ^{o}; 2) 'V-shaped' (Figure 4.7 b) with diameter 2.8 - 25.1 um, depth 106 - 929 nm, and $\alpha_{\{111\}}$ = 1- 24 ^{o}. Similarly, f/b trigons with diameter ranging from 4.8-116 um and depth from 1 to 2771 nm are divided into: 1) the predominant 'trapezoid-shaped' f/b trigons with constant $\alpha_{\{111\}}$ (Figure 4.7 c); 2) common 'trumpet-shaped' f/b trigons (Figure 4.7 d); and 3) 'rounded' trigons (Figure 4.7 e). The $\alpha_{\{111\}}$ of f/b trigons range from 0.6 to 67 ^{o}, but mainly are 5-7, 9-13, 15-17, 19-20, and 22-24 ^{o} (Table E.1), corresponding to {433}, {322}, {221}, {211}, and {441} plane.

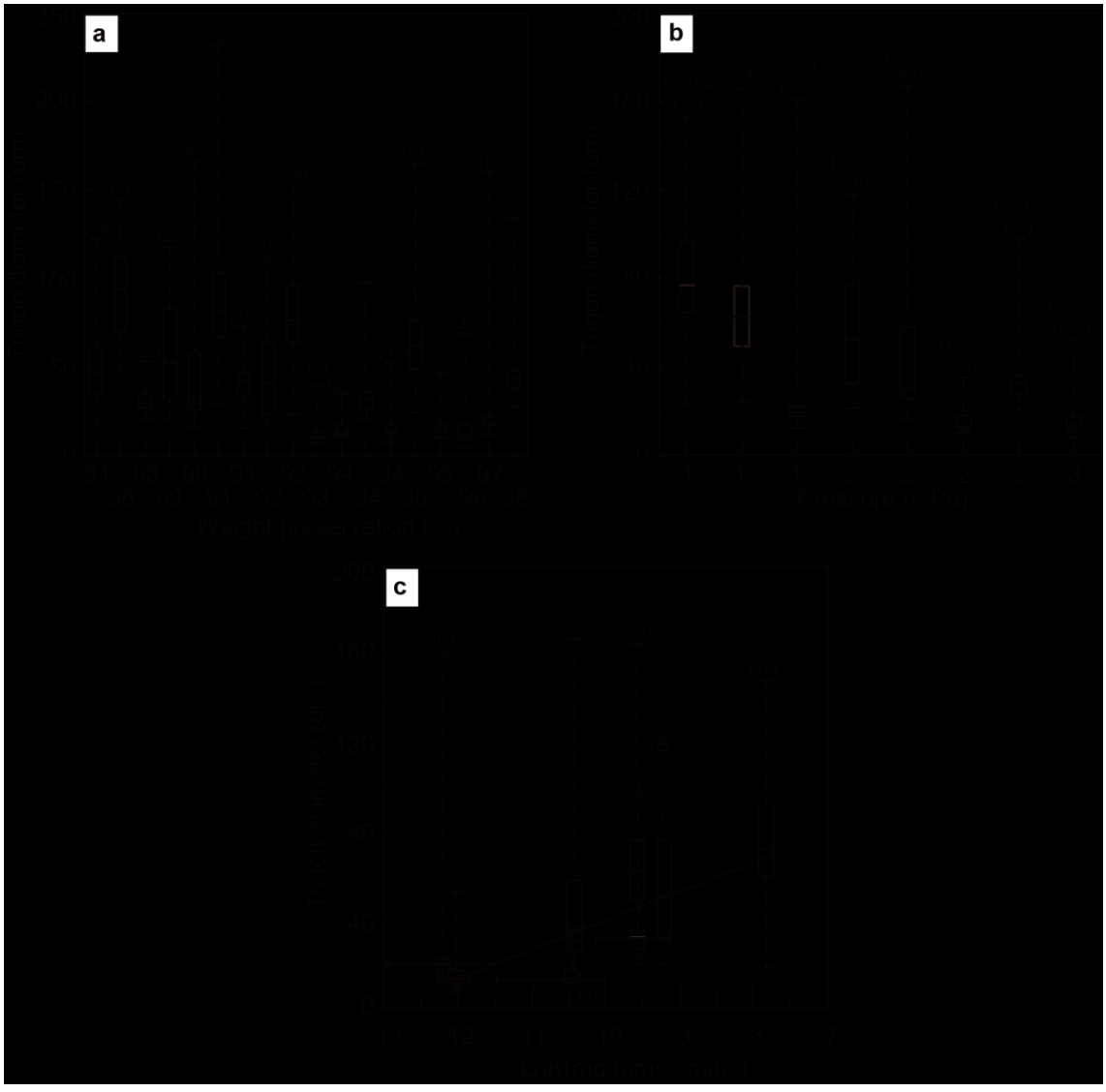

Figure 4.6 Relationship between the diameter of trigons on an etched diamond crystal and: a) initial diamond weight preservation; b) P and T conditions; c) dissolution rate (K). In b and c, only diamond crystals with similar weight preservation were selected. For each diamond dashed line covers the whole range of trigon diameters, the box includes 50% of the measurements, and the line inside each box represents the median value. The number of measured trigons on each diamond is in brackets.

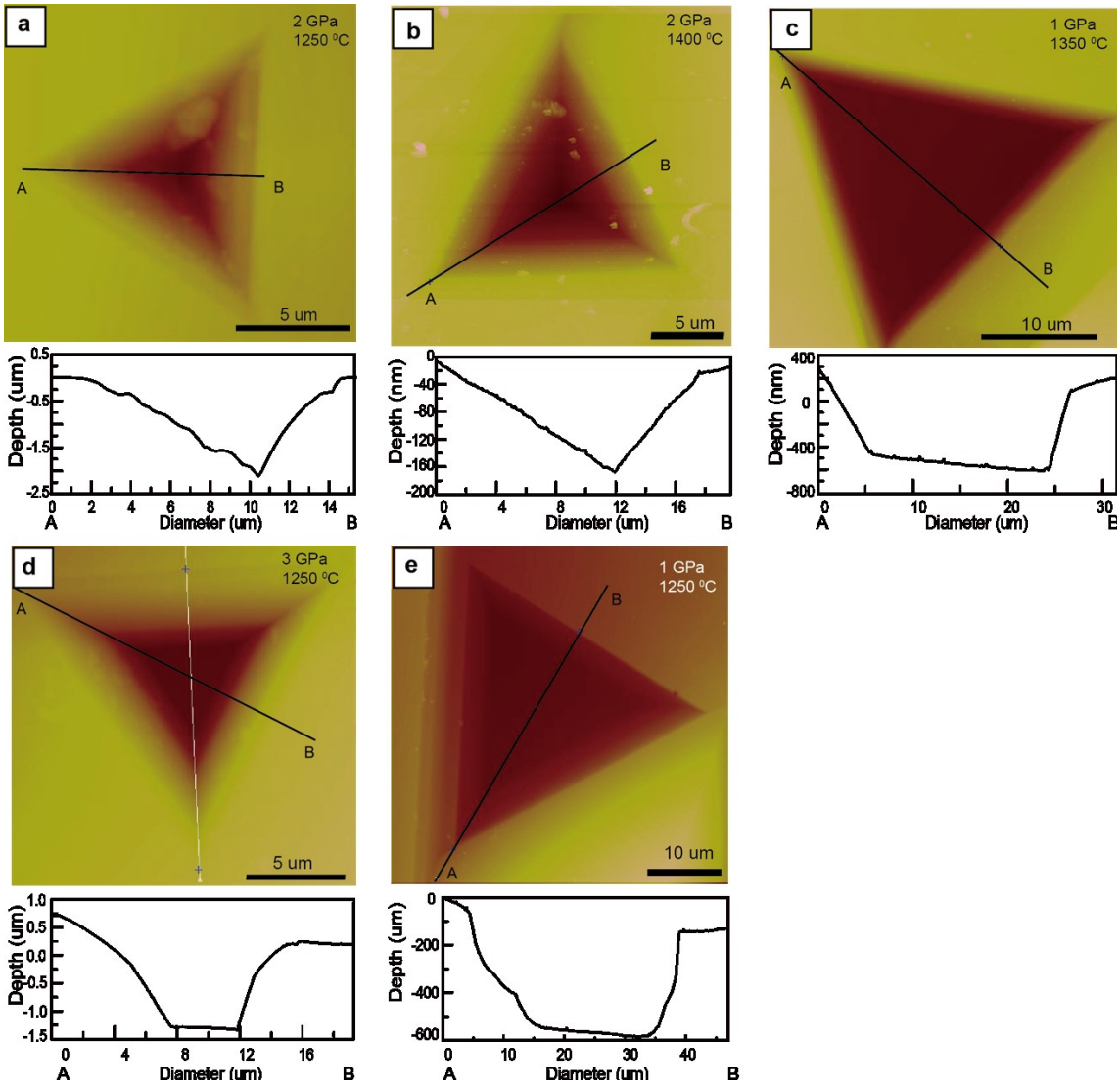

Figure 4.7 AFM images and cross-sections profiles of the five trigon types: a) trumpet-shaped p/b trigon; b) V-shaped p/b trigon; c) trapezoid f/b trigon; d) trumpet-shaped f/b trigon; e) f/b trigon with rounded corners. p/b= point-bottomed; f/b= flat-bottomed.

4.5.3.3. Evolution of Trigonal Pits

Trigon evolution was examined by scanning two faces of the same diamond (diamond ALZSP7, Table 4.1) on AFM after two successive runs PC-126 and PC-129 10 hours each at 2 GPa at 1250 ºC (Table E.1). Trigon diameter increased from the median 15 to 41 um (Table 4.2) but their abundance decreased after the second run (Figure 4.8) probably due to coalescence of trigons and crystal rounding truncating trigons (Figure 4.8. a2-b2' and d4-e4'). Two trigons were studied in detail after PC-126 run and PC-129 run, The first trigon, from a trumpet-shaped p/b with $\alpha_{\{111\}}$ =12 - 44 º (Figure 4.8 a) was enlarged and modified into a trumpet-shaped f/b trigon with similar $\alpha_{\{111\}}$ 16 - 45 º (Figure 4.8 b). The second trigon, from a trumpet-shaped f/b with $\alpha_{\{111\}}$ =18-45 º (Figure 4.8 d) was transformed into a trapezoid f/b trigon with $\alpha_{\{111\}}$ = 12-34 º and corresponding enlargement of the trigon bottom (Figure 4.8 e). Notably the trigon depth stayed nearly constant, indicating that it might be determined by the depth of the lattice defect. The wall angles gradually decrease from the bottom to the top of each trigon (Figure 4.8 c and f).

Calculation of enlargement rate parallel to the surface (V_t) for both trigons give a similar range from 0.8 at bottom to 1.2 μm/hour at top (avg. 1.0 um/hour), and the estimated vertical dissolution rate at the center of the trigons was 0.2-0.3 μm/hour using the average V_t. Comparing the dimensions of the three trigon types at 1250 ºC (Figure 4.9 a-c) shows: 1) small and shallow p/b trigons corresponding to the initial stage of trigon formation;

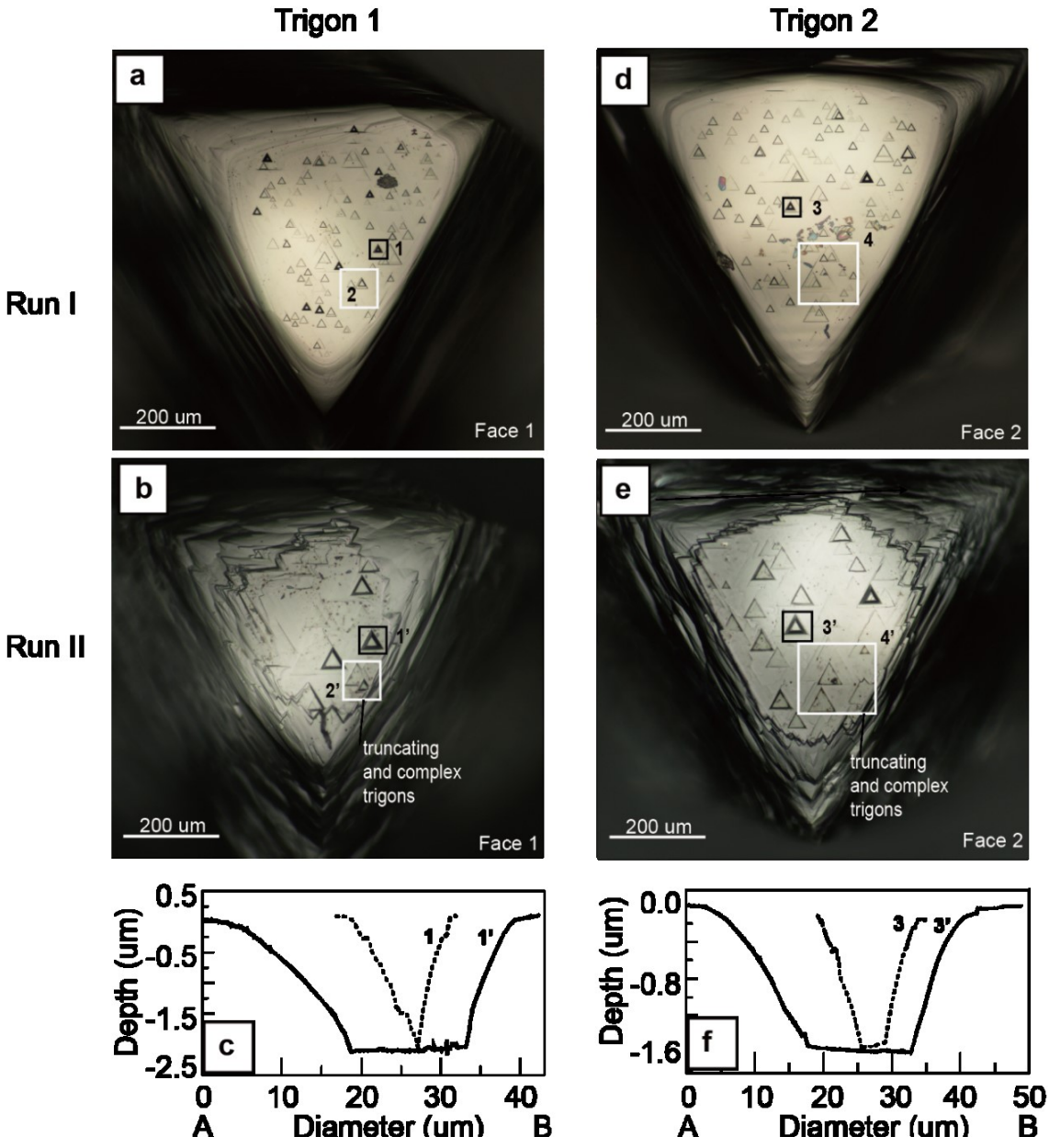

Figure 4.8 Microphotographs and AFM profiles showing evolution of two trigons on two faces of diamond crystal ALZSP7 at 2 GPa and 1250 ºC in two subsequent runs 10 hr each. (a-c) shows enlargement and transformation of trigon 1 from a trumpet-shaped p/b trigon (1) into a trumpet-shaped f/b trigon (1'); (d-f) transformation of trigon 2 from a trumpet-shaped f/b trigon (3) into a trapezoid f/b trigon (3'). Boxes 1-1', 2-2', 3-3', and 4-4' outline the same areas on {111} faces after each run. AB profiles are similar as those in Fig. 7. Note that the depth of the trigons stays nearly constant.

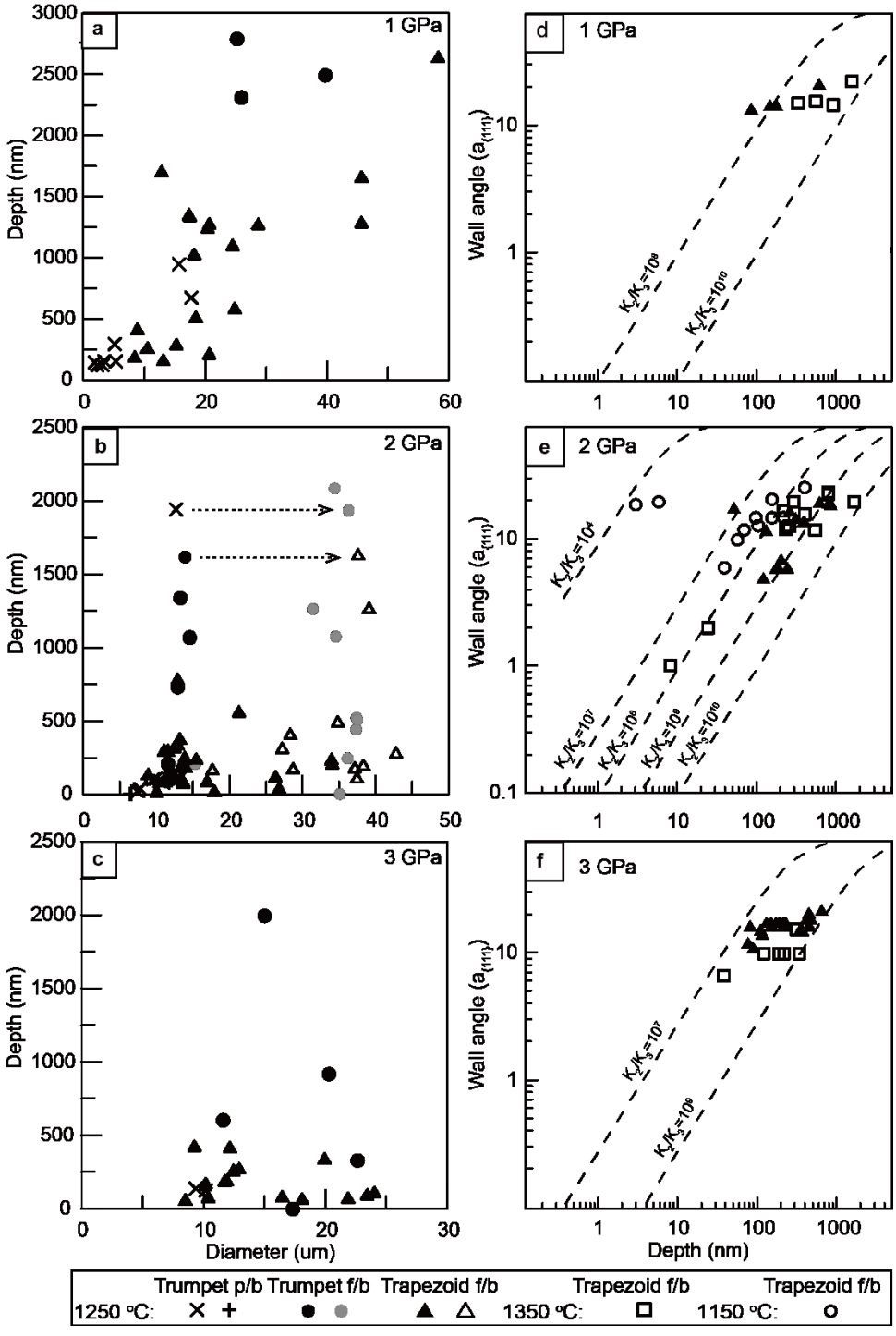

Figure 4.9 Depth of the trigons vs. their diameter (a-c) and the wall angles (e-f). The number of atoms N_d was converted into depth of f/b trigons, measured in nanometer, using equation (14). Error bars of the depth and diameter measurements are within the size of symbol.

2) dominated deeper trumpet-shaped f/b trigons implying their intermediate stage of the trigon development; 3) depths of trapezoid f/b trigons gradually decreasing as the diameter increases indicating their high evolutionary maturity and cease of trigon deepening while removal of layers from {111} face continues.

4.5.3.4. Circular Pits

The less common etch features, circular pits, were limited to the tetrahexahedral faces of some diamonds from our experiments. Circular pits with diameter 10-50 um have a concaved bottom cut through the middle by a groove perpendicular to [110] direction (Figure 4.4 a, d, g). We observed circular pits only in runs at 1 GPa within aqueous fluids with low silica molality ($\leq$ 4.2 mol/Kg) estimated from fluid inclusions (Table 4.3). They are absent in all 2 and 3 GPa runs and absent at 1 GPa with SiO_2 > 4.2 mole/kg. For example, they are absent in the runs with diopside melt and free H_2O. (12.3 mol/Kg, Fedortchouk et al., 2007).

4.6. DISCUSSION

4.6.1. Factors Determining Diamond Resorption in Silicic Aqueous Fluids

Typical diamond resorption morphology observed in experiments with H_2O fluid in P range 1 - 5.7 GPa (Kanda et al., 1977; Kozai and Arima, 2005; Fedortchouk et al., 2007; Khokhryakov and Pal'yanov, 2007; Arima and Kozai, 2008) can be summarized as: 1)

development of ditrigonal {111} faces; 2) predominantly negative flat-bottomed and less common point-bottomed trigons on {111} faces; 3) sheaf striations and hillocks along the resorbed tetrahexahedral faces. In addition to the earlier found effect of pure CO_2 and H_2O on diamond morphological transformation from octahedron into tetrahexahedron (Fedortchouk et al., 2007), here we established the P effect on fast 'rounding' of diamond crystals at minimal weight loss (Figure 4.5) in agreement with the reported complete transformation into THH after only 20-25 % weight loss at 5.7 GPa (Khokhryakov and Pal'yanov, 2007).

The factors controlling trigon morphology are not yet well known. Trigons can be associated with the lattice defects such as dislocation, dislocation loops, and ring cracks (Frank et al., 1958; Khokhryakov and Palyanov, 2006). Trigon evolution on the same diamond faces in the two successive runs at 2 GPa and 1250 ^{o}C allows us to further examine the relationship of different trigons with the lattice defects. AFM measurements of the same two trigons after both runs show that the lateral size and morphology undergo three-stage evolution at constant depth from p/b to f/b trigon (Figure 4.8) where the vertical dissolution rate decreases until becomes negligible, similarly to formation of pyramidal and flat-bottomed square pits described on LiF crystals (Gilman et al., 1958). We propose that f/b trigon depth reflects depth of initial defects (Figure 4.8) but their diameter increases with dissolution kinetics and weight loss (Figure 4.6). This explains the absence

of a correlation between diameter and depth of the trigons produced in aqueous fluids (Figure 4.9 a-c). Following Gilman et al. (1958) and previous trigon studies (Frank et al., 1958; Khokhryakov and Palyanov, 2006), we explain trigon formation depending on defect size and dissolution conditions and their shape p/b or f/b resulting from the evolution stages of trigon development. Therefore, the larger diameter of trigons is favored by lower P, higher T, and faster dissolution kinetics of diamond (Figure 4.6 b-c).

Circular etch pits are rare and occur exclusively on resorbed THH and cubic faces of natural diamonds (Robinson, 1979). Robinson (1979) considered them as post-major resorption features (e.g. trigons), caused by the exsolved CO_2 bubbles from kimberlites attaching to the diamond surfaces. We found circular pits forming on THH faces simultaneously with other common resorption features in restricted conditions of low P ($\leq$ 1 GPa) and low silica molality ($\leq$ 4.2 mol/Kg). Other experimental studies in H_2O fluid also did not report circular pits at P $\geq$ 2 GPa (Kanda et al., 1977). While occurrence of circular pits at low P agrees with immiscible fluids, presence of a homogeneous aqueous fluid in our runs confirmed by fluid inclusion data does not support this explanation. Moreover, absence of circular pits in mixed CO_2 - H_2O systems (our unpublished data) also contradicts to this mechanism. Limitation of circular pits only to the resorbed THH faces indicate crystallographic control of their development (Figure 4.4 a, d, g). An alternative explanation is that aqueous fluid is able to interact with a certain type of defects

on diamond surface developing them into the circular pits, where P or silica content can control the relation between the dissolution rates normal and parallel to THH faces. This requires further study.

4.6.2. Model of trigon formation

Mechanism of trigon formation on diamond is not well understood. Khokhryakov and Palyanov (2006) showed that positively oriented p/b trigons associated with the emergence points of edge dislocations have $\alpha_{\{111\}}$= 2, 5, 6, 8 º and those associated with larger defects (impurity clusters, microcracks and other surface defects) have $\alpha_{\{111\}}$ = 11-15 º. Angus and Dyble (1975) and Frank et al. (1958) developed a mathematical model based on observations of trigons on natural diamonds to explain their formation. The quantitative AFM data for the trigons developed in our experiments allow testing this model.

Angus and Dyble (1975) envisaged trigon formation as nucleation of monolayer etch pits at defect sites and their enlargement in width through removal of atomic layer by propagation of one kink (single-kink mechanism) or several kinks (multi-kink mechanism), assuming negligible surface diffusion. Straight linear outlines of trigons and absence of meandering steps support this assumption of surface-reaction control dissolution rather than diffusion-controlled dissolution, which would create meandering curves and no pits on calcite (e.g. De Giudici, 2002). Angus and Dyble (1975) considered

that the removal probability of carbon atoms hinges on their interactions with the adjacent neighbors, and proposed that three-bonded atoms are more reactive on trigon steps than on {111} face. Since two- and one-bonded atoms bordering defects are more vulnerable to dissolution than three- and four-bonded atoms on the defect-free surface, the authors suggested fast defect-dependent dissolution rates at defects (V_d , Figure 4.10 a, d, g, h) and negligible on defect-free surface.

The Angus and Dyble (1975) model predicted trigon geometry by considering the removal of an arbitrary carbon atom as a random Poisson process. They expressed the removal rate of n-bonded atoms as:

$$- dN_n/dt = K_n N_n \qquad (4.6)$$

where N_n is the number of n-bonded atoms; K_n is the etching rate constant determined by dissolution conditions. The pit wall angle, $\alpha_{\{111\}}$, is then calculated as:

$$\text{Tan } \alpha_{\{111\}} = 0.9428 \times V_d/V_p \qquad (4.7)$$

where V_p is the dissolution velocity of one row parallel to (111) plane and V_d is the velocity of displacement of one layer normal to the (111) plane (Figure 4.10 a, d, g, h).

Defect size and dissolution conditions determine formation mechanism of trigons. Trigon growth proceeds via single- or multiple- kink mechanism depending on defect size

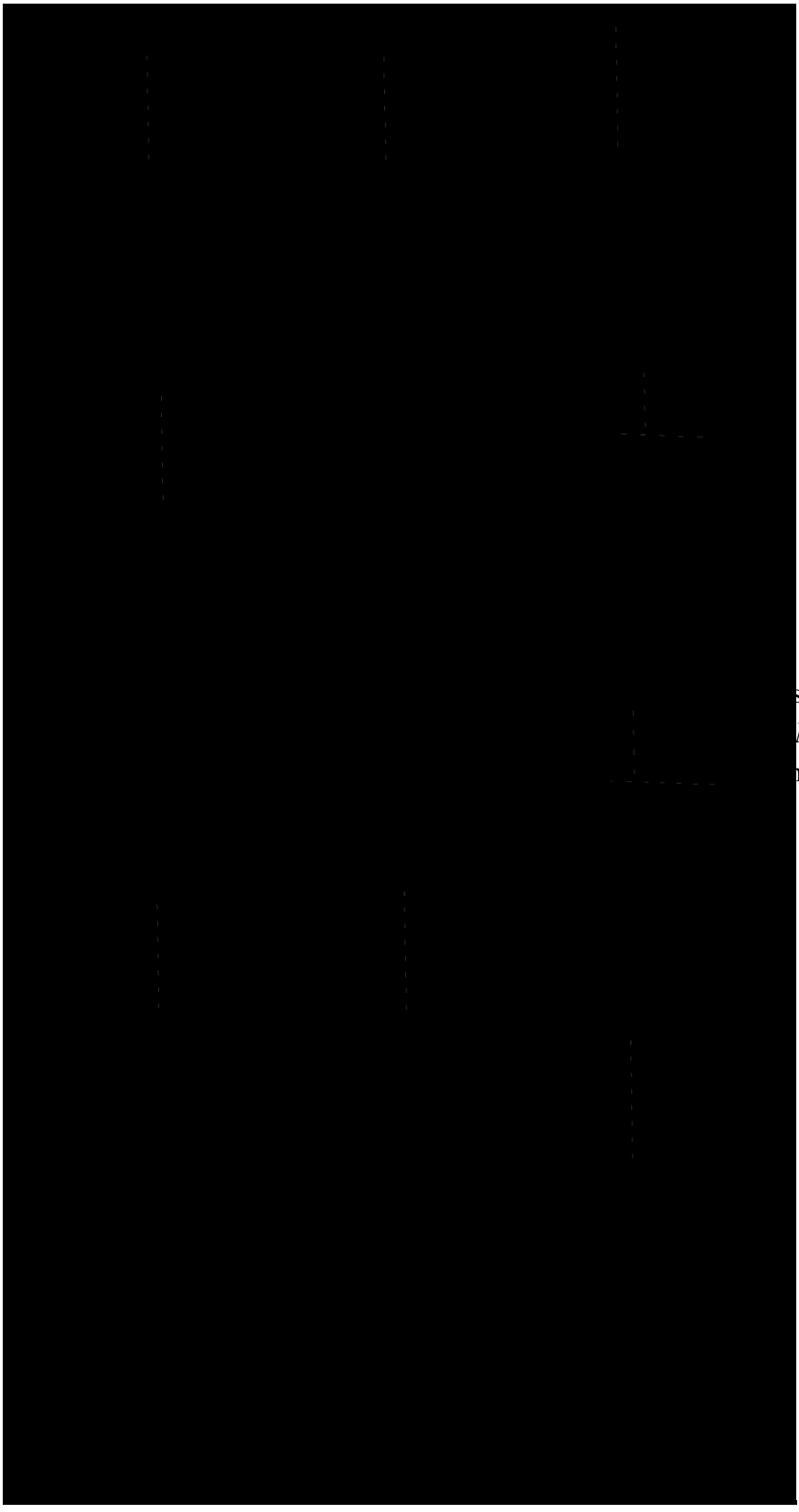

s dissolution at a defect. V_p = veloci
N_m^o, N_l^o = the number of carbon ato
reshold number for the switch be

expressed as the number of atoms (N^o) along one three-bonded edge in initial trigons encompassing defects. Small defects grow by single-kink mechanism until the step length reaches the threshold number N^c and then multiple-kink mechanism starts. Dissolution conditions (e.g. T, P) affect the ratio K_2/K_3 between the removal rate constants of two- (K_2) and three-bonded carbon atoms (K_3), and, furthermore, affect N^c estimated as $(N^c)^2 \approx K_2/K_3$ (Angus and Dyble, 1975). Angus and Dyble's model predicts that f/b trigons associated with larger defects (e.g. inclusions) have steps length > N^c, and grow by the multiple-kink mechanism with the rate:

$$V_p = (2K_2K_3)^{0.5} \quad (4.8)$$

creating straight pit walls (Figure 4.10 a-c) where

$$Tan\ \alpha_{\{111\}} = 0.9428 \times V_d/(2K_2K_3)^{0.5} \quad (4.9)$$

P/b trigons associated with small defects start as monolayer pits with steps < N^c and grow by the single-kink mechanism with the rate:

$$V_p = K_3N \quad (4.10),$$

developing curved pit walls (Figure 4.10 g) where

$$Tan\ \alpha_{\{111\}} = 0.9428 \times V_d/(K_3N) \quad (4.11),$$

As p/b trigons develop, length of the outer steps gradually increases until becomes > N^c(Figure 4.10 h), and then the multiple-kink mechanism operates, while the single-kink

mechanism continues in the inner part where step length is still < N^c.

Our diamond crystals show small p/b trigons and various sizes of f/b trigons. For f/b trigons we found no correlation between their diameter and the depth (Figure 4.8a) but constant trigon diameter for a given diamond crystal in a large range of depths (Figure 4.8b). The diameter increases with the dissolution rates (positively correlating with T and negatively with P) (Figure 4.5c). Furthermore, AFM study of trigons from the two subsequent runs (Figure 4.8) show that once the trigons reach their maximum depth corresponding to defect depth they grow laterally and combine with other trigons. Therefore, we propose that the stages of trigon evolution determine the types of particular trigons (Figure 4.10).

Our data suggest that trigons initialize as p/b trigons and evolve into f/b trigons. The shape of p/b trigons allows to examine single- vs. multiple- kink mechanism. Most of our measured p/b trigons have trumpet-shape (Figure 4.7a) indicating the single-kink mechanism, while V-shaped p/b trigons indicating the multiple-kink mechanism (Figure 4.7b) are rare. This might also be a result of our limited AFM study of p/b trigons and more data is needed to fully describe this process. Furthermore, the difference in the shape and formation mechanism of p/b trigons may indicate their association with different sizes of defects. The less abundant V-shaped p/b trigons might mark the outcropping sites of fewer large defects. Once the growing p/b trigon reaches defect depth it transforms into f/b. The

subsequent runs (Figure 4.8) show that a trumpet-shaped p/b trigon evolves into a trumpet-shaped f/b and finally to trapezoid f/b trigon. This explains why p/b trigons have smaller diameter than f/b trigons (Figure 4.9 a-c) and the positive correlation between diamond dissolution and the trigon diameter (Arima and Kozai, 2008). Our data also agrees with Angus and Dyble (1975) assumption that depth of f/b trigons approximates the initial defect size.

The evolution paths of trigons are summarized in Figure 4.10, where all trigons start at defect sites as p/b trigons; the defect sizes, crystallography of the defect outcrops, and P-T-f_{O2}-x (etchant) conditions decide their morphology and evolution (Robinson, 1979; Fedortchouk et al., 2007; Arima and Kozai, 2008; Khokhryakov and Pal'yanov, 2010). Large defects N_l^o ($N_l^o >> N^c$) under the multiple-kink mechanism develop two types: V-shaped p/b trigons and trapezoid f/b trigons (Figure 4.10 a-c). Small defects N_s^o ($N_s^o << N^c$) under the single-kink mechanism start as trumpeted p/b trigons and grow into trumpeted f/b and then trapezoid f/b trigons before their edge length > N^c (Figure 4.10 d-f). The change of $\alpha_{\{111\}}$ might be related to development of stable faces with low surface energy (e.g. Wang et al., 2010). Trigons associated with medium size defects N_m^o ($N_s^o < N_m^o < N^c$) evolve in a mixed-kink mechanism (Figure 4.10 g-j).

Previous experimental studies suggested the Arrhenius type of the rate relationship for diamond dissolution reaction (Fedortchouk et al., 2007; Arima and Kozai, 2008):

$$K_2/K_3 = Exp((E_3-E_2)/RT_k) \quad (4.12)$$

assuming identical pre-exponential factor $A_2 \approx A_3$ (Angus and Dyble, 1975), where E_3 and E_2 is the energy required for breaking three- and two- bonded carbons; R is gas constant; T_k is temperature in Kelvin.

Geometry of trigons not only records their evolutionary paths but shed some light on diamond dissolution conditions, which is expressed as the K_2/K_3 ratio. To assess the maximum K_2/K_3 ratio we use the assumption proposed by Angus and Dyble (1975) for the multiple-kink mechanism that the maximum value of V_d^{max} is three times V_p , in which case:

$$V_d^{max}=3K_3N_i \quad (4.13)$$

combining equations (9) and (13) the depth N_d of f/b trigons, measured in number of atoms, can be obtained from:

$$Tan\ \alpha_{\{111\}} = 0.9428\times3N_d/(2K_2/K_3)^{0.5} \quad (4.14)$$

Using $\alpha_{\{111\}}$ and N_d of f/b trigons with constant wall angles from our AFM measurements we evaluate the maximum K_2/K_3 ratio to be in the range of 10^6-10^9 (Figure 4.9 e-f). Figure 4.9 e-f show undetected P effect on K_2/K_3 but some T effect. Using equation (12) we observe decrease of E_3-E_2 from ~293 kJ/mol at 1350 ºC to ~209 kJ/mol at 1150-1250 ºC.

These values are lower than the energy of one carbon-carbon bond of 342 kJ/mole (Arima and Kozai, 2008) implying that diamond resorption does not go by simple removal of carbon atoms but as a more complex chemical reaction of H_2O with C atoms on diamond surface, such as the formation of C-OH and C-O. Few measurements on Figure 4.9 e-f plot along the lower values of K_2/K_3. Since all trigons formed under the same dissolution conditions, this discrepancy might imply presence of 'special' types of defects with different dissolution kinetics.

4.6.3. Diamond Resorption in the Ekati Mine Kimberlites

Volatiles influence the geology of kimberlite pipe (Brooker et al., 2011), magma eruption velocity (Russell et al., 2012), and diamond preservation in kimberlites (Fedortchouk et al., 2010). Their content and composition in kimberlites are obscured by substantial contamination by crustal and mantle material, post-eruption alternation and the lack of glasses. Our experimental results further constrain the volatile history of Ekati Mine kimberlites, Canada, using the micro-diamond parcels from our earlier studies (Fedortchouk et al., 2010; Zhang and Fedortchouk, 2012). Gurney et al. (2004) demonstrated significant differences in the features of diamond populations from neighboring Ekati kimberlites. Fedortchouk et al. (2010) used diamond morphology and types of infrared (FTIR) spectra of macrocrystal olivine from six kimberlites to propose aqueous composition of kimberlitic fluids in agreement with the low solubility of H_2O and

high solubility of CO_2 in kimberlitic melts (Brooker et al., 2011). Our experimental data demonstrate that presence of circular pits on diamond crystals from Misery and Koala kimberlites requires almost pure aqueous fluid at P < 2 GPa, which further supports aqueous composition of their latest magmatic fluids.

The effect of P on diamond resorption constrained here was used to examine the differences and evolution of aqueous fluids in Ekati kimberlite magma. During kimberlite eruption from the mantle source (~ 6 GPa) to the Earth's surface, P drop greatly affects the kinetics of diamond dissolution. Using f_{O2} estimates NNO-2 to NNO+6 (Canil and Bellis, 2007), kimberlite crystallization T = 1300 -1450 ºC (Kavanagh and Sparks, 2009), and rapid emplacement on an order of hours and days (Kelley and Wartho, 2000) we modeled preservation of a 1 cm octahedral diamond travelling from 3 GPa (~ 90 km) to the Earth's surface at NNO buffer in isothermal kimberlite eruption at 1350 ºC with the duration of 10 hours and 1 week (Figure 4.11). Our model shows that in the depth interval corresponding to P drop from 3 to 1 GPa diamond losses from 13% of its initial weight (in 1 week) to only 0.1 wt % (in 10 hours). The P effect on diamond dissolution determined in our study suggests that the final stages of kimberlite eruption (P<1 GPa) play the major role in diamond preservation. Kimberlite crystallization conditions during this stage (T, f_{O2}, presence of fluids, and ascent rate) could make significant effect on diamond grade. Fast cooling of kimberlite after the pipe emplacement would help diamond preservation.

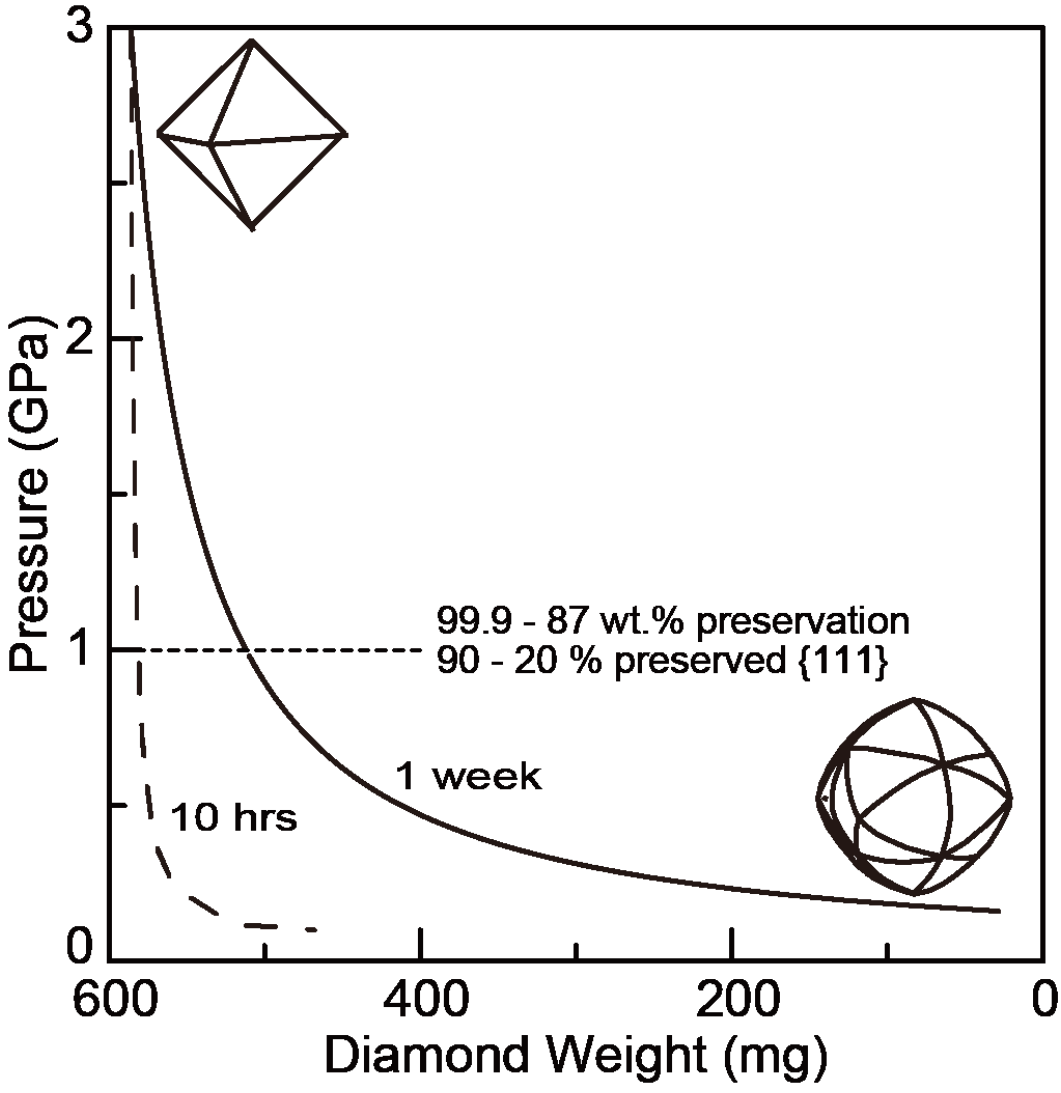

Figure 4.11 Calculated weight loss of an octahedral diamond 10 mm in diameter during oxidation in a kimberlite magma ascending from the depth corresponding to 3 GPa to the surface at 1350 ^{o}C and f_{O2} corresponding to NNO buffer. Note a negligible diamond weight lost between 3 and 1 GPa, and more aggressive dissolution at P < 1 GPa.

The rates of cooling are greater at the surface and decrease with depth, which might explain the reported decrease of the mine yield with depth (Frank et al., 1958).

On the contrary to the very minor diamond weight loss during dissolution in magma ascending from 3 GPa (~90 km) to 1 GPa (~ 30 km) (Figure 4.11), the rate of morphological transformation of octahedron into THH and decrease of the {111} faces are much faster at higher P (Figure 4.5). For example, 10 % weight loss of 1 mm octahedral diamond crystal corresponds to the following preservation of the {111} face: 20 % at 1 GPa but only 9-10 % at 2 and 3 GPa (Figure 4.5). This infers that while an early release of aqueous fluids in kimberlites (Brooker et al., 2011) can preserve diamond due to the fast emplacement, the crystal shape can still become considerably rounded. This finds support in comparison of diamond populations from two Ekati kimberlites – Misery and Panda (Gurney et al., 2004; Fedortchouk et al., 2010). Both are resedimented volcaniclastic kimberlites but with different diamond grades and octahedral / THH ratio. Misery with the grade of 4 carats /ton has 65 % THH and 30 % octahedra, while Panda with the lower grade ~1 carat /ton has 30 % THH and 56 % octahedra (Gurney et al., 2004). Given that the two pipes have sampled the same diamond reservoir, the earlier release of aqueous fluid in the Misery magma could explain the higher diamond grade but larger degree of resorption (estimated as the degree of diamond rounding).

4.6.4. Metasomatism under the Central Slave Craton

Internal zoning of natural diamond crystals (Bulanova, 1995) and micro-cavities in fibrous and cloudy diamonds (Klein-BenDavid et al., 2007b) provide evidence that diamond undergo dissolution during mantle metasomatism imposed by melts or fluids. The main candidates are carbonatitic melts (Aulbach et al., 2011; Stagno et al., 2013) or aqueous silicate melts (Klein-BenDavid et al., 2007b). Diamonds shielded by xenoliths during the kimberlite ascent preserve mantle-derived resorption features of several morphological types perhaps representing metasomatism in the different mantle domains (Zhang and Fedortchouk, 2012). These mantle-derived resorption features include trigonal {111} face, deep hexagonal pits and 'stepped-face' features. Our data show that diamond dissolution in silicic aqueous fluids at 1 to 3 GPa creates ditrigonal {111} faces and negative trigons in agreement with diamond dissolution results at 5 GPa (Kanda et al., 1977) and 5.7 GPa (Khokhryakov and Pal'yanov, 2007). P increase enhances diamond rounding developing morphology resembling kimberlite-induced resorption (Zhang and Fedortchouk, 2012). Therefore, part of diamonds with kimberlite-induced resorption were probably resorbed in the mantle in aqueous fluids (Klein-BenDavid et al., 2007b). No 'complex' and 'stepped-face' features were observed in our experiments. This points out a different metasomatic agent responsible for the formation of these morphologies. Development of hexagonal pits on {111} diamond faces in CO_2-bearing synthetic kimberlite at 2.5 GPa and 1500 ^oC

(Arima and Kozai, 2008) and in CO_2-dominated carbonate melts at 5.7-7.5 GPa, 1400 - 1750 ºC (Khokhryakov and Pal'yanov, 2010) suggests CO_2-rich metasomatic agents as a cause of the observed diamond morphologies.

4.7. CONCLUSIONS

Our study shows that diamond dissolution in silicic aqueous fluids creates typical water resorption features. Higher P increases the degree of diamond rounding (transformation into THH) and exponentially suppresses diamond dissolution rates, which infers that diamond preservation may not be controlled by the whole ascent history of kimberlites but latest emplacement conditions. We demonstrate that presence of circular pits on natural diamonds can be used as an indicator of silica-undersaturated aqueous fluid at P <2 GPa, and aqueous metasomatic fluid cannot create the mantle-derived resorption features recorded on diamonds from the central Slave craton, and suggest significant roles of CO_2 in mantle metasomatism.

4.8. ACKNOWLEDGMENTS

The authors acknowledge valuable discussions with L. Hilchie, and Dr. C.E. Manning and Dr. B. Watson. Dr. C. Shaw is thanked for providing the Pakistan olivine crystals, and Dr. A. Logvinova for providing micro-diamond stones for the experiments. This research was

supported by the Natural Sciences and Engineering Research Council of Canada (NSERC) and the Canadian Foundation for Innovation.

CHAPTER 5. P-X EFFECTS ON DIAMOND RESORPTION: EXPERIMENTAL CONSTRAINTS

5.1. PREFACE

This chapter presents the results of diamond dissolution experiments in C-O-H fluids with variable compositions designed to investigate P-x effects on diamond resorption. A version of this chapter "*Zhang, Z., Fedortchouk, Y., Hanley J. J. and Kerr, M. Diamond resorption morphology as a semi-quantitative fluid proxy: constrains from diamond dissolution in CO_2-H_2O mixture at 1-3 GPa and 1250 to 1350 ^oC*" is under preparation.

5.2. ABSTRACT

The ambiguous composition of C-O-H fluids in the mantle and kimberlites hamper our understanding of kimberlite formation, ascent, and emplacement at the Earth's surface and diamond preservation. Diamond resorption morphology is suggested to have a great potential for recording fluid compositions in diamond mantle reservoirs and kimberlites. In order to investigate the quantitative correlation between diamond resorption morphologies and fluid compositions, I conducted diamond dissolution experiments at 1-3 GPa and 1250 to 1350 ^oC in CO_2-H_2O fluids with variable molar fraction of CO_2 (X_{CO2} from 0 to 1). The composition of diamond-etching fluids was monitored with in-situ

entrapment of synthetic fluid inclusions in olivine and/or quartz. Co-existing H_2O- and CO_2-rich fluid inclusions at run conditions demonstrate a miscibility gap in the CO_2-H_2O-dominated system at 1250 ^oC under 1 and 3 GPa. The estimated compositions of aqueous and carbonic end members show that the miscibility gap contracts as P increases from 1 to 3 GPa.

Resorption features on oxidized diamonds semi-quantitatively correlate with bulk fluid composition. Increasing CO_2 in the C-O-H fluids and P suppresses diamond rounding rates. As X_{CO2} of the fluids increases, the assemblage of etch pits on {111} faces changes from negative trigons (X_{CO2}=0-0.5) to negative trigons coexisting with truncated negative trigons (X_{CO2}=0.6-0.9) to negative trigons coexisting with truncated negative trigons, hexagons, and truncated positive trigons (X_{CO2}=1). The evolutionary assemblages of etch pits on {111} faces and the correlation between diameters and depths of etch pits allow to propose that etch pits forms in a defect-initiated and condition-controlled kink mechanism. Four types of resorption morphologies on oxidized diamonds are identified: pure H_2O resorption morphology with diagnostic circular pits on resorbed THH faces, aqueous resorption morphology (e.g. ditrigonal {111} faces, negative trigons, and negative hillocks) at $Xco_2 \leq 0.5$, carbonic resorption morphology (e.g. trigonal {111} faces, truncated negative trigons) at X_{CO2} =0.50-0.9, and pure CO_2 resorption morphology (e.g. ditrigonal {111} faces, hexagon, and truncated positive trigons) in fluid with X_{CO2} =1.

Our experimental results demonstrate that diamond resorption morphology is a robust semi-quantitative proxy of diamond-etching fluids. Application to natural diamonds from three Ekati kimberlite pipes suggests that the pre-eruption kimberlite column had a gravity-induced "sandwich" structure beginning with a top CO_2–rich fluid zone, followed with an intermediate H_2O-rich fluid layer and a kimberlite magma tail, and that CO_2 fluids or carbonic melts have performed as metasomatic media in diamond mantle reservoirs.

5.3. INTRODUCTION

How to constrain the compositions of volatiles in lithospheric mantle during metasomatism and in kimberlites unambiguously and quantitatively is still a focus of worldwide research, because volatiles play significant roles in modification of the mantle composition, diamond formation and dissolution, and subsequent kimberlite formation, ascent, and emplacement to the Earth's surface (Wyllie, 1978; Taylor and Green, 1988; Gurney et al., 2004; Stachel and Luth, 2015). The identified agents in diamond-related metasomatism are carbonatite melts, C-O-H fluids, silicate melts, and brine based on geochemical signatures of garnet (Griffin et al., 1999a; Griffin et al., 2004; Stachel et al., 2004; Aulbach et al., 2007; Creighton et al., 2010; Aulbach et al., 2013), simulation of melts in equilibrium with garnet (Aulbach et al., 2013), and fluid inclusions in diamonds (Klein-BenDavid et al., 2004; Klein-BenDavid et al., 2007a). However, the compositions

of metasomatic media are still elusive and descriptive due to the limitations of conventional methods to isolate a single metasomatic event from periodic metasomatism. The high volatile content of kimberlites is evident from the high proportion of primary carbonate and phlogopite (Mitchell, 1991), the extraordinary ascent rates estimated for kimberlites (Canil and Fedortchouk, 1999), and explosive eruptions (Mitchell, 1991). Conventional methods (e.g. whole rock analysis), however, provide divergent estimates of kimberlitic volatiles. Both H_2O-rich (e.g. Kjarsgaard et al., 2009; Brett et al., 2015) and CO_2-rich (e.g. Price et al., 2000) kimberlites have been inferred, which complicates understanding of geology of kimberlites and their emplacement models (Lorenz, 1975; Skinner and Marsh, 2004; Sparks et al., 2006; Scott Smith, 2008; Skinner, 2008).

Most surface features observed on natural diamonds result from dissolution, based on morphological comparison between naturally and artificially etched diamonds (Frank and Puttick, 1958; Frank et al., 1958; Kozai and Arima, 2005; Fedortchouk et al., 2007; Khokhryakov and Pal'yanov, 2007; Arima and Kozai, 2008; Khokhryakov and Pal'yanov, 2010; Zhang et al., 2015). The experimental results of diamond dissolution suggest that resorption morphologies observed on natural diamonds formed before kimberlite eruption. At 100 kPa, appreciable diamond dissolution initiates at ≥ 600 ºC in oxygen (Evans and Phaal, 1962) and > 950 ºC in H_2O and CO_2 (Sauter, 1961), above olivine serpentinisation T ~ 400 to 600 °C (Evans, 2004). The high initiating T of dissolution indicates that

diamonds are inert in post-eruption hydrothermal events. At P ≤100 kPa, diamonds dissolved in H_2O and O_2 gases and molten kimberlites are graphitized and display negative trigons on rough and irregular {111} faces at T > 1000 ^oC (Frank and Puttick, 1958; Evans and Sauter, 1961; Harris and Vance, 1974). Although diamond dissolution studies at P = 0.00001 – 1 GPa are lacking, diamonds oxidized at P ≥ 1 GPa in C-O-H fluids, kimberlites, and H_2O-containing carbonate melts are graphite-free and display regular surface features (e.g., sharp trigons, striations, hillocks), (Kanda et al., 1977; Fedortchouk et al., 2007; Khokhryakov and Pal'yanov, 2007; Arima and Kozai, 2008; Khokhryakov and Pal'yanov, 2010; Zhang et al., 2015), similar to those observed on kimberlitic diamonds (Gurney et al., 2004; Fedortchouk and Zhang, 2011; Zhang and Fedortchouk, 2012).

Recent experimental studies suggest that diamond resorption morphology can fingerprint the composition of fluids in the latest diamond-dissolution event (Fedortchouk et al., 2007; Fedortchouk et al., 2010; Khokhryakov and Pal'yanov, 2010). Application to the Ekati diamonds (Canada) suggests that free H_2O-rich fluids coexisted with kimberlite magmas before eruption (Fedortchouk et al., 2010) and that carbonic melts or CO_2 fluids were involved during diamond-destroying mantle metasomatism (Zhang and Fedortchouk, 2012). The correlation between diamond resorption morphologies and fluid compositions, however, is still not well defined to provide quantitative constraints of fluid compositions, due to limited data of diamond dissolution in fluids with variable CO_2:H_2O ratios (X_{CO2} =

$CO_2/(CO_2+H_2O)$). Diamonds oxidized at 1 GPa in pure H_2O and CO_2 created distinct H_2O and CO_2 resorption morphologies respectively (Fedortchouk et al., 2007). Only one study investigated diamond dissolution in kimberlitic melts with initial bulk X_{CO2} = 0.24 - 0.77 at 1 GPa and 1420 ºC under the iron-wüstite oxygen buffer (Kozai and Arima, 2005). No variation of resorption features with variable X_{CO2} was reported and such reducing condition is far beyond the estimated range of f_{O2} in kimberlites (Fedortchouk and Canil, 2004; Canil and Bellis, 2007). The poorly known states of C-O-H fluids at high P and T conditions significantly obstructs our understanding of the roles of volatiles during mantle metasomatism. It is not clear if C-O-H fluid is miscible at high P and T (Manning et al., 2013) or immisicble. Studies of diamonds oxidized in volatile-bearing carbonate and silicate melts with X_{CO2} =0-1 at 5.7- 7.5 GPa and 1400-1750 ºC suggest that the boundary between H_2O- and carbonate resorption morphologies is at X_{CO2} = 0.65-0.70, although the presence of hexagons on {111} faces is assumed to occur when $X_{CO2} > 0.70$ (Khokhryakov and Pal'yanov, 2007, 2010).

In this contribution, we conducted diamond dissolution experiments in C-O-H fluids with X_{CO2} = 0 - 1. The diamond-etching fluids were in-situ monitored by synthetic fluid inclusions trapped at run conditions. The experimental results show the presence of the miscibility gap in the CO_2-H_2O-dominated system at run conditions and document the semi-quantitative correlation between fluid compositions and diamond resorption

morphologies, partially defined by quantitative measurements of etch pits using AFM. Application of diamond resorption morphologies to the natural Ekati diamonds shed more light on several important aspects of volatiles in diamond-bearing environments.

5.4. EXPERIMENTAL AND ANALYTICAL METHODS

All experiments were conducted at 1, 2, and 3 GPa and 1150 - 1350 ºC for 1 to 48 hours in an end-loaded piston-cylinder apparatus with a 12.7 mm NaCl + Pyrex assembly (Experimental Petrology Laboratory, Dalhousie University, Canada). Pressure was measured by a digital gauge with a precision better than 5%. The temperatures were measured and controlled with a Eurotherm controller using $W_{95}Re_5$-$W_{74}Re_{26}$ thermocouple without any correction for pressure on *emf*. The isothermal zone within the capsule is ±20 ºC. Thermocouple oxidation at 1 GPa is prevented by using N_2 flow in the run (Walter and Presnall, 1994). NaCl-Pyrex assembly imposes f_{O2} close to the values of the Ni-NiO (NNO) buffer system (details in Zhang et al., 2015), while diamond (carbon) reactions with C-O-H fluid buffers the system at CCO buffer. Our kinetic experiments do not reach equilibrium and have f_{O2} between NNO and CCO buffers (NNO to NNO -2.4, see also 4.2.1).

We used the simple synthetic system SiO_2±MgO±CaO±H_2O±CO_2 to examine the effect of X_{CO2} in C-H-O fluids on diamond resorption at different P. The compositions of the

diamond-etching fluids in the runs were monitored by trapping synthetic fluid inclusions (FI) in olivine or quartz chips at run conditions. The study used natural diamond crystals, chips of natural Pakistan olivine, and synthetic quartz, and reagent grade chemical powders (> 99% purity, Alfa Aesar; Table 5.1 and 5.2). Olivine and quartz chips were prefractured by quenching glowing chips into cold deionized water. The diamonds were < 1mm in diameter inclusion-free, natural, flat-faced octahedral stones from the Yakutian kimberlites with few or no dissolution features.

Table 5.1 Starting materials (mass ratio).

Term	$CaCO_3$	MgO	SiO_2	$C_2H_2O_4.2H_2O$	$C_2H_2O_4$
MSCH-1		36	22		42
MSCH-2		40	16	44	
CMS-1	38	16	46		
CS	38		63		
S			100		

Four starting mixtures provided C-H-O fluids with variable CO_2:H_2O ratios (Table 5.1). Mixture CS contained $CaCO_3$ and SiO_2 in mole ratio 1:1. At 1 GPa, 1250 ºC and 2 GPa, 1350 ºC, CO_2 was produced by the reaction $CaCO_3 + SiO_2 = CaSiO_3 + CO_2$ and $CaCO_3 + SiO_2$ = melt + CO_2 (Huang et al., 1980), respectively. At 2 GPa and 1350 ºC, we used three settings with the mixture CS: 1) runs with oxidized Ni foil inserted in the Pt capsule to control f_{O2}; 2) runs under the NNO buffer using the double capsule technique; 3) runs under the NaCl – Pyrex assembly buffer system. The three settings allow examination of

Table 1 Experimental conditions and results of diamond

Run	Diamond	Starting materials	XCO_2 [e]	Post-run phases	T (^{O}C)	P (GPa)	Time (min)	Initial weight(mg)	Weight lost (mg)	Preserved weight (wt%)	Area (mm^2)	Area weight loss (mg/mm^2)	Preserved {111} faces(%)	Dissolution rate ($(mg/mm^2*min^{-1})*10^3$)	Round rate	Max. a_{100} [f]
PC-101[a]	ALZ-4	CS+Qtz	1.00	Qtz, gl, fl	1350	2	60	1.14	0.05	96	2.59	0.019	94	0.32	0.01	0.75
PC-102[a,b]	ALZ-8	CS+Qtz	1.00	Qtz, gl, fl	1350	2	60	1.07	0.51	52	2.59	0.197	51	3.28	0.01	0.44
PC-106[c]	ALH-4	Mg(OH)2	0.00	Per, fl	1350	2	60	1.18	0.17	86	2.76	0.062	22	1.03	0.11	0.00
PC-108	ALZ-9	CS	1.00	Wo, fl	1150	1	2880	1.64	0.04	98	3.44	0.012	77	0.00	0.11	0.50
PC-124[a]	ALZ-SP-5	CS+Qtz	1.00	Qtz, gl, fl	1350	2	150	1.28	0.12	91	2.92	0.041	65	0.27	0.05	0.28
PC-125[a]	ALZ-SP-6	CS+Qtz	1.00	Qtz, gl, fl	1350	2	300	0.91	0.11	88	2.32	0.047	62	0.16	0.04	0.14
PC-135[a]	ALZ-10	(CMS-1)+Ol	1.00	Ol, Cpx, Grap	1250	1	300	1.25	0.00	100	2.87	0.000	100	0.00	-	-
P-297[d]	M-17	CS+Qtz	1.00	Wo,fl	1250	1	360	2.12	0.08	96	4.08	0.020	76	0.06	0.07	0.58
PC-136[a]	ALZ-SP-13	CS+H_2O+Qtz	0.90	Wo,Qtz, fl, gl(?)	1250	1	300	1.15	0.07	94	2.72	0.026	61	0.09	0.08	0.42
PC-138	ALZ-SP-14	CS+H_2O+Qtz+Ol	0.86	Wo,Qtz, fl	1250	1	300	0.64	0.07	89	1.84	0.038	62	0.13	0.04	0.21
PC-139	ALZ-SP-15	CS+H_2O+Qtz+Ol	0.52	Wo,Qtz, fl	1250	1	300	0.47	0.04	91	1.50	0.027	49	0.09	0.08	0.41
PC-140	ALZ-SP-16	CS+H_2O+Qtz+Ol	0.52	Wo,Qtz, fl	1250	1	300	0.57	0.06	89	1.70	0.035	60	0.12	0.05	0.15
PC-142	ALZ-SP-19	S+$C_2H_2O_4$+Qtz	0.67	Qtz,fl	1250	1	300	1.21	0.02	98	2.81	0.007	73	0.02	0.19	0.33
PC-142	ALZ-SP-20	S+$C_2H_2O_4$+Qtz	0.67	Qtz,fl	1250	1	300	0.53	0.01	98	1.62	0.006	84	0.02	0.09	-
PC-144	ALZ-SP-21	S+$C_2H_2O_4\cdot2H_2O$+Qtz	0.50	Qtz,fl	1250	1	300	0.34	0.03	93	1.19	0.021	60	0.07	0.07	0.00
PC-144	ALZ-SP-22	S+$C_2H_2O_4\cdot2H_2O$+Qtz	0.50	Qtz,fl	1250	1	300	1.36	0.02	98	3.03	0.008	70	0.03	0.19	0.00
PC-157[c]	ALZ33	MS30+Ol	0.00	Ol, Per, fl	1250	1	300	0.33	0.04	88	1.18	0.034	40	0.11	0.08	0.00
	ALZ34							0.60	0.07	88	1.76	0.040	50	0.13	0.06	0.00
PC-156	AZL-SP-31	MSCH-1+Ol	0.67	Ol, fl	1250	3	600	0.92	0.02	98	2.34	0.009	91	0.01	0.04	0.50
PC-156	ALZ-SP-32	MSCH-1+Ol	0.67	Ol, fl	1250	3	600	0.46	0.01	98	1.47	0.007	87	0.01	0.06	0.22
PC-158[a]	AZL-SP-35	MSCH-2+Ol	0.50	Ol, Per, fl	1250	3	720	0.56	0.02	96	1.68	0.012	89	0.02	0.03	0.00
PC-158[a]	ALZ-SP-36	MSCH-2+Ol	0.50	Ol, Per, fl	1250	3	720	0.72	0.01	99	1.99	0.005	93	0.01	0.05	0.00
PC-141[c]	ALZSP17	MS30+Ol	0.00	Ol, Per, fl	1250	3	600	0.77	0.03	96	2.08	0.014	53	0.02	0.16	0.00
	ALZSP18							0.49	0.03	94	1.54	0.02	54	0.03	0.10	0.00

a: graphitization; b: NNO buffered with oxidized nickel foil;

c: Fedortchouk et al. (2007); d:Zhang et al.(2015);

e: $X_{CO2}=CO_2/(CO_2+H_2O)$, mole fraction; f: $a_{100}=L_{100}/(L_{100}+L_{111})$;

Qtz: quartz; Wo: wollastonite; Ol: olivine; Per: periclase; fl: fluid; gl: glass;Grap: graphite

the Ni effect on diamond dissolution and the buffering capability of the NaCl-Pyrex assembly. The CMS mixture, comprising $CaCO_3$, MgO and SiO_2 in mole ratio 1:2:1, allowed us to preserve olivine. CO_2 was produced by the reaction $CaCO_3 + SiO_2 = CaSiO_3 + CO_2$ and deionized water was introduced with a micro-syringe. In the SiO_2 runs and the runs with MSCH mixtures consisting of SiO_2 and MgO (Table 5.1), CO_2 and H_2O introduced from anhydrous oxalic acid ($H_2C_2O_4$) and oxalic acid dihydrate ($H_2C_2O_4 \cdot 2H_2O$). Under the NNO buffer, $H_2C_2O_4$ and $H_2C_2O_4 \cdot 2H_2O$ decompose to major H_2O and CO_2 and minor H_2 and CH_4 (Holloway and Reese, 1974; McCubbin et al., 2014).

All starting materials were dried and kept at 110 ºC in the oven, except for oxalic acid and oxalic acid dihydrate, which were sealed and stored at room temperature. In each capsule, we placed one or two diamond crystals at the center, followed by a thin layer of starting powder and then olivine/quartz plates. Pt capsules using the "ash-can" design (Sneeringer and Watson, 1985) were welded shut using a Lampert PUK 3 welder in micro-mode. The Pt capsules with crushable MgO sleeves were inserted into the pressure assemblies and stored at 110 ºC in the oven for > 8 hrs. We followed the heating procedure described in Zhang et al. (2015), similar to steps recommended by Brooker (1998) to limit C mobility in the run duration.

The recovered capsules were cleaned in a dilute HCl bath and dried, weighed, and punctured when submerged under ethanol to observe release of gas bubbles in order to

confirm preservation of fluid during the runs. Recovered olivine and quartz fragments were separated from the experimental products, cleaned in the ethanol bath, and examined under an optical microscope to select chips with a high density of inclusions. Diameters of inclusions and vapor bubbles were measured using *ImageJ* software (1.5 % uncertainty). Olivine and quartz chips were mounted in epoxy, polished, and used for microthermometric analysis with a Linkam FTIR heating-freezing stage mounted on an Olympus BX51 microscope (Ore Fluids Laboratory, Saint Mary's University, Halifax, Canada). The stage was calibrated using synthetic fluid inclusion standards containing pure CO_2 (melting at -56.6 ºC) and pure, critical density H_2O (melting at 0 ºC and homogenizing at 374.1 ºC). The accuracy is ±3 ºC for temperatures recorded near the extremes of working conditions for the heating-freezing stage (-190 to 560 ºC).

Characterization of the species in synthetic inclusions was performed at 25ºC with Raman spectroscopy at Saint Mary's University using a HORIBA Jobin-Yvon LabRAM HR confocal Raman microscope equipped with a 70mW 532 nm diode laser as an excitation source, and a Synapse CCD detector (HORIBA Jobin-Yvon). Analyses were done using a 25 mm confocal hole diameter to maximize depth resolution. An 1800 grooves/mm grating was used for all analyses, yielding a spectral resolution of approximately ± 2 cm^{-1}. A 100× magnification Olympus MPlanN objective with ~0.21 mm working distance was used to minimize Raman scattering by atmospheric gases. Spectra were collected using an

accumulation time of 3 × 40s, with a laser spot size of ~1 mm at 100% laser power (using a neutral-density filter), collected in 4 windows over a spectral range from 150 - 4200 cm^{-1}. Semi-quantitative determination of the relative abundances of gas species (in mol%, Table 5.3) was done using the empirical quantification parameters and methodologies (Wopenka and Pasteris, 1987; Dubessy et al., 1989; Burke, 2001; Beeskow et al., 2005). Wavelength-dependent relative Raman scattering cross-sections (532 nm) for each gas species were determined by interpolation from Table 5.2 in Burke (2001). Instrument efficiencies (z) for CO_2 and CH_4 were determined by comparing microthermometrically-determined CO_2 and CH_4 contents with those determined by Raman spectroscopy for quartz-hosted CO_2-CH_4 standard inclusions from the South Wales Coal Field (Beeskow et al., 2005). Instrument efficiencies for other gas species were assumed to be 1, in the absence of standards, and may lead to slight overestimation of the mole fractions of H_2S, CO, N_2, and H_2.

Recovered diamond crystals were cleaned in ethanol using an ultrasonic bath and weighed to estimate the weight loss. For morphological comparison, all diamond faces were photographed under the reflected light microscope (at 100 × to 200 × magnification) and the remnant area of {111} faces was measured using ImageJ software. The diamonds were then cleaned in mixture of concentrated nitric acid and concentrated sulfuric acid (volume ratio 3:5) for mapping etch pits using a Bruker-Nano MultiMode 8 Atomic Force

Table 4.1 Summary of microthermometric data of synthetic fluid inclusions

Run	P (GPa)	X_{CO2} [a]	Host [b]	Type [c]	Size (um)	Phases (25°C)	Vol.% (No.) [d] Vapor	Liquid	T_{Carb} (°C)	T_{aq} (°C)	Number [e]	Mole fractions in gas bubble [f] CO_2	CH_4	CO	N_2	H_2S	H_2	number	X_{H2O} [g]	Bulk density (g/cm^3) [h]
PC-135	1	1	Ol	II	0.3-1.8	$L_{carb.}$	100 (3)	0												
PC-136	1	0.90	Qtz	I	0.7-3.8	$L_{carb}+L_{H2O}$	51.07 (1)	49	25			0.89	0.00	0.08	0.00	0.00	0.03	2	0.74	0.84
			Qtz	II		$L_{carb.}$	>95 (3)	<5				0.88	0.00	0.12	0.00	0.00	0.00	1		
PC-138	1	0.86	Qtz	I	3.4-5.1	$L_{carb}+L_{H2O}$	61.65 (2)	39	-8.9			0.91	0.00	0.09	0.00	0.00	0.00	2	0.60	0.95
			Qtz	II	1	$L_{carb.}$	>95 (7)	<5												
			Ol	II	1.3-4.9	$L_{carb.}$	>95 (8)	<5				0.97	0.00	0.03	0.00	0.00	0.00	4	0.11	0.94
PC-139	1	0.52	Qtz	I	1.3-3.5	$L_{carb}+L_{H2O}$						0.85	0.00	0.15	0.00	0.00	0.00	2	0.66	0.95
			Qtz	II		$L_{carb.}$	>95	<5												
			Ol	I	7.5-11.2	$L_{carb}+L_{H2O}$	54.9(2)													
			Ol	II	0.6-1.5	$L_{carb.}$	>95 (7)	<5	5			0.91	0.00	0.09	0.00	0.00	0.00	2	0.13	0.82
PC-140	1	0.52	Qtz	I	4.1-10.1	$L_{carb}+L_{H2O}$	43 (4)	57												
			Qtz	II		$L_{carb.}$	>95 (7)	<5												
			Ol	I		$L_{carb}+L_{H2O}$														
			Ol	II	1.2-6.8	$L_{carb.}$	>95 (15)	<5	14.1-8.7			0.97	0.00	0.03	0.00	0.00	0.00	2	0.13	0.83
PC-142	1	0.67	Qtz	I	6.3-30.6	$L_{carb}+L_{H2O}$	66.28 (7)	34				0.82	0.03	0.08	0.00	0.04	0.02	2	0.57	0.87
			Qtz	II	2.19	$L_{carb.}$	>95 (12)	<5				0.81	0.03	0.09	0.00	0.04	0.02	1	0.12	0.80
PC-144	1	0.50	Qtz	I	4-9.2	$L_{carb}+L_{H2O}$	66.78 (8)	33				0.76	0.03	0.15	0.00	0.00	0.06	2	0.54	0.90
			Qtz	II	1.2-2.7	$L_{carb.}$	>95 (3)	<5				0.77	0.02	0.15	0.00	0.00	0.05	1	0.11	0.85
PC-157	1	0.00	Ol	III	4-40	$L_{carb}+L_{H2O}$	30 (10)	70		376	9	0.00	0.24	0.05	0.02	0.00	0.68	2	0.53	0.97
PC-156	3	0.67	Ol	I	6.5-7.1	$L_{carb.}$	22 (4)	78												
			Ol	II	3.4-11.5	$L_{carb}+L_{H2O}$	>95 (10)	<5				0.98	0.01	0.01	0.00	0.00	0.00	2	0.13	0.84
PC-158	3	0.50	Ol	I	3.4-25.5	$L_{carb}+L_{H2O}$	18.8 (11)	81												

a: initial $X_{CO2}=CO_2/(CO_2+H_2O)$;

b: Qtz: quartz; Ol: olivine; c: type I = aqueous ; type II= carbonic;

d: Vapor (vol%) - average vapor proportions; No.= number of measuerd samples

e: the number of analyzed inclusions by microthermometry ;

f: data from laser Raman spectroscopy

g: X_{H2O}: bulk mole fraction of H_2O in inclusion;

h: Density at room temperture - measured density using measured isochore;

Microscope (AFM) equipped with a 125 um × 125 um × 5 um (in x, y and z dimension) J scanner in tapping mode under ambient conditions. AFM images were collected using Si_3N_4 tips (Bruker, tip model: TESP) with resonant frequency of 320 kHz at a slow scan rate (0.4 Hz) with 512 and 1024 sample lines. Etch-pit parameters (diameter, depth, wall angles, and profile configuration) were obtained using the section analysis of Nanoscope Software (V 8.10). At least ten representative trigons on each diamond were examined. The uncertainty is ≤1.5% for diameters and depths and ≤ 6% for the angle measurements. The details of the precision measurements are given by Zhang et al. (2015).

5.5. RESULTS

5.5.1. C-O-H Fluids in Experiments

In the runs, C-O-H fluids coexisted with the subsolidus matrix and quenched melts. All diamond stones were found at the middle of the capsules. Retention of fluids was confirmed by bubble release during piercing the capsules in the ethanol bath.

5.5.1.1. Immiscible C-O-H Fluids with the Subsolidus Matrix

At ~ 25 ^{o}C, most synthetic fluid inclusions trapped in olivine ± quartz (Table 5.3 and Figure 5.1) are clearly isolated and translucent with diameters of 2 - 40 um. The diameters of inclusions roughly decrease with increasing X_{CO2} in fluids. Inclusion shapes are dominantly rounded to sub-rounded (Figure 5.1b, d, l), commonly tube-shaped and

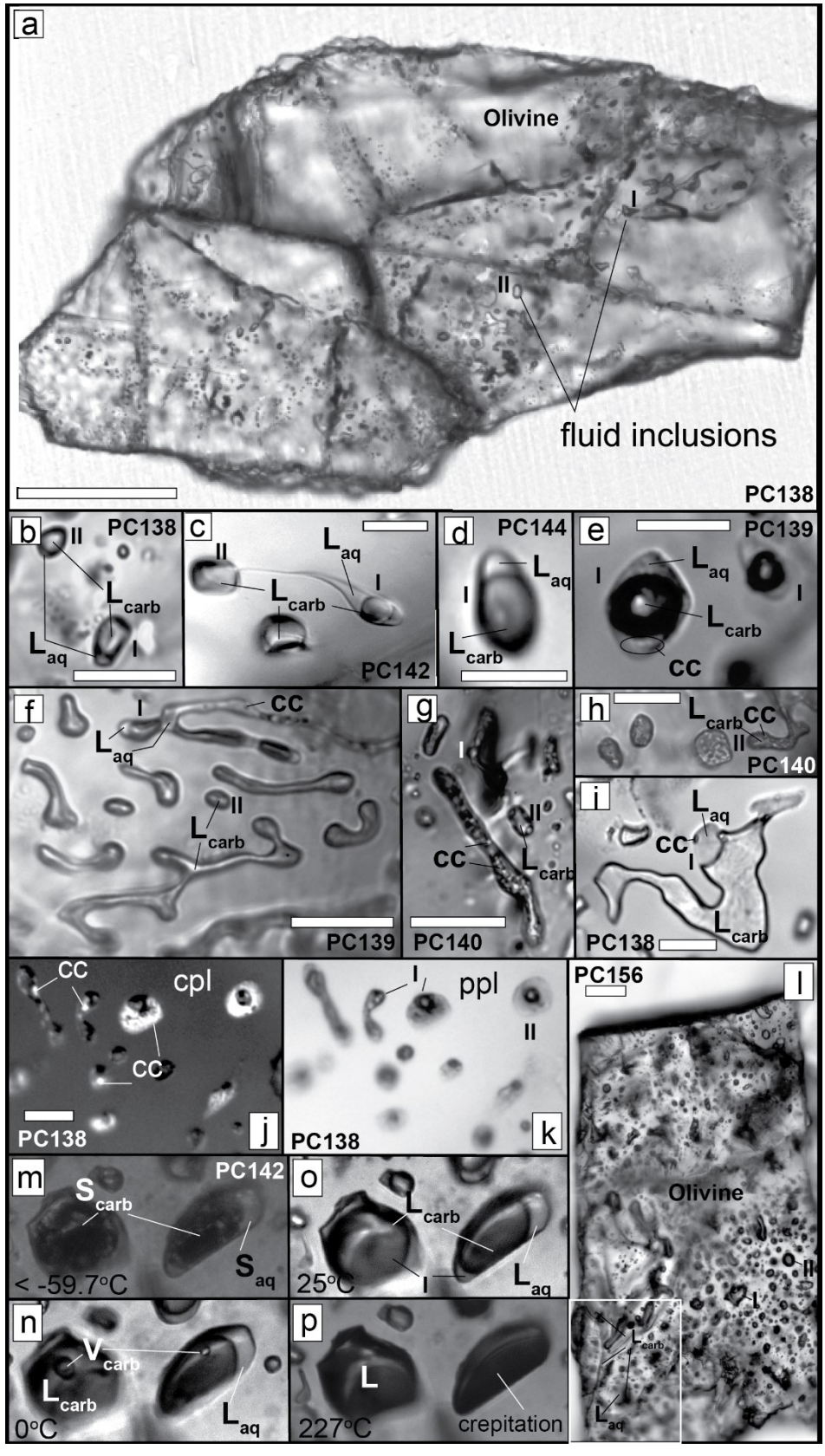
a
Olivine
I
II
fluid inclusions
PC138
b
PC138
II
L carb
L aq
I
c
II
L aq
L carb
I
PC142
d
PC144
L aq
I
L carb
e
PC139
L aq
I
I
L carb
CC
f
I
CC
L aq
II
L carb
PC139
g
I
II
CC
L carb
PC140
h
L carb
CC
II
PC140
i
L aq
CC
I
L carb
PC138
CC
cpl
CC
PC138
j
I
ppl
II
PC138
k
PC156
l
Olivine
II
I
m
PC142
S carb
S aq
< -59.7°C
o
L carb
25°C
I
L aq
n
V carb
L carb
L aq
0°C
p
L
227°C
crepitation
L carb
L aq

Figure 5.1 Photomicrographs of aqueous-carbonic synthetic fluid inclusions in olivine and quartz. All images taken in plane-polarized light (ppl) except (j) in cross-polarized light (cpl). White scale bars are 10 μm long, except for frame (a) which is 50 μm. Experiment number is indicated in each frame. All images were taken at 25°C except frames (m), (o), and (p). (a) Olivine fragment showing abundant trails of aqueous (Type I)-carbonic (Type II) inclusions within freshly precipitated olivine (dissolution-replacement channels). (b-d) Inclusions containing volumetrically dominant carbonic liquid phase (L_{carb}) and minor aqueous liquid phase (L_{aq}) trapped in quartz. Note the quenched necking-down trails in (c). (e) Two phase L_{carb}-L_{aq} inclusions in olivine; calcite (cc) daughter crystals cling to the carbonic fluid bubble. (f-i) assemblages of tube-shaped (texturally immature) to isometric L_{carb}-L_{aq} inclusions containing high relief calcite (cc) daughter crystals; note the high abundance of crystals in (g) and (h) indicating high carbonate solubility. (j-k) cross-polarized and plane-polarized light images showing an assemblage of inclusions containing abundant, high relief, and birefringent calcite crystals; (l) fragment of olivine inundated by aqueous-carbonic inclusions with a high CO_2:H_2O ratio, and the inserted image show two types of fluid inclusions. (m-p) inclusions showing different phases present during microthermometry experiments. I: Type I aqueous inclusions; II: Type II carbonic inclusions.

irregular (Figure 5.1f, g, i). Some inclusions show hourglass shapes, tracking the necking down processes; rare negative crystal shapes were also observed (Figure 5.1c, e, m). Fluid inclusions in host minerals randomly distributed in the host minerals.

Three types of fluids inclusions are recognized (Table 5.3). Aqueous fluid inclusions (Type I) are common and comprise both appreciable CO_2-(L_{carb}) and H_2O-rich (L_{aq}) liquid phases (Figure 5.1c, d, e, m). Abundant carbonic fluid inclusions (Type II) consist of predominant CO_2-rich (L_{carb}) (Figure 5.1a, b, l) and trace H_2O-rich liquid phases, detected by Raman spectroscopy, as films on inclusion walls. Aqueous fluid inclusions (Type III) in PC-157 display the vapor and liquid H_2O phases (Zhang et al., 2015). All runs have both Type I and II inclusions, expect PC-158 with Type II and PC-157 with Type III (Table 5.3). The proportions of the vapor/CO_2-rich phase to inclusion volume (P_{Vol}) of all types of fluid inclusions vary, except in PC-157 and PC-158, where P_{vol} is consistent and independent of inclusion sizes. It is worth noting that fluid inclusions from in runs with calcite always contain calcite as the daughter crystal, and phase ratios for calcite:fluid are highly variable, indicating that calcite was saturated in fluids at 1 GPa and 1250 ^oC and then precipitated during quenching.

The compositions of CO_2-rich or vapor phase in three types of fluid inclusions are listed in Table 5.3. Volatile species detected by Raman spectroscopy include H_2O, CO_2, CO, CH_4, H_2, and H_2S (Table 5.3, Figure 5.2). Sulfur is probably from sulfide inclusions in the

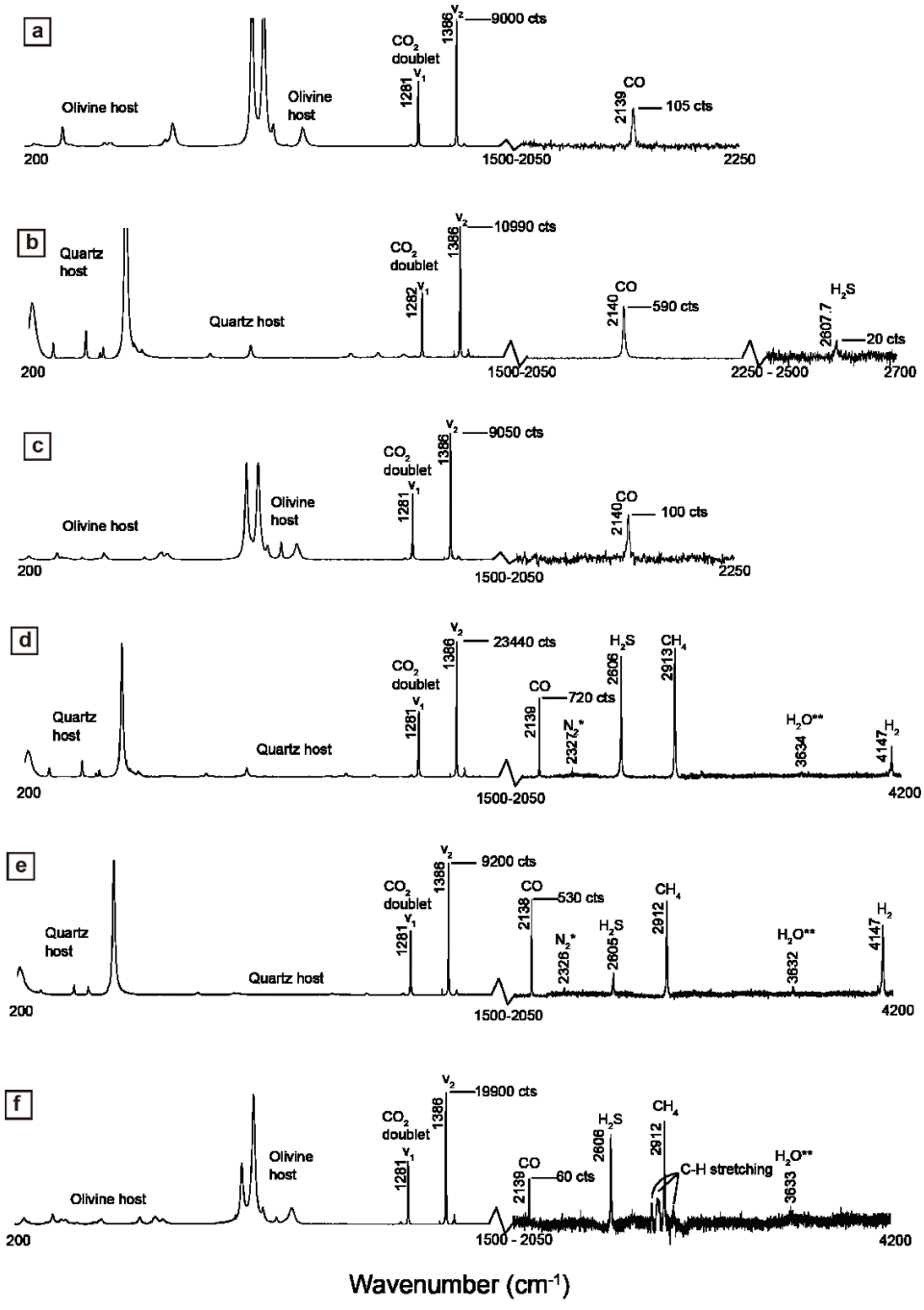

Figure 5.2 Representative laser Raman spectra (counts vs. wavenumber) of carbonic phases in synthetic fluid inclusions trapped in olivine and quartz for experimental run products: (a) PC138 (b) PC139; (c) PC140; (d) PC142; (e) PC144; (f) PC156. Reference spectral intensities are displayed for the CO_2 v2 band and for CO.

reactant diamonds. Fluid inclusions in calcite-bearing runs contain only H_2O, CO_2, trace CO, and rare H_2, while the other runs show appreciable amounts of CH_4, H_2, H_2S, and CO, indicating more reducing conditions than of calcite-bearing experiments.

Entrapment of immiscible aqueous and carbonic fluids in all runs (except for PC-157 and 158) was confirmed by petrography and microthermometry. The presence of immiscible fluids in one run is evident from the presence of both Type I and II fluid inclusions, variable P_{vol} of inclusions, and the hourglass shape formed by coupled Type I and II inclusions (Figure 5.1 c). The aqueous compositions of Type I fluid inclusions were confirmed by freezing at < - 59.7 ºC followed by melting of ice at ~ 0 ºC and homogenization of the aqueous and carbonic phases by dew point transition at T<230 ºC (Figure 5.1 m-p). The carbonic compositions of inclusions (Type II) were confirmed by freezing at < - 59.7 ºC, followed by two phases (V_{carb} + L_{carb}) and homogenization at T = 0 - 25 ºC (Figure 5.1 m-p). The compositions of Type III inclusions in PC-157 were H_2O with minor dissolved constituents, indicated by the final ice melting temperature between -3 and 0 ºC (Zhang et al., 2015). The homogenization temperatures of fluid inclusions in one run are variable, consistent with the presence of immiscible fluids at the run conditions.

5.5.1.2. Compositions of the Aqueous and Carbonic End Members

The compositions of the aqueous and carbonic end members in the immiscible CO_2-H_2O-dominated system at the run conditions were estimated based on the compositions of Type I and II inclusions. Only fluid inclusions with P_{Vol} identical to that of aqueous inclusions with necking-down trails and the most CO_2-rich inclusions were used to estimate the compositions of aqueous and carbonic end members respectively. The estimated bulk compositions of inclusions were calculated on the BULK program (Bakker, 2003) using non-aqueous compositions obtained by Raman spectroscopy on the carbonic/vapor phase, homogenization temperatures of the non-aqueous phase, and P_{Vol} of fluid inclusions (Figure 5.3). The average homogenization T for 3 - 9 inclusions and P_{Vol} introduce an uncertainty on the bulk fluid composition of ± 20%. Since only trace amounts of H_2S, H_2, CH_4 and CO were found in most runs (except PC-157), only H_2O and CO_2 contents in the immiscible aqueous and carbonic end members were estimated at 1250 ºC. At 1 GPa, the compositions of the aqueous and carbonic end member were estimated to be $(H_2O)_{0.38}(CO_2)_{0.62}$ and $(H_2O)_{0.12}(CO_2)_{0.88}$. Given the presence of the miscible fluids at 1 GPa at X_{CO2}=0.9, the carbonic end member is adjusted to be $(H_2O)_{0.10}(CO_2)_{0.90}$ within uncertainly. At 3 GPa, only Type II inclusions present in PC-158 with X_{CO2}=0.5 and both Type I and II in PC-156 with X_{CO2}=0.67 indicate that the composition of the aqueous end member is $(H_2O)_{0.5\text{-}0.67}(CO_2)_{0.5\text{-}0.33}$. Same as at 1 GPa, the estimated composition of

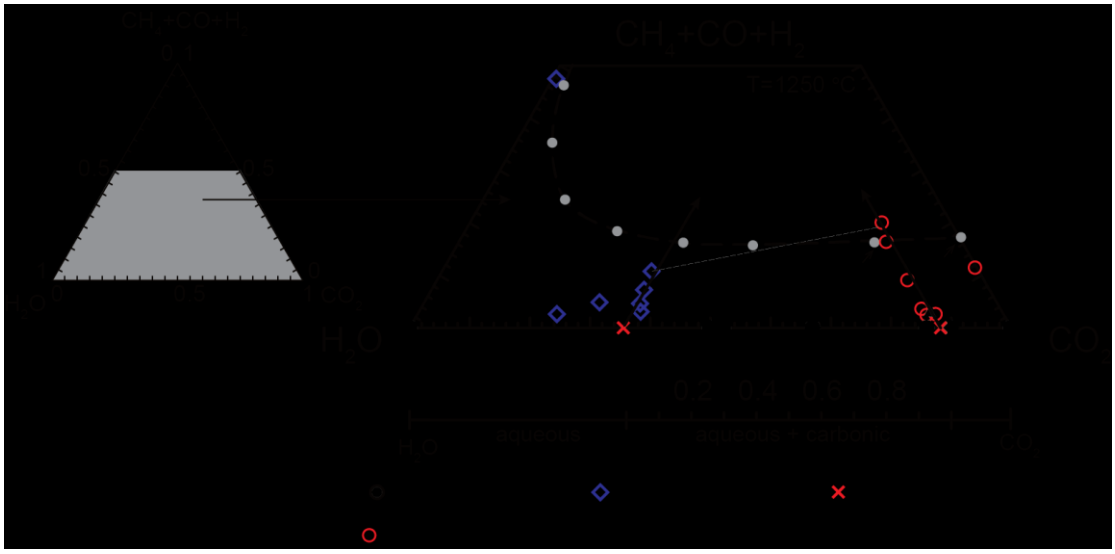

Figure 5.3 Bulk compositions and volume proportions of aqueous and carbonic synthetic fluid inclusions. The numbers on carbon saturation line (dash line) are values of oxygen fugacity relative to the nickel–nickel oxide buffer (NNO) calculated using '*Gfluids*' (Zhang and Duan, 2010) at 1 GPa and 1250 °C. The solid lines show compositional trends of the aqueous and carbonic end members; the dotted lines connect the compositions of the aqueous and carbonic fluid from the same two runs (PC-144, upper; PC-142, lower). V_{carb} = Volume of carbonic fluids; V_{aq} = Volume of aqueous fluids.

carbonic endmember in PC-156 is adjusted to be $(H_2O)_{0.10}(CO_2)_{0.90}$ (Figure 5.3). Some data from calcite-bearing runs are far away from the end member composition, possibly due to re-equilibration of FI containing daughter minerals (Cesare, 1995).

The compositions of aqueous (X_{CO2}=0.38) and carbonic (X_{CO2}=0.90) fluid inclusions allow to calculate their volume proportions $P_{carb/aq}= V_{carb}/ (V_{aq} + V_{carb})$ of end members at each bulk X_{CO2}. Given trace amounts of H_2S, H_2, CH_4 and CO present and small weight loss of diamonds in each run, the initial bulk C-O-H fluids were assumed to be fully converted into CO_2 and H_2O. Molar volumes of both aqueous and carbonic end members were computed using the program Loner H at 1 GPa and 1250 ºC (Holloway, 1981; Bakker et al., 2009). At 1 GPa and 1250 ºC, as X_{CO2} increases from 0 to 0.5 to 0.52 to 0.67 to 0.86 to 0.90, the $P_{carb/aq}$ increases from 0 to 0.20 to 0.24 to 0.52 to 0.95 to1.

5.5.1.3. Formation of Fluid Inclusions

All fluid inclusions in our runs were trapped at the run conditions. During the heating stage at 1 GPa, SiO_2 solubility in H_2O-CO_2 fluids increases continuously with increasing T (Newton and Manning, 2000). Increasing SiO_2 solubility in C-O-H fluids with increasing T at 3 GPa is evident from the decreasing sizes and vermicular surfaces of olivine or quartz chips, indicating the initial stage of dissolution. This precludes sealing fractures in the minerals during the heating stage by reprecipitation of quartz or olivine. The sluggish

healing rate of cracks in olivine (Tingle et al., 1992) excludes formation of negative crystallographic inclusions during quenching. Although the healing rate of cracks in quartz is fast and increases as P-T increases (Brantley et al., 1990), and decreases with increasing X_{CO2} in fluids (Brantley, 1992), preservation of the necking-down trails in quartz suggests that formation of fluid inclusions with negative crystallographic shapes requires longer time than the quenching period, indicating most fluid inclusions in quartz formed at run conditions.

It is generally recognized that entrapment of fluid inclusions in crystals involves dissolution and reprecipitation (Roedder, 1984; Sterner and Bodnar, 1989). In our runs, the aqueous fluid at any Xco_2 acted as a solvent for SiO_2 and MgO, which helped FI entrapment in host minerals. The role of aqueous fluids is supported by the higher densities of of FI in runs with lower Xco_2 (Table 5.3). The available aqueous fluid also permits the recrystallization of host minerals, which is required to yield negative crystal shapes of FI (Roedder, 1984). Similar to FI formation in the H_2O runs (Zhang et al., 2015), increasing CO_2 as a result of diamond oxidation in C-O-H fluids suppresses SiO_2 solubility, which assistants to approach equilibrium between dissolution and reprecipitation of the host minerals.

5.5.1.4. CO_2-saturated Melts

Mixture QS+Qtz produced the silicocarbonatitic melt at 2 GPa and 1350 ºC, close to the invariant point for the reaction of wollastonite + CO_2 = quartz + melt (Huang et al., 1980). All samples show coexisting melt, needle-shaped and euhedral juvenile quartz crystals, and voluminous bubbles in the quenched glass. The melt composition estimated from the phase diagram (Fig. 4B in Huang et al., 1980) is $Ca_{1.2}SiO_3(CO_3)_{0.2}$, which is CO_2 saturated (~ 6.5 wt%). No inclusions were observed in the juvenile quartz.

5.5.2. Diamond Dissolution

The general description of crystal forms and surface features resulting from resorption follows the terminology of Robinson (1979) and Zhang et al. (2015).

5.5.2.1. Diamond Dissolution Rates

Diamond dissolution rates at 1-3 GPa and 1150 – 1350 ºC were obtained by fitting a linear regression through the experimental data points and the coordinate origin (Figure 5.4). The main contribution to the uncertainty is the large uncertainty of diamond weight loss. In C-O-H fluids with the subsolidus phases, diamond dissolution rates are similar to those in pure H_2O within uncertainty (Figure 5.4 a-b). Dissolution rates within uncertainty are higher in calcite-bearing runs (Figure 5.4 a-b) than in $H_2C_2O_4$- and $H_2C_2O_4 \cdot 2H_2O$-bearing runs due to the higher f_{O2} in the calcite-bearing runs than that in the runs with more reduced

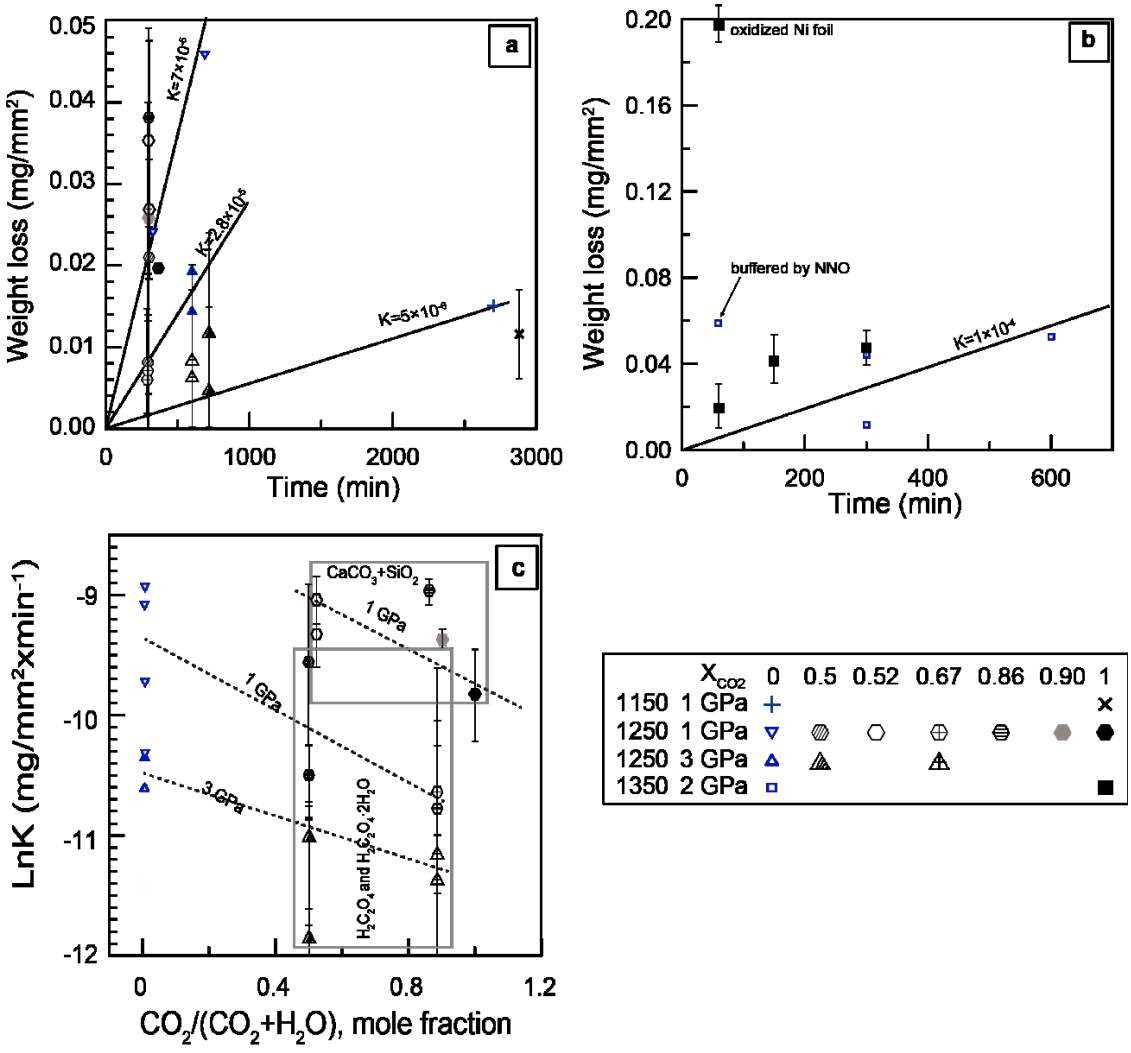

Figure 5.4 Diamond dissolution rates (K) calculated from diamond weight loss as a function of time in our experiments compared to the previous data in pure water: (a-b) at 1-3 GPa and 1150-1350 °C in volatiles with variable X_{CO2}; (c) the effect of intrinsic f_{O2}, buffered by coexisting volatiles species, on diamond dissolution rate.

oxalic acid, which is suggested by lower contents of reducing volatile species in the former runs than in the later runs (Table 5.3). The suppressing effect of increase X_{CO2} in the fluids on dissolution rates is within the uncertainty of the measurements and therefore needs further investigation (Figure 5.4 c).

Diamond dissolution rates in the CO_2-saturated silicocarbonatitic melts (PC-101/102/124/125) are comparable to those in the pure H_2O fluid (Figure 5.4 b), even though all diamonds showed variable degree of graphitization (Figure 5.5 a-b). Extremely high dissolution rates in the CO_2 runs, which used a partially oxidized Ni foil inserted inside the capsule (PC-102), is significantly over the rate of diamond dissolution under the NNO buffer (Figure 5.4 b), which indicates a significant catalytic effect of Ni on diamond dissolution rates. The catalytic effect of Ni on diamond dissolution is similar to Fe on diamond dissolution in kimberlite melts (Harris and Vance, 1974), and may be due to Ni as a C solvent (Kennedy and Kennedy, 1976).

All runs with the subsolidus matrix bore fluids at run conditions, confirmed by capsule puncturing, and show no signs of graphitization, except for PC-135, PC-136, and PC-158. Previous studies suggested that diamond surface graphitization results from fluid loss (Sonin et al., 2006; Fedortchouk et al., 2007; Zhang et al., 2015). In fluid-loss runs, graphite forms on the etched surfaces, suggesting a post-resorption formation, perhaps due to lowering f_{O2} when fluids lost, causing graphite epitaxial precipitation (Kurihara et al.,

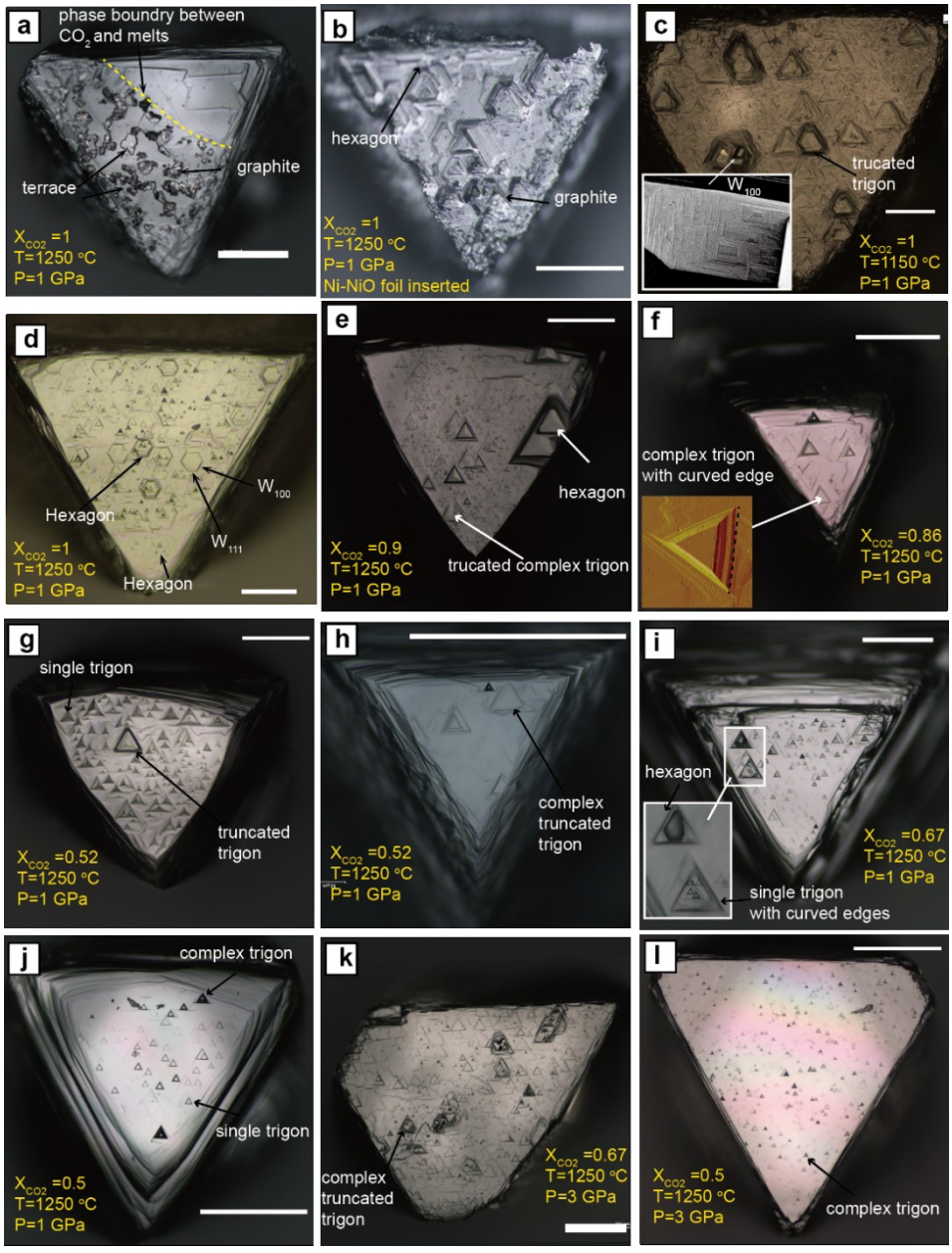

Figure 5.5 Microphotographs of diamond resorption morphologies produced at 1-3 GPa and 1150-1250 ºC in fluids with variable initial X_{CO2}. (a-b) two distinct diamond resorption morphologies created by immiscible silicocarbonatic melts and CO_2; (c-d) hexagonal pits with two types of walls (W_{100} and W_{111}) on diamond etched by CO_2 in crystalline phase ($CaSiO_3$), and W_{100} is identified due to the presence of tetragonal pits illustrated in the inserted image in (c); (e-l) diamond resorption morphologies at 1 and 3 GPa corresponding to variable X_{CO2}. Scale bar is equal to 200 µm.

1991). However, the diamonds in three fluid-bearing runs also displayed graphitization, indicating different mechanisms of graphitization. In PC-135 graphite was evenly distributed in the matrix, indicating f_{O2} buffering by the reaction $CaMg(CO_3)_2 + 2\ SiO_2 = CaMgSi_2O_6 + 2\ C + 2\ O_2$ (DQDG), similar to the buffering reaction at 5 GPa (Luth, 1993). In PC-136 and PC-158, graphite accumulated as thin layers at the bottom of the Pt capsules may due to graphite precipitation during quenching or at run because of a lower T at the capsule bottom. In the runs with the CO_2-satured silicocarbonatic melt (e.g. PC-125), graphite depositing on some areas of the diamond {111} faces prevented further oxidation (Figure 5.4b). The exact processes and mechanisms of diamond graphitization in the CO_2-saturated melts are unknown and need further investigation.

5.5.2.2. Transformation of the Diamond Forms

Diamonds transform from octahedra into tetrahexahedra (THH) during dissolution. Initially trigonal {111} faces develop ditrigonal outlines in H_2O-rich fluids or preserve in CO_2-rich fluids (Fedortchouk et al., 2007; Arima and Kozai, 2008; Zhang et al., 2015). The process of diamond rounding can be described as a relationship between the preservation of {111} faces and the weight loss (Figure 5.6). Since graphitization depresses the rounding rates (Fedortchouk et al., 2007), only diamonds from graphite-free runs were selected for estimation of diamond rounding rates. Despite of the significant uncertainty, increasing X_{CO2} and P do not seem to affect diamond rounding rates (Figure 5.6 a-b, Table

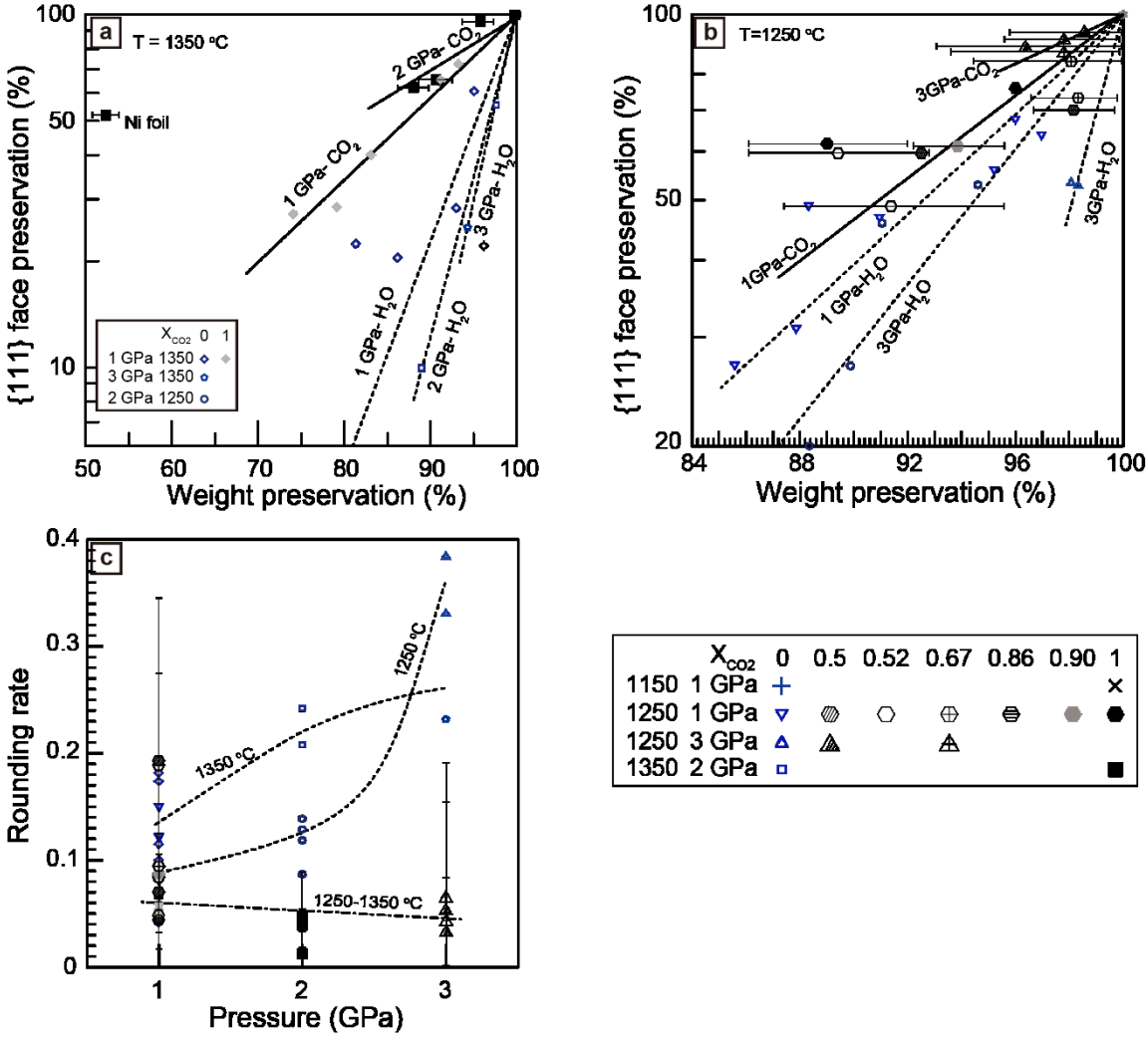

Figure 5.6 The rates of diamond rounding presented as preservation of {111} face vs. preservation of the initial diamond weight: (a) at 1350 ºC, (b) at 1250 ºC. (c) the opposite pressure effect on rounding rate in fluids with pure H_2O and with variable X_{CO2}. The dash-dot line displays a general trend of diamond rounding rates in CO_2-bearing runs from 1 to 3 GPa, and diamond rounding rates in two runs at 1250 ºC and 2 GPa also plot in the trend.

5.2), which requires more investigation in future. Interestingly, increasing P suppresses diamond rounding rates in CO_2-dominated fluids but advances diamond rounding in pure H_2O (Figure 5.6 c).

5.5.2.3. Surface Features on the Etched Diamonds

In addition to the crystal form transformation, the diamonds oxidized in the C-O-H fluids also display variable etch pits, striation, and negative hillocks (Figure 5.5). No correlation between diamond surface features and trace amounts of CH_4, H_2, H_2S, and CO is observed.

The outlines of the etch pits on oxidized diamonds are sensitive to bulk fluid composition and the volume proportion ($P_{carb/aq}$) of aqueous and carbonic fluids (Fig. 5.3). Based on the arrangement of C atoms on the walls of the etch pits, I introduce two new parameters: W_{111} characterizing a wall with three-bonded C atoms, and W_{100} defining a wall with two-bonded C atoms. The two types of walls are supported by the presence tetragons on W_{100} (inset, Figure 5.4 c), indicating a (100) face, and trigons on W_{111} (Robinson, 1979), indicating a (111) face. Negative trigons are bounded by three W_{111} walls, positive trigons by three W_{100} walls, and hexagons by both W_{111} and W_{100} in turn (Figure 5.4 d). To quantify the outlines of the etch pits on {111} faces and its correlation with the fluid compositions, a coefficient $a_{100} = L_{100}/(L_{100}+L_{111})$, where L_{100} and L_{111} are the lengths of W_{100} and W_{111} respectively can be introduced. Figure 5.7 shows the quantitative definitions of etch pits

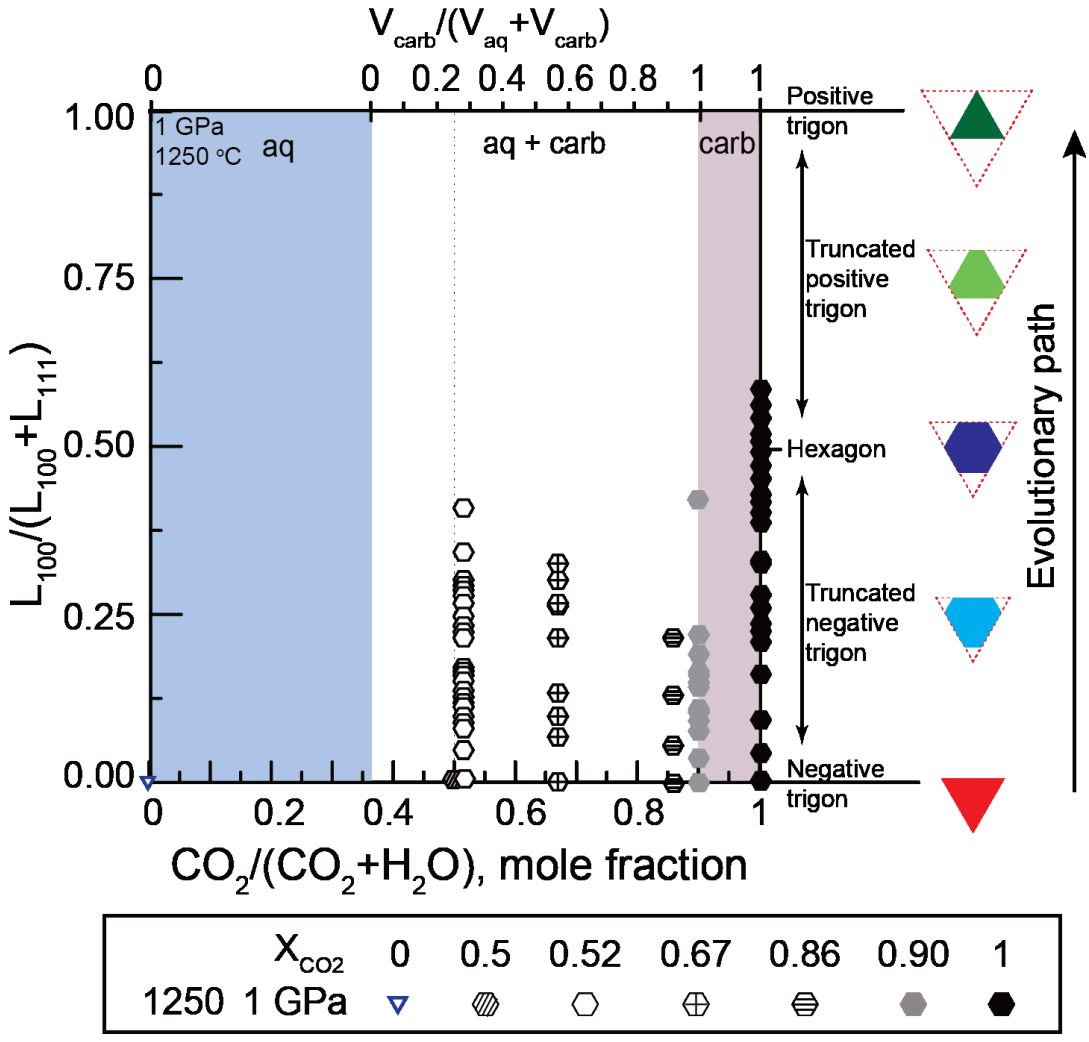

Figure 5.7 The relationship between bulk X_{CO2} and the maturity of etch pits on {111} faces. At the right side, the definition of etch pits (right) is based on $a_{100} = L_{100}/(L_{100}+L_{111})$, illustrated by the evolution etch pits as dissolution continues. Regular negative trigons have $a_{100} = 0$, truncated negative trigons have $0<a_{100}<0.5$; hexagons have $a_{100} = 0.5$; positive truncated trigons have $0.5<a_{100}<1$; and positive trigons have $a_{100} = 1$. The dotted line shows the boundary between aqueous and carbonic resorption morphologies.

on {111} faces based on the value of a_{100}. For example, negative trigons, hexagons, and positive trigons have a_{100} =1, 0.5, and 0 respectively. Figure 5.7 shows that: in H_2O-dominated fluids (X_{CO2} =0 - 0.5) etch pits developed on {111} faces are sharp, regular, negative trigons (a_{100} = 0); in CO_2-dominated fluids (X_{CO2} =0.5 – 0.9) etch pits include negative trigons and truncated negative trigons (continuous a_{100} with maximum value <0.5); in pure CO_2 fluids (X_{CO2} =1) etch pits include negative trigons, truncated negative trigons, hexagonal pits, and truncated positive trigons (continuous a_{100} with maximum value <0.7) (Figure 5.7). No correlation between outlines and diameters of etch pits is observed (Figure 5.8).

Quantitative AFM measurements of the etch pits allow further examination of the effect of fluid compositions on geometry and evolution of etch pits on {111} faces (Table F.1). In addition to the outlines of the etch pits observed under optical microscope, negative trigons with curved edges on diamonds oxidized in fluids with $X_{CO2} \geq 0.5$ are identified under AFM (Figure 5.8, Figure 5.9 a-e). Following the classification of trigons based on the configuration of their cross-section profiles (Zhang et al., 2015), we recognized trumpeted-and V-shaped p/b trigons, trapezoid- and trumpet-f/b trigons, and U-bottomed trigons (Figure 5.9 and 5.8 e-f). The U-bottomed trigons show many small steps on the walls and numerous small nesting p/b and f/b trigons at the bottom (Figure 5.9 e). Figure 5.9 summaries the diameters of trigons with distinct profiles on the diamonds oxidized in

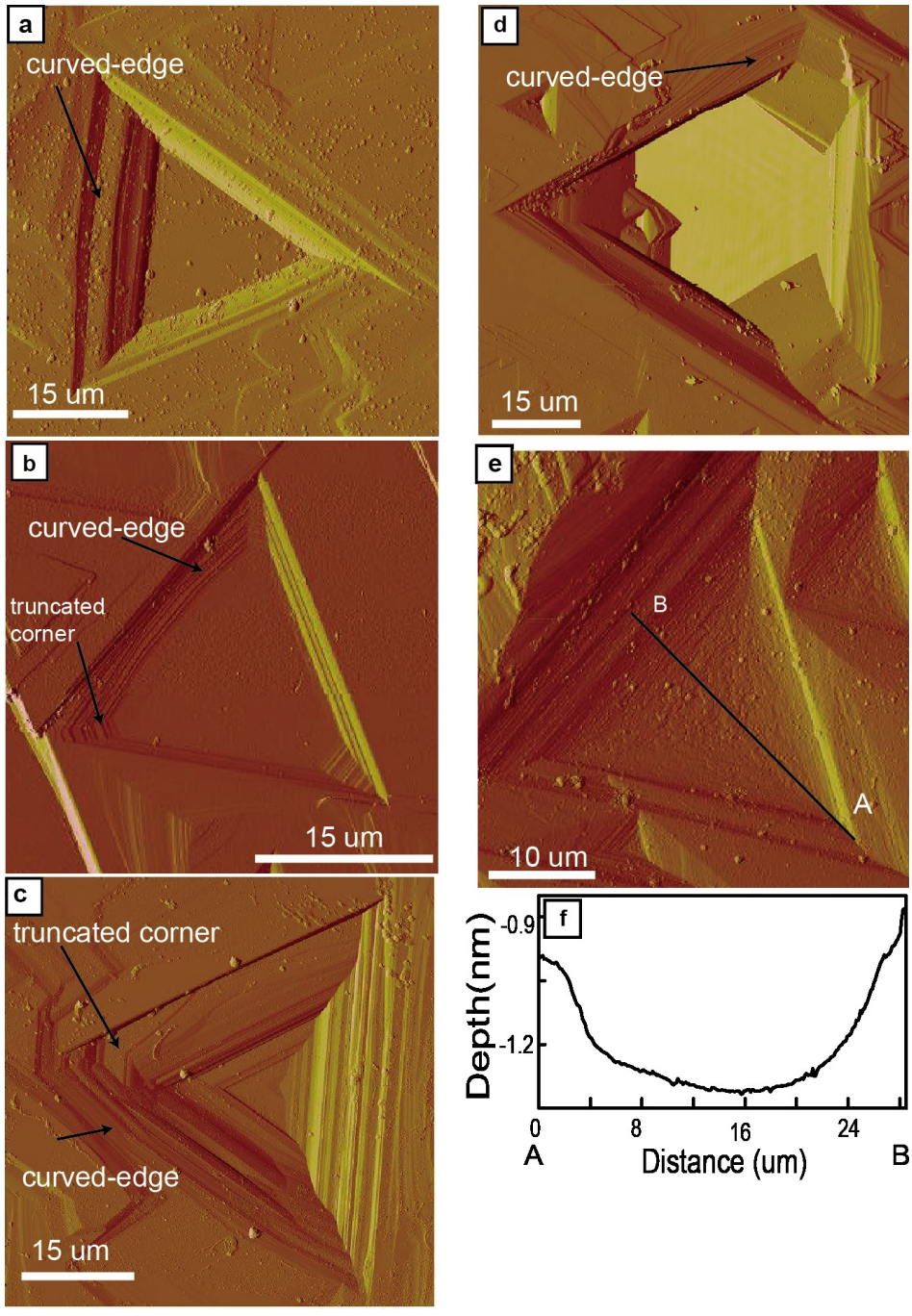

Figure 5.8 AFM images of characteristic etch pits forming on {111} faces in fluids with bulk $X_{CO2} > 0.5$. (a) flat-bottomed trigons with curved edges; (b-d) flat-bottomed trigons with curved edges and one to three truncated corners;(e-f) a U-bottomed trigon and its cross section (PC-136). Note the tiny steps on the walls and small etch pits at the bottom of the U-bottomed trigons.

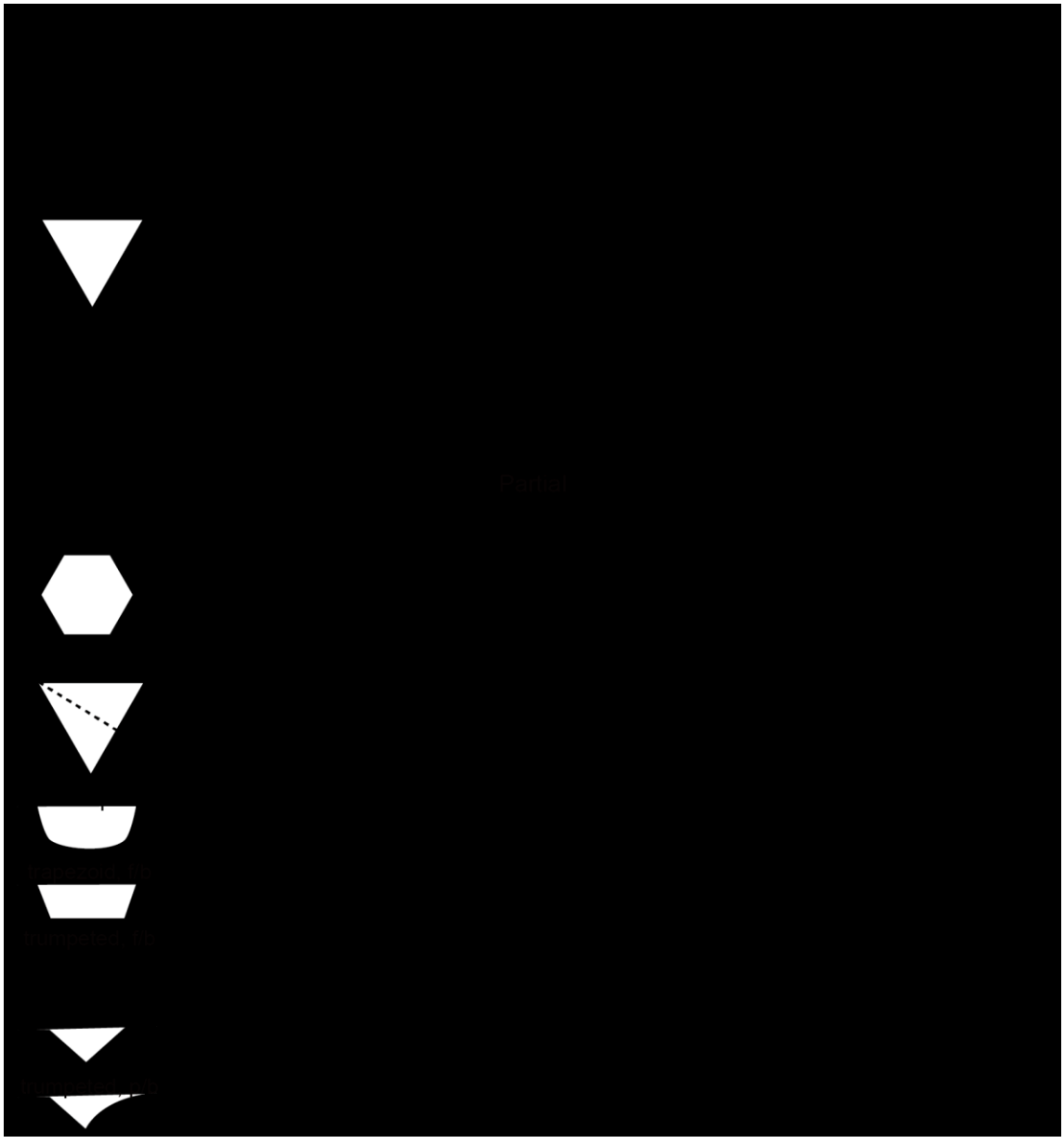

Figure 5.9 Diameter range (μm) of various types of etch pits on {111} faces created at 1-3 GPa and 1250 ºC and in diamond-etching fluids with variable bulk X_{CO2}. The range of diameters of etch pits is not continuous. For example, in the third row, the second column 2-73 means that the minimum and maximum diameter of trigons is 2 and 73 μm. "Partial" refers to only part of etch pits preserved. f/b: flat-bottomed; p/b: point-bottomed.

the C-O-H fluids.

The relationship between diameters and depths of the etch pits (Figure 5.10) shows that numerous p/b trigons (diameter < 15 um) and some f/b negative trigons cluster in the small diameter vs. depth corner (Figure 5.10a, b and d). The dominant f/b trigons have intermediate diameters and greater depths; the truncated trigons evolving into hexagons are widened at various depths (Figure 5.10). The increase in trigon dimensions corresponds to an evolution of the etch pits from p/b to f/b to truncated trigons to hexagons in CO_2 dominated system. In $CaCO_3$-bearing runs, a size limit line of etch pits can be drawn, defining the upper limit of depth for a given diameter of trigons, while this limit sector line is absent in $CaCO_3$-free runs (Figure 5.10 d-f). This may suggest a suppressing effect of calcite or f_{O2} on dissolution rates at defects in the normal direction of (111) faces during trigon enlargement.

Diamond oxidation in the C-O-H fluids produces four distinct resorption morphologies, correlating with the bulk fluid X_{CO2}.and the volume proportion of aqueous and carbonic fluids ($P_{carb/aq}$), summarized below.

Pure H_2O. The diamond oxidized in the pure H_2O system at 1 GPa and 1250 ºC displays glossy ditrigonal {111} faces, sharp and regular negative trigons, sheaf striations, negative hillocks parallel to <110>, and circular pits on the THH faces (Figure 4.4, Zhang et al.,

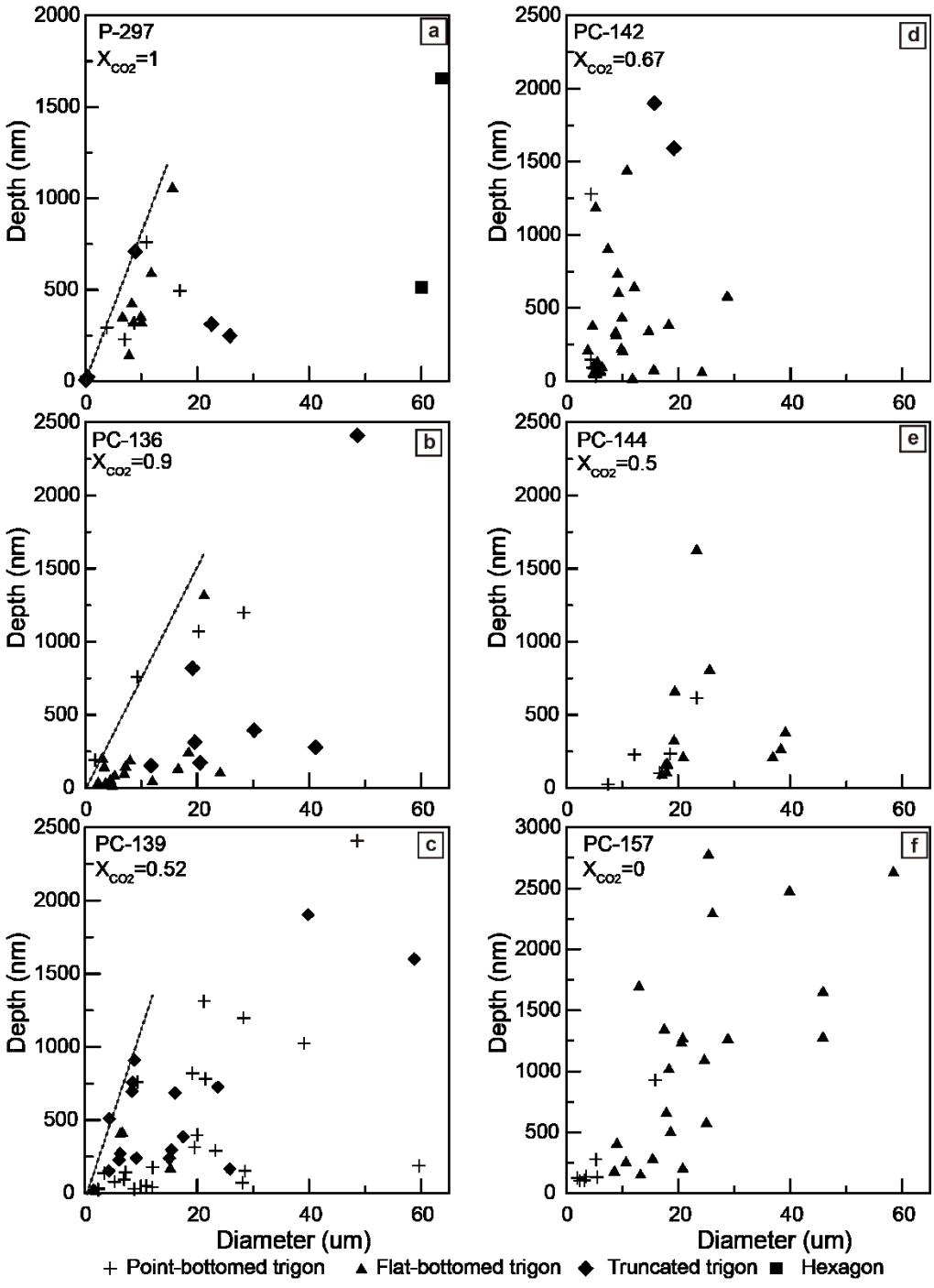

Figure 5.10 Correlation between depth and diameter of etch pits created at 1 GPa and 1250 ºC and in fluids with variable bulk X_{CO2} in selected runs. The dashed line repents the size limit line of etch pits, defining the upper limit of depth for a given diameter of trigons. (a-c) etch pits in $CaCO_3$-bearing runs with the limit sector line; (d-f) the absence of limit sector in $CaCO_3$-absent runs.

2015). Negative trigons with sharp corners (a_{100} = 0) are single (Figure 5.7 and 5.8) or complex due to coalescence of few pits and nesting trigons. The surface features are defined as the pure H_2O resorption morphology and the presence of circular pits on THH faces is a diagnostic feature.

Bulk X_{CO2} = 0.5 with $P_{carb/aq}$ = 0.20. The diamonds etched in the C-O-H fluid with X_{CO2}=0.5 at 1-3 GPa and 1250 ºC display glossy ditrigonal {111} faces, sharp and regular negative trigons, U-bottomed negation trigons, sheaf striations, and negative hillocks parallel to <110> (Figure 5.4 i-j, 5.7 and 5.8), although both aqueous and carbonic fluids coexist in the capsule ($P_{carb/aq}$ = 0.20). No circular pits were observed on the THH faces at 1 GPa (Figure 5.4 i-j). This resorption morphology is referred to as the aqueous resorption morphology.

Bulk X_{CO2} = 0.5-0.52 with $P_{carb/aq}$ = 0.20 - 0.24. At X_{CO2} = 0.52, where $P_{carb/aq}$ increases to 0.24, the etched diamonds at1 GPa and 1250 ºC show trigonal {111} faces, regular negative trigons, truncated negative trigons, negative hillocks, and thick striations (Figure 5.4 g-h, 5.7 and 5.8). The a_{100} of etch pits is continuous and ranges from 0 to 0.41 (ALZ-SP-15) and 0.15 (ALZ-SP-16) (Table 5.2, Figure 5.7). The diamond ALZ-SP-15 exhibits ragged (110) edges and rough surfaces due to numerous irregular etch pits, and some edges of the diamond ALZ-SP-16 are jagged due to trigons truncated on resorbed edges (Figure 5.4 h). The resorption morphology at X_{CO2}=0.52 is named as the carbonic resorption

morphology by showing distinct outlines of resorbed {111} faces and types of etch pits from the aqueous resorption morphology at X_{CO2}=0.5 (Figure 5.4 i-j). The boundary between the aqueous and carbonic resorption morphology at X_{CO2} = 0.5-0.52 rather than at X_{CO2} = 0.38, the aqueous fluid end member, indicates the controlling effect of both fluid compositions and volume proportions of aqueous and carbonic fluids on resorption morphologies.

Bulk X_{CO2} = 0.67-0.9 with $P_{carb/aq}$ from 0.52 to 1. In the C-O-H fluids with X_{CO2}=0.67-0.9, the oxidized diamonds display the carbonic resorption morphology (Figure 5.4 d, e, h and Figure 5.8). The a_{100} of the etch pits varies from 0 to the maximum value (<0.5) (Figure 5.7). In PC-142, the diamond ALZ-19 shows the carbonic resorption morphology, while the diamond ALZ-20 displays the aqueous resorption morphology (Table F.1). The presence of two distinct types of resorption morphology in one run indicates either two different diamonds or heterogeneous distribution of aqueous and carbonic fluids. At X_{CO2} = 0.86, the diamond shows trigons with curved edges and preserved corners of the earlier truncated trigons (Figure 5.4 f, Figure 5.8).

Pure CO_2. In the pure CO_2 fluid, the etched diamond displays trigonal {111} faces with negative trigons, truncated negative trigons, hexagons, and truncated positive trigons (Figure 5.4d, 5.7 and 5.8), named the CO_2 resorption morphology. The continuous a_{100} ranges from 0 to the maximum value (≥0.5) (Figure 5.7). The CO_2-resorption features at 1

GPa are comparable to those on diamond resorbed in CO_2-bearing synthetic kimberlite at 1500 ºC and 2.5 GPa (Arima and Kozai, 2008).

Diamonds oxidized in the free CO_2-bearing silicocarbonatic melt at 2 GPa and 1350 ºC show two resorption morphologies on one diamond: smooth and pitted surfaces, and terrace-bearing surfaces partially covered with graphite (Figure 5.4 a). This differs from the homogeneous resorption morphology of diamonds dissolved in CO_2-containing carbonate and kimberlite melts at 5.7-7.5 GPa and 1400-1750 ºC (Khokhryakov and Pal'yanov, 2007, 2010) and in free CO_2-bearing synthetic kimberlite melts at 2.5 GPa and 1500 ºC (Arima and Kozai, 2008). One octahedral face of the diamond ALZ-SP-6 (PC-125) shows both resorption styles separated by a curved line (Figure 5.4 a). The pitted and smooth domain shows typical CO_2-resorption features (trigonal {111} faces, truncated trigons, Figure 5.4 a), and the terrace-bearing domain shows selective etching on graphite-free areas (Figure 5.4a). This indicates that a CO_2 bubble attached to the diamond surface resulted in the pitted and smooth resorption feature, and the rest part in contact with melts developed the terrace-bearing resorption morphology.

5.6. DISCUSSION

5.6.1. Immiscibility of the C-O-H System

The mutual solubility of CO_2 and H_2O is restricted due to substantial dissimilarity in polarity between CO_2 (non-polar) and H_2O (polar), and depends on P, T and X_{CO2} (Diamond, 2003). The binary CO_2-H_2O system at T over the critical point of H_2O (374 ºC) is assumed to be completely miscible in natural geological settings (Manning et al., 2013) and modeling of volatiles under the mantle conditions (Zhang and Duan, 2010). However, our knowledge of the binary CO_2-H_2O system at high P and T is mainly based on experiments at low P (<1 GPa) and low T (<1100 ºC) (Zhang and Duan, 2010 and references therein). So far, the binary system at 1-2 GPa was only investigated in two experimental studies. The C-O-H fluids with X_{CO2} = 0 - 0.86 are assumed to be miscible at 1 GPa and 950 - 1150 ºC (Watson and Brenan, 1987). The presence of only one type of synthetic fluid inclusions in olivine suggests miscible CO_2-H_2O fluids with X_{CO2} = 0.2 - 0.8 at 0.95 GPa and 1200 ºC, and miscible fluids with X_{CO2} < 0.5 at 1.45 – 1.94 GPa and 1100 - 1400 ºC (Frost and Wood, 1997).

Our experimental study demonstrates a miscibility gap present in the CO_2-H_2O-dominated system at 1 -3 GPa and 1250 ºC (Figure 5.11). This is evident from entrapment of both aqueous and carbonic fluid inclusions in olivine and quartz (Figure 5.1 b), hourglass-shape

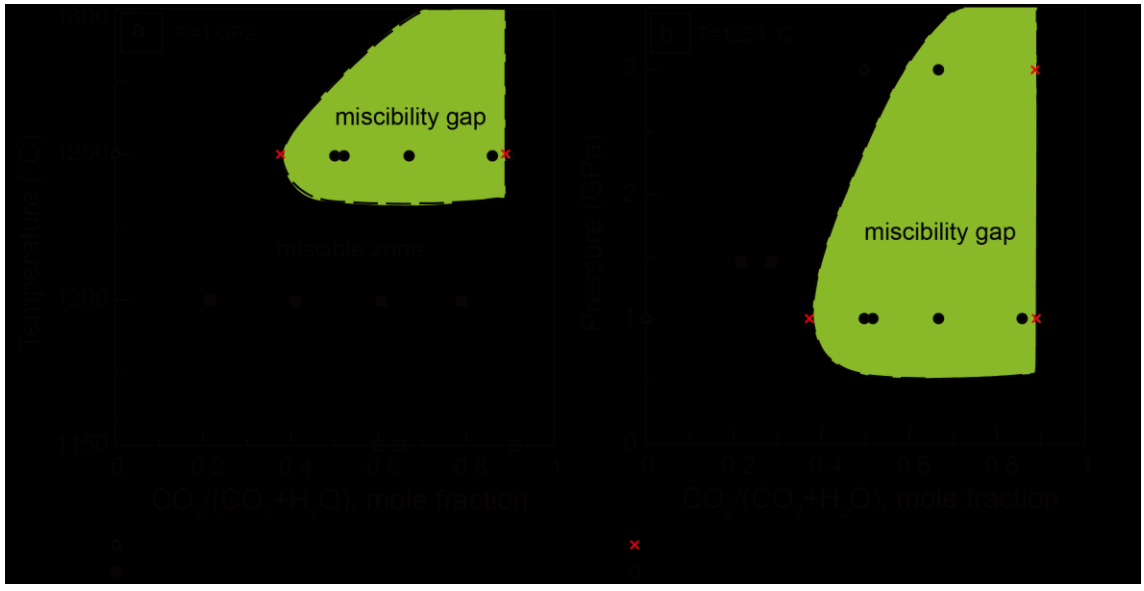

Figure 5.11 P-T effect on the miscibility gap in the binary CO_2-H_2O system. Laq: aqueous liquid; Lcarb: carbonic fluid.

created by coupled aqueous and carbonic fluid inclusions (Figure 5.1 c), variable P_{vol} of fluid inclusions in one run (Table 5.3), and inconsistent homogenization T of fluid inclusions in one run (Table 5.3). The compositions of the coexisting phases derived from the bulk compositions of fluids inclusions are $(H_2O)_{0.62}$ $(CO_2)_{0.38}$ and $(H_2O)_{0.10}$ $(CO_2)_{0.90,}$ at 1 GPa and are $(H_2O)_{0.5\text{-}0.67}$ $(CO_2)_{0.5\text{-}0.33}$ and $(H_2O)_{0.10}(CO_2)_{0.90}$ at 3 GPa (Figure 5.3). The estimated compositions of aqueous and carbonic end members allow to roughly define the miscibility gap in the binary H_2O-CO_2 system (Figure 5.11 a-b). At 1250 ^oC, the immiscible fluids coexist over a wide range of P–X conditions, but with increasing P the miscibility gap contracts due to enlargement of the aqueous field at high P (Figure 5.11 b). Comparison of our experimental data at 1 GPa with the previous work (Watson and Brenan, 1987; Frost and Wood, 1997), the boundary of the miscibility gap is close to 1 GPa and 1250^{o}C at X_{CO2} = ~ 0.4.

5.6.2. Diamond Resorption Morphology as a Semi-quantitative Fluid Proxy

Comparing the conditions of diamond dissolution experiments with those of diamond-bearing environments suggests that the compositions of C-O-H fluids control resorption morphologies on natural diamonds. Factors affecting diamond resorption morphologies, P-T-f_{O2} -X, have been experimentally investigated (Yamaoka et al., 1980; Kozai and Arima, 2005; Sonin et al., 2006; Fedortchouk et al., 2007; Khokhryakov and Pal'yanov, 2007; Arima and Kozai, 2008; Khokhryakov and Pal'yanov, 2010; Zhang et al., 2015).

Figure 5.11a summarizes resorption features on diamonds oxidized in H_2O-rich systems. In the lithospheric mantle, diamonds are stable at T = 900 – 1400 ºC, P = 4 to 7 GPa, and f_{O2} at NNO-5 to NNO-1 (Dasgupta and Hirschmann, 2010; Stagno et al., 2013; Stachel and Luth, 2015). Kimberlites are believed to form at 1450 ºC (Kavanagh and Sparks, 2009) and their average crystallization T is ~ 1030 ºC estimated by the olivine-spinel thermometry (Fedortchouk and Canil, 2004). The f_{O2} of the Ekati kimberlites constrained by the olivine-spinel oxygen barometry ranges from NNO-2 to NNO-4 (Fedortchouk and Canil, 2004). For the conditions estimated for natural diamond-bearing environments, only negative trigons are expected in H_2O-rich systems (Figure 5.12a). The variable resorption morphologies observed on the Ekati diamonds (Zhang and Fedortchouk, 2012) require variable compositions of diamond-etching fluids. This is supported by formation of distinct resorption features in pure H_2O and CO_2 at 1 GPa (Fedortchouk et al., 2007) and in CO_2 - and H_2O- containing melts (Khokhryakov and Pal'yanov, 2007; Arima and Kozai, 2008; Khokhryakov and Pal'yanov, 2010), summarized in Figure 5.12b. The relationship between diamond resorption morphology and fluid composition has been used to constraint the presence and composition of fluids in kimberlites (Fedortchouk et al., 2007; Fedortchouk et al., 2010; Khokhryakov and Pal'yanov, 2010; Zhang and Fedortchouk, 2012). It is, therefore, important to constrain the quantitative correlation between diamond resorption morphology and the composition of diamond-etching fluids.

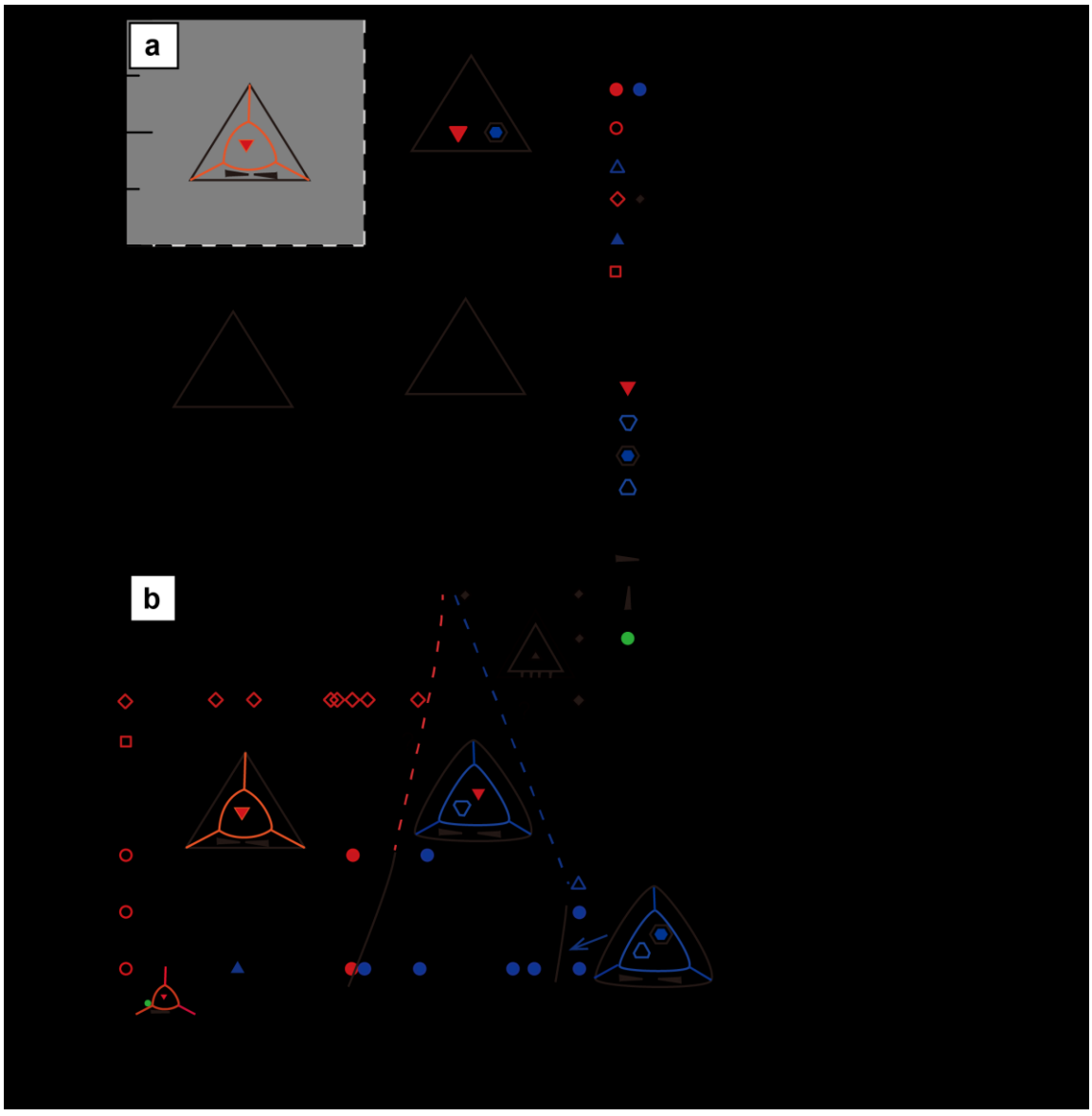

Figure 5.12 Formation condition of diamond resorption morphologies. (a) T-f_{O2} effects on diamond resorption morphologies (P =0.0001 to 5.7 GPa). The shaded area represents the common T-f_{O2} conditions of diamond-bearing environments (Fedortchouk and Canil, 2004; Stachel and Luth, 2015); (b) The P-X conditions of pure H_2O, aqueous, carbonic, and pure CO_2-carbonate resorption morphologies (f_{O2} = NNO - 4 to NNO + 0.4, T > 1100 ^{o}C). Note the positive of hillocks on diamonds etched in carbonate melts at 5.7-7.5 GPa.

This experimental study documents a semi-quantitative correlation between diamond resorption morphologies and the compositions of C-O-H fluids. Combing with previous studies, I define pure H_2O, aqueous, carbonic, and CO_2-carbonate resorption morphologies (Figure 5.12).

Pure H_2O resorption morphology

The experimental results demonstrate that the presence of circular pits on newly created THH faces is the diagnostic feature of pure H_2O resorption morphology (Figure 5.12b), in addition to ditrigonal {111} faces, negative trigons, sheaf striations, and hillocks (Zhang et al., 2015). Circular pits on natural diamonds are proposed to be after the formation of main resorption features (e.g., trigons) and result from dissolution by the CO_2 bubbles attached to resorbed diamonds (Robinson, 1979; Tappert and Tappert, 2011; Nicolas, 2014). The circular pits coexisting with the main resorption features in pure H_2O systems at $P \leq 1$ GPa (Zhang et al., 2015) and absence of circular pits in immiscible H_2O-CO_2 fluids at 1 GPa confirm that circular pits are the unique feature of pure H_2O resorption morphology at shallow depth (<~ 30 Km).

Aqueous resorption morphology

My study shows that, at $X_{CO2} \leq 0.5$, 1 GPa and 1250 ºC, the aqueous resorption morphology is distinguishable from the pure H_2O resorption morphology by the absence of circular pits (Figure 5.12 b). At $X_{CO2} = 0.5$, U-bottomed trigons occur at 1 GPa, which

is not observed on diamonds oxidized in the pure H_2O fluids (Figure 5.8). The boundary between pure H_2O and aqueous resorption morphology is defined by the forming condition of circular pits on THH faces. The development of the aqueous resorption morphology rather than the carbonic resorption morphology at bulk $X_{CO2} = 0.5$ indicates that the high volume proportion of the aqueous fluid ($P_{carb/aq}$) in the immiscible CO_2-H_2O system controls resorption. The boundary between the aqueous and carbonic resorption morphologies marks the conditions of preserving trigonal {111} face and formation of truncated negative trigons. Volatile-undersaturated carbonate and kimberlite melts at 5.7-7.5 GPa (Khokhryakov and Pal'yanov, 2007, 2010) and Wesselton kimberlite melt with undefined composition of C-O-H fluid at 1 GPa (Kozai and Arima, 2005) create resorption features on diamonds similar to those etched in the aqueous fluids, indicating that aqueous resorption morphology can occur in a wide range of P-T-f_{O2}-X conditions (Figure 5.12 b). The extrapolation of the boundary between the aqueous and carbonic resorption morphologies from 3 GPa to 7.5 GPa shows that X_{CO2} of the bulk diamond-etching media increases from 0.5-0.52 at 1 GPa to 0.5-0.67 at 3 GPa and 0.65 – 0.7 at 5.7-7 GPa (Figure 5.12 b), perhaps due to the increase of CO_2 component in aqueous fluids (Figure 5.11) and the corresponding increase in the volume proportion of aqueous fluids with pressure.

Carbonic resorption morphology

This experimental study shows that diamonds oxidized at X_{CO2}=0.5 – 0.9 under 1 GPa, and 1250 ºC display the carbonic resorption morphology, including characteristic trigonal {111} faces and truncated negative trigons (Figure 5.7, 5.9, and 5.12 b). The boundary between carbonic and CO_2-carbonate resorption morphologies is marked by the presence of hexagons, forming at X_{CO2} = 0.9-1.0 at 1-2.5 GPa. Extrapolation the boundary to P = 5.7-7 GPa (Khokhryakov and Pal'yanov, 2010) seems to be inappropriate due to the presence of positive hillocks at 5.7-7 GPa instead of negative hillocks at 1-2.5 GPa (Figure 5.12). The identical carbonic resorption morphologies on diamonds oxidized in fluids with X_{CO2} = 0.52 - 0.9 at 1 GPa and 1250 ºC support similar compositions of carbonic diamond-etching fluids. The presence of carbonic resorption morphologies on diamond oxidized in fluids with bulk X_{CO2} = 0.52 ($P_{carb/aq}$ =0.24) rather than 0.66 ($P_{carb/aq}$ =0.50) indicates that the wetting angle of carbonic $(H_2O)_{0.10}$ $(CO_2)_{0.90}$ fluid is smaller than that of aqueous $(H_2O)_{0.62}$ $(CO_2)_{0.38}$ fluid on diamond surface. My finding is in agreement with smaller wetting angle of non-polar liquids on hydrophobic diamond surface (Hansen et al., 1989; Ostrovskaya et al., 2002).

Pure CO_2 or carbonate melt resorption morphology

The pure CO_2 resorption morphology is different from the carbonic resorption morphology by characteristic truncated positive trigons and even positive trigons (Figure 5.7 and 5.12

b). The presence of pure CO_2 in peridotite is non-realistic due to the reaction between CO_2 and olivine under normal mantle conditions (Newton and Sharp, 1975). Therefore, the CO_2-bearing metasomatic media in peridotite are probably carbonate melts. It is worth to notice that diamonds resorbed in CO_2-containing and volatile-free carbonate melts at 5.7-7 GPa and 1500 ºC show positive hillocks (Khokhryakov and Pal'yanov, 2007, 2010), which are evidently different from the negative hillocks created on diamonds in CO_2 fluid at 1- 2.5 GPa (Fedortchouk et al.,2007; Arima and Kozai, 2008). Forming conditions of hillocks are still elusive, and requires more investigations.

5.6.3. What Controls the Geometry of Etch Pits on Diamond

Many details of the formation mechanism of etch pits on octahedral faces during diamond dissolution are unclear. Etch pits on {111} faces are proposed to form by a defect-controlled kink mechanism (Frank et al., 1958; Evans and Sauter, 1961; Ponton et al., 1974; Angus and Dyble, 1975; Yamaoka et al., 1980). In this mechanism, initial etch pits nucleate at defects, and then widen by removal of atomic C through propagation of kinks at atomic steps and deepen by continuous dissolution at defects. This proposed mechanism is referred to as a static mechanism, because wall angles, outlines, and orientations of etch pits under controlled conditions are restricted (Frank et al., 1958; Ponton et al., 1974; Angus and Dyble, 1975). For example, hexagons are predicted to form under the conditions where neither negative nor positive trigons should occur. The predicted

hexagons have never been created in diamond dissolution experiments under such conditions (Evans and Sauter, 1961; Yamaoka et al., 1980; Khokhryakov and Pal'yanov, 2010). In contrast, the experimental studies show coexisting hexagons and negative or positive trigons (Kozai and Arima, 2005; Fedortchouk et al., 2007; Arima and Kozai, 2008), similar to the coexisting hexagons and negative or positive trigons observed on natural diamonds (Robinson, 1979; Fedortchouk and Zhang, 2011; Zhang and Fedortchouk, 2012). Geometry of etch pits, particularly hexagons, on diamonds has been used to constrain the fluids compositions in kimberlites and diamond mantle reservoirs (Fedortchouk et al., 2010; Khokhryakov and Pal'yanov, 2010; Fedortchouk et al., 2011; Zhang and Fedortchouk, 2012). It is, therefore, very important to understand the formation mechanism of etch pits on {111} faces. The quantitative measurements of etch pits using AFM in this study can help us to learn more about the formation mechanism of etch pits.

The assemblages of different types of etch pits under the specific dissolution conditions (Figure 5.7 and 5.8), the relationships between depths and dimeters of etch pits on {111} faces (Figure 5.10), and their correlation with fluid compositions (Figure 5.8) suggest that etch pits evolved from regular trigons to trigons with curved-edges to truncated trigons to hexagons to positive truncated trigons. Following the defect- and condition- controlled formation mechanism of negative trigons (Angus and Dyble, 1975; Zhang et al., 2015), I propose a defect-initiated and condition-controlled formation model of etch pits on {111}

by introducing the concept of defect-derived strain fields (Hull and Bacon, 2011). In this model, the dissolution rate normal to (111) planes at defects V_d and the bottom shapes of etch pits depend on the type and depth of defects; defects and dissolution conditions decide the relative removal rates of two- (V_p') and three-bonded carbon atom (V_p) on (111) planes (Figure 5.13).

The formation process of etch pits can be divided into three stages: an initial defect-controlled dissolution stage at defects, a final condition-controlled dissolution stage in strain-free fields, and an intermediate stage competing between defect- and condition-controlled dissolution in strain fields (Figure 5.13). At the initial stage, negative p/b trigons nucleate at defects due to easy removal of one- or two-bonded atoms around defects during dissolution. Defect sizes not only affect initial geometry of trigons by controlling V_d (Figure 5.13 a, d), but also decide the enlargement process of trigons via single- or multiple- kink mechanism (Zhang et al., 2015). In strain fields around defects, the distortion degree at the outer rims of trigons decreases as trigon diameters increase. The effects of conditions on enlargement of trigons progressively increase, finally overcome those of defects, and then completely control V_p and V_p' to modify trigon geometry (Figure 5.13 b-c, e-h). At the final stage, the condition-controlled dissolution determines the outlines, wall angles, and orientations of etch pits (Figure 5.13 b-c, e-h). Initial negative trigons can be either enlarged (V_p' >>V_p, Figure 5.13 b-c) or converted into truncated

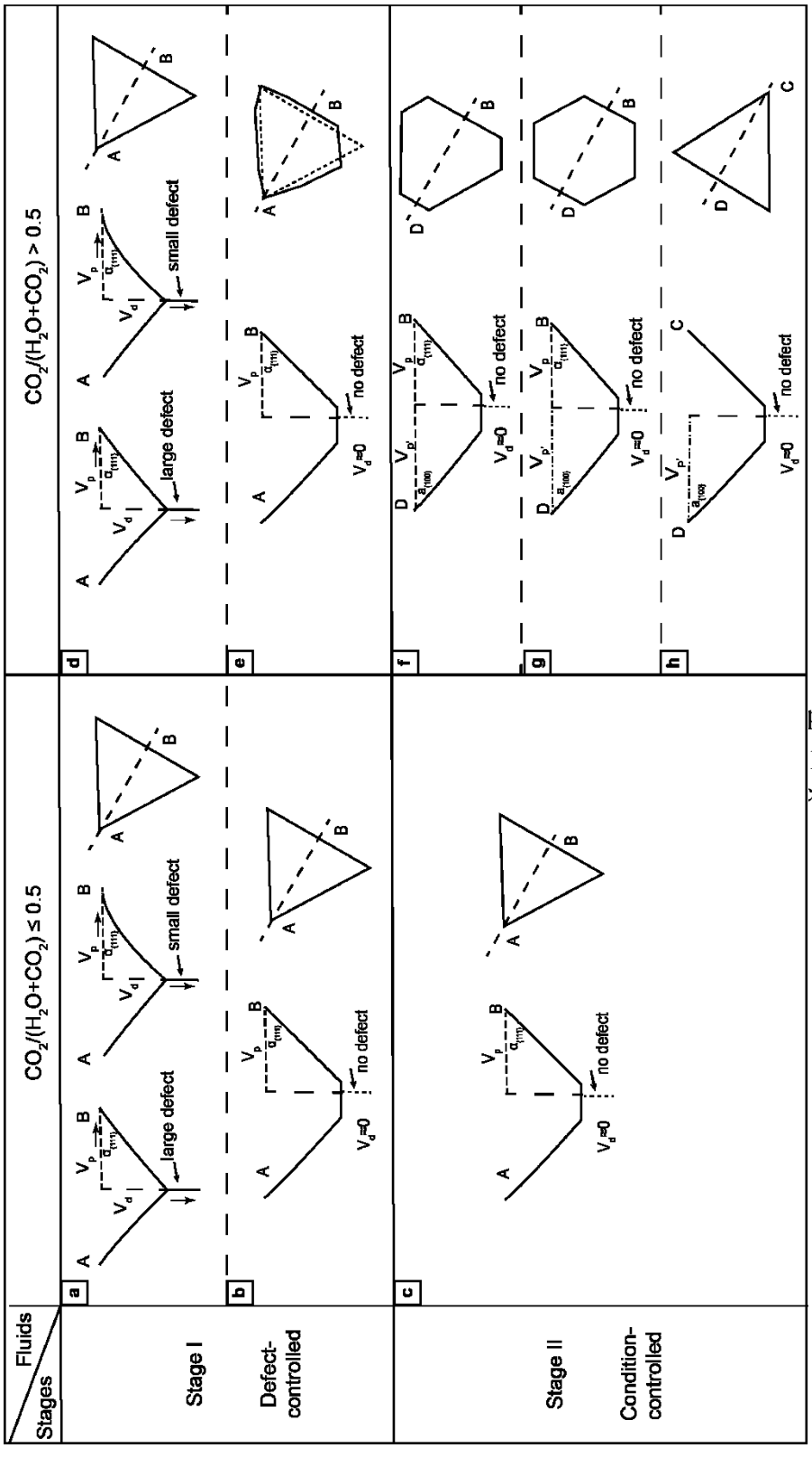

pits via continuous dissolution at d
parallel to the surface; V_p' = remo
city normal to the surface at the def
1} face, respectively. See details in

trigons ($V_p' > V_p$, Figure 5.13 f), hexagons ($V_p' = V_p$, Figure 5.13 g), or positive trigons ($V_p' << V_p$, Figure 5.13 h) depending on dissolution conditions. The final outlines of etch pits on {111} faces are time-independent.

This model can explain features of etch pits on natural and experimentally etched diamonds. First, variable wall angles of the same f/b etch pits on oxidized diamonds (Fedortchouk et al., 2011), which is contrary to consistent wall angles predicted for etch pits in the static model (Angus and Dyble, 1975; Khokhryakov and Palyanov, 2006, 2007), can be easily explained by the enlargement process of etch pits via single or multiple kink mechanism (Zhang et al., 2015). Second, four assemblages of etch pits on {111} faces predicted in this dynamic model include negative trigons (Figure 5.13 a-c), negative trigons coupled with truncated negative trigons (Figure 5.13 d-f), negative trigons coexisting with truncated negative trigons, hexagons, and truncated positive trigons (Figure 5.13 d-g), and hexagons coexisting with truncated positive trigons and positive trigons (Figure 5.13 d-h). The first three assemblages of etch pits in succession correspond to the pure H_2O-aqueous, carbonic, pure CO_2-carbonate resorption morphologies respectively (Figure 5.12b). The four assemblages are consistent with assemblies of etch pits observed on natural diamonds (Robinson, 1979; Hall and Smith, 1984; Zhang and Fedortchouk, 2012).

The defect-initiated and condition-dependent formation mechanism of etch pits on {111} faces shed light on the formation of etch pits on THH and {100} faces. This experimental study shows that circular pits on the THH faces coexisting with main dissolution features occur in the pure H_2O fluid rather than in the immiscible C-O-H fluids, which contradicts the proposed formation mechanism of circular pits via attachment of CO_2 bubbles to surfaces of resorbed diamonds (Robinson, 1979). At 100 kPa, negative tetragons coexisting with octagons and positive tetragons on the cubic diamond faces (Fedortchouk and Canil, 2009) suggest an T-f_{O2}-dependent evolutionary path of etch pits on {100} face, although more details are required for comprehensive understanding of the evolution of etch pits on cubic faces. I propose the "defect-initiated and condition"-controlled formation mechanism for the circular pits on THH faces and etch pits on cubic faces.

5.6.4. Volatiles in Kimberlites before Eruption

The compositions of free fluids in kimberlites are still not well constrained due to significant alteration and contamination to kimberlites. Free fluids in pre-eruption kimberlites are either CO_2-rich based on bulk chemistry analysis of aphanitic kimberlites (Price et al., 2000) or H_2O-rich according to bulk chemistry analysis of kimberlites worldwide, diamond resorption morphologies, infrareds spectra in olivine, fluid properties in ascent kimberlites, and decompression cracks in olivine (Russell et al., 2008; Kjarsgaard et al., 2009; Fedortchouk et al., 2010; Zhang and Fedortchouk, 2012; Brett et al., 2015).

The semi-quantitative correlation between diamond resorption morphologies and the compositions of C-O-H fluids demonstrated in this study can help us to better constrain distribution and compositions of fluids in pre-eruption diamondiferous magmas and emplacement processes of kimberlites.

Our experiments show four resorption morphologies corresponding to the bulk compositions of diamond-etching C-O-H fluids (Figure 5.12). We apply this classification to 403 octahedral diamonds from three kimberlite pipes in the Ekati Mine property (Fox, Koala, and Leslie). Some of the studied diamonds in the three pipes display circular pits on the THH faces, sharp and regular negative trigons, sheaf striations, and negative hillocks (Figure 5.14), identical to the pure H_2O resorption morphology defined in this study. All these features indicate the presence of a pure H_2O zone during the latest stage of kimberlite emplacement. Most diamonds from the Fox, Koala, and Leslie pipes in the Ekati mine (Figure 5.14) and southern African kimberlite pipes (Robinson, 1979) show the resorption morphologies similar to the aqueous resorption morphology characterized in this study, indicating the presence of free C-O-H fluids with $X_{CO2}<0.5$, consistent with low X_{CO2} in the estimated composition of fluids in kimberlites at shallow depth (Russell et al., 2008; Kjarsgaard et al., 2009; Fedortchouk et al., 2010; Brett et al., 2015). In addition, a comparison of resorption morphologies recognized in this study and resorption features reported on diamonds from the Argyle lamproite (Australia) (Hall and Smith,

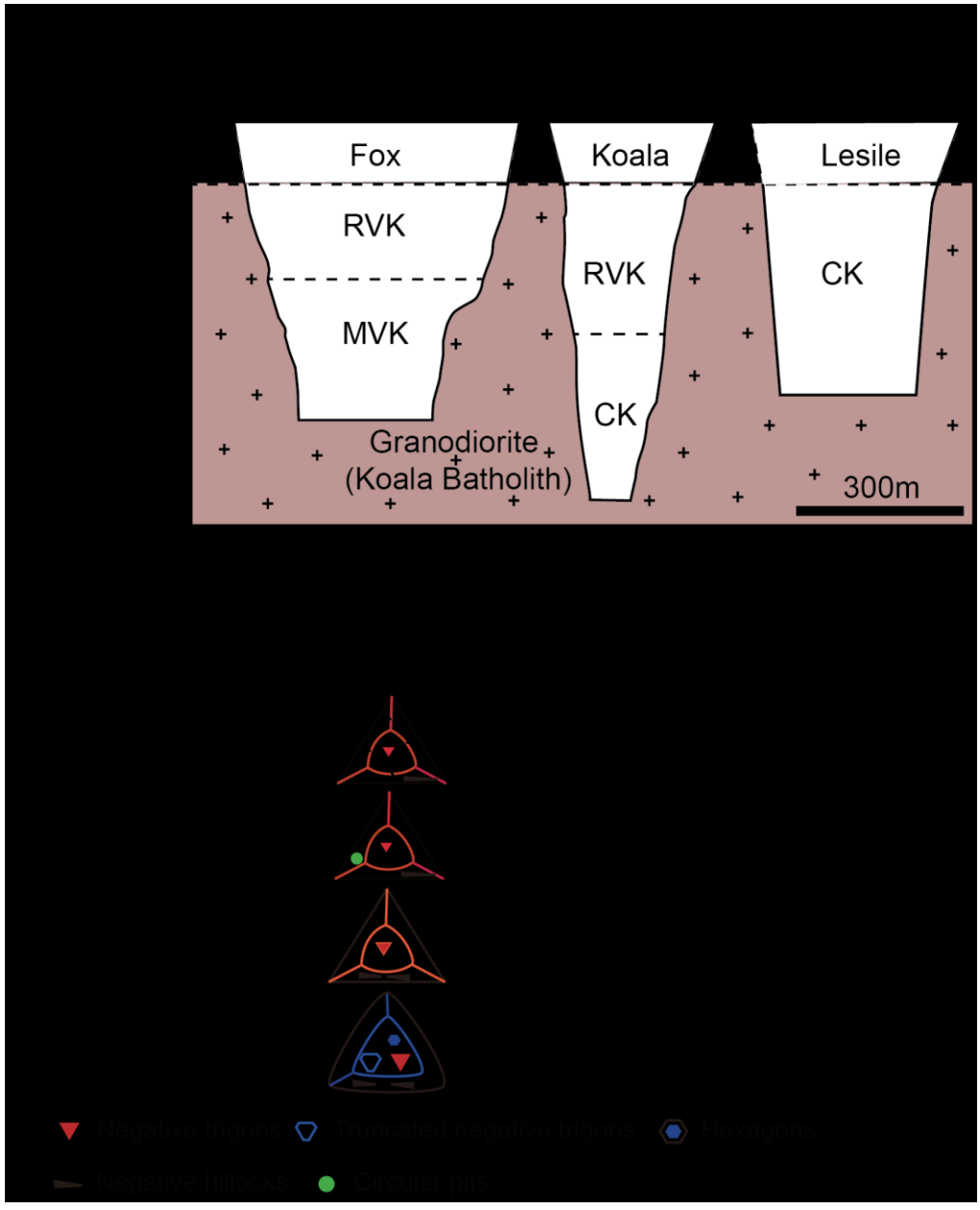

Figure 5.14 Schematic cross-section of three characteristic types of kimberlite pipes in the Ekati mine and diamond morphologies in the pipes. The profiles of kimberlite pipes are modified after Scott Smith (2008). RVK = resedimented volcaniclastic kimberlite, MVK = massive volcaniclastic kimberlite, CK = coherent kimberlite. Dashed line = present surface. Country rock is the granodioritic Koala basement. All three pipes were reconstructed to the time of emplacement on the lithological data of the Koala pipe (Nowicki et al., 2004; Scott Smith, 2008).

1984) shows that a large proportion of Argyle diamonds exhibit the pure CO_2 resorption features preserved in the central areas of {111} and the aqueous resorption features developed along the edges and corners, indicating that the free fluid in the lamproite was CO_2-rich (X_{CO2} = 0.9-1) at depths and evolved into H_2O-rich ($X_{CO2} \leq 0.5$) composition closer to the surface, in agreement with the changes of fluid compositions computed under the conditions of rising kimberlites (Russell et al., 2008; Russell et al., 2012). The evolving compositon of C-O-H fluids in lamproite may be due to carbonate crystallization before eruption, in agreement with the primary magma origin of Ba- and Sr-rich carbonate in the Argyle lamproites (Skinner et al., 1985) or due to CO_2 solubility in melts decreasing at much greater depth than that of H_2O, and therefore H_2O will exsolve from melts at the depths shallower than CO_2.

Variable emplacement mechanisms of Lac de Gras kimberlites are envisaged because of lacking of well constrained compositions of fluids during kimberlite emplacement. The Fox pipe is classified as Class 1 (southern African) kimberlite (Skinner and Marsh, 2004), and the Koala and Leslie pipes are termed as Class 3 (Lac de Gras) kimberlites (Field and Scott Smith, 1999; Skinner and Marsh, 2004) (Figure 5.14). Because of the similar geological setting (Figure 5.14), lack of aquifers across the Ekati Mine (Field and Scott Smith, 1999), and insufficient groundwater supply for phreatomagmatic emplacement of kimberlites in crystalline basement rocks (Sparks et al., 2006), variable crystallization

depth of kimberlites due to either H_2O/CO_2 ratios of fluid phases or insufficient fluids exsolved from kimberlites (Skinner and Marsh, 2004) are proposed to explain variable geology among the Lac de Gras kimberlites. However, Fedortchouk et al. (2010) found similar H_2O-resproiotn features on natural diamonds and the difference of FTIR spectra of olivine between six Lac de Gras kimberlites, and suggest that the depth of fluid exsolution and the degree of fluid retention control eruption styles and geology of kimberlite pipes.

The correlation between diamond resorption morphologies and fluid compositions demonstrated in my study provides better constraints of volatiles in pre-eruption kimberlites, assisting to test the two hypotheses proposed for kimberlite emplacement. The morphological comparison between four defined resorption morphologies and those observed on natural diamonds from the Fox, Koala and Leslie pipes (Figure 5.14) show that all three kimberlite pipes had pure H_2O fluids ($X_{CO2} = 0$) and aqueous fluids ($X_{CO2} \leq 0.5$) at the latest stage of kimberlite emplacement. The H_2O-rich fluids in kimberlites agrees with the suggestion of the presence of hydrous diamond-etching fluids at the latest stage of Lac de Gras kimberlites (Russell et al., 2008; Fedortchouk et al., 2010), rather than with the model of variable fluids on kimberlite liquids (Skinner and Marsh, 2004).

Considering the composition of the estimated primary kimberlites (Dalton and Presnall, 1998; Sparks et al., 2006; Russell et al., 2012) and the miscibility gap in the binary CO_2-H_2O system addressed in this study, I propose a “sandwich” kimberlite column before

eruption, although the depth of fluid separation from kimberlite is unknown. The carbonic fluid (X_{CO2}=0.90) is denser than the aqueous fluid (X_{CO2}=0.38-0.5) calculated using the software Loner H and Loner W (Holloway, 1981; Bakker, 2009). However, significant amount of silica (0.13-0.19 wt%) (Newton and Manning, 2008; Zhang et al., 2015) and other oxides (Zhang and Frantz, 2000; Dolejs and Manning, 2010) dissolved into aqueous fluids and negligible amounts of dissolved silica in carbonic fluids (X_{CO2}=0.9-1, Newton and Manning, 2000) make the aqueous fluid denser than the carbonic fluid in pre-eruption kimberlite columns. Due to the density contrast among three coexisting phases, the kimberlite column shows a "sandwich" structure beginning with a CO_2-rich ($X_{CO2} > 0.5$) fluid zone, followed by a H_2O-rich ($X_{CO2} < 0.5$) fluid zone and a magma body at tail.

Based on the "sandwich" kimberlite column, I suggest four stages of emplacement model of the Ekati kimberlites in agreement with the pervious kimberlite emplacement models (Sparks et al., 2006; Cas et al., 2008): 1) a crater initiated after the first CO_2 explosion due to over-pressurization relative to the atmosphere; 2) carter widened and deepened by the following H_2O explosion; 3) The subsequent extruding kimberlitic magma; 3) carter filled with explosive materials and extruding magma. Although fluids play significant roles is not new, this model gives more details of compositions of fluids and their roles during diamond eruption, which is not constrained well in previous models (Sparks et al., 2006; Cas et al., 2008).

This model can explain the morphological similarities of kimberlite pipes and geological differences between Class 1 and 3 kimberlites (Field and Scott Smith, 1999; Skinner and Marsh, 2004) in terms of volume sizes and viscosity among pipes. The pre-eruption kimberlite in the Fox pipe had a large volume, and continuous explosions at the third stage created the deep and large Class 1 kimberlite pipe. The small Koala pipe resulted from a smaller volume magma, which was only enough for one explosion of kimberlitic magma at the third stage. Degassing of trace amounts of CK was not powerful enough to create MVK. The frosted kimberlite-induced resorption morphology on the Leslie diamonds suggests a fluid loss after the major resorption. Absence of graphite on diamonds, if graphite was not removed during industrial cleaning, may indicate the fluid loss during eruption rather than before eruption. This fluid-loss depth is significantly shallower than that of graphitization (> 20 km) proposed by Fedortchouk et al. (2010), assuming that development of fluid-loss resorption features is hours-long and graphite on diamonds was removed during industrial cleaning. I suggest that the Leslie kimberlite in large volume experienced fluid loss at the third stage. The violent explosion of exsolved volatiles enlarged the crater, followed by fluid-poor magmas infilling.

Kimberlites with high volatile contents and low viscosity (0.1 to 1 Pa s) (Sparks et al., 2006 and references therein) can be treated as a Newtonian fluid for simplicity. Dense mantle-derived material, such as diamonds and mantle xenoliths, in kimberlites are

brought to the surface by the drag force of the fast ascending magmas (McGetchin, 1968; Sparks et al., 1977). However, this mechanism requires the rising speed difference between magmas and diamonds to overcome the gravitational force, and in turn, results in increasing concentration of diamonds from top to bottom in kimberlites, which, to my knowledge, is not reported in natural kimberlites. Alternatively, my study suggests that the attachment of CO_2 or carbonic fluids to moderately hydrophobic diamond surfaces provides additional buoyance for diamond suspension in kimberlites. Continuous release of CO_2 from rising kimberlites due to decompression (Brooker et al., 2011) or decarbonisation through reactions between silicate and carbonate melts (Russell et al., 2012) makes this mechanism possible. The volume ratios of CO_2 to diamonds (with the density of 3.15 g/cm^3) required to balance gravitational force is 0.15, assuming the densities of kimberlites and CO_2 (at 2 GPa) are 2.9 and 1.2 g/cm^3 respectively (Russell et al., 2013). This mechanism also explains diamondiferous Argyle lamproite (Hall and Smith, 1984) in terms of CO_2 enrichment in magmas, which is suggested by the presence of hexagonal ethc pits on most diamonds similar to pure CO_2 resorption morphology. The proposed mechanism suggests diamond resorption morphology as an additional tool for assessing diamond potential in diamondiferous magmas.

5.6.5. Diamond-destructive Metasomatism in the Mantle

Metasomatism not only modifies the compositions of lithospheric mantle, but also affect diamond grade in the mantle by being constructive or destructive to diamonds. Diamonds crystallize in the mantle through redox reactions between silicates and C-bearing metasomatic media and/or due to carbon oversaturation (Stachel and Luth, 2015 and references therein). In the lithospheric mantle beneath the central Slave craton, diamond-forming metasomatic media are C-bearing brine, C-O-H fluids, volatile-bearing carbonate melts, and C-bearing silicate melts (Stachel et al., 2003; Westerlund et al., 2006; Klein-BenDavid et al., 2007a; Creighton et al., 2008; Creighton et al., 2010; Aulbach et al., 2011). Diamond dissolution in the mantle is evident from resorption morphologies observed on diamonds from xenoliths (Robinson, 1979; Hall and Smith, 1984; Viljoen et al., 1992; Spetsius, 1995; Aulbach et al., 2011). However, the diamond-destructive metasomatic media are still elusive. Hydrous fluids are suggested to produce cavities in diamonds (Klein-BenDavid et al., 2007b). However, the irregular cavities do not represent any etch pits on diamonds oxidized in H_2O-rich fluids (Fedortchouk et al., 2007; Zhang et al., 2015) or H_2O-rich melts (Khokhryakov and Pal'yanov, 2007; Arima and Kozai, 2008; Khokhryakov and Pal'yanov, 2010). The recently proposed diamond classification based on resorption morphology (Zhang and Fedortchouk, 2012) provides an independent method to examine diamond-destroying metasomatic media. Our study advances the

classification by providing a quantitative correlation between diamond resorption morphology and the composition of diamond-etching fluids.

Following the diamond classification (Zhang and Fedortchouk, 2012), I found that a significant amount of diamonds from the Fox, Koala and Leslie pipes show the hexagon-bearing mantle-derived resorption morphology (Figure 5.14 b), similar to the surface features created on diamonds in pure CO_2 fluids in this study. The morphological similarities indicate a pure CO_2 fluid or carbonate melts in the lithospheric mantle under the central Slave craton, consistent with the oxidizing C-O-H metasomatic media estimated by the geochemical signatures of garnets from peridotites (Creighton et al., 2008; Creighton et al., 2010; Aulbach et al., 2013). The composition of diamond-destroying metasomatic media depends on host lithology. For examples, hexagon-bearing mantle-derived resorption morphologies on diamonds from peridotite in Argyle lamproite (Hall and Smith, 1984) indicates a carbonate metasomatic media; either carbonate melts or CO_2 fluids can act as the etching agents to create hexagons on diamonds from eclogite (Robinson, 1979). It is worthy to notice that the forming conditions of many complex resorption features on diamonds, proposed to result from mantle-derive dissolution (e.g. step-faced morphologies), are unconstrained, and require more investigations.

5.7. CONCLUSIONS

1. This experimental study shows that the immiscible aqueous and carbonic fluids coexist over a wide range of P–X conditions at 1250 ºC and the correlation between diamond resorption morphology and the fluid composition suggest the controlling effects of diamond wettability and the volume proportions of aqueous and carbonic fluids on resorption morphologies.

2. My study shows that higher bulk X_{CO2} in the C-O-H fluids and P suppress diamond rounding rates.

3. The experimental results show that outlines of etch pits on {111} faces depends on the bulk composition of diamond-etching C-O-H fluids at 1-3 GPa and 1250 ºC. The correlation between assemblages of etch pits and fluid composition and the relationship between depth and diameter of etch pits developed on the diamonds in one run suggest a defect-initiated and condition-controlled formation mechanism of etch pits on {111} faces.

4. The study has defined four diamond resorption morphologies those show semi-quantitative correlation with the composition of diamond-etching C-O-H fluids. This correlation demonstrates that diamond resorption morphology in most

diamond-bearing environments is a robust semi-quantitative fluid proxy of the latest dissolution event.

5. Application of experimental results to the natural diamonds from three Ekati kimberlites suggests that the pre-eruption Ekati kimberlites had a “sandwich” structure with CO2-rich fluid forming the head of the eruption column, followed by a layer of H2O-rich fluid, and a degassing magma body. Pure CO2 fluids or carbonate melts acted as one of the diamond-destructive metasomatic media in diamond mantle reservoirs under the central Slave craton.

CHAPTER 6. DISCUSSION AND CONCLUSIONS

6.1. INTRODUCTION

The study of diamond dissolution presented here is motivated by the essential question: *how to quantify fluid composition robustly in kimberlites and mantle metasomatic media using diamond resorption morphology?* To reach this objective, the factors (internal vs. external) controlling diamond resorption morphologies in nature need to be defined. My thesis combines a detailed description of external forms and surface features of 733 diamonds recovered from five kimberlite pipes in the Ekati mine, a detailed study of the relationships between resorption morphologies and internal properties of 109 diamonds representing distinct resorption morphology groups (Chapter 2, 3) and an experimental investigation of pressure-temperature-fluid composition (P-T-X) control on diamond resorption (Chapter 4 and 5).

The results of this work are: 1) novel classification of Ekati diamonds in terms of resorption morphologies; 2) empirical clarification of the links between diamond resorption morphologies and internal properties (growth habit, N content and aggregation state, C isotopic composition) of the outer rims of diamonds; 3) experimental determination of P-T-X effects on diamond dissolution; 4) improved understanding the

formation mechanism of etch pits on {111} faces based on the quantitative measurements of etch pits using AFM.

This chapter combines the discussion parts of Chapters 2 to 5, including a comprehensive section on diamond resorption (§ 6.2), a preliminary model of diamond dissolution in terms of fluid compositions (§ 6.3), comparison to previous studies (§ 6.4), directions of future studies (§ 6.5), and finally the conclusions of this thesis (§ 6.6).

6.2. DIAMOND RESORPTION

6.2.1. Classification of Diamonds Based on Resorption Morphology

Diamond history includes both growth and dissolution events, which affect diamond grades and quality. Existing classifications of diamonds based on growth forms and their aggregates (Orlov, 1977; Sunagawa, 1984) only address the growth history rather than the dissolution events. However, diamond resorption morphologies can provide the valuable information on the latest dissolution history. Here I present a novel diamond classification based on resorption morphologies (resorbed crystal forms and associated surface features) through combining experimental and empirical studies of diamond resorption morphology (Figure 6.1).

This classification system shows systematical criteria to distinguish kimberlite-induced from mantle-derived resorption morphologies. To characterize diamond resorption

sorption morphologies. p/b: point-bot
nduced resorption; UnR: unresorbed;

morphologies in a pipe, the following diamond samples must be systematically examined: diamonds in the matrix of kimberlites (kimberlite-induced resorption morphology), diamonds enclosed by mantle xenoliths (mantle-derived resorption morphology), and pseudohemimorphic diamonds (indicating partially kimberlite-induced resorption and partially mantle-derived resorption morphology). The novel classification system (Figure 6.1) includes four groups: 1) undefined morphology (UnD), including stones/fragments with irregular {111} faces or without {111} faces; 2) kimberlite-induced morphologies (KIM) on most diamonds in the population of a pipe, given most diamonds were released from xenoliths; 3) mantle-derived morphologies (MR), occurring on minor diamonds protected by xenoliths from kimberlites; 4) Unresorbed morphology (UnR), showing on diamonds with non-appreciable resorption features, such as sharp corners, unpitted, and straight edges.

My new classification of diamonds provides a foundation for deciphering dissolution history of diamonds in kimberlites and mantle reservoirs. Diamond dissolution in H_2O-dominated mantle fluids also creates resorption morphology similar to the type 1 kimberlite-induced morphology (KIM-1) (Figure 6.1). Only the presence of circular pits on the kimberlite-induced morphology suggests diamond oxidation at shallow depth ($P \leq$ 1 GPa). The formation conditions of other types of resorption morphologies (e.g. SM-2), perhaps resulting from dissolution during mantle metasomatism, are still unknown. The

present classification system can be used to constrain the composition of diamond-destroying fluids in both environments, which shows the semi-quantitative correlation between diamond resorption morphologies and the composition of fluids in normal diamond-bearing environments.

6.2.2. Internal vs. External Factors

Diamond resorption is affected by diamond internal properties (e.g., zonings, defects), referred to here as internal factors (Harrison and Tolansky, 1964; Sunagawa, 1984; Mendelssohn and Milledge, 1995), and dissolution conditions (P-T-f_{O2}-X), termed external factors (Yamaoka et al., 1980; Kozai and Arima, 2005; Fedortchouk et al., 2007; Khokhryakov and Pal'yanov, 2007; Arima and Kozai, 2008; Zhang et al., 2015). Internal properties cause distortions in an ideal diamond lattice, which influence diamond resorption morphologies by affecting removal rates of carbon atoms on diamond surfaces. The external factors determine the activation energy of removal of carbon atoms from diamond surfaces and relative removal rates of 2-/3-bonded C atoms, which, in turn, determine diamond resorption morphologies.

My study suggests that the effects of internal factors (crystal forms, N contents, and dislocations) are minor (Chapter 2-5). The absent correlation between the variable external forms (with external {111} face) reconstructed from CL patterns and resorption

morphologies of natural diamonds (Chapter 3) is supported by similar resorption morphologies of octahedral and step-faced octahedral diamonds under the same dissolution conditions (Kozai and Arima, 2005; Fedortchouk et al., 2007; Khokhryakov and Pal'yanov, 2007; Arima and Kozai, 2008; Zhang et al., 2015). The effect of N contents on diamond resorption morphologies suggested by dissolution experiments (Mendelssohn and Milledge, 1995) is not supported by our study of Ekati diamonds (Chapter 3). The lack of correlation between N contents and resorption morphologies is further supported by similar resorption morphologies of diamonds from variable sources, with potentially different N contents and aggregation states, under similar dissolution conditions (Kozai and Arima, 2005; Fedortchouk et al., 2007; Arima and Kozai, 2008; Zhang et al., 2015), and by similar resorption morphology of diamonds with variable N contents and aggregation states under the same dissolution conditions (Fedortchouk et al., 2007). While etch pits are associated with defects (Lang, 1964; Khokhryakov and Palyanov, 2006, 2007), and dislocations are suggested to control the geometry of point-bottomed trigons (Khokhryakov and Palyanov, 2006, 2007), the evolution of the etch pits on {111} faces recorded by AFM in this study suggests that etch pits formation is defect-initiated but their further growth is via condition-controlled kink mechanism. Therefore, the geometry of well-developed etch pits depends on dissolution conditions (Figure 6.2, Chapters 4-5). In the evolution path, all trigons are assumed to start as p/b trigons growing until defects are

ng diamond resorption in C-O-H fluids
ending on defect size; the final outline
t defects; Vp: horizontal dissolution ra
on of each stage under different conditio

etched out, and then become f/b trigons. Trigons with flat bottoms may act as initial trigons (Y. Fedortchouk, personal communication); the curbed-bottomed trigons are treated as large f/b trigons with numerous small trigons at their bottom, as show in Figure 5.9e.

Variable dissolution morphologies (resorption forms and etch pits) reproduced in resorption experiments are similar to those observed on Ekati diamonds, suggesting that external conditions (P, T, f_{O2} and fluid composition) control diamond resorption morphologies. This is also supported by the similarities between experimental resorption morphologies produced in different laboratories under similar conditions (Mendelssohn and Milledge, 1995; Kozai and Arima, 2005; Fedortchouk et al., 2007; Khokhryakov and Pal'yanov, 2007; Arima and Kozai, 2008; Zhang et al., 2015), between experimental and natural resorption morphologies, and between natural diamonds from different pipes. The controlling effects of external over internal factors on diamond resorption morphology are similar to the effects of over-etching conditions on resorption features of diamond plates, which show no correlation between densities of etch pits and internal defects (Harrison and Tolansky, 1964). I propose that all resorbed natural diamonds undergo powerful condition-controlled dissolution, which overwhelms the effects of internal factors on diamond resorption.

6.2.3. The Effects of External Factors on Diamond Dissolution

External factors that can affect diamond dissolution are P, T, f_{O2}, and fluid composition (X). The effects of T, f_{O2}, pure CO_2, and H_2O on diamond dissolution have been experimentally investigated (Kanda et al., 1977; Yamaoka et al., 1980; Cull and Meyer, 1986; Kozai and Arima, 2005; Fedortchouk et al., 2007; Khokhryakov and Pal'yanov, 2007; Arima and Kozai, 2008; Khokhryakov and Pal'yanov, 2010; Zhang et al., 2015). However, P effects were not previously systemically studied. The quantitative effects of fluid composition on diamond resorption morphologies were also unknown due to limited data on diamond oxidization in fluids with variable composition. This study addressed the effects of P and fluid composition on the kinetics of diamond dissolution and the resulting resorption morphology, and derives a semi-quantitative relationship between fluid composition and resorption morphologies (Chapters 4-5). My study showed that increasing P suppresses diamond dissolution rates, decreases diamond rounding from octahedral to THH forms in carbonic fluids with $X_{CO2} \geq 0.5$, and eliminates the formation of circular pits on THH faces (Chapters 4-5). My experimental results suggest that: 1) the depth at which fluids were released from kimberlites affects the relationship between diamond weight loss and resorbed forms; 2) diamond preservation estimated by resorbed THH does not necessarily indicate high weight loss; 3) development of circular pits only

at $P \leq 1$ GPa may offer a simple barometer indicating the minimum depth of the presence free H_2O fluids in kimberlites.

This study addressed miscibility of C-O-H fluids at high P and T, and quantified the effects of fluid composition on diamond resorption. My experimental results show that an increase in X_{CO2} (0.5-0.9) creates immiscible aqueous and carbonic fluid phases in the binary CO_2-H_2O system, suppresses diamond rounding rates, and affects the evolution of etch pits on {111} faces (Chapter 5, Figure 5.12 and 6.2). Based on the results of these studies, I propose that 1) rising kimberlite magmas contain immiscible aqueous and carbonic fluids; 2) the bulk X_{CO2} of the C-O-H fluid system determines resorption morphologies on natural diamonds, probably by controlling the volume proportion of aqueous fluids in the system (Chapter 5).

6.2.4. Revised Formation Mechanism of Etch Pits

Etch pits are associated with defects (e.g., dislocations) and form via kink mechanisms (Frank et al., 1958; Lang, 1964; Ponton et al., 1974; Angus and Dyble, 1975; Khokhryakov and Palyanov, 2006, 2007). The early proposed defect-controlled kink model predicts that all flat-bottomed trigons with size larger than depth bear constant wall angles and unalterable outlines (Ponton et al., 1974; Angus and Dyble, 1975; Khokhryakov and Palyanov, 2007), which is referred here to as a static model. The static kink model,

however, cannot explain all the features of etch pits observed on natural diamonds and resorbed diamonds in experiments, thus hampering attempts to decipher the dissolution history of diamonds using resorption morphologies. My work uses AFM to monitor the evolution of the etch pits on {111} faces quantitatively and provides an improved kink model through introducing the concept of strain fields around defects to reconcile similarities and differences among etch pits on octahedral diamonds (Chapters 2-5). Compared with the previous static kink model, my new conceptual model of etch pit formation predicts that wall angles and outlines of etch pits change as dissolution conditions vary, which is referred to as a dynamic kink model. The dynamic model includes an initial "defect-controlled" stage, a "condition-controlled" stage in defect-free areas, and a "competition" stage between defect- and condition-controlled dissolution in strain fields around defects (Figure 6.2). Two advantages of this dynamic model are: 1) it explains variable wall angles of the same etch pits observed on natural diamonds (Fedortchouk et al., 2011), which is inconsistent with constant wall angles of etch pits during formation at defects predicted by the static model (Angus and Dyble, 1975; Khokhryakov and Palyanov, 2006, 2007); 2) it explains four assemblages of etch pits produced on {111} faces: simple negative trigons, negative trigons coexisting with truncated trigons, negative trigons coexisting with truncated trigons, hexagons, and truncated positive trigons, hexagons coexisting with truncated positive trigons and simple

positive trigons (Figure 6.2). These four predicted clusters are consistent with experimental results (Kozai and Arima, 2005; Fedortchouk et al., 2007; Arima and Kozai, 2008) and observations of natural diamonds (Robinson, 1979; Hall and Smith, 1984). My new dynamic model can reconcile the uncorrelated explanation of the formation of negative trigons, hexagons, and positive trigons proposed in the static kink model (Frank and Puttick, 1958; Evans and Sauter, 1961; Kanda et al., 1977; Kozai and Arima, 2005).

The new "defect-initiated and condition-controlled" model proposed for the formation of etch pits on {111} faces is probably also applicable to etch pits on THH and cubic faces. Circular pits on THH are conventionally envisaged to be created by CO_2 bubbles attached to the THH faces after the formation of main diamond dissolution features (e.g., trigons) (Robinson, 1979; Tappert and Tappert, 2011). My study showed that circular pits at $P \leq 1$ GPa form during diamond resorptions in pure H_2O and are absent in the immiscible H_2O- and CO_2-rich fluids, at silica-saturated conditions, or at ≥ 1 GPa (Chapter 4-5), inconsistent with the bubble-attachment mechanism (Robinson, 1979). I propose a "defect-initiated and condition-controlled" mechanism for the formation of circular pits. On cubic diamond faces, the "defect-initiated and condition-controlled" model can also explain the coexistence of negative tetragons, octagons, and positive tetragons at 100 kPa (0.0001 GPa, Fedortchouk and Canil, 2009), although more investigations are required to understand the formation of etch pits on cubic faces.

6.2.5. Diamond Resorption Morphology as a Fluid Proxy

Experimental and empirical studies of diamond dissolution features have recently suggested that resorption morphology may constrain the fluid composition during diamond resorption events (Fedortchouk et al., 2007; Fedortchouk et al., 2010; Khokhryakov and Pal'yanov, 2010). The addressed "condition"-dependence of diamond resorption morphologies (Chapters 2-3) and quantified effects of P-T-X on diamond resorption morphologies (Chapters 4-5) demonstrate that, under the conditions of most common diamond-bearing environments, the bulk fluid composition determines diamond resorption morphologies. I characterized four types of diamond resorption morphologies in terms of fluid composition (pure H_2O, aqueous, carbonic and pure CO_2 fluids or carbonate melts), which can semi-quantitatively constrain the composition of C-O-H fluid(s) present in the latest diamond-dissolution event (Figure 5.12, Chapter 5). The application of the experimental results of diamond dissolution to Ekati diamonds and comparison to reported resorption morphology of diamonds from southern African kimberlites (Chapter 6) show that all Ekati and most southern Africa kimberlites had free aqueous fluid ($X_{CO2}<0.5$) coexisting with kimberlite magmas in agreement with the immiscible fluids and magma phases simulated at the conditions of kimberlite ascent (Russell et al., 2008).

6.3. A TALE OF DIAMOND RESORPTION OF EKATI DIAMONDS

I use the experimental and empirical data on diamond resorption to investigate the dissolution history of Ekati diamonds from the mantle to the Earth's surface. Figure 6.3 shows the general stratification of the lithospheric mantle below the central Slave craton, kimberlite ascent from the mantle source to the Earth's surface, evolution of C-O-H fluid in kimberlite columns at different depth, and corresponding resorption morphologies of diamonds.

6.3.1. Diamond Dissolution during Mantle Metasomatism

The diamond-bearing low lithospheric mantle beneath the central Slave craton have a very complex metasomatic history. Studies on mantle xenoliths and silicate and fluid inclusions in diamonds suggest that mantle metasomatic agents cover a continuum from hydrous silicic melts to carbonate melts to brine fluids (Klein-BenDavid et al., 2004, 2009; Creighton et al., 2008, 2010; Aulbach et al., 2011, 2013). Chronologically, the metasomatic history can be divided at least into four periods: 1) at ~ 3.3 Ga, infiltration of carbonate-bearing C-O-H fluids/brine or melts into harzburgite triggered diamond crystallization (Klein-BenDavid et al., 2004, 2009; Creighton et al., 2008, 2010; Aulbach et al., 2011, 2013); 2). At 3300 – 350 Ma, the diamond-bearing harzburgite mantle was metasomatized by oxidizing C-O-H fluids and kimberlite-like melts, which converts harzburgite

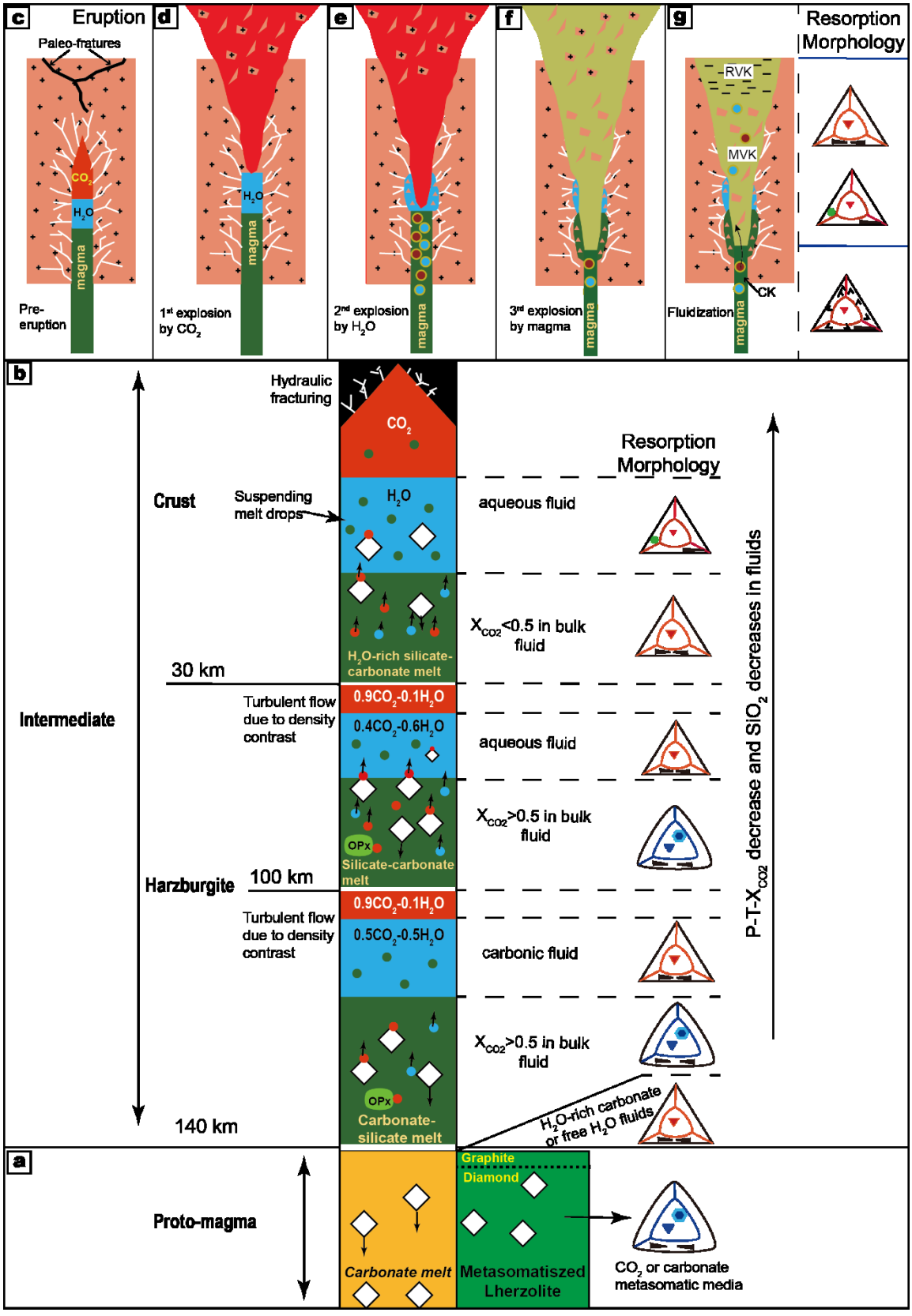
c
Eruption
Paleo-fratures
CO2
H2O
magma
Pre-eruption
d
H2O
magma
1st explosion by CO2
e
magma
2nd explosion by H2O
f
magma
3rd explosion by magma
g
RVK
MVK
CK
magma
Fluidization
Resorption Morphology
b
Hydraulic fracturing
CO2
Crust
Suspending melt drops
H2O
aqueous fluid
XCO2<0.5 in bulk fluid
H2O-rich silicate-carbonate melt
30 km
Intermediate
Turbulent flow due to density contrast
0.9CO2-0.1H2O
0.4CO2-0.6H2O
aqueous fluid
XCO2>0.5 in bulk fluid
OPx
Silicate-carbonate melt
Harzburgite
100 km
Turbulent flow due to density contrast
0.9CO2-0.1H2O
0.5CO2-0.5H2O
carbonic fluid
XCO2>0.5 in bulk fluid
OPx
Carbonate-silicate melt
140 km
H2O-rich carbonate or free H2O fluids
Resorption Morphology
P-T-XCO2 decrease and SiO2 decreases in fluids
a
Proto-magma
Carbonate melt
Graphite
Diamond
Metasomatiszed Lherzolite
CO2 or carbonate metasomatic media

Figure 6.3 Schematic diagram of diamond mantle reservoirs and three stages of kimberlites and their linkage with diamond resorption morphology in the Ekati mine at 1250 ºC. See text for details. (a) Diamond mantle reservoirs which were sampled by proto-kimberlites (carbonate melt). Diamond resorption morphology is at the right. (b) Evolution of kimberlite columns, fluid composition, and corresponding diamond resorption morphologies at the right. (c-g) Kimberlite emplacement. Diamonds from the H_2O-neck and kimberlite magmas (RVK and MVK) keep pre-eruption resorption morphology and diamonds in quietly intruding kimberlite (CK) show frosted kimberlite-induced resorption morphology due to degassing. RVK: resedimented volcaniclastic kimberlite; MVK: massive volcaniclastic kimberlite; CK: coherent kimberlite. Symbols used in sketches of diamond resorption morphologies refer to Figure 5.14. The boundary between the harzburgitic and metasomatised lherzolitic mantle is from Griffin et al. (2004), and the diamond-graphite boundary at 1250 ºC is from Day (2012).

into lherzolite (Creighton et al., 2008, 2010; Aulbach et al., 2011, 2013) ; 3) at 2.1- 1.9 Ga, the formation of eclogitic diamonds resulted from metasomatism by reducing C-O-H-N fluids from deserpentinisation of subducted oceanic mantle (Aulbach et al., 2011); 4) At max. 350 Ma to ~ 55Ma (kimberlite eruption age, Sarkar et al., 2015), the diamond-bearing harzburgite mantle was converted into lherzolite by kimberlite-like melts (Creighton et al., 2008, 2010; Aulbach et al., 2011, 2013). All reported metasomatic media are suggested to be diamond-friendly according to diamond resorption morphologies based on old and inappropriate classification system (Creighton et al., 2008) and estimation of oxygen fugacity of host rocks (Creighton, et al. 2010, Aulbach et al., 2013). However, McCammon et al. (2001) suggest that increasing carbonate activity in metasomatic fluids/melts can cause diamond dissolution even at f_{O2} in the diamonds stable field, which is supported by diamond dissolution experiments under diamond-stable conditions (Khokhryakov and Pal'yanov, 2007, 2010). Additionally, the estimates of the mantle f_{O2} suggests aqueous fluids or carbonate-poor silicate melts as the diamond-precipitating agent (Stagno et al. 2013), indicating that there must be diamond-destroying metasomatic events, evident from the presence of cavities in fibrous and cloudy Ekati diamonds (Klein-BenDavid et al., 2007). Klein-BenDavid et al. (2007) suggest hydrous fluids as the diamond-etching agent according to the compositions of materials trapped in cavities. However, no cavity in diamonds shows regular geometry, which is normally expected for etch pits on diamonds

resorbed in aqueous fluids (Kozai and Arima, 2005; Fedortchouk et al., 2007; Khokhryakov and Pal'yanov, 2007). My study of resorption features on Ekati diamonds provides better constraints on diamond-destructive metasomatic media in the diamond-bearing mantle beneath the central Slave craton.

According to the proposed diamond classification based on resorption morphology (Zhang and Fedortchouk, 2012), minor proportion of Ekati diamonds in this study preserves mantle resorption morphologies, which has been demonstrated to be a fluid proxy during the latest diamond dissolution. Ekati diamonds with hexagon-bearing mantle-derived resorption morphology are minor but common in all the five kimberlite pipes (Fox, Misery, Koala, Grizzly and Leslie) (Chapters 2-3, 5), indicating the presence of pure CO_2 fluid or carbonate melts as metasomatic media in diamond mantle reservoirs. The exact diamond-destructive agent depends on lithology (peridotite vs. eclogite). For example, pure CO_2 fluid can only exist in eclogite rather than peridotite under the mantle conditions due to the reaction between CO_2 and olivine at the mantle conditions (Smith et al., 2015; Stachel and Luth, 2015). This suggestion agrees very well with the latest metasomatic media recorded by trace elements in garnet (Creighton et al., 2008, 2010; Aulbach et al., 2011, 2013). Although CO_2 fluid and carbonate melts as metasomatic media is far from new (e.g. Griffin et al., 1999; Creighton et al., 2008), the novelty of my study is that it provides better constraints on the composition of diamond-destroying metasomatic media.

6.3.2. Diamond Dissolution in Kimberlites

Mantle-derived resorption features on diamonds can be modified by reactions with kimberlite magmas and exsolved C-O-H fluids, creating kimberlite-induced resorption morphologies. Phases present in a kimberlite column divide kimberlite ascent into three linked stages: 1) the proto-kimberlite stage where diamonds and diamondiferous xenoliths are sampled and carried in magmas; (2) the intermediate stage with diamonds carried and oxidized; (3) the emplacement stage where diamonds are ejected to the Earth's surface

6.3.2.1. Proto-kimberlite Stage (≤ 130 km)

A proto-kimberlite forms at the base of the cratonic lithospheric mantle or deeper (Mitchell, 2008), and is thought to be a H_2O-containing, low-silica, carbonate-bearing magma constrained by partial melt compositions of carbonated peridotite, estimated compositions of primary kimberlite magmas, and volatile solubility in kimberlites (Dalton and Presnall, 1998; Price et al., 2000; Sparks et al., 2006; Kopylova et al., 2007; Brey et al., 2008; Brey et al., 2009; Sparks et al., 2009; Russell et al., 2012). Before intersecting the T-dependent stability field of olivine in the presence of CO_2 (Newton and Sharp, 1975), the proto-kimberlite must be a miscible H_2O-bearing silicate-carbonate melt. Given the assumed composition of proto-kimberlites (Sparks et al., 2006 and references therein), diamonds in the proto-kimberlite will be oxidized and show aqueous resorption morphology (Figure 6.3 b), as documented by diamond oxidation in H_2O-containing

carbonate and kimberlite melts (Khokhryakov and Pal'yanov, 2007, 2010). The product CO_2 of diamond oxidization may dissolve into CO_2-undersaturated proto-kimberlitic melts.

6.3.2.2. Intermediate Stage (130 – few km)

The proto-kimberlite at this stage releases H_2O and CO_2 due to decarbonation (Newton and Sharp, 1975; Russell et al., 2012) or depressurization (Mitchell, 1986). The miscibility gap in the binary CO_2-H_2O system at 1250 ºC and 1-3 GPa documented in this study and resorption morphologies on the Ekati diamonds (Chapters 2 and 5) indicate the presence of three coexisting phases in the pre-eruption kimberlite column: aqueous fluid, carbonic fluid, and the melt.

Immiscible carbonic and aqueous fluids released from proto-kimberlite and evolved kimberlite magmas result in a "sandwich" kimberlite column due to density contrast between three coexisting phases. While the carbonic fluid (X_{CO2}=0.90) is denser than the aqueous fluid (X_{CO2}=0.38-0.5) at 1-3 GPa and 1250 ºC calculated using the software Loner H and Loner W (Holloway, 1981; Bakker, 2009), significant amounts of silica (0.13-0.19 wt%) (Newton and Manning, 2008; Zhang et al., 2015) dissolved in aqueous (H_2O) fluids will make the aqueous fluid denser than the carbonic fluid. Considering other dissolved species in aqueous fluids (Zhang and Frantz, 2000; Dolejs and Manning, 2010) and

negligible amounts of dissolved species in carbonic fluids (X_{CO2}=0.9-1) (Newton and Manning, 2000), it is a valid assumption that the aqueous fluid with dissolved oxides is invariably denser than the carbonic fluid in the kimberlite column. Due to the density contrast, the kimberlite column becomes progressively stratified with a carbonic head, an aqueous neck (H_2O + dissolved species), and a magma body with immiscible carbonic and aqueous fluids. As the kimberlite rises by diapiric upwelling in the upper mantle (Green and Gueguen, 1974) and through channels at shallow depth created byhydraulic fracturing at the fluid head (Phillips, 1972), the composition of carbonic and aqueous fluids changes to pure CO_2 and pure H_2O at shallow depth (<1 GPa) respectively, due to depressurization (Figure 6.1 b). The corresponding resorption morphologies on diamonds in the kimberlite column change from carbonic and coexisting aqueous resorption morphologies at 130 - ~30 km to pure H_2O and aqueous resorption morphologies at < 30 km (Figure 6.1b). Earlier morphologies are modified by later ones if time permits.

The question arises: how diamonds are transported by kimberlites to the Earth's surface? Traditionally, diamonds like other xenocrysts and xenoliths were brought to the Earth's surface by the drag force of fast rising kimberlites with low viscosity (Sparks et al., 2006), which can be assumed to act as a Newtonian fluid for simplicity (McGetchin, 1968; Sparks et al., 1977). However, this mechanism requires the ascent speed difference between diamonds and kimberlites, which results in diamond concentration at the bottom of

kimberlite pipes, which, to my knowledge, has not been reported yet. My work suggests that diamonds are carried in stratified kimberlites by the attachment of carbonic bubbles to intermediate hydrophobic diamonds, as proposed in this study (Chapter 5). In this mechanism, diamonds with carbonic bubbles/films can migrate upward in magmas, and then enter into the aqueous section (Figure 6.3 b). This mechanism predicts high diamond grades in CO_2-rich magmas, and may explain why H_2O-rich group II kimberlites are depleted in diamonds. It may also explain the diamondiferous Argyle lamproite (Australia), where abundant diamonds with hexagon-bearing morphologies (Hall and Smith, 1984), same as resorpion morphologies created in pure CO_2. The presence of major diamonds with hexagonal etch ptis indicates predominant CO_2 fluids during lamproite ascent. The proposed mechanism may suggest analysis of diamond resorption morphology as an additional tool for estimating diamond grades in kimberlites and lamproites.

6.3.2.3. Emplacement Stage (few km)

Diamond resorption morphologies correlate with the geology of the Ekati kimberlite pipes. Most diamonds from the resedimented volcaniclastic kimberlite (RVK) of the Misery and Koala pipes and the massive volcaniclastic kimberlite (MVK) of the Fox pipe show aqueous and pure H_2O resorption morphologies, indicating a stratified structure of the pre-eruption kimberlite column. The coherent kimberlites (CK) of the Leslie and Grizzly pipes bore frosted diamonds with kimberlite-induced resorption morphologies (Chapters 2, 3

and 6), similar to resorption morphologies created in H_2O-loss runs at 1 GPa (Fedortchouk et al., 2007). The question arises: *when was the aqueous fluid lost*? Post-eruption fluid loss is excluded by the absence of fluid-loss resorption morphologies in the Misery, Koala, and Fox pipes. Because diamond dissolution in volatile-undersaturated melts leads to graphitization (Fedortchouk et al., 2007), the absence of graphite on run-of-mine diamonds (Gurney et al., 2004) and on diamonds from exploration reverse circulation drilling of the Grizzly and Leslie pipes in this study (Chapter 2) suggests the loss of fluid during eruption. Therefore, the presence of aqueous kimberlite resorption morphology on diamonds from all five kimberlite pipes suggests the presence of aqueous fluids (X_{CO2}<0.5), which is inconsistent with the early envisaged controlling roles of fluid composition or insufficient fluids on the internal geology of five Ekati pipes (Skinner and Marsh, 2004).

Based on the stratified column model for pre-eruption Ekati kimberlites, here I envisage four sequential stages of kimberlite emplacement (Figure 6.3 c-g). This emplacement model is inspired by previously proposed kimberlite emplacement models, where kimberlite craters deepen downward by continuous explosions (Sparks et al., 2006; Cas et al., 2008). The Sparks et al. (2006) model includes four defined emplacement stages: I. initial cratering, II. pipe formation, III. pipe filling, and IV. post-emplacement metamorphism and alteration; The Cas et al. (2008) emplacement model comprises six stages: 1. conduit formation, 2. vent opening, 3. vent clearing, reaming and sculpting, 4.

pyroclastic vent in-filling, 5. late stage filling of the pipe and alteration, and 6. on-going diagenetic alteration.

My four-stage emplacement model contains: 1. crater initiation, 2. crater enlargement, 3. pipe filling, and 4. post-eruptional alteration (Figure 6.1d-g). A crater is initiated after the first explosion driven by the release of CO_2 due to over-pressurization relative to the atmosphere when juvenile hydraulic fractures and pre-existing faults are encountered. This stage is similar to the stage 1 of the Sparks et al. (2006) model and stage 2 of the Cas et al. (2008) model. However, both the Sparks and Cas model do not specialize the fluid composition at this stage. The second explosion driven by H_2O-rich fluid widens and deepens the crater, and creates contact breccias in the country rocks (Figure 6.1e). Simultaneously, small amounts of diamonds with the circular pit-bearing resorption morphology are ejected into the crater. Subsequently, the extruding kimberlitic magma (Figure 6.1f) explodes downward due to fast cumulated volatiles from the upper magma body until the upper part is relatively depleted in volatiles. During the serial downward explosion of the magma, the upper magma body acts as a temporary cap over the lower part. This stage is alluded to in stage 3 of the Cas et al. (2008) model and stage 2 of the Sparks et al. (2006) model. At this stage, abundant diamonds with aqueous resorption morphology enter the crater as the carrier, kimberlite magma, is ejected into the atmosphere. Finally, the crater is filled with the volatile-depleted magma (becoming CK)

in the root zone (Figure 6.1g), and then dense ejecting materials deposited in the diatreme zone, followed by light ejecting materials (creating PK or RVK). In the diatreme zone, degassing of the volatile-containing magma in the root zone causes the formation of MVK.

Based on diamond resorption morphologies and the geology and morphologies of the five Ekati kimberlite pipes, I suggest that the Fox pipe is a mature Class 1 kimberlite pipe (Skinner and Marsh, 2004) and the Misery, Koala, Leslie and Grizzly pipes are failed Class 1 kimberlites, either due to variations of magma volumes of kimberlites or due to difference in viscosities between the four pipes. The large and deep Fox pipe underwent all four episodes, although the root zone is still unknown. The small Misery (a cluster of nine mall pipes) and Koala pipes result from a small magma volume, which produced only one explosion in the third emplacement stage. Degassing of trace volatile-bearing kimberlites may be not powerful enough to form MVK. The Leslie and Grizzly pipes formed super-violent explosions that emptied the craters after the second explosion. This model is consistent with the violent pipe excavation of the proposed two-stage emplacement model (Nowicki et al., 2004 and references therein). The violent explosion may have been due to extreme exsolution of volatiles in kimberlites with ultra-low viscosity. The resulting volatile-poor magmas quietly filled the empty craters. This model reconciles the morphological similarities and geological differences between Class 1 and 3 kimberlites (Field and Scott Smith, 1999; Skinner and Marsh, 2004).

6.4. COMPARISONS WITH PREVIOUS STUDIES

The goal of the present study, rooted in empirical and experimental work on diamond resorption morphologies, was to develop a quantitative correlation between diamond resorption morphology and fluid composition applicable to most diamond-bearing environments. Underlying the reconstructed model of resorption morphologies of the Ekati diamonds are the fluid-dependent resorption morphologies of diamonds. The model supports many previous general conclusions concerning fluids in kimberlites and diamond mantle reservoirs (Chapter 4 and 5), such as H_2O-rich kimberlites (Fedortchouk et al., 2010) and increasing carbonate activity in fluids/melts oxidizing diamonds (MacComman et al., 2001). This model not only confirms that the earlier proposed presence of free aqueous fluids in the pre-eruption kimberlitic magmas (Russell et al., 2008; Fedortchouk et al., 2010), but also indicates a stratified structure of the pre-eruption kimberlitic magma column starting with a top-layer of CO_2 –rich fluid, followed by a middle layer of H_2O-rich fluid and a magma body at tail. A stratified kimberlite column develops from the previous two-layered kimberlite column with a CO_2 cap and a magma tail (Sparks et al., 2006; Cas et al., 2008; Russell et al., 2012; Brett et al., 2015).

The model also suggests that the presence of hexagon-bearing mantle-derived resorption features is the indicator of pure CO_2 fluids or carbonate melts acting as mantle metasomatic

media, depending on the lithology of diamond reservoirs. Similar metasomatic media can play different roles for diamond preservation. The rim-wards $\delta^{13}C$ enrichment in two Misery diamonds suggests that oxidizing CO_2 or carbonate melts were the diamond-growth media (Chapter 3), which agrees with geochemical signatures of garnet enclosed in diamonds (Stachel et al., 2003; Creighton et al., 2010). In contrast, the metasomatic CO_2 or carbonate melts recorded by the geochemical signatures of garnets from peridotite (Creighton et al., 2008; Aulbach et al., 2013) may be diamond-destructive, as suggested by the hexagon-bearing mantle-derived resorption morphology on the Ekati diamonds (Chapters 2, 3, and 5). The different contributions of similar metasomatic media to diamonds may be due to C saturation levels, lithology, or f_{O2} (Khokhryakov and Pal'yanov, 2007; Stagno et al., 2015).

The emplacement process of Class 1 kimberlites in the conceptual model is very simplified, and does not consider other factors, such as the properties of country rocks (Field and Scott Smith, 1999), external water bodies (Lorenz, 2003), and volatile effects on liquidus of kimberlites (Skinner and Marsh, 2004). This simple model accounts not only for the key features of diamond resorption morphologies, but also for some similarities and differences of pipe geology for Class 1 and 3 kimberlites, indicating the importance of other factors, such as magma volume and viscosity, during kimberlites emplacement.

The resorption morphology-based classification is applicable to all natural diamonds, although the model is specific to the Ekati diamonds. Comparisons with resorption morphologies of natural diamonds from the southern African kimberlites (Chapter 5) suggest that most kimberlitic magmas had free aqueous fluid, and that only some kimberlitic magmas have free carbonic fluid. The aqueous type of resorption morphology reported on major diamonds from the Jericho kimberlite (Canada) (De Stefano, 2011), recognized as a CO_2-dominanted magma by bulk analysis of aphanitic kimberlite (Price et al., 2000; Kopylova et al., 2007), suggests a free aqueous fluid-bearing kimberlitic magma.

6.5. FUTURE STUDY

The present model is considered preliminary until many assumptions are justified and predictions are tested. Although the hexagon-bearing mantle-derived resorption morphology (CM-1) results from dissolution in CO_2 or carbonate melts, the effect of reducing fluids (CH_4) on diamond dissolution has not been investigated. In addition, diamonds oxidized in carbonate melts develop exclusively positive trigons at 5.7-7 GPa and 1400-1750 ºC (Khokhryakov and Pal'yanov, 2010), beyond the estimated P-T conditions of carbonate melts in the mantle (Kavanagh and Sparks, 2009). Adding a silicate component into a carbonate melt can increase the f_{O2} limit at which diamonds can be oxidized to CO_2 or carbonate (Stagno et al., 2013). Future experimental work should

investigate the effects of reducing conditions and mixed carbonate-silicate melts on diamond resorption under normal mantle P-T conditions.

The intermediate stage of the kimberlite ascent model proposed here predicts three immiscible phases. However, the binary CO_2-H_2O system at high P and T is widely assumed to be completely miscible (Zhang and Duan, 2010). One experimental study of the binary CO_2-H_2O system reported a single fluid under at 1 GPa and 1200 ºC with X_{CO2}=0.2-0.8 and at 2 GPa and 1200-1300 ºC with X_{CO2} = 0.1-0.4 (Frost and Wood, 1997). The presence of a miscibility gap requires more investigation to measure the properties of the binary CO_2-H_2O system at high P-T conditions. At the same time, the most robust evidence of presence of fluid immiscibility in pre-eruption kimberlite columns is the circular pits observed on natural diamonds. Although circular pits form at restricted conditions (low pressure, low SiO_2 activity, pure H_2O fluid), the exact P-T-X formation conditions are not well constrained. Future experimental work should focus on the boundary of the miscibility gap in the binary CO_2-H_2O system and on the forming conditions of circular pits.

Third, based on the different emplacement models, diamond resorption morphology may be able to test the proposed kimberlite emplacement models (Scott Smith, 2008; Lorenz, 2003). Further empirical study of diamond resorption morphology should focus on the relationship between resorption morphologies and internal geology of kimberlites. For

example, in kimberlites that experience phreatomagmatic eruption (Field and Scott Smith, 1999; Lorenz, 2003), diamonds should bear one consistent kimberlite-induced resorption morphology and circular pits should not be observed. The phreatomagmatic model is not suitable for the Ekati kimberlites because of the presence of both aqueous and pure H_2O resorption morphologies on Ekati diamonds. Kimberlites with dominant CO_2 fluids are proposed to explain the formation of Class 2 kimberlites (Skinner and Marsh, 2004). In this case, diamonds should show the corresponding carbonic or CO_2-resorption morphology.

6.6. CONCLUSIONS

The main scientific findings of this thesis can be summarized as follows:

- A systematic classification of diamonds based on resorption morphology is developed. This classification relies on the empirical study of natural Ekati diamonds and substantial experimental data on diamond dissolution. It can be applied to all natural diamonds to constrain the compositions of diamond-etching C-O-H fluids in diamond-bearing environments.

- Diamond resorption morphology has no apparent relationship with N contents and aggregation states, defects, or growth habit.

- The experimental evidence shows that C-O-H fluids form two immiscible phases at 1-3 GPa and 1250 ºC. The miscibility gap contracts as P increases from 1 to 3 GPa.

- Increasing P suppresses diamond dissolution rates, accelerates diamond rounding rates in pure H_2O, and decelerates diamond rounding rates in carbonic fluids. Diamond preservation estimated for resorbed THH may indicate the depth of fluid exsolution from kimberlitic magmas.

- Etch pits form under a defect-initiated and condition-controlled dynamic kink mechanism. Etch pits initiate at defects, but their final geometry depends on dissolution conditions. This is supported by quantifying evolution of etch pits on {111} faces using AFM. On {111} faces, the geometry of etch pits can help to constrain the compositions of C-O-H fluids.

- Circular pits form on TTH faces in pure H_2O under the MgO-forsterite buffer at $P \leq 1$ GPa, suggesting a pure H_2O regime in kimberlites at shallow depth. The presence of circular pits may be a simple barometer indicating the minimum depth of the presence of free pure H_2O fluids in kimberlites.

- Fluid composition (X_{CO2}) controls diamond resorption morphology in nature. The quantitative correlation between diamond resorption morphologies and fluid

composition demonstrates that diamond resorption morphology is an unambiguous proxy of fluid composition for the latest diamond-destroying event.

- The resorption morphologies on Ekati diamonds suggest the stratified structure of pre-eruption Ekati kimberlite magmas, including a CO_2–rich fluid head, a H_2O-rich fluid neck, and a magma body containing free aqueous fluids ($X_{CO2}<0.5$).

- Diamonds entrained in diamondiferous magmas are proposed to be via attachment of carbonic fluids on intermedia hydrophobic diamonds.

- Ekati diamonds with the mantle-derived resorption morphology (CM-1) indicate metasomatism in diamond mantle reservoirs by pure CO_2 or carbonate melts, depending on the host lithology (peridotite vs. eclogite).

REFERENCES

Alexandrov, D.V., Nizovtseva, I.G., 2014. Nucleation and particle growth with fluctuating rates at the intermediate stage of phase transitions in metastable systems. P. Roy. Soc. Lond. A. Mat. 470.

Anand, M., Taylor, L.A., Misra, K.C., Carlson, W.D., Sobolev, N.V., 2004. Nature of diamonds in Yakutian eclogites: views from eclogite tomography and mineral inclusions in diamonds. Lithos. 77, 333-348.

Angus, J.C., Dyble, T.J., 1975. Etching models for A {111} diamond surface: Calculation of trigon slopes. Surf. Sci. 50, 157-177.

Arima, M., Kozai, Y., 2008. Diamond dissolution rates in kimberlitic melts at 1300–1500 °C in the graphite stability field. Eur. J. Mineral. 20, 357-364.

Arima, M., Nakayama, K., Akaishi, M., Yamaoka, S., Kanda, H., 1993. Crystallization of diamond from a silicate melt of kimberlite composition in high-pressure and high-temperature experiments. Geology. 21, 968-970.

Aulbach, S., Griffin, W.L., Pearson, N.J., O'Reilly, S.Y., 2013. Nature and timing of metasomatism in the stratified mantle lithosphere beneath the central Slave craton (Canada). Chem. Geol. 352, 153-169.

Aulbach, S., Griffin, W.L., Pearson, N.J., O'Reilly, S.Y., Doyle, B.J., 2007. Lithosphere formation in the central Slave Craton (Canada): plume subcretion or lithosphere accretion? Contrib. Mineral. Petrol. 154, 409-427.

Aulbach, S., Griffin, W.L., Pearson, N.J., O'Reilly, S.Y., Kivi, K., Doyle, B.J., 2004. Mantle formation and evolution, Slave Craton: constraints from HSE abundances and Re–Os isotope systematics of sulfide inclusions in mantle xenocrysts. Chem. Geol. 208, 61-88.

Aulbach, S., Stachel, T., Creaser, R.A., Heaman, L.M., Shirey, S.B., Muehlenbachs, K., Eichenberg, D., Harris, J.W., 2009. Sulphide survival and diamond genesis during formation and evolution of Archaean subcontinental lithosphere: A comparison between the Slave and Kaapvaal cratons. Lithos. 112, 747-757.

Aulbach, S., Stachel, T., Heaman, L.M., Carlson, J.A., 2011. Microxenoliths from the Slave craton: Archives of diamond formation along fluid conduits. Lithos. 126, 419-434.

Bakker, R.J., 2003. Package FLUIDS 1. Computer programs for analysis of fluid inclusion data and for modelling bulk fluid properties. Chem. Geol. 194, 3-23.

Bakker, R.J., 2009. Package FLUIDS. Part 3: correlations between equations of state, thermodynamics and fluid inclusions. Geofluids 9, 63-74.

Bataleva, Y.V., Palyanov, Y.N., Sokol, A.G., Borzdov, Y.M., Palyanova, G.A., 2012. Conditions for the origin of oxidized carbonate-silicate melts: Implications for mantle metasomatism and diamond formation. Lithos. 128–131, 113-125.

Beeskow, B., Rankin, A.H., Murphy, P.J., Treloar, P.J., 2005. Mixed CH4–CO2 fluid inclusions in quartz from the South Wales Coalfield as suitable natural calibration standards for microthermometry and Raman spectroscopy. Chem. Geol. 223, 3-15.

Boyd, S.R., Pineau, F., Javoy, M., 1994. Modelling the growth of natural diamonds. Chem. Geol. 116, 29-42.

Brantley, S.L., 1992. The effect of fluid chemistry on quartz microcrack lifetimes. Earth Planet. Sci. Lett. 113, 145-156.

Brantley, S.L., Evans, B., Hickman, S.H., Crerar, D.A., 1990. Healing of microcracks in quartz: Implications for fluid flow. Geology. 18, 136-139.

Brett, R.C., Russell, J.K., Andrews, G.D.M., Jones, T.J., 2015. The ascent of kimberlite: Insights from olivine. Earth Planet. Sci. Lett. 424, 119-131.

Brey, G.P., Bulatov, V.K., Girnis, A.V., 2009. Influence of water and fluorine on melting of carbonated peridotite at 6 and 10 GPa. Lithos. 112, Supplement 1, 249-259.

Brey, G.P., Bulatov, V.K., Girnis, A.V., Lahaye, Y., 2008. Experimental Melting of Carbonated Peridotite at 6–10 GPa. J. Petrol. 49, 797-821.

Brooker, R.A., 1998. The Effect of CO_2 Saturation on Immiscibility between Silicate and Carbonate Liquids: an Experimental Study. J. Petrol. 39, 1905-1915.

Brooker, R.A., Sparks, R.S.J., Kavanagh, J.L., Field, M., 2011. The volatile content of hypabyssal kimberlite magmas: some constraints from experiments on natural rock compositions. Bull. Volcanol. 73, 959-981.

Bulanova, G.P., 1995. The formation of diamond. J. Geochem. Explor. 53, 1-23.

Bulanova, G.P., Griffin, W.L., Ryan, C.G., Shestakova, O.Y., Barnes, S.J., 1996. Trace elements in sulfide inclusions from Yakutian diamonds. Contrib. Mineral. Petrol. 124, 111-125.

Burke, E.A.J., 2001. Raman microspectrometry of fluid inclusions. Lithos. 55, 139-158.

Canil, D., Bellis, A.J., 2007. Ferric iron in $CaTiO_3$ perovskite as an oxygen barometer for kimberlite magmas II: applications. J. Petrol. 48, 231-252.

Canil, D., Fedortchouk, Y., 1999. Garnet dissolution and the emplacement of kimberlites. Earth Planet. Sci. Lett. 167, 227-237.

Carlson, J.A., Ravenscroft, P.J., Lavoie, C., Cunning, J., 2015. Ekati diamond mine: Northwest Territories, Canada NI 43-101 Technical Report. Dominion Diamond Corporation, p. 389.

Cartigny, P., 2005. Stable isotopes and the origin of diamond. Elements 1, 79-84.

Cartigny, P., Harris, J.W., Javoy, M., 2001. Diamond genesis, mantle fractionations and mantle nitrogen content: a study of $\delta^{13}C$–N concentrations in diamonds. Earth Planet. Sci. Lett. 185, 85-98.

Cartigny, P., Palot, M., Thomassot, E., Harris, J.W., 2014. Diamond Formation: a stable isotope perspective. Annual Review of Earth and Planetary Sciences 42, 699-732.

Cas, R.A.F., Hayman, P., Pittari, A., Porritt, L., 2008. Some major problems with existing models and terminology associated with kimberlite pipes from a volcanological perspective, and some suggestions. J. Volcanol. Geotherm. Res. 174, 209-225.

Cesare, B., 1995. Graphite precipitation in C—O—H fluid inclusions: closed system compositional and density changes, and thermobarometric implications. Contrib. Mineral. Petrol. 122, 25-33.

Chacko, T., Mayeda, T.K., Clayton, R.A., Goldsmith, J.R., 1991. Oxygen and carbon isotope fractionations between CO_2 and calcite. Geochim. Cosmochim. Acta. 55, 2867-2882.

Creaser, R.A., Grütter, H., Carlson, J., Crawford, B., 2004. Macrocrystal phlogopite Rb–Sr dates for the Ekati property kimberlites, Slave Province, Canada: evidence for multiple intrusive episodes in the Paleocene and Eocene. Lithos. 76, 399-414.

Creighton, S., Stachel, T., Eichenberg, D., Luth, R., 2010. Oxidation state of the lithospheric mantle beneath Diavik diamond mine, central Slave craton, NWT, Canada. Contrib. Mineral. Petrol. 159, 645-657.

Creighton, S., Stachel, T., McLean, H., Muehlenbachs, K., Simonetti, A., Eichenberg, D., Luth, R., 2008. Diamondiferous peridotitic microxenoliths from the Diavik Diamond Mine, NT. Contrib. Mineral. Petrol. 155, 541-554.

Cull, F.A., Meyer, H.O.A., 1986. Oxidation of diamond at high temperature and 1 atm total pressure with controlled oxygen fugacity, 4th International Kimberlite Conference, Perth, Western Australia, pp. 377-379.

Dalton, J.A., Presnall, D.C., 1998. Carbonatitic melts along the solidus of model lherzolite in the system CaO-MgO-Al2O3-SiO2-CO2 from 3 to 7 GPa. Contrib. Mineral. Petrol. 131, 123-135.

Dasgupta, R., Hirschmann, M.M., 2010. The deep carbon cycle and melting in Earth's interior. Earth Planet. Sci. Lett. 298, 1-13.

Davies, R.M., Griffin, W.L., O'Reilly, S.Y., Doyle, B.J., 2004. Mineral inclusions and geochemical characteristics of microdiamonds from the DO27, A154, A21, A418, DO18, DD17 and Ranch Lake kimberlites at Lac de Gras, Slave Craton, Canada. Lithos. 77, 39-55.

Davies, R.M., Griffin, W.L., Pearson, N.J., Andrew, A.S., Doyle, B.J., O'Reilly, S.Y., 1999. Diamonds from the deep: pipe DO-27, Slave craton, Canada, Procedings 7th International Kimberlite Conference. Red Roof Desgin, Cape Town, pp. 148-155.

Davis, W.J., Bleeker, W., 1999. Time and plutonism, deformation, and metamorphism in the Yellowknife Domain, Slave Province, Canada. Can. J. Earth Sci. 36, 1169-1187.

Day, H.W., 2012. A revised diamond-graphite transition curve. Am. Mineral. 97, 52-62.

De Giudici, G., 2002. Surface control vs. diffusion control during calcite dissolution: Dependence of step-edge velocity upon solution pH. Am. Mineral. 87, 1279-1285.

De Stefano, A., 2011. Diamonds in cratonic and orogenic settings: a study of Jericho and Wawa diamonds. University of British Columbia, Vancouver, p. 211.

De Stefano, A., Kopylova, M., Cartigny, P., Afanasiev, V., 2009. Diamonds and eclogites of the Jericho kimberlite (Northern Canada). Contrib. Mineral. Petrol. 158, 295-315.

de Theije, F.K., van Veenendaal, E., van Enckevort, W.J.P., Vlieg, E., 2001. Oxidative etching of cleaved synthetic diamond {111} surfaces. Surf. Sci. 492, 91-105.

Deines, P., 1980. The carbon isotopic composition of diamonds: relationship to diamond shape, color, occurrence and vapor composition. Geochim. Cosmochim. Acta. 44, 943-961.

DeVries, R.C., 1975. Plastic deformation and “work-hardening” of diamond. Materials Research Bulletin 10, 1193-1199.

Diamond, L.W., 2003. Introduction to gas-bearing, aqueous fluid inclusions, in: Samson, I., Anderson, A., Marshall, D. (Eds.), Fluid inclusions: Anaylsis and interpretation. Mineralogical Association of Canada, Vancouver, British Columbia, p. 374.

Dolejs, D., Manning, C.E., 2010. Thermodynamic model for mineral solubility in aqueous fluids: theory, calibration and application to model fluid-flow systems. Geofluids 10, 20-40.

Donnelly, C.L., Stachel, T., Creighton, S., Muehlenbachs, K., Whiteford, S., 2007. Diamonds and their mineral inclusions from the A154 South pipe, Diavik Diamond Mine, Northwest territories, Canada. Lithos. 98, 160-176.

Dubessy, J., Poty, B., Ramboz, C., 1989. Advances in C-O-H-N-S fluid geochemistry based on micro-Raman spectrometric analysis of fluid inclusions. Eur. J. Mineral. 1, 517-534.

Evans, B.W., 2004. The serpentine multisystem revisited: chrysotile is metastable. Int. Geol. Rev. 46, 479-506.

Evans, T., 1992. Aggregation of nitrogen in diamond, in: Field, J.E. (Ed.), The properties of natural and synthetic diamond. Academic Press, London, UK, pp. 259-290.

Evans, T., Phaal, C., 1962. Imperfections in Type I and Type II Diamonds. Proceedings of the Royal Society of London. Series A, Mathematical and Physical Sciences 270, 538-552.

Evans, T., Sauter, D.H., 1961. Etching of diamond surfaces with gases. Phil. Mag. 6, 429-440.

Fagan, A., Luth, R., 2011. Growth of diamond in hydrous silicate melts. Contrib. Mineral. Petrol. 161, 229-236.

Fedortchouk, Y., Canil, D., 2004. Intensive variables in kimberlite magmas, Lac de Gras, Canada and implications for diamond survival. J. Petrol. 45, 1725-1745.

Fedortchouk, Y., Canil, D., 2009. Diamond oxidation at atmospheric pressure: development of surface features and the effect of oxygen fugacity. Eur. J. Mineral. 21, 623-635.

Fedortchouk, Y., Canil, D., Carlson, J., 2005. Dissolution forms in Lac de Gras diamonds and their relationship to the temperature and redox state of kimberlite magma. Contrib. Mineral. Petrol. 150, 54-69.

Fedortchouk, Y., Canil, D., Semenets, E., 2007. Mechanisms of diamond oxidation and their bearing on the fluid composition in kimberlite magmas. Am. Mineral. 92, 1200-1212.

Fedortchouk, Y., Manghnani, M.H., Hushur, A., Shiryaev, A., Nestola, F., 2011. An atomic force microscopy study of diamond dissolution features: The effect of H_2O and CO_2 in the fluid on diamond morphology. Am. Mineral. 96, 1768-1775.

Fedortchouk, Y., Matveev, S., Carlson, J.A., 2010. H_2O and CO_2 in kimberlitic fluid as recorded by diamonds and olivines in several Ekati Diamond Mine kimberlites, Northwest Territories, Canada. Earth Planet. Sci. Lett. 289, 549-559.

Fedortchouk, Y., Zhang, Z., 2011. Diamond resorption: Link to metasomatic events in the mantle or record of magmatic fluid in kimberlitic magma? Can. Mineral. 49, 707-719.

Ferry, J.M., Newton, R.C., Manning, C.E., 2002. Experimental determination of the equilibria: rutile + magnesite = geikielite + CO_2 and zircon + 2 magnesite = baddeleyite + forsterite + 2 CO_2. Am. Mineral. 87, 1342-1350.

Field, M., Scott Smith, B.H., 1999. Contrasting geology and near surface emplacement of kimberlite pipes in southern African and Canada, in: Gurney, J.J. (Ed.), Proc. 7th Int. Kimberlite Conference. Red Roof Design, Cape Town, pp. 214-237.

Frank, F.C., Puttick, K.E., 1958. Etch pits and trigons on diamond: II. Phil. Mag. 3, 1273-1279.

Frank, F.C., Puttick, K.E., Wilks, E.M., 1958. Etch pits and trigons on diamond: I. Phil. Mag. 3, 1262-1272.

Frost, D.J., Wood, B.J., 1997. Experimental measurements of the properties of H_2O-CO_2 mixtures at high pressures and temperatures. Geochim. Cosmochim. Acta. 61, 3301-3309.

Gainutdinov, R.V., Shiryaev, A.A., Boyko, V.S., Fedortchouk, Y., 2013. Extended defects in natural diamonds: An Atomic Force Microscopy investigation. Diam. Relat. Mater. 40, 17-23.

Gilman, J.J., Johnston, W.G., Sears, G.W., 1958. Dislocation etch pit formation in lithium fluoride. J. Appl. Phys. 29, 747-754.

Green, H.W., Gueguen, Y. 1974. Origin of kimberlite pipes by diapiric upwelling in the upper mantle. Nature 249, 617-620.

Griffin, W.L., Doyle, B.J., Ryan, C.G., Pearson, N.J., O'Reilly, S.Y., Davies, R.M., 1999a. Layered mantle lithosphere in the Lac de Gras Area, Slave Craton: composition, structure and origin. J. Petrol. 40, 705-727.

Griffin, W.L., O'Reilly, S.Y., Doyle, B.J., Pearson, N.J., Coopersmith, H., Kivi, K., Malkovets, V., Pokhilenko, N., 2004. Lithosphere mapping beneath the North American plate. Lithos. 77, 873-922.

Griffin, W.L., Shee, S.R., Ryan, C.G., Win, T.T., Wyatt, B.A., 1999b. Harzburgite to lherzolite and back again: metasomatic processes in ultramafic xenoliths from the Wesselton kimberlite, Kimberley, South Africa. Contrib. Mineral. Petrol. 134, 232-

250.

Gurney, J.J., Hildebrand, P.R., Carlson, J.A., Fedortchouk, Y., Dyck, D.R., 2004. The morphological characteristics of diamonds from the Ekati property, Northwest Territories, Canada. Lithos. 77, 21-38.

Hall, A.E., Smith, C.B., 1984. Lamproite diamonds - are they different?, in: Glover, J.E., Harris, P.G. (Eds.), Kimberlite occurrence and origin: a basis for conceptual models in exploration. Geology Department, University of Western Australia, and University Extension, pp. 167-212.

Hansen, J.O., Copperthwaite, R.G., Derry, T.E., Pratt, J.M., 1989. A tensiometric study of diamond (111) and (110) faces. J. Colloid Interf. Sci. 130, 347-358.

Harris, J.W., Vance, E.R., 1974. Studies of the reaction between diamond and heated kimberlite. Contrib. Mineral. Petrol. 47, 237-244.

Harrison, E.R., Tolansky, S., 1964. Growth history of a atural octahedral diamond. P. Roy. Soc. Lond. A. Mat. 279, 490-496.

Harte, B., Fitzsimons, I.C.W., Harris, J.W., Otter, M.L., 1999. Carbon isotope ratios and nitrogen abundances in relation to cathodoluminescence characteristics for some diamonds from the Kaapvaal Province, S. Africa. Mineral. Mag. 63, 829-829.

Holloway, J.R., 1981. Compositions and volumes of supercritical fluids in the Earth's crust, in: Hollister, L.S., Crawford, M.L. (Eds.), Fluid inclusions, application to petrology. Short Course MAC, pp. 13-38.

Holloway, J.R., Reese, R.L., 1974. The generation of N_2-CO_2-H_2O fluids for use in hydrothermal experimentation I. Experimental method and equilibrium calculations in the C-O-H-N system. Am. Mineral. 59, 587-597.

Huang, W.L., Wyllie, P.J., Nehru, C.E., 1980. Subsolidus and liquidus phase relationships in the system CaO-SiO_2 -CO_2 to 30 kbar with geological applications. Am. Mineral. 65, 285-301.

Hull, D., Bacon, D.J., 2011. Chapter 4 - Elastic Properties of Dislocations, in: Hull, D., Bacon, D.J. (Eds.), Introduction to Dislocations (Fifth Edition). Butterworth-Heinemann, Oxford, pp. 63-83.

Jacob, D., Fung, A., Jagoutz, E., Pearson, D.G., 2003. Petrology and geochemistry of eclogite xenoliths from the Ekati kimberlites area, Extended abstract: the 8th Internation Kimberlite Conference, Victoria, p. FLA_0239.

Johnson, M.C., Walker, D., 1993. Brucite [$Mg(OH)_2$] dehydration and the molar volume of H_2O to 15 GPa. Am. Mineral. 78, 271-284.

Kamenetsky, V.S., Grütter, H., Kamenetsky, M.B., Gömann, K., 2013. Parental carbonatitic melt of the Koala kimberlite (Canada): Constraints from melt inclusions in olivine and Cr-spinel, and groundmass carbonate. Chem. Geol. 353, 96-111.

Kanda, H., Yamaoka, S., Setaka, N., Komatsu, H., 1977. Etching of diamond octahedrons by high pressure water. J. Cryst. Growth. 38, 1-7.

Kavanagh, J.L., Sparks, R.S.J., 2009. Temperature changes in ascending kimberlite magma. Earth Planet. Sci. Lett. 286, 404-413.

Kelley, S.P., Wartho, J.A., 2000. Rapid kimberlite ascent and the significance of Ar-Ar ages in xenolith phlogopites. Science. 289, 609-611.

Kennedy, C.S., Kennedy, G.C., 1976. The equilibrium boundary between graphite and diamond. J. Geophys. Res. 81, 2467-2470.

Khokhryakov, A.F., Pal'yanov, Y.N., 2007. The evolution of diamond morphology in the process of dissolution: Experimental data. Am. Mineral. 92, 909-917.

Khokhryakov, A.F., Pal'yanov, Y.N., 2010. Influence of the fluid composition on diamond dissolution forms in carbonate melts. Am. Mineral. 95, 1508-1514.

Khokhryakov, A.F., Palyanov, Y.N., 2006. Revealing of dislocations in diamond crystals by the selective etching method. J. Cryst. Growth. 293, 469-474.

Khokhryakov, A.F., Palyanov, Y.N., 2007. Revealing of planar defects and partial dislocations in large synthetic diamond crystals by the selective etching. J. Cryst. Growth. 306, 458-464.

Kjarsgaard, B.A., 2007. Kimberlite pipe models: significance for exploration, in: Milkereit, B. (Ed.), Proceedings of Exploration 07: Fifth Decennial International Conference on Mineral Exploration, pp. 667-677.

Kjarsgaard, B.A., Pearson, D.G., Tappe, S., Nowell, G.M., Dowall, D.P., 2009. Geochemistry of hypabyssal kimberlites from Lac de Gras, Canada: Comparisons to a global database and applications to the parent magma problem. Lithos. 112S, 236-248.

Klein-BenDavid, O., Izraeli, E.S., Hauri, E., Navon, O., 2004. Mantle fluid evolution - a tale of one diamond. Lithos. 77, 243-253.

Klein-BenDavid, O., Izraeli, E.S., Hauri, E., Navon, O., 2007a. Fluid inclusions in diamonds from the Diavik mine, Canada and the evolution of diamond-forming fluids. Geochim. Cosmochim. Acta. 71, 723-744.

Klein-BenDavid, O., Wirth, R., Navon, O., 2007b. Micrometer-scale cavities in fibrous and cloudy diamonds — A glance into diamond dissolution events. Earth Planet. Sci. Lett. 264, 89-103.

Kopylova, M.G., Matveev, S., Raudsepp, M., 2007. Searching for parental kimberlite melt. Geochim. Cosmochim. Acta. 71, 3616-3629.

Kopylova, M.G., Russell, J.K., Cookenboo, H., 1998. Upper-mantle stratigraphy of the Slave craton, Canada: Insights into a new kimberlite province. Geology. 26, 315-318.

Kozai, Y., Arima, M., 2005. Experimental study on diamond dissolution in kimberlitic and lamproitic melts at 1300–1420 °C and 1 GPa with controlled oxygen partial pressure. Am. Mineral. 90, 1759-1766.

Kurihara, N.I., Hirabayashi, K., Suzuki, K., Ichihara, M., Takeuchi, S., 1991. Epitaxial growth of graphite layer on {111} surface of vapor-deposited diamond. J. Appl. Phys. 69, 6360-6363.

Lang, A.R., 1964. Dislocations in diamond and the origin of trigons. P. Roy. Soc. Lond. A. Mat. 278, 234-242.

Lang, A.R., Bulanova, G.P., Fisher, D., Furkert, S., Sarua, A., 2007. Defects in a mixed-habit Yakutian diamond: studies by optical and cathodoluminescence microscopy, infrared absorption, Raman scattering and photoluminescence spectroscopy. J. Cryst. Growth. 309, 170-180.

Lang, A.R., Meaden, G.M., 1991. Complementary orientation-dependent distributions of

1.40 and 2.56 eV cathodoluminescence on vicinals on {111} in synthetic diamonds. J. Cryst. Growth. 108, 53-62.

Logvinova, A.M., Taylor, L.A., Fedorova, E.N., Yelisseyev, A.P., Wirth, R., Howarth, G., Reutsky, V.N., Sobolev, N.V., 2015. A unique diamondiferous peridotite xenolith from the Udachnaya kimberlite pipe, Yakutia: role of subduction in diamond formation. Russ. Geol. Geophys. 56, 306-320.

Lorenz, V., 1973. On the formation of maars. Bulletin Volcanologique 37, 183-204.

Lorenz, V., 1975. Formation of phreatomagmatic maar-diatreme volcanoes and its relevance to kimberlite diatremes. Phys. Chem. Earth. 9, 17-27.

Lorenz, V., 2003. Maar-diatreme volcanoes, their formation, and their setting in hard-rock or soft-rock environments. Geolines 15, 72-83.

Lorenz, V., Kurszlaukis, S., 2007. Root zone processes in the phreatomagmatic pipe emplacement model and consequences for the evolution of maar–diatreme volcanoes. J. Volcanol. Geotherm. Res. 159, 4-32.

Luth, R., Stachel, T., 2014. The buffering capacity of lithospheric mantle: implications for diamond formation. Contrib. Mineral. Petrol. 168, 1-12.

Luth, R.W., 1993. Diamonds, eclogites, and the oxidation state of the Earth's mantle. Science. 261, 66-68.

Luzi, H.W., 1892. Artificial figures of corrosion on rough diamonds. Berichte der deutschen chemischen Gesellschaft 25, 2470 - 2472.

Manning, C.E., Shock, E.L., Sverjensky, D.A., 2013. The chemistry of carbon in aqueous fluids at crustal and upper-Mantle conditions: Experimental and theoretical constraints. Rev. Mineral. Geochem. 75, 109-148.

McCallum, M.E., Huntley, P.M., Falk, R.W., Otter, M.L., 1994. Morphological, resorption and etch feature trends of diamonds from kimberlite populations within the Colorado-Wyoming State Line district, USA, in: Meyer, H.O.A., Leonardos, O.H. (Eds.), Proceedings of the 5th International Kimberlite Conference. Diamonds Characterization, Genesis and Exploration, Rio de Janeiro.

McCubbin, F.M., Sverjensky, D.A., Steele, A., Mysen, B.O., 2014. In-situ characterization of oxalic acid breakdown at elevated P and T: Implications for organic C-O-H fluid sources in petrologic experiments. Am. Mineral. 99, 2258-2271.

McGetchin, T.R., 1968. The Moses Rock dike: Geology, petrology, and mode of emplacement of a kimberlite bearing breccia dike, San Juan County, Utah. California Institute of Technology, p. 450.

Mendelssohn, M.J., Milledge, H.J., 1995. Morphological characteristics of diamond populations in relation to temperature-dependent growth and dissolution rates. Int. Geol. Rev. 37, 285-312.

Menzies, A., Westerlund, K., Grütter, H., Gurney, J., Carlson, J., Fung, A., Nowicki, T., 2004. Peridotitic mantle xenoliths from kimberlites on the Ekati Diamond Mine property, N.W.T., Canada: major element compositions and implications for the lithosphere beneath the central Slave craton. Lithos. 77, 395-412.

Mitchell, R.H., 1986. Kimberlites : mineralogy, geochemistry, and petrology Plenum Press, New York.

Mitchell, R.H., 1991. Kimberlites and lamproites: primary sources of diamond. Geosci. Can. 18, 1-16.

Mitchell, R.H., 2008. Petrology of hypabyssal kimberlites: Relevance to primary magma compositions. J. Volcanol. Geotherm. Res. 174, 1-8.

Newton, R.C., Manning, C.E., 2000. Quartz solubility in H_2O-NaCl and H_2O-CO_2 solutions at deep crust-upper mantle pressures and temperatures: 2–15 kbar and 500–900°C. Geochim. Cosmochim. Acta. 64, 2993-3005.

Newton, R.C., Manning, C.E., 2002. Solubility of enstatite + forsterite in H_2O at deep crust/upper mantle conditions: 4 to 15 kbar and 700 to 900 °c. Geochim. Cosmochim. Acta. 66, 4165-4176.

Newton, R.C., Manning, C.E., 2008. Thermodynamics of SiO_2–H_2O fluid near the upper critical end point from quartz solubility measurements at 10 kbar. Earth Planet. Sci. Lett. 274, 241-249.

Newton, R.C., Manning, C.E., 2009. Hydration state and activity of aqueous silica in H_2O-

CO_2 fluids at high pressure and temperature. Am. Mineral. 94, 1287-1290.

Newton, R.C., Sharp, W.E., 1975. Stability of forsterite + CO_2 and its bearing on the role of CO_2 in the mantle. Earth Planet. Sci. Lett. 26, 239-244.

Nicolas, K.M.A., 2014. Diamond sources beneath the Hall Peninsula, Baffin Island, Nunavut: A preliminary assessment based on Chidliak diamonds, Earth and Atmospheric Sciences. University of Alberta, p. 184.

Nowicki, T., Crawford, B., Dyck, D., Carlson, J., McElroy, R., Oshust, P., Helmstaedt, H., 2004. The geology of kimberlite pipes of the Ekati property, Northwest Territories, Canada. Lithos. 76, 1-27.

Nowicki, T., Porritt, L., Crawford, B., Kjarsgaard, B., 2008. Geochemical trends in kimberlites of the Ekati property, Northwest Territories, Canada: Insights on volcanic and resedimentation processes. J. Volcanol. Geotherm. Res. 174, 117-127.

Omar, M., Kenawi, M., 1957. The etching of diamonds by low pressure oxygen. Phil. Mag. 2, 859-863.

Orlov, I.L., 1977. The mineralogy of the diamond. Wiley, New York.

Ostrovskaya, L., Perevertailo, V., Ralchenko, V., Dementjev, A., Loginova, O., 2002. Wettability and surface energy of oxidized and hydrogen plasma-treated diamond films. Diam. Relat. Mater. 11, 845-850.

Palyanov, Y.N., Sokol, A.G., 2009. The effect of composition of mantle fluids/melts on diamond formation processes. Lithos. 112, Supplement 2, 690-700.

Palyanov, Y.N., Sokol, A.G., Khokhryakov, A.F., Kruk, A.N., 2015. Conditions of diamond crystallization in kimberlite melt: experimental data. Russ. Geol. Geophys. 56, 196-210.

Patel, A.R., Patel, S.M., 1973. Characteristic etch patterns on (111) faces of diamond. Acta Crystallogr., Sect. A: Found. Crystallogr. A29, 571-572.

Patel, A.R., Ramanathan, S., 1962. Etch pits on diamond surfaces. Phil. Mag. 7, 1305-1314.

Phillips, W.J., 1972. Hydraulic fracturing and mineralization. J. Geol. Soc. 128, 337-359.

Ponton, J.W., Reekie, T.D.R., Angus, J.C., 1974. Computer simulation of etching of diamond surfaces. Diamond Research 1974, 33-38.

Porritt, L.A., Cas, R.A.F., Crawford, B.B., 2008. In-vent column collapse as an alternative model for massive volcaniclastic kimberlite emplacement: An example from the Fox kimberlite, Ekati Diamond Mine, NWT, Canada. J. Volcanol. Geotherm. Res. 174, 90-102.

Price, S.E., Russell, J.K., Kopylova, M.G., 2000. Primitive magma from the Jericho Pipe, N.W.T., Canada: constraints on primary kimberlite melt chemistry. J. Petrol. 41, 789-808.

Richardson, S.H., Gurney, J.J., Erlank, A.J., Harris, J.W., 1984. Origin of diamonds in old enriched mantle. Nature. 310, 198-202.

Robinson, D.K., 1979. Surface textures and other features of diamonds. University of Cape Town, p. 418.

Roedder, E., 1984. Fluid inclusions, in: Ribbe, P.H. (Ed.), Reveiws in Mineralogy. Mineralogical Society of America, Washington, p. 644.

Rudenko, A.P., Kulakova, I.I., Shturman, V.L., 1979. Oxidation of natural diamond, New Data on Minerals of the USSR. Fersman Mineralogical Museum, Moscow, pp. 105-125.

Russell, J.K., Gordon, T.M., Moss, S., 2008. Volatiles in kimberlite: volume relationships and implications for conduit and eruption dynamics, 9th International Kimberlite Conference Extended Abstract, pp. No. 9IKC-A-00299.

Russell, J.K., Porritt, L.A., Lavallee, Y., Dingwell, D.B., 2012. Kimberlite ascent by assimilation-fuelled buoyancy. Nature. 481, 352-356.

Sarkar, C., Heaman, L.M., Pearson, D.G., 2015. Duration and periodicity of kimberlite volcanic activity in the Lac de Gras kimberlite field, Canada and some recommendations for kimberlite geochronology. Lithos. 218–219, 155-166.

Sauter, D.H., 1961. Etching of low index faces of diamond in gases. University of Reading.

Schmidberger, S.S., Simonetti, A., Heaman, L.M., Creaser, R.A., Whiteford, S., 2007. Lu–Hf, in-situ Sr and Pb isotope and trace element systematics for mantle eclogites from the Diavik diamond mine: Evidence for Paleoproterozoic subduction beneath the Slave craton, Canada. Earth Planet. Sci. Lett. 254, 55-68.

Schrauder, M., Navon, O., 1993. Solid carbon dixoide in a natural diamond. Nature. 365, 42-44.

Scott Smith, B.H., 2008. Canadian kimberlites: Geological characteristics relevant to emplacement. J. Volcanol. Geotherm. Res. 174, 9-19.

Seal, M., 1965. Structure in diamonds as revealed by etching. Am. Mineral. 50, 105-123.

Shee, S.R., Gurney, J.J., Robinson, D.N., 1982. Two diamond-bearing peridotite xenoliths from the finsch kimberlite, South Africa. Contrib. Mineral. Petrol. 81, 79-87.

Skinner, E.M.W., 2008. The emplacement of class 1 kimberlites. J. Volcanol. Geotherm. Res. 174, 40-48.

Skinner, E.M.W., Bristow, J.W., Smith, C.B., Scott Smith, B.H., Dawson, J.B., 1985. Proterozoic kimberlites and lamproites and a preliminary age for the Argyle lamproite pipe, Western Australia. Trans. Geol. Soc. S. Afr. 88, 335-340.

Skinner, E.M.W., Marsh, J.S., 2004. Distinct kimberlite pipe classes with contrasting eruption processes. Lithos. 76, 183-200.

Smart, K.A., Chacko, T., Stachel, T., Muehlenbachs, K., Stern, R.A., Heaman, L.M., 2011. Diamond growth from oxidized carbon sources beneath the Northern Slave Craton, Canada: A $\delta^{13}C$–N study of eclogite-hosted diamonds from the Jericho kimberlite. Geochim. Cosmochim. Acta. 75, 6027-6047.

Smit, K.V., Stachel, T., Stern, R.A., 2014. Diamonds in the Attawapiskat area of the Superior craton (Canada): evidence for a major diamond-forming event younger than 1.1 Ga. Contrib. Mineral. Petrol. 167, 1-16.

Smith, E.M., Kopylova, M.G., Frezzotti, M.L., Afanasiev, V.P., 2015. Fluid inclusions in Ebelyakh diamonds: Evidence of CO_2 liberation in eclogite and the effect of H_2O on diamond habit. Lithos. 216–217, 106-117.

Sneeringer, M.A., Watson, E.B., 1985. Milk cartons and ash cans: two unconventional welding techniques. Am. Mineral. 70, 200-201.

Snyder, D.B., Hillier, M.J., Kjarsgaard, B.A., de Kemp, E.A., Craven, J.A., 2014. Lithospheric architecture of the Slave craton, northwest Canada, as determined from an interdisciplinary 3-D model. Geochem. Geophys. Geosyst. 15, 1895-1910.

Sobolev, V.N., Taylor, L.A., Snyder, G.A., Sobolev, N.V., 1994. Diamondiferous Eclogites from the Udachnaya Kimberlite Pipe, Yakutia. Int. Geol. Rev. 36, 42-64.

Sokol, A.G., Pal'yanov, Y.N., Pal'yanova, G.A., Khokhryakov, A.F., Borzdov, Y.M., 2001. Diamond and graphite crystallization from C–O–H fluids under high pressure and high temperature conditions. Diam. Relat. Mater. 10, 2131-2136.

Sokol, A.G., Pal'yanov, Y.N., 2008. Diamond formation in the system $MgO–SiO_2–H_2O–C$ at 7.5 GPa and 1,600°C. Contrib. Mineral. Petrol. 155, 33-43.

Sonin, V.M., Zhimulev, E.I., Fedorov, I.I., Chepurov, A.I., 2006. Effect of oxygen fugacity on the etching rate of diamond crystals in silicate melt. Geol. Ore Deps. 48, 499-501.

Sparks, R.S.J., Baker, L., Brown, R.J., Field, M., Schumacher, J., Stripp, G., Walters, A., 2006. Dynamical constraints on kimberlite volcanism. J. Volcanol. Geotherm. Res. 155, 18-48.

Sparks, R.S.J., Pinkerton, H., Macdonald, R., 1977. The transport of xenoliths in magmas. Earth Planet. Sci. Lett. 35, 234-238.

Sparks, S.R., Brooker, R., Field, M., Kavanagh, J., 2009. Volatiles in kimberlite magmas: Experimental constraints. AGU Spring Meeting Abstracts, A5.

Spetsius, Z.V., 1995. Occurrence of diamond in the mantle: a case study from the Siberian Platform. J. Geochem. Explor. 53, 25-39.

Stachel, T., Aulbach, S., Brey, G.P., Harris, J.W., Leost, I., Tappert, R., Viljoen, K.S., 2004. The trace element composition of silicate inclusions in diamonds: a review. Lithos. 77, 1-19.

Stachel, T., Brey, G.P., Harris, J.W., 2005. Inclusions in Sublithospheric Diamonds: Glimpses of Deep Earth. Elements 1, 73-78.

Stachel, T., Harris, J.W., 2008. The origin of cratonic diamonds — Constraints from mineral inclusions. Ore Geol. Rev. 34, 5-32.

Stachel, T., Harris, J.W., 2009. Formation of diamond in the Earth's mantle. J. Phys.: Condens. Matter. 21, 364-206.

Stachel, T., Harris, J.W., Muehlenbachs, K., 2009. Sources of carbon in inclusion bearing diamonds. Lithos. 112, Supplement 2, 625-637.

Stachel, T., Harris, J.W., Tappert, R., Brey, G.P., 2003. Peridotitic diamonds from the Slave and the Kaapvaal cratons—similarities and differences based on a preliminary data set. Lithos. 71, 489-503.

Stachel, T., Luth, R.W., 2015. Diamond formation — Where, when and how? Lithos. 220–223, 200-220.

Stagno, V., Frost, D.J., McCammon, C.A., Mohseni, H., Fei, Y., 2015. The oxygen fugacity at which graphite or diamond forms from carbonate-bearing melts in eclogitic rocks. Contrib. Mineral. Petrol. 169, 1-18.

Stagno, V., Ojwang, D.O., McCammon, C.A., Frost, D.J., 2013. The oxidation state of the mantle and the extraction of carbon from Earth's interior. Nature. 493, 84-88.

Stepanov, A.S., Shatsky, V.S., Zedgenizov, D.A., Sobolev, N.V., 2007. Causes of variations in morphology and impurities of diamonds from the Udachnaya Pipe eclogite. Russ. Geol. Geophys. 48, 758-769.

Stern, R.A., Palot, M., Howell, D., Stachel, T., Pearson, D.G., Cartigny, P., Oh, A., 2014. Methods and Reference Materials for SIMS Diamond C- and N-isotope Analysis, Canadian Centre for Isotopic Microanalysis Technical Report 14-01, University of Alberta.

Sterner, S.M., Bodnar, R.J., 1989. Synthetic fluid inclusions - VII. Re-equilibration of fluid inclusions in quartz during laboratory-simulated metamorphic burial and uplift. J. Metamorph. Geol. 7, 243-260.

Sunagawa, I., 1984. Morphology of natual and sysnthetic diamond crystals, in: Sunagawa, I. (Ed.), Matersials scicence of the Earth's interior Terra Sicentific, Tokyo, pp. 303-330.

Sunagawa, I., 1990. Growth and morphology of diamond crystals under stable and metastable contitions. J. Cryst. Growth. 99, 1156-1161.

Sunagawa, I., 2005. Crystals: growth, morphology, and perfection. Cambridge University Press.

Tappert, R., Stachel, T., Harris, J.W., Shimizu, N., Brey, G.P., 2005. Mineral inclusions in diamonds from the Panda kimberlite, Slave Province, Canada. Eur. J. Mineral. 17, 423-440.

Tappert, R., Tappert, M., 2011. The Morphology of Diamonds, Diamonds in Nature. Springer Berlin Heidelberg, pp. 13-42.

Taylor, L.A., Anand, M., 2004. Diamonds: time capsules from the Siberian Mantle. Chem. Erde Geochem. 64, 1-74.

Taylor, W.R., Canil, D., Judith Milledge, H., 1996. Kinetics of Ib to IaA nitrogen aggregation in diamond. Geochim. Cosmochim. Acta. 60, 4725-4733.

Taylor, W.R., Green, D.H., 1988. Measurement of reduced peridotite-C-O-H solidus and implications for redox melting of the mantle. Nature. 332, 349-352.

Thomassot, E., Cartigny, P., Harris, J.W., Viljoen, K.S., 2007. Methane-related diamond crystallization in the Earth's mantle: Stable isotope evidences from a single diamond-bearing xenolith. Earth Planet. Sci. Lett. 257, 362-371.

Tingle, T.N., Roedder, E., Green, H.W., 1992. Formation of fluid inclusions and etch tunnels in olivine at high pressure. Am. Mineral. 77, 296-302.

Tolansky, S., Wilcock, W.L., 1947. Interference studies of diamond faces. A crossed fringe technique. P. Roy. Soc. Lond. A. Mat. 191, 182-194.

Varma, C.K.R., 1967. Trigons on diamond. Phil. Mag. 16, 959-974.

Viljoen, K.S., Dobbe, R., Smit, B., Thomassot, E., Cartigny, P., 2004. Petrology and geochemistry of a diamondiferous lherzolite from the Premier diamond mine, South Africa. Lithos. 77, 539-552.

Viljoen, K.S., Swash, P.M., Otter, M.L., Schulze, D.J., Lawless, P.J., 1992.

Diamondiferous garnet harzburgites from the Finsch kimberlite, Northern Cape, South Africa. Contrib. Mineral. Petrol. 110, 133-138.

Walter, M.J., Presnall, D.C., 1994. Melting behavior of simplified lherzolite in the system CaO-MgO-Al_2O_3-SiO_2-Na_2O from 7 to 35 kbar. J. Petrol. 35, 329-359.

Wang, H., Zhang, Z., Wong, L.M., Wang, S., Wei, Z., Li, G.P., Xing, G., Guo, D., Wang, D., Wu, T., 2010. Shape-controlled fabrication of micro/nanoscale triangle, square, wire-like, and hexagon pits on silicon substrates induced by anisotropic diffusion and silicide sublimation. ACS nano 4, 2901-2909.

Watson, B.E., Brenan, J.M., 1987. Fluids in the lithosphere, 1. Experimentally-determined wetting characteristics of CO_2-H_2O fluids and their implications for fluid transport, host-rock physical properties, and fluid inclusion formation. Earth Planet. Sci. Lett. 85, 497-515.

Watson, E., Wark, D., Price, J., Van Orman, J., 2002. Mapping the thermal structure of solid-media pressure assemblies. Contrib. Mineral. Petrol. 142, 640-652.

Westerlund, K., Shirey, S., Richardson, S., Carlson, R., Gurney, J., Harris, J., 2006. A subduction wedge origin for Paleoarchean peridotitic diamonds and harzburgites from the Panda kimberlite, Slave craton: evidence from Re–Os isotope systematics. Contrib. Mineral. Petrol. 152, 275-294.

Williams, A.F., 1932. The genesis of the diamond. Ernest Benn, London.

Williams, D.W., Kennedy, G.C., 1969. Melting curve of diopside to 50 kilobars. J. Geophys. Res. 74, 4359-4366.

Wilson, L., Head, J.W., 2007. An integrated model of kimberlite ascent and eruption. Nature. 447, 53-57.

Wopenka, B., Pasteris, J.D., 1987. Raman intensities and detection limits of geochemically relevant gas mixtures for a laser Raman microprobe. Analytical Chemistry 59, 2165-2170.

Wunder, B., 1998. Equilibrium experiments in the system MgO–SiO_2–H_2O (MSH): stability fields of clinohumite-OH [$Mg_9Si_4O_{16}(OH)_{\square}$], chondrodite-OH [$Mg_5Si_2O_8(OH)_2$] and phase A ($Mg_7Si_2O_8(OH)_6$). Contrib. Mineral. Petrol. 132, 111-

120.

Wykes, J.L., Newton, R.C., Manning, C.E., 2011. Forsterite solubility in NaCl-H_2O fluids at upper mantle P-T conditions, AGU Fall Meeting Abstract, U53B-0059.

Wyllie, P.J., 1978. The effect of H_2O and CO_2 on planetary mantle. Geophys. Res. Lett. 5, 440-442.

Yamaoka, S., Kanda, H., Setaka, N., 1980. Etching of diamond octahedrons at high temperatures and pressure with controlled oxygen partial pressure. J. Mater. Sci. 15, 332-336.

Zedgenizov, D.A., Harte, B., Shatsky, V.S., Politov, A.A., Rylov, G.M., Sobolev, N.V., 2006. Directional chemical variations in diamonds showing octahedral following cuboid growth. Contrib. Mineral. Petrol. 151, 243-244.

Zhang, C., Duan, Z., 2010. GFluid: An Excel spreadsheet for investigating C–O–H fluid composition under high temperatures and pressures. Comput. Geosci. 36, 569-572.

Zhang, Y.-G., Frantz, J.D., 2000. Enstatite-forsterite-water equilibria at elevated temperatures and pressures. Am. Mineral. 85, 918-925.

Zhang, Z., Fedortchouk, Y., 2012. Records of mantle metasomatism in the morphology of diamonds from the Slave craton. Eur. J. Mineral. 24, 619-632.

Zhang, Z., Fedortchouk, Y., Hanley, J.J., 2015. Evolution of diamond resorption in a silicic aqueous fluid at 1–3 GPa: Application to kimberlite emplacement and mantle metasomatism. Lithos. 227, 179-193.

Zimanowski, B., 1998. Phreatomagmatic explosions, in: Freundt, A., Rosi, M. (Eds.), From magma to tephra: Developments in volcanology. Elsevier, Amsterdam, pp. 25-54.

APPENDIX A. CONTRIBUTIONS OF AUTHORS

I wrote all the chapters of this dissertation solely. My supervisor Yana Fedortchouk edited all the chapters.

For chapter 2, Z. Zhang described the morphologies of diamonds under the guidance from Y. Fedortchouk, polished all diamonds in UBC with the assistance of E. Smith, and imaged all diamonds in UBC with the help from Mati Raudsepp and Jenny Lai. All infrared spectra of diamonds were collected by Z. Zhang in UofA under the guidance from Sergei Matveev. A version of this chapter has been published as: *Z. Zhang, Y. Fedortchouk, 2012. Records of mantle metasomatism in the morphology of diamonds from the Slave craton. European Journal of Mineralogy, 24, 619-632.*

For chapter 3, Z. Zhang prepared all the samples and collected all the BSE and CL images of diamonds in UofA under the guidance from R. Stern and A. Crowell. Z. Zhang did all analysis work (C isotope and N contents) in UofA under the guidance from R. Stern. R. Stern did all the calibration of the results.

For chapter 4, Z. Zhang conducted all diamond dissolution experiments under the guidance from Y. Fedortchouk and J. Hanley. Z. Zhang described all experimental results, selected inclusion-bearing samples, calibrated the AFM, and collected the microsurface features of all diamonds using AFM. J. Hanley prepared the fluid inclusion samples, collected all

microthermometric data in SMU. All the results and interpretations are Z. Zhang's own work with minor contributions from J. Hanley. This chapter has been published as: *Zhang, Z., Fedortchouk, Y., Hanley, J.J., 2015. Evolution of diamond resorption in a silicic aqueous fluid at 1–3 GPa: Application to kimberlite emplacement and mantle metasomatism. Lithos. 227, 179-193.*

For chapter 5, Z. Zhang conducted all diamond dissolution experiments under the guidance from Y. Fedortchouk and with the help from C. Manning. Z. Zhang described all experimental results, collected the surface features on diamonds using AFM, and chose inclusion-bearing samples for subsequential analysis. J. Hanley prepared the fluid inclusion samples, collected microthermometric data, and calculated the bulk composition of fluid inclusions in SMU. M. Kerr and Z. Zhang collected Raman spectra of synthetic inclusions in SMU. Results and interoperation of fluid inclusions were Z. Zhang's own work with significant contributions from Y. Fedortchouk and J. Hanley. A version of the chapter is in preparation for submission as: *Zhang, Z., Fedortchouk, Y., Hanley, J., Kerr, M., Diamond resorption morphology as a semi-quantitative fluid probe: constrains from diamond dissolution in CO_2-H_2O mixture at 1-3 GPa and 1250 to 1350 ^oC.*

APPENDIX B. SUPPLEMENTARY MATERIAL FOR CHAPTER 2: MANTLE-DERIVED MORPHOLOGY OF DIAMOND: RECORDS OF DIAMOND-DESTROYING MANTLE METASOMATISM IN THE SLAVE CRATON

Table B.1 Morphology, nitrogen data and zoning patterns on CL images of diamond from Grizzly, Misery, Leslie, and Koala kimberlite pipes.

Resorp. Style	Diamond	Twin	Color & Intensity	CL data		FTIR data		
				sequences,core to rim	Surf. type	Spot	N_T, ppm	IaB, %B
Grizzly kimberlite (95 stones)								
CM-1	G97-1-1	twin	Br 3	1_5_3b	R	rim	156	64
	G97-1-3		Br 2	5	R	rim	79	56
	G97-1-4		Br 1	6_5	R	rim	135	56
	G97-1-5		Br 4	1	R	rim	99	30
	G97-1-6		Br 1	4	R	rim	663	70
						core	740	71
	G97-1-7		W	1_2a_3b_2b_11	R	rim	149	72
						core	131	80
	G97-1-8		Br 2	5_1	R	rim	190	37
						core	187	43
	G97-1-9		W	10_3b_5_1	R	rim	102	52
SM-1	G97-3-3		Br 1	2b	G	rim	791	37
SM-2	G97-2-1		Br 2	5_3b_3b_1_3a	R	core	195	74
	G97-2-2		W	6_3b_3b	R	rim	57	61
	G97-2-3		Br 1	2a_2b_2b	R	core	67	56
	G97-2-5		Br 3	3b_4_3b_11	R	rim	403	88
	G97-5-1		Br 3	1_2a_3a_3b_3b	R	rim	364	83
	G97-5-2		W	3a_2b_3b	R	core	39	51
	G97-3-1		Br 1	1_3b	R	rim	132	75
	G97-4-1		Br 1	2b_3b_3b	R	rim	572	65
						core	632	67
KIM-2	G97-5-3		Br 1	1_2b	R	rim	140	32
	G97-5-5		Br 1	5_3b_3b	R	core	141	56

Continued on next page…

Resorp. Style	Diamond	Twin	Color & Intensity	CL data		FTIR data		
				sequences,core to rim	Surf. type	Spot	N_T, ppm	IaB, %B
Misery kimberlite (235 stones)								
CM-1	M95-1-1		Br 1	6_3a_3a_6	R	rim	299	92
						core	289	92
	M95-1-4		Br 1	2b_1_2a	R	rim	586	88
						core	1052	12
SM-1	M95-2-1		W	5_3b	R	rim	1116	37
	M95-1-5		Br 2	4_3a_4_3b	R	rim	763	16
	M95-2-2		Br 2	2a_3b_4_3b	R	rim	1045	26
						core	1073	18
	M95-2-3		W	2b	R	rim	1156	37
						core	202	91
	M95-2-4		W	2b	U	rim	1505	25
	M95-2-5		Br 1	1_3a_3b_2b	R	core	1376	41
	M95-2-14		W	2b_3a	U	rim	903.5	3
						core	946	8
SM-2	M95-2-6		W	4	U	rim	1110	3
	M95-2-7		W	1_3b_11	R	rim	913	2
SM-2	M95-2-8		W	2b_8	R	rim	997	12
						core	982	11
	M95-2-9		W	4_3a_3b	U	rim	949	3
	M95-2-10		W	4_3a_3b	R	rim	944	10
	M95-2-11		W	9_1_2b	R	rim	929	97
						core	934	98
	M95-2-12		W	1_2b_3b_3b	R	rim	804	98
	M95-2-12		W			core	839	98
	M95-2-13		Br 1	1_2b_3b_3b	R	rim	171	85
	M95-2-15		Br 1	1_3b_3b_3b	R	rim	370	94
						core	390	94
	M95-1-2		Br 1	4_3b	U	rim	714	5
						core	782	9
	sM95-3-1		Br 2	5_3b_8_11	R	rim	1009	14
						core	239	64
	sM95-3-10		W	4_3a_4_3b_11	R	rim	848	9
						core	642	22
SM-3a	M95-4-2		W	9_1_2b_1	U	rim	1697	31
						core	1441	27
	M95-3-6		W	6_3b	R	core	733	0
	M95-3-1		W	5_3a_5_2a_3a	U	rim	306	52
						core	359	59
	M95-3-5		W	5_3a_1_2b	R	rim	948	12

Continued on next page…

Resorp. Style	Diamond	Twin	Color & Intensity	CL data		FTIR data		
				sequences,core to rim	Surf. type	Spot	N_T, ppm	IaB, %B
SM-3b	M95-3-2		Br 1	5_2b	U	rim	784	14
						core	800	11
	M95-3-3		W	9_2b	R	core	1174	12
						core	1042	15
	M95-3-8		W	2b	R	rim	1223	13
						core	1211	12
	M95-3-10		W	5_3a_3b	R	rim	1092	13
						core	1072	11
	sM95-3-7		W	5_3b	R	rim	1235	36
						core	1275	46
	M95-3-4	twin	Br 1	5_3a_3b	R	rim	550	98
						core	459	97
	M95-4-5	twin	Br 1	5_3a_3a_1_8	U	rim	397	75
						core	378	76
	M95-4-6	twin	Br 1	1_8_3a_1_3b	R	rim	336	14
						core	255	5
	M95-4-7	twin	Br 1	10_2b_1_8	U	rim	230	73
						core	182	68
	M95-4-1	twin	W	1_5_8_3b	U	rim	64	23
KIM-1	M95-5-3		W	9_2b	R	rim	1074	13
						core	1073	20
	M95-5-4		W	6_1_3b	R	rim	20	55
						core	63	75
	M95-5-5		W	4_5_2b_8	R	core	830	13
	M95-5-7		W	4_3b	R	core	1157	46
Unr.	M34 *		W			rim	1082	15
	M83 *		W			rim	1241	15
	M45 *		W			rim	1053	14
	M17 *		W			rim	1194	12
Leslie kimberlite (159 stones)								
CM-2	L97-1-2		W	2a_2b_1_7_1/11	R	rim	927	35
						core	872	31
	L97-1-3		Br 2	1_3a_1/11	R	rim	217	71
						core	300	73
CM-3	L97-1-1		W	2b_8_7	R	rim	563.4	0
						core	697	15
	L97-1-5		W	2b	R	rim	920	12
						core	896	19
SM-1	L97-2-2		W	3a_2b	R	rim	1025	8
						core	1004	6

Continued on next page…

Resorp. Style	Diamond	Twin	Color & Intensity	CL data		FTIR data		
				sequences,core to rim	Surf. type	Spot	N_T, ppm	IaB, %B
SM-1	L97-2-3		Br 1	3a_1_4_3b	R	rim	783	14
	L97-2-7		W	2b_5_3b_2b	R	rim	542	14
						core	458	3
	L97-5-7		W	2b	U	core	937	18
	sL97-A2-5		W	4_11_8_3b	U	rim	980	5
						core	846	9
	sL97-A2-8	twin	W	5_7_1_3b?	R	rim	832	81
						core	709	84
SM-2	L97-2-4		W	2b_3b_1	R	rim	501	88
	L97-2-5		Br 1	3a_3b_11	U	rim	106	50
	L97-2-5		Br 1			core	281	80
	L97-2-8		Br 1	2b_5_11	R	rim	368	31
			Br 1			core	304	30
	L97-2-6		Br 2	5_2a_3b_3b	R	rim	300	81
	L97-2-9		Br 3	2a_3a_3b	R	rim	370	38
						core	456	50
	L97-3-5		Br 2	5	R	rim	148	34
SM-3a	L97-4-1	twin	W	2b_3a_3b_3a_3b	U	rim	360	97
	L97-4-3		W	6_2b_1_2b_3b_1	U	rim	328	84
						core	314	85
	L97-4-4	twin	W	2a_2b_3a_3b_1_3a	U	rim	461	63
						core	484	62
SM-3a	L97-4-2		Br 1	5_3b_1_3a_1_11	U	rim	303	63
	L97-4-5		W	5_1_3b	R	rim	309	53
						core	493	70
	L97-4-7	twin	Br 1	3a_3b_11?	R	core	174	21
	L97-4-8	twin	Br 1	6_3a_3b_3b	R	rim	184	46
						core	384	85
	L97-3-4		W	6_2b	R	rim	923	8
						core	950	14
SM-3b	L97-3-2		W	2b_3a_2b_1	R	rim	234	74
						core	161	67
	L97-3-3	twin	Br 1	5_2a_1_3b_1_3a	R	rim	200	35
	L97-4-6	twin	W	1_1_2b_2a	U	rim	472	26
	L97-2-1		W	1_1_2b_2a	U	core	1031	4
KIM-2	L97-5-3		W	2b_1_2b	R	rim	1128	20
						core	1177	23
	L97-5-4		Br 1	2b_6_3a_1_11_1	R	rim	64	44
						core	66	56

Continued on next page…

Resorp. Style	Diamond	Twin	Color & Intensity	CL data		FTIR data		
				sequences,core to rim	Surf. type	Spot	N_T, ppm	IaB, %B
KIM-2	L97-5-5		W	2b_1_2b	R	rim	829	28
						core	789	27
	L97-5-6		W	2b_3a_2b_3b	R	rim	410	8
						core	263	21
	L97-4-9		W	1_2b_2b	R	rim	1001	20
						core	961	31
Unr.	L97-5-1		W	2b	G	rim	932	7
						core	1005	15
Koala kimberlite (141 stones)								
CM-1	K95-1-5		Br 1	6_2b_1_3a_1	R	rim	266	74
CM-2	K95-1-2		W	1_2a_7_1/11	R	rim	441	6
	K95-1-3		W	6_2a_2b_1/11	R	rim	719	9
	K95-1-3		W			core	716	8
CM-3	K95-1-4		W	3a_2b_3a_2b_2a_2b	R	rim	1092	20
						core	1034	23
SM-1	K95-2-1		W	2b	U	rim	904	15
						core	816	15
	sK95-3-2		W	2b_3b	R	core	740	6
SM-2	K95-2-2		W	2b_3a_3b	R	rim	784	19
						core	809	35
	K95-1-1		W	4_1_3b_3b	R	rim	872	0
						core	702	0
	K95-3-1		W	9_2b_11	U	core	349	1
	K95-3-4		W	2b_7_1_8	U	core	802	50
SM-3b	K95-3-2		W	6_1_9_2b	R	rim	262	38
	sK95-3-3		W	9_1	U	rim	1073	4
SM-4	K95-3-3		W	2b_3b_4	R	rim	704	9
KIM-1	K95-5-2		W	2b_3b_2b/3b	R	rim	663	16
						core	840	32
	K95-5-3		W	3b_5_2b	R	rim	553	17
						core	587	25
	K95-5-4		W	2a_2b_1	R	core	925	22
Unr.	K95-5-1		W	2b	G	rim	950	20
						core	921	19

* = Data from Fedortchouk & Zhang (2011);

Resorp. = Resorption; Unr. = Unresorbed; Surf. = Surface;

W = White (Colorless);

Br = Brown color with intensity of color increases from 1 to 4 following scheme from Gurney et al. (2004);

G = Growth; R = Resorption; U = Uncertain;

N_T = total N content.

APPENDIX C. SUPPLEMENTARY MATERIAL FOR CHAPTER 3: REFERENCES OF DIAMONDIFEROUS XENOLITHS

C.1. REFERENCES FOR DIAMONDIFEROUS PERIDOTITE

Aulbach, S., Stachel, T., Heaman, L.M., Carlson, J.A., 2011. Microxenoliths from the Slave craton: Archives of diamond formation along fluid conduits. Lithos. 126, 419-434.

Creighton, S., Stachel, T., McLean, H., Muehlenbachs, K., Simonetti, A., Eichenberg, D., Luth, R., 2008. Diamondiferous peridotitic microxenoliths from the Diavik Diamond Mine, NT. Contrib. Mineral. Petrol. 155, 541-554.

Daniels, L.R.M., Richardson, S.H., Menzies, A., de Bruin, D., Gurney, J.J., 1995. Diamondiferous garnet macrocrysts in the Newlands kimberlite, South Afric - Rosetta stones from the Kaapvaal craton keel, Extended abstracts 6th Internationl Kimberlite Conference Novosibirsk, Russia.

Dawson, J.B., Smith, J.V., 1975. Occurrence of diamond in a mica-garnet lherzolite xenolith from kimberlite. Nature. 254, 580-581.

Deines, P., Gurney, J.J., Harris, J.W., 1984. Associated chemical and carbon isotopic composition variations in diamonds from Finsch and Premier kimberlite, South Africa. Geochim. Cosmochim. Acta. 48, 325-342.

Gurney, J.J., Hatton, C.J., 1986. Diamondiferous Minerals From the Star Mine, South Africa, Extended Abstract 4th International Kimberlite Conference. Geological Society of Australia, Perth, Australia, pp. 392-394.

Hall, A.E., Smith, C.B., 1984. Lamproite diamonds - are they different?, in: Glover, J.E., Harris, P.G. (Eds.), Kimberlite occurrence and origin: a basis for conceptual models in exploration. Geology Department, University of Western Australia, and University Extension, pp. 167-212.

He, G., 1987. Mantle xenoliths from kimberlites in China, in: Nixon, P.H. (Ed.), Mantle

xenoliths John Wiley & Sons, New York, pp. 181-185.

Jaques, A.L., O'Neill, H.S.C., Smith, C.B., Moon, J., Chappell, B.W., 1990. Diamondiferous peridotite xenoliths from the Argyle (AK1) lamproite pipe, Western Australia. Contrib. Mineral. Petrol. 104, 255-276.

Kiviets, G.B., 2000. A detailed geochemical investigation of diamond-bearing eclogite xenoliths from the Kaalvallei kimberlite, South Africa, Department of Geological Sciences. University of Cape Town, South Africa, p. 159.

Logvinova, A.M., Taylor, L.A., Fedorova, E.N., Yelisseyev, A.P., Wirth, R., Howarth, G., Reutsky, V.N., Sobolev, N.V., 2015. A unique diamondiferous peridotite xenolith from the Udachnaya kimberlite pipe, Yakutia: role of subduction in diamond formation. Russ. Geol. Geophys. 56, 306-320.

Malkovets, V., Zedgenizov, D.A., Griffin, W.L., Dak, A., O'Reilly, S.Y., Pokhilenko, N.P., Mityukhin, S., 2008. Diamondiferous microxenoliths and xenocrysts from the Nyurbinskaya kimberlite pipe, Yakutia Extended Abstract 9th International Kimberlite Conference, Frankfurt, Germany, pp. No. 9IKC-A-00224.

McCallum, M.E., Eggler, D.H., 1976. Diamonds in an Upper Mantle Peridotite Nodule from Kimberlite in Southern Wyoming. Science. 192, 253-256.

Shee, S.R., Gurney, J.J., Robinson, D.N., 1982. Two diamond-bearing peridotite xenoliths from the finsch kimberlite, South Africa. Contrib. Mineral. Petrol. 81, 79-87.

Sobolev, N.V., Pokhilenko, N.P., Efimova, E.S., 1984. Diamond-bearing peridotite xenoliths in kimberlites and the problem of the origin of diamonds. Russ. Geol. Geophys. 25, 63-80.

Sobolev, V.S., Nay, B.S., Sobolev, N.V., Lavrent'yev, Y.G., Pospelova, L.N., 1969. Xenoliths of diamond-bearing pyrope serpentinite from the " Aykhal" pipe, Yakutia. Doklady Akad. Nauk 188, 168-170.

Spetsius, Z.V., 1995. Occurrence of diamond in the mantle: a case study from the Siberian Platform. J. Geochem. Explor. 53, 25-39.

Thomassot, E., Cartigny, P., Harris, J.W., Viljoen, K.S., 2007. Methane-related diamond crystallization in the Earth's mantle: Stable isotope evidences from a single diamond-

bearing xenolith. Earth Planet. Sci. Lett. 257, 362-371.

Viljoen, K.S., Dobbe, R., Smit, B., Thomassot, E., Cartigny, P., 2004. Petrology and geochemistry of a diamondiferous lherzolite from the Premier diamond mine, South Africa. Lithos. 77, 539-552.

Viljoen, K.S., Robinson, D.N., Swash, P.M., Griffin, W.L., Otter, M.L., Ryan, C.G., Win, T.T., 1994. Diamond- and graphite- bearing peridotite xenoliths from the Roberts Victor kimberlite, South Africa in: Meyer, H.O.A., Leonardos, O.H. (Eds.), Proceedings of the 5th International Kimberlite Conference. Rio de Janeiro, Brazil, CPRM, Araxa, Brazil, pp. 285-303.

Viljoen, K.S., Swash, P.M., Otter, M.L., Schulze, D.J., Lawless, P.J., 1992. Diamondiferous garnet harzburgites from the Finsch kimberlite, Northern Cape, South Africa. Contrib. Mineral. Petrol. 110, 133-138.

C.2. REFERENCES FOR DIAMONDIFEROUS ECLOGITE

Anand, M., Taylor, L.A., Misra, K.C., Carlson, W.D., Sobolev, N.V., 2004. Nature of diamonds in Yakutian eclogites: views from eclogite tomography and mineral inclusions in diamonds. Lithos. 77, 333-348.

Aulbach, S., Stachel, T., Heaman, L.M., Carlson, J.A., 2011. Microxenoliths from the Slave craton: Archives of diamond formation along fluid conduits. Lithos. 126, 419-434.

Beard, B.L., Fraracci, K.N., Clayton, R.A., Mayeda, T.K., Snyder, G.A., Sobolev, N.V., Taylor, L.A., 1996. Petrography and geochemistry of eclogites from the Mir kimberlite, Yakutia, Russia. Contrib. Mineral. Petrol. 125, 293-310.

Bonney, T.G., 1899. The Parent-Rock of the Diamond in South Africa. Proceedings of the Royal Society of London 65, 223-236.

Hatton, C.J., Gurney, J.J., 2013. A Diamond-Graphite Eclogite from the Roberts Victor Mine, Extende abstract 2nd Int Kimberlite Conference. American Geophysical Union, Santa Fe.

Hills, D., Haggerty, S., 1989. Petrochemistry of eclogites from the Koidu Kimberlite Complex, Sierra Leone. Contrib. Mineral. Petrol. 103, 397-422.

Howarth, G.H., Sobolev, N.V., Pernet-Fisher, J.F., Barry, P.H., Penumadu, D., Puplampu, S., Ketcham, R.A., Maisano, J.A., Taylor, D., Taylor, L.A., 2014. The secondary origin of diamonds: multi-modal radiation tomography of diamondiferous mantle eclogites. Int. Geol. Rev. 56, 1172-1180.

Ireland, T.R., Rudnick, R.L., Spetsius, Z., 1994. Trace elements in diamond inclusions from eclogites reveal link to Archean granites. Earth Planet. Sci. Lett. 128, 199-213.

Ishikawa, 2008. Compositional layering in a hihgly diamondiferous eclogite xenolith from the Roberts Victor Kimberlite, South Africa and its implications for diamond genesis, Extended Abstract 9th International Kimberlite Conference, Frankfurt, Germany pp. No. 9IKC-A-00078.

Jacob, D., Jagoutz, E., Lowry, D., Mattey, D., Kudrjavtseva, G., 1994. Diamondiferous eclogites from Siberia: Remnants of Archean oceanic crust. Geochim. Cosmochim. Acta. 58, 5191-5207.

Jerde, E., Taylor, L., Crozaz, G., Sobolev, N., Sobolev, V., 1993. Diamondiferous eclogites from Yakutia, Siberia: evidence for a diversity of protoliths. Contrib. Mineral. Petrol. 114, 189-202.

Keller, R.A., Taylor, L.A., Snyder, G.A., Sobolev, V.N., Carlson, W.D., Bezborodov, S.M., Sobolev, N.V., 1999. Detailed pullapart of a diamondiferous eclogite xenolith: implications for mantle processes during diamond genesis., in: Gurney, J.J., Gurney, J.L., Pascoe, M.D., Richardson, S.H. (Eds.), Proceedings of the 7th International Kimberlite Conference. Red Roof Design, Cape Town, pp. 397-402.

Kiviets, G.B., 2000. A detailed geochemical investigation of diamond-bearing eclogite xenoliths from the Kaalvallei kimberlite, South Africa, Department of Geological Sciences. University of Cape Town, South Africa, p. 159.

Liu, Y., Taylor, L.A., Sarbadhikari, A.B., Valley, J.W., Ushikubo, T., Spicuzza, M.J., Kita, N., Ketcham, R.A., Carlson, W., Shatsky, V., Sobolev, N.V., 2009. Metasomatic origin of diamonds in the world's largest diamondiferous eclogite. Lithos. 112, Supplement 2, 1014-1024.

Malkovets, V., Zedgenizov, D.A., Griffin, W.L., Dak, A., O'Reilly, S.Y., Pokhilenko, N.P., Mityukhin, S., 2008. Diamondiferous microxenoliths and xenocrysts from the Nyurbinskaya kimberlite pipe, Yakutia Extended Abstract 9th International

Kimberlite Conference, Frankfurt, Germany, pp. No. 9IKC-A-00224.

McCandless, T.E., Collins, D.S., 1989. A diamond-graphite eclogitef roint he Sloan2 kimberlite, Colorado U.S.A., in: Ross, J. (Ed.), Kimberlites and related rock. Blackwell, C arlton, Australia, pp. 1061-1069.

Misra, K., Anand, M., Taylor, L., Sobolev, N., 2004. Multi-stage metasomatism of diamondiferous eclogite xenoliths from the Udachnaya kimberlite pipe, Yakutia, Siberia. Contrib. Mineral. Petrol. 146, 696-714.

Palot, M., Cartigny, P., Viljoen, F., 2009. Diamond origin and genesis: A C and N stable isotope study on diamonds from a single eclogitic xenolith (Kaalvallei, South Africa). Lithos. 112, Supplement 2, 758-766.

Peltonen, P., Kinnunen, K.A., Huhma, H., 2002. Petrology of two diamondiferous eclogite xenoliths from the Lahtojoki kimberlite pipe, eastern Finland. Lithos. 63, 151-164.

Reid, A., Brown, R.W., Dawson, J.B., Whitfield, G.G., Siebert, J.C., 1976. Garnet and pyroxene compositions in some diamondiferous eclogites. Contrib. Mineral. Petrol. 58, 203-220.

Reid, A.M., Brown, R.W., Dawson, J.B., Whitfield, G.G., Siebert, J.C., 1973. Diamond-bearing eclogites, Extended abstract 1st International Kimberlite Abstract, Cape Town.

Robinson, D.K., 1979. Surface textures and other features of diamonds. University of Cape Town, p. 418.

Schulze, D.J., 1992. Diamond eclogite from Sloan Ranch, Colorado, and its bearing on the diamond grade of the Sloan Kimberlite. Econ. Geol. 87, 2175-2179.

Shatsky, V., Ragozin, A., Zedgenizov, D., Mityukhin, S., 2008. Evidence for multistage evolution in a xenolith of diamond-bearing eclogite from the Udachnaya kimberlite pipe. Lithos. 105, 289-300.

Smart, K.A., Chacko, T., Stachel, T., Muehlenbachs, K., Stern, R.A., Heaman, L.M., 2011. Diamond growth from oxidized carbon sources beneath the Northern Slave Craton, Canada: A δ13C–N study of eclogite-hosted diamonds from the Jericho kimberlite. Geochim. Cosmochim. Acta. 75, 6027-6047.

Snyder, G.A., Jerde, E.A., Taylor, L.A., Halliday, A.N., Sobolev, V.N., Sobolev, N.V., 1993. Nd and Sr isotopes from diamondiferous eclogites, Udachnaya Kimberlite Pipe, Yakutia, Siberia: Evidence of differentiation in the early Earth? Earth Planet. Sci. Lett. 118, 91-100.

Snyder, G.A., Taylor, L.A., Crozaz, G., Halliday, A.N., Beard, B.L., Sobolev, V.N., Sobolev, N.V., 1997. The Origins of Yakutian Eclogite Xenoliths. J. Petrol. 38, 85-113.

Snyder, G.A., Taylor, L.A., Jerde, E.A., Clayton, R.N., Mayeda, T.K., Deines, P., Rossman, G.R., Sobolev, N.V., 1995. Archean mantle heterogeneity and the origin of diamondiferous eclogites, Siberia; evidence from stable isotopes and hydroxyl in garnet. Am. Mineral. 80, 799-809.

Sobolev, N.V., Snyder, G.A., Taylor, L.A., Keller, R.A., Yefimova, E.S., Sobolev, V.N., Shimizu, N., 1998. Extreme Chemical Diversity in the Mantle during Eclogitic Diamond Formation: Evidence from 35 Garnet and 5 Pyroxene Inclusions in a Single Diamond. Int. Geol. Rev. 40, 567-578.

Sobolev, V.N., Taylor, L.A., Snyder, G.A., Sobolev, N.V., 1994. Diamondiferous Eclogites from the Udachnaya Kimberlite Pipe, Yakutia. Int. Geol. Rev. 36, 42-64.

Spetsius, Z.V., 1995. Occurrence of diamond in the mantle: a case study from the Siberian Platform. J. Geochem. Explor. 53, 25-39.

Spetsius, Z.V., Taylor, L.A., 2002. Partial Melting in Mantle Eclogite Xenoliths: Connections with Diamond Paragenesis. Int. Geol. Rev. 44, 973-987.

Spetsius, Z.V., Wiggers de Vries, D.F., Davies, G.R., 2009. Combined C isotope and geochemical evidence for a recycled origin for diamondiferous eclogite xenoliths from kimberlites of Yakutia. Lithos. 112, Supplement 2, 1032-1042.

Stepanov, A.S., Korsakov, A.V., Yuryeva, O.P., Nadolinniy, V.A., Perraki, M., De Gussem, K., Vandenabeele, P., 2011. Brown diamonds from an eclogite xenolith from Udachnaya kimberlite, Yakutia, Russia. Spectrochim. Acta, Part A 80, 41-48.

Stepanov, A.S., Shatsky, V.S., Zedgenizov, D.A., Sobolev, N.V., 2007. Causes of variations in morphology and impurities of diamonds from the Udachnaya Pipe eclogite. Russ. Geol. Geophys. 48, 758-769.

Taylor, L.A., Keller, R.A., Snyder, G.A., Wang, W., Carlson, W.D., Hauri, E.H., McCandless, T., Kim, K.-R., Sobolev, N.V., Bezborodov, S.M., 2000. Diamonds and Their Mineral Inclusions, and What They Tell Us: A Detailed "Pull-Apart" of a Diamondiferous Eclogite. Int. Geol. Rev. 42, 959-983.

Viljoen, K.S., 1995. Graphite- and diamond-bearing eclogite xenoliths from the Bellsbank kimberlites, Northern Cape, South Africa. Contrib. Mineral. Petrol. 121, 414-423.

Viljoen, K.S., Schulze, D.J., Quadling, A.G., 2005. Contrasting group I and group II eclogite xenolith petrogenesis: petrological, trace element and isotopic evidence from eclogite, garnet-websterite and alkremite xenoliths in the Kaalvallei Kimberlite, South Africa. J. Petrol. 46, 2059-2090.

Viljoen, K.S., Smith, C.B., Sharp, Z.D., 1996. Stable and radiogenic isotope study of eclogite xenoliths from the Orapa kimberlite, Botswana. Chem. Geol. 131, 235-255.

APPENDIX D. SUPPLEMENTARY MATERIAL FOR CHAPTER 3: DIAMOND RESORPTION IN THE MANTLE: A STUDY OF INTERNAL STRUCTURES, $\Delta^{13}C$ AND N CONTENTS IN DIAMONDS FROM THE EKATI MINE, CANADA

Table D.2 $\delta^{13}C$ values, nitrogen contents and growth patterns of diamonds from the Grizzly, Misery, Koala, and Leslie kimberlite pipes.

Diamond	Twin	Color *	Spot	CL	FTIR *		$\delta^{13}C$	2σ	N
					N_T (ppm)	IaB, %B	(VPDB)	(‰)	(ppm)
G97-1-7		W	r	P11	149	72	-5.56	0.12	
			m	P1			-5.14	0.12	
			c	P1	131	80	-4.78	0.13	217
G97-1-8		Br2	r	P5	190	37	-4.55	0.12	798
			m	P1			-5.08	0.13	
			c	P10	187	43	-3.55	0.14	
G97-1-9		W	r	P1	102	52	-5.31	0.12	356
			c	P6			-5.40	0.13	
			r	P1			-5.44	0.13	
G97-1-3		Br2	r	P2	79	56	-3.72	0.13	711
			m	P1			-4.57	0.14	
			c	P4			-4.54	0.12	762
G97-1-4		Br1	r	P1	135	56	-4.00	0.12	
			m	P3			-4.00	0.12	
			c	P5			-3.74	0.12	
G97-1-5		Br4	r	P3	99	30	-2.67	0.12	13
			m	P1			-3.30	0.12	
			c	P1			-2.54	0.13	81
G97-3-3		Br1	r	P5	791	37	-4.98	0.13	67
			m	P1			-5.09	0.13	
			c	P5			-5.11	0.12	
G97-1-6		Br1	r	P4	663	70	-5.35	0.13	608
				P4			-5.20	0.14	
				P4			-5.21	0.13	
				P4			-5.07	0.13	

Continued on next page…

Diamond	Twin	Color *	Spot	CL	FTIR *		$\delta^{13}C$	2σ	N
					N_T (ppm)	IaB, %B	(VPDB)	(‰)	(ppm)
G97-1-6			m	P4			-5.05	0.15	
				P4			-5.35	0.12	
				P4			-5.44	0.13	
				P4			-5.08	0.12	
			c	P6	740	71	-5.20	0.13	
G97-2-1		Br2	r	P8			-4.64	0.16	376
			m	P1			-5.31	0.16	
			c	P5	195	74	-4.68	0.12	
G97-3-1		Br1	r	P1	132	75	-4.72	0.16	333
			m_1	P2			-4.87	0.15	
			m_2	P3			-5.13	0.14	
			c	P1			-4.72	0.16	
G97-2-3		Br1	r	P4			-4.53	0.15	348
			m	P4			-4.98	0.15	
			c	P1	67	56	-4.89	0.15	
G97-5-2		W	r	P1			-4.50	0.15	70
			m_1	P2			-5.21	0.15	
			m_2	P2			-4.70	0.16	
			c	P1	39	51	-5.10	0.15	
G97-4-1		Br1	r	P3	572	65	-5.14	0.16	848
			m	P3	632	67	-5.23	0.15	
G97-5-1		Br3	r	P1	364	83	-5.44	0.15	180
			m	P3			-5.33	0.15	
			c	P1			-4.29	0.15	519
G97-2-5		Br3	r	P2	403	88	-5.84	0.12	1066
M95-1-1		Br1	r	P10	299	92	-4.68	0.14	122
			m	P1			-3.96	0.13	
			c	P1	289	92	-3.80	0.12	
M95-2-5		Br1	r	P11			-4.26	0.14	734
			m	P3			-4.54	0.12	
			c	P1	1376	41	-4.88	0.13	
M95-2-1		W	r	P3	1116	37	-3.91	0.13	835
				P3			-4.12	0.13	
			m	P1			-4.51	0.12	
				P1			-4.10	0.12	1207
			c	P5			-3.66	0.13	
M95-2-4		W	r	P2	1505	25	-3.68	0.14	1051
			c	P2			-4.38	0.13	
M95-2-2		Br2	r	P3	1045	26	-4.24	0.12	750
			m	P3			-4.80	0.12	
			m_2	P4	1073	18	-4.96	0.13	

Continued on next page…

Diamond	Twin	Color *	Spot	CL	FTIR *		$\delta^{13}C$	2σ	N
					N_T (ppm)	IaB, %B	(VPDB)	(‰)	(ppm)
M95-1-4		Br1	r_1	P1	586	88	-5.07	0.13	879
			r_2	P1			-5.06	0.13	
			m_1	P3			-4.91	0.13	
			m_2	P3			-4.99	0.13	
			m_3	P3			-5.03	0.13	
			c_1	P2			-4.94	0.13	17
			c_2	P2	1052	12	-5.24	0.13	54
M95-2-3		W	r	P3	1156	37	-3.53	0.14	726
			c	P2	202	91	-3.52	0.12	
M95-1-5		Br2	r	P3	763	16	-3.89	0.13	784
			m	P3			-3.98	0.13	
			m_2	P4			-4.02	0.13	
			c	P4			-4.16	0.13	
M95-2-14		W	r	P1	904	3	-3.15	0.14	694
			c	P2			-2.62	0.14	
			m	P1	946	8	-2.81	0.13	
Sm95-3-1		Br2	r	P11	1009	14	-2.44	0.13	2129
			m	P1			-2.79	0.13	
			c	P1	239	64	-4.26	0.13	3
M95-2-11		W	r	P2	929	97	-4.48	0.14	52
				P2			-4.90	0.13	
				P1			-4.59	0.12	
			m	P1			-5.29	0.13	
				P1			-5.14	0.13	
			c	P1	934	98	-5.10	0.14	
M95-2-12		W	r	P3	804	98	-4.25	0.12	40
			m_1	P3			-4.48	0.14	
			m_2	P1			-4.67	0.13	
			c	P2	839	98	-4.77	0.12	
M95-2-6		W	r	P1	1110	3	-4.68	0.13	955
			m	P4			-4.25	0.13	0
			c	P4			-4.71	0.13	
			m_2	P4			-4.98	0.14	
M95-2-8		W	r	P4	997	12	-4.67	0.13	12
			m	P8			-4.79	0.12	
			c	P1	982	11	-4.33	0.15	
sm95-3-10		W	r	P4	848	9	-3.58	0.12	897
			m	P3			-2.02	0.12	1263
			c	P4	642	22	-3.05	0.12	53
M95-2-9		W	m	P3	949	3	-4.68	0.13	
			c	P4			-4.97	0.12	

Continued on next page…

Diamond	Twin	Color *	Spot *	CL	FTIR *		$\delta^{13}C$	2σ	N
					N_T (ppm)	IaB, %B	(VPDB)	(‰)	(ppm)
M95-2-13		Br1	m	P2	171	85	-4.25	0.13	56
			c	P3			-5.00	0.12	
			m	P2			-4.82	0.12	
M95-1-2		Br1	m	P4	714	5	-4.13	0.14	
			c	P4	782	9	-4.40	0.14	719
M95-2-15		Br1	r	P1	370	94	-5.48	0.15	88
			m	P3			-5.61	0.13	
			c	P6	390	94	-5.25	0.12	
M95-4-2		W	r	P4	1697	31	-2.29	0.13	905
				P4			-2.52	0.13	1316
			m	P2			-3.82	0.13	2108
				P4			-3.95	0.13	1704
			c	P4	1441	27	-3.91	0.13	1688
M95-3-5		W	r	P2	948	12	-4.19	0.13	1260
			c	P1			-4.12	0.14	
			m	P5			-3.85	0.15	
M95-4-7	twin	Br1	r	P8	230	73	-3.71	0.13	906
			m	P1			-3.95	0.14	
			c	P10	182	68	-3.87	0.14	
M95-3-6		W	r	P2			-4.02	0.13	690
			c	P6	733	0	-3.48	0.12	
M95-3-8		W	r	P2	1223	13	-5.71	0.13	
			m	P2			-6.82	0.14	
SM95-3-7		W	r	P2	1235	36	-3.03	0.13	1225
			m	P3			-3.85	0.15	
			c	P2	1275	46	-3.87	0.13	
M95-4-5	twin	Br1	r	P8	397	75	-4.86	0.12	778
				P1			-4.50	0.12	
				P3			-5.07	0.13	
			m	P1			-5.18	0.14	
				P5			-2.93	0.12	
			c	P5	378	76	-2.98	0.13	
M95-3-2		Br1	r	P3	784	14	-4.29	0.13	699
			m	P1			-4.39	0.13	
			c	P3	800	11	-4.22	0.13	
M95-3-10		W	r	P1	1092	13	-3.17	0.13	721
			m	P2			-3.82	0.13	
			c	P1	1072	11	-3.78	0.12	
M95-3-3		W	r	P2	1174	12	-5.16	0.12	1563
			m	P9			-4.79	0.12	
			c	P9	1042	15	-5.37	0.13	

Continued on next page…

Diamond	Twin	Color *	Spot *	CL	FTIR *		$\delta^{13}C$	2σ	N
					N_T (ppm)	IaB, %B	(VPDB)	(‰)	(ppm)
K95-1-2		W	r	P2	441	6	-4.18	0.13	1378
			r_m	P7			-4.10	0.13	
			c	P2			-3.70	0.13	443
K95-1-3		W	r	P2	719	9	-5.64	0.12	1310
			m	P2			-5.35	0.12	
			c	P2	716	8	-4.05	0.13	
K95-1-4		W	r	P2	1092	20	-5.96	0.13	1044
			m	P2			-5.90	0.13	739
			c	P2	1034	23	-5.77	0.14	
K95-1-1		W	r	P8	872	0	-4.71	0.12	930
			m	P6			-4.59	0.13	
			c_1	P1			-4.76	0.12	
			c_2	P4	702	0	-4.94	0.14	551
Sk95-3-2		W	r	P2			-5.02	0.13	521
			m	P3			-3.89	0.13	
			c	P5	740	6	-3.77	0.12	715
K95-2-1		W	r	P2	904	15	-4.57	0.13	762
			m	P2			-4.34	0.13	
			c	P2	816	15	-4.67	0.12	
K95-3-1		W	m	P2			-4.69	0.12	14
			c	P1	349	1	-5.15	0.12	
K95-3-4			r	P8			-5.23	0.12	1067
		W	m	P7			-3.32	0.13	1183
			c	P1	802	50	-3.75	0.12	
SK95-3-3		W	m	P9	1073	4	-5.14	0.12	1008
			c	P9			-5.01	0.12	
K95-3-2			r	P2	262	38	-5.55	0.13	967
		W	m	P8			-5.49	0.13	
			c	P1			-2.73	0.14	8
			c_2	P1			-2.74	0.12	
K95-3-3		W	r	P8	704	9	-4.98	0.12	1301
				P8			-5.26	0.12	
				P8			-4.24	0.13	
			m	P3			-4.10	0.13	
				P3			-3.74	0.13	
				P2			-3.91	0.13	
			c	P2			-4.30	0.13	

Continued on next page…

Diamond	Twin	Color *	Spot *	CL	FTIR *		$\delta^{13}C$	2σ	N
					N_T (ppm)	IaB, %B	(VPDB)	(‰)	(ppm)
K95-5-1		W	r	P2	950	20	-4.00	0.13	1235
				P2			-4.33	0.12	
			m	P2			-4.31	0.13	
				P2			-4.10	0.14	
				P2			-4.30	0.15	
			c	P2	921	19	-4.24	0.14	
L97-1-3		Br2	r	P3	217	71	-4.84	0.12	657
				P3			-4.65	0.13	
			m	P3			-3.29	0.13	
				P1			-4.49	0.14	
			c	P5	300	73	-4.41	0.13	
L97-1-2		W	r	P3	927	35	-5.36	0.12	1594
			m	P7			-3.69	0.12	
			c	P2	872	31	-4.74	0.13	690
L97-1-5		W	r_1	P2	920	12	-3.67	0.12	903
			r_3	P2			-3.92	0.13	
			r_2	P2			-3.84	0.13	
			c	P1	896	19	-4.57	0.13	1836
			r_4	P2			-4.96	0.12	
SL97-A2-5		W	r	P2	980	5	-4.50	0.12	664
			m	P8			-5.20	0.13	1020
			c	P4	846	9	-5.18	0.14	
SL97-A2-8	twin	W	r	P1	832	81	-5.40	0.12	881
			m	P3			-5.65	0.13	
			c	P1	709	84	-5.19	0.13	
L97-2-2		W	r	P2	1025	8	-3.51	0.12	807
			m	P2			-3.57	0.13	
			c	P4	1004	6	-4.74	0.12	
L97-2-3		Br1	r	P2	783	14	-3.96	0.13	843
			m	P1			-3.70	0.13	
			c	P3			-3.30	0.12	
L97-2-7		W	r	P2	542	14	-4.66	0.12	990
			r_2	P8			-4.76	0.12	
			c	P6	458	3	-3.63	0.13	
L97-2-4		W	r	P1	501	88	-4.60	0.14	
			m	P3			-4.67	0.13	
			c	P2			-4.62	0.12	
L97-2-6		Br2	r	P5	300	81	-4.65	0.12	34
			m	P3			-5.01	0.12	
			c	P1			-5.01	0.12	

Continued on next page…

Diamond	Twin	Color *	Spot *	CL	FTIR *		$\delta^{13}C$	2σ	N
					N_T (ppm)	IaB, %B	(VPDB)	(‰)	(ppm)
L97-2-9		Br3	r	P3	370	38	-5.08	0.12	597
			m	P3			-5.54	0.13	
			c	P2	456	50	-5.50	0.12	
L97-3-5		Br2	r	P11	148	34	-5.75	0.12	552
			m	P1			-5.38	0.12	
			c	P5			-5.81	0.13	
L97-2-5		Br1	r	P11	106	50	-4.30	0.13	496
			m	P1			-3.57	0.14	
			c	P3	281	80	-3.54	0.13	
L97-3-4		W	r	P10	923	8	-4.99	0.14	562
			r_2	P10			-2.67	0.14	890
			c	P10	950	14	-2.78	0.12	
L97-1-1		W	r	P12	563	0	-6.42	0.12	1523
L97-4-8	twin	Br1	r	P3	184	46	-5.06	0.12	720
			m	P3			-5.31	0.12	
			c	P6	384	85	-4.15	0.12	
L97-4-1	twin	W	r	P11	360	97	-5.15	0.13	224
			m	P3			-5.39	0.13	
			c	P1			-4.59	0.13	
L97-4-2		Br1	r	P1	303	63	-5.60	0.13	670
			m	P10			-4.19	0.13	
			c	P5			-5.09	0.12	
L97-4-3		W	r	P1	328	84	-4.11	0.12	228
			m	P3	314	85	-4.84	0.13	
			c	P5			-4.93	0.12	
L97-4-5		W	r	P3	309	70	-4.24	0.12	556
			m	P3			-4.64	0.14	
			c	P1	493	70	-4.63	0.13	
L97-2-1		W	r	P2	1031	4	-3.82	0.14	1251
			c_1	P2			-3.93	0.13	
			c_2	P1			-3.78	0.13	
L97-3-2		W	r	P1	234	74	-5.32	0.12	10
			m	P2			-5.03	0.12	
			c	P2	161	67	-4.51	0.14	
L97-3-3	twin	Br1	r	P1	200	35	-5.19	0.13	1132
			m	P3			-3.17	0.14	154
			c	P5			-4.70	0.12	
L97-4-6	twin	W	r	P1	472	26	-4.82	0.13	271
			m	P12			-5.08	0.13	
			c	P5			-5.27	0.13	1

Continued on next page…

Diamond	Twin	Color *	Spot *	CL	FTIR *		$\delta^{13}C$	2σ	N
					N_T (ppm)	IaB, %B	(VPDB)	(‰)	(ppm)
L97-5-1		W	r	P2	932	7	-4.67	0.13	756
			m	P2			-4.54	0.13	
			c	P2	1005	15	-4.59	0.13	

W = White (Colorless); Br = Brown color with color intensity inease from 1 to 4 .

* = Data from Zhang and Fedortchok (2012)

P1=homogenious zone; P2=rectilinear zone; P3=stepped rectilinear zone;

P4=agate texture;P5=multi-core pattern;P6=sector pattern;

P7=dendritic zone;P8=octagonal zone;P9=four-sided star zone;

P10=Plaid structure;P11=black rim;P12=shattered pattern

APPENDIX E. SUPPLEMENTARY MATERIAL FOR CHAPTER 4: EVOLUTION OF DIAMOND RESORPTION IN A SILICIC AQUEOUS FLUID AT 1-3 GPA: APPLICATION TO KIMBERLITE EMPLACEMENT AND MANTLE METASOMATISM

Table E.3 Results of AFM measurements of trigons pits on dissolved diamond crystals after experiments

T (°C)	Run no.	Trigon no.	trigon type [a]	Diameter(um)	Depth (nm)	Angles of wall of micro-planes to (111) plane
1 GPa						
1350	PC-120	1	f/b-2	10.1	537	8,11,17,22,28,35
		2	f/b-2	19.5	1109	7,12,20,42,49,57
		3	f/b-1	21.6	656	21,17,11
		4	f/b-1	25.4	667	17
		5	f/b-1	23.3	540	16,19
		6	f/b-1	26.5	900	16,19
		7	f/b-1	32.6	400	16
		8	p/b-1	10.0	510	11,19
		9	f/b-1	20.0	750	19,43
		10	f/b-1	48.7	700	11,16,19
		11	f/b-1	28.8	144	13,19
		12	f/b-1	40.4	370	11,19
		13	f/b-1	28.0	200	11,15
		14	f/b-1	56.1	1100	15
		15	f/b-1	64.1	1900	23
1250	PC-157	1	p/b-1	14.0	26	0.5
	Dia33	2	f/b-3	34.0	207	1.3,2.6,3.5,6
		3	f/b-3	34.1	423	2,4,5,7,12,18
		4	f/b-3	35.9	374	1.7,2.8,5,7,13
		5	f/b-1	36.3	977	13,17
		6	f/b-3	37.2	145	0.9,2.7,4,8,13
		7	f/b-1	37.9	557	8,15
		8	f/b-1	39.2	717	11,16
		9	f/b-3	53.2	502	10,17
		10	f/b-1	73.1	307	2.6,4.5,14,19,21
	Dia34	1	p/b-1	2.0	126	11
		2	p/b-1	2.5	103	8
		3	p/b-1	3.3	106	6
		4	p/b-1	3.6	137	7
		5	p/b-1	5.3	277	10
		6	p/b-1	5.5	133	8,14
		7	f/b-1	8.6	175	5,7
		8	f/b-1	9.1	403	11,18,26,38
		9	f/b-1	10.7	250	7，11，17
		10	f/b-1	13.0	1692	11,15,20,38,59

Continued on next page…

T (°C)	Run no.	Trigon no.	trigon type [a]	Diameter(um)	Depth (nm)	Angles of wall of micro-planes to (111) plane
		11	f/b-1	13.3	148	6,11,15
		12	f/b-1	15.4	277	1.7,5,7,15,24,44
		13	p/b-1	15.9	929	1,7,13,17,24
		14	f/b-1	17.5	1339	16,22,31,47
		15	f/b-1	17.6	1327	9,16,24,34,43,53
		16	f/b-2	17.9	655	6,22
		17	f/b-1	18.4	1014	6,10,21,33,35
		18	f/b-1	18.6	499	9,17,24,51,62
		19	f/b-1	20.6	1233	18,24,30
		20	f/b-1	20.8	200	2,6,14,22,36
		21	f/b-1	20.8	1266	16,27,51
		22	f/b-1	24.7	1088	7,18,24
		23	f/b-1	25.0	572	4,7,12,20
		24	f/b-2	25.4	2771	8,14,23,32,40
		25	f/b-2	26.1	2291	10,27,37,64
		26	f/b-1	28.9	1261	6,9,12,15,21,31,41
		27	f/b-2	39.9	2472	3,7,10,16,26,37,58
		28	f/b-1	45.8	1274	22,29
		29	f/b-1	45.9	1647	17,24
		30	f/b-1	58.4	2627	10,14,23,34,44
1250	PC-148	1	p/b-1	4.0	70	1.7,3.1,4,5
	ALZ-25	2	f/b-2	5.7	772	18,26,34,46
		3	p/b-1	5.8	53	0.5,2.2,6,15
		4	f/b-1	6.1	105	2.2,5,16
		5	f/b-2	6.5	83	1,2,5,6,10,15
		6	f/b-2	6.6	449	8,16,26
		7	f/b-3	6.7	114	1.6,10,17
		8	f/b-3	6.7	138	4,9,17
		9	f/b-3	6.9	109	10,16,21
		10	f/b-3	7.1	214	5,7,12,19,27
		11	p/b-1	8.7	737	1.3,2.1,10,22
		12	f/b-2	9.4	652	3,9,16,20,29
		13	f/b-2	13.7	516	1.2,5,15,24
		14	f/b-1	16.0	2	7,14,19,28
		15	f/b-1	18.7	25	0.6,5,14
		16	f/b-1	25.5	374	6,18,24
		17	f/b-1	26.2	1403	1.8,19
	ALZ-26	1	f/b-1	8.3	123	8,12
		2	f/b-1	10.6	103	14
		3	f/b-3	10.6	177	15
		4	f/b-1	13.5	229	9,13,18
		5	f/b-3	13.7	160	3.4,19
		6	f/b-3	14.4	276	1.9,9,15
		7	p/b-1	14.7	256	1,14
		8	f/b-1	14.8	213	15
		9	f/b-3	15.1	152	1.8,9,13
		10	f/b-1	15.3	116	3,13,20
		11	f/b-1	15.6	584	1,15,21
		12	p/b-1	15.7	274	1.5,7,10,17
		13	f/b-1	16.1	126	11,19
		14	p/b-1	16.2	378	11,17,22
		15	f/b-1	17.0	732	22
		16	f/b-2	19.0	1771	18,25
		17	f/b-1	22.5	38	4.5
		18	f/b-2	23.5	964	13,17,22,28
		19	f/b-2	23.5	1721	1.8,15,20,26,34
		20	f/b-1	50.8	204	10,15
2 GPa						
1400	PC-98	1	f/b-2	4.8	172	16,28
		2	p/b-2	16.7	141	1.4

Continued on next page…

T (^{o}C)	Run no.	Trigon no.	trigon type [a]	Diameter(um)	Depth (nm)	Angles of wall of micro-planes to (111) plane
1400	PC-98	3	f/b-1	31.6	838	16,27
		4	f/b-1	34.4	192	21,35
		5	f/b-1	46.5	635	14
		6	f/b-1	57.0	1359	16,52
		7	f/b-1	59.8	622	15,22
		8	f/b-1	97.7	154	3,20
		9	f/b-1	116.6	159	15
1350	PC-106	1	p/b-1	1.0	41	6
		2	p/b-2	2.8	106	7
		3	f/b-1	8.0	36	4,8
		4	f/b-1	10.1	90	6
		5	f/b-1	19.1	105	6
		6	f/b-1	20.0	444	15,24
		7	f/b-1	24.8	120	6,10,18,32
		8	f/b-1	26.7	130	7,12
		9	p/b-1	29.1	99	0.7
		10	p/b-1	31.4	448	1,4,15
		11	f/b-1	31.5	11	16
		12	f/b-1	40.3	115	8,13
		13	f/b-1	41.9	1	6,11
		14	p/b-1	43.2	418	8
		15	f/b-1	46.7	396	8
		16	f/b-1	72.3	289	6,12
1350	PC-121	1	p/b-1	2.9	25	2
		2	f/b-1	5.1	26	2
		3	p/b-1	22.5	98	0.7,1.6,5
		4	f/b-1	22.6	29	1,2,16
		5	f/b-1	24.8	9	1
		6	f/b-1	25.6	834	23
		7	f/b-1	26.1	836	24
		8	p/b-1	26.3	400	2,3
		9	f/b-1	27.4	1769	20
		10	f/b-1	28.9	422	16
		11	f/b-3	29.2	162	1.3,3,7,10
		12	f/b-3	29.3	132	1,2,11,15
		13	f/b-3	29.4	225	17
		14	f/b-1	30.3	624	2,3,9,20
		15	f/b-1	30.3	133	1,2,3,14
		16	f/b-1	30.5	135	0.8,1.7,2.2,7,11
		17	f/b-1	36.1	321	20
		18	f/b-1	39.4	198	4,9,17
1350	PC-132	1	p/b-1	2.1	38	2.7,4
		2	p/b-1	18.0	1184	8,12,23
		3	f/b-1	20.7	1334	11,19,28
		4	f/b-2	21.9	1463	17,22
		5	f/b-1	22.9	238	12
		6	f/b-2	23.1	1495	16,20,33
		7	f/b-1	23.2	250	4,6,11
		8	f/b-3	37.2	122	1.1,2.9,10
		9	f/b-1	37.8	275	13
		10	f/b-1	40.1	938	10,15,27
		11	f/b-1	52.4	588	10,16
		12	f/b-1	60.1	957	4,10,15
		13	f/b-1	68.2	523	9,3
		14	f/b-1	77.1	567	12
		15	f/b-1	91.1	215	9,12
		face 1.1	p/b-1	7.2	33	0.7,1.9,5
		face 1.2	p/b-1	7.6	49	0.8,1.3,2.1
		face 1.3	f/b-1	8.7	150	2,3,5,8,14
		face 1.4	p/b-1	9.3	114	0.9,1.4,3.2,6,11

Continued on next page…

T (^{o}C)	Run no.	Trigon no.	trigon type [a]	Diameter(um)	Depth (nm)	Angles of wall of micro-planes to (111) plane
1250	PC-126	face 1.5	p/b-1	9.7	116	4,6,10
		face 1.6	f/b-1	9.8	31	1.3,5
		face 1.7	p/b-1	10.3	102	1,2,4,7
		face 1.8	p/b-1	10.8	92	1,2,3
		face 1.9	f/b-1	10.8	312	11,17,7
		face 1.10	f/b-1	11.1	133	13,3,20,7,17
		face 1.11	f/b-1	11.1	102	5,15,7
		face 1.12	f/b-3	11.2	113	1,2.2,4,7,11
		face 1.13	f/b-3	11.2	203	3,5,10,17
		face 1.14	f/b-2	11.4	220	2.3,5,7,11,17,20
		face 1.15	f/b-1	11.4	313	9,20
		face 1.16	f/b-1	11.5	147	3,5,9,15
		face 1.17	f/b-2	11.8	143	7,10,15
		face 1.18	p/b-1	13.7	2106	19,25,36,43
		face 1.19	f/b-3	12.1	123	2,5,8,11,16
		face 1.20	f/b-1	12.2	140	2,3,9,15,22
		face 1.21	f/b-1	12.7	798	10,15,22,28
		face 1.22	f/b-2	12.7	742	15,23,40
		face 1.23	f/b-1	13.5	105	11,18
		face 1.24	f/b-1	33.9	225	9,13,20
		face 2.1	f/b-1	11.5	131	5,7,11,16
		face 2.2	f/b-1	12.3	333	7,17,23
		face 2.3	f/b-1	12.7	352	13,19,25
		face 2.4	p/b-1	12.9	121	0.4,1.7,2.5,3,5
		face 2.5	p/b-1	12.9	120	0.7,1.7,2.8,3.5
		face 2.6	f/b-1	13.0	393	15,19,26
		face 2.7	f/b-2	13.1	1349	20,24,33,45
		face 2.8	f/b-1	13.1	203	10,15,20
		face 2.9	f/b-2	13.1	125	1.2,5.6,5,8,12
		face 2.10	f/b-1	13.5	89	11,16,38
		face 2.11	f/b-1	13.7	268	6,13,16,23
		face 2.12	f/b-1	13.8	253	13,20,26
		face 2.13	f/b-1	13.8	202	7,17,22
		face 2.14	f/b-2	14.4	1080	23,34,41
		face 2.15	f/b-1	15.3	256	4,13,22
		face 2.16	f/b-1	16.7	104	7,12,17
		face 2.17	f/b-1	17.7	36	4,9
		face 2.18	f/b-1	21.1	578	6,17,24
		face 2.19	f/b-1	26.1	135	8,14,24
		face 2.20	f/b-1	26.6	55	18
1250	PC-129	face 1.1	p/b-1	6.3	12	0.5,1
		face 1.2	f/b-2	34.2	2095	18,33,39,45
		face 1.3	f/b-2	34.4	1086	6,14
		face 1.4	f/b-1	37.3	127	5
		face 1.5	f/b-1	38.9	1282	9,17,28
		face 2.1	f/b-1	8.9	117	5,50,23
		face 2.2	f/b-2	15.1	218	4,8,11
		face 2.3	f/b-1	17.5	184	5,7
		face 2.4	f/b-1	27.0	328	5,11
		face 2.5	f/b-1	28.1	423	14
		face 2.6	f/b-1	28.5	191	6,9,14
		face 2.7	f/b-2	31.2	1273	14,34
		face 2.8	f/b-1	33.8	253	4,8
		face 2.9	f/b-1	34.6	509	7,11
		face 2.10	f/b-2	34.9	12	13,16,30
		face 2.11	f/b-2	36.0	257	6
		face 2.12	f/b-1	37.0	197	6
		face 2.13	f/b-2	37.2	453	5,9
		face 2.14	f/b-2	37.2	533	5,7,11
		face 2.15	f/b-2	37.3	519	5,9,11

Continued on next page…

T (°C)	Run no.	Trigon no.	trigon type [a]	Diameter(um)	Depth (nm)	Angles of wall of micro-planes to (111) plane
		face 2.16	f/b-1	38.1	213	7
		face 2.17	f/b-1	42.6	298	7,12
1250	PC-130	1	p/b-1	20.3	90	0.7
		2	f/b-1	24.5	178	3,5,13,15
		3	f/b-1	24.7	138	12
		4	f/b-1	25.6	326	15
		5	f/b-2	26.2	547	14,20
		6	f/b-1	27.3	217	4,10
		7	f/b-1	27.4	841	19
		8	f/b-1	27.6	406	14
		9	f/b-1	27.6	105	2,3,9
1250	PC-131	1	p/b-1	2.6	68	4
		2	f/b-3	12.1	95	1,3
		3	f/b-2	14.2	1656	19,35,47
		4	f/b-1	18.0	865	20
		5	f/b-1	19.6	645	20
		6	f/b-1	21.3	890	19
		7	f/b-1	23.8	272	17
		8	f/b-1	25.5	401	3,12,21
		9	f/b-1	26.5	159	2,18
		10	f/b-2	27.1	1591	19,27,39
1150	PC-127	1	f/b-1	6.8	286	17,24
		2	f/b-1	8.1	35	2,4,14
		3	f/b-1	8.6	350	14,30
		4	p/b-1	3.3	66	2.5,5,12
		5	f/b-1	8.6	194	18,29
		6	f/b-1	9.0	275	23,28
		7	f/b-1	9.7	362	23,28
		8	f/b-1	10.9	29	9,21
		9	f/b-1	12.2	745	10,17,21,28
		10	f/b-2	12.8	1867	16,20,29,44
		11	f/b-1	12.9	291	8,15,23,30
		12	f/b-1	13.3	423	26
		13	f/b-2	15.6	37	7,10
		14	f/b-1	20.4	60	3,10,16
		15	f/b-1	23.4	163	21
1150	PC-133	1	f/b-1	9.3	3	19
		2	f/b-1	9.4	93	17,22
		3	f/b-1	9.5	163	15
		4	f/b-2	9.5	102	15
		5	f/b-1	9.7	205	13,21
		6	f/b-1	10.4	73	12
		7	f/b-1	10.5	41	6
		8	p/b-1	10.6	119	0.5,5,10
		9	f/b-1	10.7	178	12,17
		10	f/b-1	10.7	228	15
		11	f/b-1	11.2	61	10
		12	f/b-1	17.6	450	17,22,34
		13	f/b-1	17.9	6	20
		14	f/b-1	21.6	99	4,9,15
		15	f/b-1	28.2	110	13
3 GPa						
1350	PC-134	1	f/b-1	24.3	296	14
		2	p/b-2	25.1	157	8
		3	f/b-1	26.6	256	6,9,22
		4	f/b-1	26.8	207	9
		5	f/b-1	27.4	158	1,7,11
		6	f/b-1	27.9	179	9
		7	f/b-1	28.4	115	9
		8	p/b-1	28.9	527	4,10

Continued on next page…

T (^{o}C)	Run no.	Trigon no.	trigon type [a]	Diameter(um)	Depth (nm)	Angles of wall of micro-planes to (111) plane
		9	f/b-2	29.4	2470	13,18,37
		10	f/b-1	30.1	322	9
		11	f/b-1	34.9	43	1.4,4,12
		12	f/b-1	36.3	50	0.9,9
		13	f/b-1	51.7	36	6
1250	PC-141	1	f/b-1	4.6	32	5,10,18
	(ALZ-17)	2	f/b-1	6.5	125	16
		3	f/b-1	7.0	404	15,31
		4	f/b-1	7.0	200	11,22
		5	f/b-1	7.4	144	15
		6	f/b-1	7.5	399	17
		7	f/b-1	7.5	217	16
		8	p/b-1	7.5	145	13,19
		9	f/b-1	7.6	105	14
		10	f/b-1	8.0	183	16
		11	f/b-1	8.3	242	13,19,31
		12	f/b-1	8.5	258	4,17
		13	f/b-1	8.8	494	14,19
		14	f/b-1	8.9	211	15
		15	f/b-1	9.5	70	19,40
		16	f/b-1	9.6	165	16
		17	f/b-1	11.0	451	17
		18	f/b-3	12.2	426	19
		19	f/b-1	12.3	142	16
		20	f/b-1	13.8	244	8,16
		21	f/b-1	14.0	23	4,8
		22	f/b-2	14.3	1752	20,43
		23	f/b-2	18.6	2039	17,23,38,45,67
		24	f/b-2	26.9	1316	20,37,50
	ALZ-18	1	f/b-1	8.5	74	11
		2	f/b-1	9.3	438	15,37
		3	p/b-1	9.4	147	2,3,4
		4	f/b-1	10.1	171	3,10,16
		5	p/b-1	10.2	134	2,6
		6	f/b-1	10.2	185	12,21
		7	f/b-1	10.4	92	4,12,18
		8	f/b-2	11.6	612	20
		9	f/b-1	11.7	203	16
		10	f/b-1	11.9	204	15
		11	f/b-1	12.2	431	15
		12	f/b-1	12.5	273	4,8,15
		13	f/b-1	12.9	285	8,14
		14	f/b-3	13.1	5	10,19
		15	f/b-2	15.0	2004	11,17,24,32,46
		16	f/b-1	16.5	97	6,13
		17	f/b-2	17.3	6	14,20,28,33,41
		18	f/b-1	18.1	78	15
		19	f/b-1	19.9	352	14
		20	f/b-2	20.3	927	11,19,34
		21	f/b-1	21.9	85	10
		22	f/b-2	22.7	337	14
		23	f/b-1	23.4	110	13
		24	f/b-1	24.0	124	12,17

a point-bottomed trigons: p/b-1)trumpet-shaped;p/b-1)stepped trumpet-shaped;p/b-3)V-shaped;
flat-bottomed trigon: f/b-1)trapezoid-shaped;f/b-2)trumpet-shaped;f/b-3)rounded;

APPENDIX F. SUPPLEMENTARY MATERIAL FOR CHAPTER 5: P-X EFFECTS ON DIAMOND RESORPTION: EXPERIMENTAL CONSTRAINTS

Table F.4 AFM measurements of etch pits on {111} faces.

P [a]	T °C	Exp No.	Trigon	Outline [b]	edge [c]	bottom [d]	Size(um)	Depth (nm)	$a_{\{111\}}$ [e]	$a_{\{100\}}$ [f]
1	1150	PC-108	0.3	TT		f/b-1	4.1	28.4	5,9	3.40
			1.3	TT		f/b-1	4.6	28.4	7.35	2.90
			7.2	TT		f/b-3	5.0	17.0	7.10	3.40
			0.2	TT		f/b-2	5.3	93.6	4,10	3.1
			1.2	TT		f/b-2	5.5	68.7	3.7,6.1,9.0,10.5	2.90
			3.1	TT		f/b-2	5.6	78.7	7.0,13.6,17,32.1	2.30
			9.1	TT		f/b-2	6.2	51.6	2.0,5.9,6.9,12.3	0.70
			8.4	TT		f/b-1	4.2	46.1	6.8,10.6,15.9	3.90
			6.1	TT	c-edges	f/b-3	10.3	199.6	7.9,12.2,25.5,33.4	1.7,3.2
			2.1	TT	c-edges	f/b-3	10.5	153.5	1.2,7.2,13.1,20.4	1.7,2.7,5.7
			2.3	TT	c-edges	f/b-1	11.5	323.5	13.2,30.3	2.5,3.1
			8.3	TT	c-edges	f/b-2	11.6	477.1	11.5,16.1,31.3,45.6	3.0,5.0
			5.1	TT	c-edges	f/b-3	14.3	304.7	2.4,8.7,10.8,23.4,44.2	2.10
			9.4	TT	c-edges	f/b-2	14.4	213.5	9.6,14.7,29.7	2.60
			1.1	TT		f/b-1/?	6.8	92.9	5,15,24	2.7,3.5,5.0
			8.1	TT		f/b-1	7.6	44.2	3.4,11.9,17	3.20
			10.1	TT		f/b-2	8.5	167.3	6.9,13.0,17.6,20.5,46.1	2.50
			2.2	TT		f/b-3	8.9	97.2	1.1,5.3,11.4,15.8,19.8	3.30
			2.4	T		f/b-1	2.4	46.6	23.00	
			9.2	T		f/b-3	2.9	33.0	10.5,17.1	
			7.3	T		f/b-3	3.0	86.6	6.9,8.9,20.9,27.2	
			10.2	T		f/b-1	3.5	108.5	8.2,12.3,15.1	
			7.4	T		f/b-3	4.4	83.7	3.2,14.7,21.7,44.6	
			4.2	T		f/b-3	4.4	74.0	2.6,7.8,13.8,26.6	
			7.6	T		f/b-1	4.7	119.7	20.10	
			7.5	T		f/b-1	5.5	92.7	12.50	
			9.3	T		f/b-3	5.5	65.6	1.5,2.8,4.2,22.5	
			4.1	T		f/b-2	6.3	161.8	3.6,6.8,12.6,18.7,33.2	
			8.2	T		f/b-1	9.5	104.6	2.2,3.5,8.1,28.1	2.10
			0.1	T	c-edges	f/b-3	14.8	137.3	8.00	
			7.1	T		f/b-3	25.3	318.1	15.2,37.4,55.3	
1	1250	P-297	24.1	H		U	60.4	516.9	1,2.5,4.3,6.8	0.7,1.5,2.4,5.4
			28.4	H		f/b-1	63.6	1656.5	1.1,2.3,3.5,4.5,5.2,6.2,9.7	4.6,5.9
			26.2	TT at bottom		f/b-2	11.8	588.4	1.7,5.9,9.7,11.3,13.2,14.8,23.5,32.3,59.7	-
			31.2	smalle H in big T		f/b-2	10.1	317.7	2.4,3.4,6.1,8.2,10.9,14.1	-
			32.2	smalle H in big T		f/b-1	8.6	317.1	2.2,4.6,5.4,6.5,8.7,13.5,15.6,20.8,31.6	5.7
			30.1	TT		f/b-2	22.5	312.6	1.6,8,10.6	2.9,3.7,4.9
			30.2	TT		f/b-2	8.9	710.0	7.2,148,18.4,23,26.7	4.8,25.8,30.4

Continued on next page…

P [a]	T °C	Exp No.	Trigon	Outline [b]	edge [c]	bottom [d]	Size(um)	Depth (nm)	$a_{\{111\}}$ [e]	$a_{\{100\}}$ [f]
			30.2b	TT		f/b-1	0.4	23.1	22.3	5.2,17.7
			25.2	TT		U	25.8	249.6	0.9,2.7,3.8,4.8,8.9	1.1,1.7
			27.b	TT		f/b-1	0.2	6.0	14.1	4.2
			24.2	T		p/b-2	7.0	228.8	2.8,4.5,5.6,11.5,15.4,21.1	
			24.3	T		f/b-3	7.8	139.4	0.9,6.5,9.3,13.5	
			25.1	T		U	17.4	233.0	0.5,1.7,4.1,6.1,7.8,11.4	
			26.1	T		f/b-1	6.6	346.3	2.2,6.1,7.6,8.7,11.4,13.1,14.8	
			27	T		f/b-3	9.9	350.5	2.7,3.5,6.1,8.9,11.1,14.2,17.6	
			28.1	T		p/b-2	3.8	293.7	5.1,7.9,10.7,14.7,18.7	
			28.2	T		p/b-2	8.7	318.6	2.1,3.4,5.6,6.8,7.8,9,14.4	
			28.3	T		p/b-2	10.9	761.2	7.4,10.8,11.6,12.7,17.1,19.9,24.9	
			29	T		p/b-1	16.9	495.3	1.5,2.7,4,5.5,8.1,9.2,12.1,16.2,18.2	
			31.1	T		f/b-1	15.6	1053.7	6.3,8.5,9.3,12.8,15.3,25.9,41.6	
			31.3	T		U	7.2	215.4	2.1,3.3,5.3,7.3,9.3	
			32.1	T		f/b-2	8.3	421.5	3.3,11.6,12.8,14,15.6	
1	1250	PC-136	f623.001-5	TT	c-edge	f/b-2	41.1	277.9	18.1,5.0	2.1
			f623.002-1	TT		f/b-1	20.5	173.4	2,9,11,17	3
			f623.004-1	TT		fb-2	11.8	153.0	11,15,20,25	4.5
			f634.001-1	TT		f/b-2	30.2	393.8	1,7,10,17,21,25	3,6,8,10
			f634.003-1	TT		f/b-1	48.6	2410.0	7,12,15,20,24	3,7,9
			f634.005-3	TT	c-edge	U	19.2	818.9	2,9,17,25,33	7,8
			f634.006-3	TT	c-edge	f/b-2	19.6	313.7	3,4,7,13,20	2.1,3
			f623.001-1	T		p/b-2	20.3	1069.7	9,12,16,19,26	
			f623.001-2	T		f/b-1	24.1	100.4	3,5,8,11,25,30	
			f623.001-3	T		f/b-1	8.0	183.8	5,7,14,18	
			f623.001-4	T		f/b-1	3.1	198.5	17	
			f623.002-2	T	c-edge	f/b-1	16.6	127.0	10	2.2
			f623.003-1	T		p/b-2	1.7	191.3	17,24	
			f623.003-2	T		f/b-1	4.5	51.1	11,15,18	
			f623.003-3	T		U	2.0	136.3	6,16,25,28	
			f623.003-4	T	c-edge	fb-1	18.5	239.8	5,7,17,28	
			f623.003-5	T		fb-1	3.6	28.9	7,13,30	
			f623.003-6	T		U	2.0	64.2	15,23	
			f652.002-1	T	c-edge	fb-1	4.9	14.3	1,5,9	
			f634.001-2	T		f/b-2	2.3	33.0	13	
			f634.001-3	T		U	2.4	23.5	11,17	
			f634.002-1	T		p/b-2	28.3	1198.0	2,22,31	
			f634.002-2	T		f/b-1	5.3	79.7	9,12,26	
			f634.003-2	T		f/b-2	7.0	93.0	13	
			f634.004-1	T		U	23.3	292.5	1,3	
			f634.004-2	T	c-edge	U	12.1	178.1	3,4,10	
			f634.004-3	T		f/b-2	7.2	144.1	14	
			f634.005-1	T	c-edge	f/b-2	21.2	1312.7	13,16,22,30	
			f634.005-2	T		p/b-1	9.3	759.4	7,13,17,20,24,38	
			f634.006-1	T		f/b-1	3.4	138.2	10,14,17,26	
			f634.006-2	T	c-edge	f/b-1	12.0	42.1	4,7,10,17,28	
		PC-138	1	T		f/b-2	20.0	398.1	0.7,2,6,11	
			1b	T		p/b-2	8.8	29.3	0.4	
			2-curved	T	c-edge	fb-1	39.1	1026.0	7,10,16,20	
			3-1t	T	c-edge	f/b-2	59.6	188.7	1.7,2.3,9	
			3-1	T		f/b-2	21.5	783.1	5,10,18,23	
			3-2	T		p/b-1	28.5	151.6	0.8,7	
			4t	T	c-edge	f/b-1	28.1	73.1	1.8,9	
			4	T		p/b-2	10.9	50.2	0.8	

Continued on next page…

P [a]	T °C	Exp No.	Trigon	Outline [b]	edge [c]	bottom [d]	Size(um)	Depth (nm)	$a_{\{111\}}$ [e]	$a_{\{100\}}$ [f]
			5-1	T		U	19.3	84.1	0.2,1.1,2.4,5	
			5-2	T		f/b-1	4.1	21.4	4	
			6-1	T	c-edge	U	22.8	475.7	1.5,7,11	
			6-2	T		fb-1	17.9	198.7	4,8	
		PC-139	f145.001-1	TT	c-edge	pb-2	6.3	272.4	3,5,7,13,19	3,7,10
			f145.001-2	TT	c-edge	f/b-1	17.5	387.2	1.9,3,17,25,31	6,10
			f145.001-3	TT	c-edge	f/b-2	6.1	227.5	3,10,20	4,6
			f145.003-1	TT	c-edge	f/b-1	16.1	685.7	1.3,4,10,16,20,23	2,5
			f145.003-2	TT		f/b-1	4.3	154.0	5,7,13,23	4,6,12
			f145.003-3	TT	c-edge	U	8.4	696.4	4,7,12,15,20,25,32,54	3,6,7
			f645.001-1	TT		U	8.5	758.3	53,36,13	13
			f645.001-2	TT		p/b-1	4.3	510.5	6,11,14,27,31,38,48	11
			f645.002-1	TT	c-edge	f/b-2	23.7	725.4	10,16,21,26,35	5,8
			f645.002-2	TT		p/b-2	8.8	909.3	6,10,15,23,31,39,60	11
			f645.003-1	TT		f/b-1	39.8	1904.0	5,11,16,24,27	9
			f645.004-1	TT	c-edge	f/b-2	15.4	296.2	1,7,11,20,27	3
			f645.005-1	TT	c-edge	fb-1	9.2	241.6	4,7,9,11,15,21,27	3,6,7
			f123.002-1	TT		f/b-1	25.8	166.5	4.577	2.4
			f123.003-1	TT		f/b-1	58.8	1600.0	27.3	8,11
			f123.006-5a	TT		f/b-1	15.1	239.1	4.95	0.7
			f145.002	T		f/b-1	6.3	403.1	3,11,17,20,25,29	
			f645.003-2	T		f/b-1	6.7	410.6	25,30	
			f123.001-1	T		p/b-2	16.1	504.4	4.559	
			f123.001-2	T		p/b-2	6.0	164.2	4.5	
			f123.001-3	T		p/b-2	9.3	225.8	4.58	
			f123.001-4	T		p/b-2	6.3	96.3	3.03	
			f123.001-5	T		p/b-2	7.4	212.7	3.812	
			f123.001-6	T		p/b-2	2.0	42.9	3.99	
			f123.001-7	T		f/b-1	1.5	25.8	11.2	
			f123.002-2	T		p/b-2	20.8	775.5	6.128	
			f123.002-3	T		p/b-2	5.0	114.0	4.188	
			f123.003-1b	T		p/b-2	25.9	278.7	1.59,3.8	
			f123.003-2	T		p/b-2	8.7	247.7	5.99	
			f123.004-1	T		p/b-2	6.2	153.3	4.39	
			f123.004-2	T		p/b-2	4.2	99.8	4.06	
			f123.004-3	T		p/b-2	8.6	193.6	5.4	
			f123.004-4	T		p/b-2	13.9	347.5	3.59	
			f123.004-5	T		f/b-1	1.9	12.4	10.06	
			f123.005-1	T		p/b-2	31.6	575.5	2.75	
			f123.006-1	T		p/b-2	14.6	408.6	4.139	
			f123.006-2	T		p/b-2	5.8	111.8	3.333	
			f123.006-3a	T		f/b-1	15.2	167.2	4.811	
			f123.006-3b	T		p/b-2	8.2	193.7	4.093	
			f123.006-4	T		p/b-2	8.7	221.7	4.73	
			f123.006-5	T		p/b-2	5.4	104.4	3.777	
			f123.006-6	T		p/b-2	3.6	112.7	6.141	
			f123.006-7	T		p/b-2	16.2	557.4	5.013	
			f123.006-8	T		p/b-2	17.1	484.1	4.813	
		PC-140	f134.1	TT	c-edge	fb-2	43.8	1085.7	1,1.6,3,5,7,9,13,27,34,48	4
			f134.1b	T		f/b-1	9.5	114.9	7	
			f134.2	T		fb-2	13.6	2246.0	12,19,27,33,69	
			f623.7	T	c-edge	fb-1	36.3	241.1	6,14,28.4	
			f623.1	T	c-edge	fb-1	38.7	178.3	4,5,10,18,25	
			f623.2-1	T		pb-2	13.1	366.0	4,6	
			f623.2-2	T		pb-1	6.4	81.7	1.5	

Continued on next page…

P [a]	T °C	Exp No.	Trigon	Outline [b]	edge [c]	bottom [d]	Size(um)	Depth (nm)	$a_{\{111\}}$ [e]	$a_{\{100\}}$ [f]
			f623.2-3	T		fb-1	31.2	420.8	4,12,20,25,31	
			f623.2-4	T		pb-1	7.1	110.1	1.3,2.4,4,5	
			f623.3-1	T		fb-1	34.9	2168.3	21,26,29,32	
			f623.3-2	T		pb-1	8.4	100.3	1.7,2.1,2.5	
			f623.3-3	T		pb-1	6.7	78.6	1.7,2.1,2.9	
			f623.3-4	T		pb-1	7.9	94.8	1.9	
			f623.4.1	T		pb-2	11.7	122.9	0.6,1.1,1.7,2.1,2.8,4	
			f623.4.2	T		pb-1	20.6	557.3	3,4,6,12,24	
			f623.5.1	T		pb-1	14.6	171.2	1.8,2.8	
			f623.5-2	T		pb-1	16.7	218.1	1.1,3,4	
			f623.5-3	T		pb-1	3.8	32.1	1.4	
			f623.6-1	T		fb-1	30.5	78.8	4,8,14,20,28	
			f623.6-2	T		pb-1	15.8	214.7	2,2.5,3.7	
		PC-142	3-2b	TT		fb-1	15.7	1900.7	44,52	3.83
		ALZ-19	6-1	TT		fb-2	19.2	1593.0	8,14,17,24,40,46,61	10,19
			1-1	T		f/b-3	15.6	73.7	4,8,12	
			1-2	T		f/b-2	11.8	14.4	14,17,20,41,52	
			2-1	T		f/b-1	10.0	202.1	18	
			2-2	T		f/b-1	4.8	50.5	14	
			2-3	T		f/b-1	5.5	128.5	0.9,9,14,18	
			2-4	T		f/b-1	5.3	63.7	18	
			3-1	T		f/b-2	14.7	339.8	1.6,5,12,16,33	
			3-2	T		fb-1	28.7	577.5	2.2,9,15,22,40,50	
			3-3	T		fb-1	5.9	65.3	12	
			3-4	T		U	6.1	39.8	1.5,2.4,4,5	
			3-5	T		fb-1	5.2	49.2	3,7,11,17	
			3-6	T		fb-1	4.8	103.5	9,14	
			3-7	T		fb-1	8.8	330.4	13,23	
			4-1	T		fb-1	24.2	59.0	17	
			4-2	T		fb-1	5.1	42.6	9,18	
			4-3	T		fb-1	18.3	382.4	2,7,15,20,26	
			4-4	T		pb-1	4.4	1280.3	22,33,48	
			5-1	T		pb-1	4.7	92.7	2.5,6,11,17	
			5-2	T		fb-2	10.8	1437.7	13,18,25,33,47,57,69	
			5-3	T		fb-1	6.3	93.1	1.5,2.5,7,14	
			5-4	T		fb-2	7.4	901.9	17,20,26,30,38	
			5-5	T		pb-1	5.3	35.7	0.6,10	
			5-6	T		fb-2	9.2	731.5	16,23,32,44,53	
			5-7	T		fb-1	9.9	431.1	19,27	
			6-1b	T		f/b-1	8.9	311.2	10	
			6-2	T		fb-1	5.2	1184.3	36,45,60	
			6-3	T		fb-1	12.1	638.9	20,37,45,59	
			7-1	T		fb-1	9.8	219.3	7,10,12,15	
			7-2	T		fb-1	3.8	209.9	7,13,24	
			7-3	T		fb-1	4.7	374.3	14,18,22	
			7-4	T		pb-1	4.4	146.7	6,20	
			8-1	T		f/b-2	9.3	600.6	18,32,37	
		ALZ-20	1	T		fb-2	9.3	724.6	25	
			3	T		fb-2	12.2	2286.7	20,33,40,52,63	
			4	T		fb-1	14.8	520.9	13,20,23	
			5	T		fb-1	19.0	1161.0	16,23	
			9	T		f/b-1	11.0	163.0	4,10,16	
			10	T		f/b-2	10.1	249.7	20,27	
			11	T		f/b-1	15.4	839.7	13,21	

Continued on next page…

P [a]	T °C	Exp No.	Trigon	Outline [b]	edge [c]	bottom [d]	Size(um)	Depth (nm)	$a_{\{111\}}$ [e]	$a_{\{100\}}$ [f]
			6-1	T		f/b-1	11.0	194.7	19	
			6-2	T		pb-1	11.3	51.6	0.5,2.8,10	
			7-1	T		U	10.3	77.1	0.2,1.5,12	
			7-2	T		f/b-2	13.2	113.0	0.7,3,6,12	
			8-1	T		fb-1	17.2	1845.3	12,18,23,28,31,36	
			8-2	T		fb-1	21.4	884.3	9,18,25,31	
			13-1	T		fb-1	12.2	209.7	0.5,18	
			13-2	T		fb-1	11.4	355.4	18,21,27	
			13-3	T		fb-1	11.4	131.5	18,24	
			13-4	T		fb-1	11.4	443.0	19,24	
			13-5	T		U	7.9	125.4	0.5,0.7,1.8	
		PC-144	1	T		fb-1	15.2	613.6	21,24,35,58	
			2-1	T		pb-2	12.5	64.7	0.8,3,10	
			2-2	T		pb-2	2.3	12.9	0.9	
			3-1	T		fb-1	24.7	149.0	0.7,7,19	
			3-2	T		pb-2	9.1	108.3	1.7	
			4	T		U	12.3	326.7	21	
			5	T		Pb-1	24.3	2335.0	11,17,22,27,33,40,64	
			6	T		fb-1	12.3	388.0	18,22	
			7	T		U	12.6	73.8	2.2,7,19	
			8-1	T		f/b-2	13.2	267.9	0.7,18	
			8-2	T		fb-1	17.4	351.0	0.4,7,20	
		ALZ-22	6-1	broken-TT		fb-1	39.1	376.6	5,12,17	
			1	T		pb-2	23.3	615.0	0.7,20	
			2	T		f/b-1	20.9	206.3	16	
			2b	T		pb-2	16.7	102.1	1.8	
			3	T		pb-2	18.9	171.0	0.9,4,7	
			4-1	T		fb-1	36.9	206.5	10,15,22	
			4-2	T		pb-2	7.5	25.6	0.6	
			5-1	T		fb-1	23.3	1622.3	21	
			6-2	T		fb-1	17.9	101.9	0.6,8,16	
			6-3	T		pb-2	12.2	228.2	1.2.15.20	
			7-1	T		U	26.2	69.6	2.1,5	
			7-2	T		f/b-1	38.3	260.4	1.4,3,12,16	
			7-3	T		pb-2	18.6	234.4	0.9,18,27	
			7-4	T		fb-3	17.1	86.6	10	
			8-1	T		fb-1	18.0	156.6	4,6,17,20	
			8-2	T		fb-1	19.4	655.8	20,23	
			8-3	T		fb-1	19.3	320.3	17	
			8-4	T		fb-1	25.6	804.4	0.6,5,10,18,22	
3	1250	PC-156	1-2	TT	c-edge	fb-2	32.3	55.0	0.5,1.1,7	3
			2-1	TT	c-edge	fb-1	25.5	159.6	6,17	2.8
			2-2	TT	c-edge	fb-1	43.6	333.9	0.9,5,14,17	4,5
			4-3	TT	c-edge	fb-3	35.5	396.9	3,7,17,28	4,6
			6-1	TT	c-edge	fb-1	26.4	462.4	10,16,20,29	-
			8-2	TT	c-edge	f/b-1	60.1	2530.0	8,19,48,67	4,8
			1-1	T		U	6.1	92.6	1.3,4	
			1-3	T		U	7.4	22.3	0.2,5	
			2-3	T		pb-1	9.1	153.2	1.1,7	
			2-4	T		U	7.0	58.6	1.5,3	
			2-5	T		fb-1	6.3	107.2	8.3	
			2-6	T		fb-1	17.6	97.7	8.3	
			3-1	T		fb-1	38.1	107.8	7	
			3-2	T		pb-2	11.4	184.0	3,8	
			3-3	T		f/b-2	11.2	396.4	9,13	

Continued on next page…

P [a]	T °C	Exp No.	Trigon	Outline [b]	edge [c]	bottom [d]	Size(um)	Depth (nm)		$a_{\{111\}}$ [e]	$a_{\{100\}}$ [f]
			3-4	T		f/b-1	8.2	61.7	7.2		
			4-1	T		fb-1	12.6	225.6	2.2,7,9		
			4-2	T		fb-1	8.6	156.7	7		
			4-4	T		fb-1	8.9	196.5	7		
			5	T		fb-1	3.2	94.2	1.7,7		
			6-2	T		pb-1	7.1	135.3	0.9,8		
			7	T		fb-1	8.8	174.1	8		
			8-1	T		pb-1	9.4	656.2	10,18,26		
		ALZ-32	0-1	TT	c-edge	f/b-1	42.9	392.1	2,8		2,3,4
			1-4	TT		fb-1	30.7	171.6	6		1.1
			5-2	TT	c-edge	fb-1	24.7	410.8	8		1
			9-1	TT	c-edge	fb-1	36.3	33.1	5		1.7
			4-1	TT		fb-1	34.5	478.7	8.2		0.9
			0-2	T		pb-2	10.8	65.6	1		
			0-3	T		fb-1	11.9	38.8	7		
			0-4	T		fb-1	11.9	62.5	1,6		
			0-5	T		fb-1	13.3	490.7	8		
			0-6	T		pb-2	9.4	89.9	1,3		
			1-1	T		fb-1	13.6	453.3	7		
			1-2	T		fb-1	10.6	93.4	6		
			1-3	T		fb-1	12.7	73.9			
			1-5	T		pb-2	8.3	42.1	0.9		
			2	T		fb-1	14.2	427.3	4,8		
			3	T		fb-1	21.5	159.3	2,8		
			4-2	T		pb-1	7.9	92.9	2.2		
			4-3	T		fb-1	9.6	69.1	8.2		
			4-4	T		fb-1	18.0	232.3	9.3		
			4-5	T		fb-1	13.8	147.3	7		
			5-1	T		pb-2	9.5	430.8	8		
			6	T	c-edge	fb	5.1	89.6	0.7,9		
			7	T		fb-1	12.0	66.2	6		
			7b	T		pb-1	6.0	124.5	4		
			8-1	T		fb-1	16.5	106.4	7		
			8-2	T		fb-1	23.6	193.8	1.7,5,9		
			9-2	T		fb-1	24.8	139.4	8		
			9-3	T		fb-1	9.7	254.4	7		
			9-4	T		pb-2	6.1	28.2	0.9		
			10-1	T		fb-1	16.8	457.7	1.5,8,22,47		
			10-2	T		fb-1	12.2	162.6	7		
			10-3	T		pb-1	11.1	191.3	0.6,1.6,7		
			10-4	T		fb-1	15.0	240.0	8		
			10-5	T		pb-1	9.3	38.2	0.5,1.3		
		PC-158	2-5	broken-TT		fb-1	17.1	113.4	5		
		ALZ-35	5-1	broken-TT	c-edge	fb-1	23.3	117.7	5		
			1-1	T		fb-1	8.0	16.5	8		
			1-2	T		pb-2	7.6	69.4	2		
			1-3	T		pb-2	8.9	47.4	0.9		
			1-4	T		fb-2	5.8	38.4	0.5,3		
			1-5	T		fb-1	8.8	51.0	5		
			1-6	T		fb-2	9.8	221.4	6,5		
			2-1	T		U	9.5	38.4	0.3,2.5		
			2-2	T		U	11.5	59.6	0.6,4,7		
			2-3	T		pb-2	5.6	25.8	0.8		
			2-4	T		pb-2	11.4	136.1	1,5		

Continued on next page…

P [a]	T °C	Exp No.	Trigon	Outline [b]	edge [c]	bottom [d]	Size(um)	Depth (nm)	$a_{\{111\}}$ [e]	$a_{\{100\}}$ [f]
			2-6	T		fb-1	10.3	32.3	3	
			3-1	T		pb-1	3.5	19.9	0.4,1.7	
			3-2	T		fb-2	10.6	387.0	7,11	
			3-3	T		fb-2	37.5	277.1	3,5,12	
			3-4	T		pb-1	9.4	451.0	5,8,11,16	
			4	T		fb-2	14.4	1046.0	7,15,38,42	
			5-2	T		fb-1	7.2	68.7	10	
			5-2b	T		U	4.3	152.6	4,6,9	
			5-3	T		fb-1	10.4	109.6	5	
		ALZ-36	1	T		fb-1	19.8	305.0	2.6,4,7	
			2-1	T		fb-2	13.2	207.5	4,7	
			2-2	T		fb-1	10.3	19.4	3	
			2-3	T		pb-2	6.6	57.7	1.1,3	
			2-4	T		pb-2	4.5	34.5	1.7	
			2-5	T		fb-1	15.9	60.4	4	
			3-1	T		pb-2	8.0	98.6	2.3	
			3-2	T		fb-1	20.5	311.4	4,6	
			3-3	T		fb-1	9.4	26.4	6	
			4-1	T		U	7.6	60.1	4	
			4-2	T		pb-1	13.5	395.8	3,7,17	
			4-3	T		U	6.0	67.1	1.2,1.9,4	
			4-4	T		pb-1	4.6	29.5	1,1.4,2	
			4-5	T		fb-2	5.9	49.5	5	
			5-1	T		pb-1	15.5	411.2	5,6,11,29,35	
			5-2	T		U	5.6	98.3	3	
			5-3	T		pb-1	7.3	187.5	5,11	
			5-4	T		pb-1	11.2	371.0	6,7,13	
			5-5	T		pb-1	11.2	247.7	4,7,10	
			5-6	T		pb-1	10.7	396.5	7,12	
			5-7	T		fb-1	5.8	39.3	3	
			6-1	T		fb-1	7.4	82.7	1,2.1,5	
			6-2	T		pb-1	12.6	303.5	2.4,7,13,17	
			6-3	T		pb-1	8.6	285.3	2.7,6,9	
			6-4	T		fb-1	10.0	269.9	6	
			6-5	T		fb-1	23.8	118.7	4	
			6-6	T		fb-1	9.2	9.1	5	
2	1350	PC-101	003-2	TT		f/b-1	36.4	551.4	6.9,9.4,12.9,21.3	7,9,5
			001-1	T		f/b-1	14.9	77.5	5.3	
			001-2	T		f/b-2	16.5	332.6	5.0,7.1,8.9,10.4,14.8	
			001-3	T		f/b-2	15.9	293.4	4.8,5.5,6.6,10.3,12.8,13.8	
			002	T		f/b-2	9.7	1157.0	16.8,21.2,29.7,36.2,40.4,43,,54.5	
			003-1	T		f/b-2	10.1	2035.2	8.0,10.3,12.7,17.1	
			005-1	T		f/b-1	13.9	180.3	9	
			005-2	T		f/b-2	10.2	136.1	10.3,8.2,5.6,2.7	
			005-3	T		f/b-1	15.6	173.2	8.8	
			006-1	T		f/b-2	9.6	119.1	7.3,4.3	
			006-2	T		f/b-2	13.7	484.3	13,9.0,7.3,5.5	
			007-1	T		f/b-2	8.7	1096.0	11.5,15.2,30.5,35.4,40.1,46.3	
			007-2	T		f/b-2	6.2	260.7	27.6,11.6,9.1	
			008-1	T		f/b-2	22.5	172.4	6,8.3,12	
			008-3	T		f/b-1	16.6	42.2	7.5	
			009-1	T		f/b-2	6.2	354.5	8,9.5,15.3	
			009-2i	T		f/b-2	9.0	290.4	13.1,9.7,6.5	
			009-2o	T		f/b-1	14.6	75.1	6.12	

Continued on next page…

P [a]	T °C	Exp No.	Trigon	Outline [b]	edge [c]	bottom [d]	Size(um)	Depth (nm)	$a_{\{111\}}$ [e]	$a_{\{100\}}$ [f]
	1350	PC-124	002	TT		f/b-1	70.1	1050.0	8.608	1
			001	T		f/b-1	51.9	244.3	7.246	
	1350	PC-125	002-i	TT		f/b-1	7.8	6.0		1.3
			002-6	TT		f/b-1	8.8	73.1	6.127	4
			001	T		p/b-2	30.9	1688.0	34.1,21.4,10.9,7.7	
			002-0	T		f/b-1	22.4	279.6	6.931,7.526	
			002-1	T		p/b-2	0.9	14.2	3.67	
			002-2	T		f/b-1	3.0	23.1	3.01	
			003	T		f/b-2	45.2	2704.0	12.79,7.27,9.725,6.89	
			004	T		f/b-1	41.2	797.7	22.46,4.264	
			005	T		f/b-1	10.3	236.2	6.4	
			006	T		p/b-1	20.8	1390.0	12.06,7.994,6.773	

a: P in GPa;

b: H= hexagon;T= trigon; TT= truncated trigon;

c: C-edges= curved edges;

d: f/b-1= trapzoid flat-bottomed trigon; f/b-2: trumpted flat-bottomed trigon;p/b-1: trumpted point-bottomed trigon; p/b-2: V-shaped point-

e: $a_{\{111\}}$: wall angle of W_{111} face relative to {111} face

f: $a_{\{100\}}$: wall angle of W_{100} relative to {111} face;

APPENDIX G. COPYRIGHT AGREEMENT

Schweizerbart science publishers

Dear Dr. Zhang,

We herewith grant you permission to use your Word document in your thesis. Please state the original source and mention our website: www.schweizerbart.de

Kind regards

A. Nägele

> > >Content: Records of mantle metasomatism in the morphology of diamonds from the Slave craton. Volume 24, Number 4, August 2012, pp. 619-632.

> > > Thesis title: DIAMOND RESORPTION MORPHOLOGY AS A FLUID PROXY IN DIAMOND-BEARING ENVIRONMENTS: CONSTRAINTS FROM EMPIRICAL AND EXPERIMENTAL STUDY.
> > > Language: En
> > > E. Schweizerbart Science Publishers
> > > Gebr. Borntraeger Science Publishers (Berlin-Stuttgart)
> > > Johannesstr. 3A 70176 Stuttgart, Germany
> > > Phone ++49-(0)711-3514560 / Fax ++49-(0)711-351456-99

> > > www.schweizerbart.de

ELSEVIER LICENSE
TERMS AND CONDITIONS

Feb 23, 2016

This is a License Agreement between Zhihai Zhang ("You") and Elsevier ("Elsevier") provided by Copyright Clearance Center ("CCC"). The license consists of your order details, the terms and conditions provided by Elsevier, and the payment terms and conditions.

All payments must be made in full to CCC. For payment instructions, please see information listed at the bottom of this form.

Supplier	Elsevier Limited The Boulevard,Langford Lane Kidlington,Oxford,OX5 1GB,UK
Registered Company Number	1982084
Customer name	Zhihai Zhang
Customer address	Dalhousie University Halifax, NS B3H2Z9
License number	3814830011253
License date	Feb 23, 2016
Licensed content publisher	Elsevier
Licensed content publication	Lithos
Licensed content title	Evolution of diamond resorption in a silicic aqueous fluid at 1–3GPa: Application to kimberlite emplacement and mantle metasomatism
Licensed content author	Zhihai Zhang,Yana Fedortchouk,Jacob J. Hanley
Licensed content date	15 June 2015
Licensed content volume number	227
Licensed content issue number	n/a

Number of pages	15
Start Page	179
End Page	193
Type of Use	reuse in a thesis/dissertation
Portion	full article
Format	electronic
Are you the author of this Elsevier article?	Yes
Will you be translating?	No
Title of your thesis/dissertation	DIAMOND RESORPTION MORPHOLOGY AS A FLUID PROXY IN DIAMOND-BEARING ENVIRONMENTS: CONSTRAINTS FROM EMPIRICAL AND EXPERIMENTAL STUDY
Expected completion date	Mar 2016
Estimated size (number of pages)	300
Elsevier VAT number	GB 494 6272 12
Permissions price	0.00 CAD
VAT/Local Sales Tax	0.00 CAD / 0.00 GBP
Total	0.00 CAD
Terms and Conditions	